



The University of Sheffield

**DISPERSION OF A HIGHLY VISCOUS
SURFACTANT BINDER IN A
HIGH SHEAR BATCH MIXER FOR
DETERGENT GRANULATION**

by

Menan Balashanmugam

THESIS SUBMITTED IN PARTIAL FULFILMENT OF THE REQUIREMENTS FOR
THE DEGREE OF DOCTOR OF PHILOSOPHY

DEPARTMENT OF CHEMICAL & BIOLOGICAL ENGINEERING
JANUARY 2017

Abstract

A key difference in detergent granulation, compared to most granulation processes conducted in the pharmaceutical and food industries is the high viscosity of the surfactant binder. These surfactants are approximately $\times 10^4$ more viscous than water and this makes handling the substance a challenge. Previous studies have primarily focused on systems using liquid binders that are of a lower viscosity. This research aims to understand the initial dispersion of a highly viscous, semi or soft-solid binder (surfactant) in a high shear wet agglomeration process. Experiments were conducted with a view to outlining a mechanism for binder dispersion, which involves the breakup of lumps of binder, as a result of the mechanical action of the impeller and the powder bed. The mechanistic understanding was subsequently used to create and validate a model that describes binder breakage. Another key deliverable of this research was to develop a technique for monitoring the dispersion of a binder *in situ*.

The influence of the method of binder delivery on granule attributes such as size, binder content and granule strength were investigated in a vertical shaft 10 L high shear granulator. A typical powdered detergent formulation was used for this study, and consists of a mixture of surfactant (binder), zeolite (powder) and soda ash (powder). The binder was either injected (as a continuous stream) or preloaded into the mixer (as one large blob). Varying the method of binder delivery changes both the rate of binder addition and initial size of the semi-solid binder. At low to moderate agitation intensities, the results suggest that injection improves initial dispersion and subsequent distribution of binder in a moving bed of powder.

In order to develop a mechanistic understanding of the binder dispersion process, small scale experiments were conducted in a 100 ml high shear mixer (this equipment is a scaled down replica of the 10 L high shear mixer). This is the first study to introduce the concept of “breakage” of lumps of binder, during its initial dispersion. In other words, binder dispersion occurs when lumps of binder get coated with powder and are subsequently broken up within the mixer. The coated lumps of binder are referred to as powder coated binder particles (PCBPs). Scaling down the operation enables binder breakage to be monitored in more detail. These PCBPs undergo a size reduction process. Experiments were conducted using zeolite and soda ash (of two different sizes), and the

Abstract

mixer was operated at different speeds. Results reveal that larger and rougher primary particles disperse the binder more effectively in a moving bed of powder, and also a high impeller speed is required for better initial dispersion of the binder into powder formulations that consist of a large proportion of fine material.

A population balance model that describes the breakage of the semi-solid binder was also developed. The model predicts the change in the length of the binder particles, as a function of time. Other features of the model include a selection function for the binder particles based on their initial length (larger binder particles are more likely to undergo breakage than smaller ones). There are two parameters which could be changed in the model: the initial length of the parent binder particle and the selection constant. The analytical solution to the population balance equation indicates that the variation in the size distribution is self-similar with time. It was also found that the mean length of the PCBPs predicted using the model is in good agreement with the experimentally determined mean length. A population balance model, coupled with a kinetics approach has, therefore, been used to successfully describe the binder dispersion (breakage) process.

This is the first study to also introduce a non-invasive technique (thermal imaging) for online monitoring of binder dispersion in a moving bed of powder. Experiments were conducted in a 10 L high shear mixer and a pilot scale 32 L paddle mixer. Thermal imaging was used to study the influence of the method of binder delivery on its subsequent dispersion for a non-reactive system. Results suggest injecting the binder leads to a more rapid and even distribution throughout the powder bed. The thermal imaging technique was also used to understand binder dispersion in a reactive granulation process. The exothermic reaction between the acidic binder and basic powder produces a heat signature that could be traced. The effect of particle size and impeller speed on the dispersion of the reactive binder was monitored and the results suggest that larger particles disperse the binder more evenly, and higher impeller speeds promote improved dispersion too.

“It may not mean nothing to y'all
But understand nothing was done for me
So I don't plan on stopping at all
And I want this to be forever mine”

- *Aubrey D. Graham*

Acknowledgements

I would like to extend my thanks to the many people who so generously contributed to the work presented in this thesis. Special mentions go to my enthusiastic supervisors, Professor Agba Salman for his sound advice on experimental work and Professor Michael Hounslow for his guidance with the modelling work. My PhD has been an amazing experience, and I thank Agba and Mike wholeheartedly, not only for their tremendous academic support, but also for giving me so many wonderful opportunities throughout the duration of my course.

I would also like to thank Procter & Gamble for funding this research work. My profound gratitude goes to Dr. Yuen Sin Cheong and Dr. Hong Sing Tan at P&G, who have been truly dedicated industrial supervisors. I am particularly indebted to Yuen Sin for his constant faith in my lab work, and for generously hosting me in Beijing. I have very fond memories of my time there.

I thank Dr. Martin Pitt and Dr. Seetharaman Vaidyanathan for encouraging me to embark on a PhD and for providing me with a sound academic foundation for doing so. I am also grateful for the assistance given by the departmental technicians. Notably Horace McFarlane, Usman Younis, Keith Penny, Mark Jones and Adrian Lumby for their help in building, improving and repairing various equipment for my PhD.

My gratitude also extends to members of the Particle Products Group (both past and present alike) for all their help, support and encouragement and also for making my life as PhD student a thoroughly enjoyable experience. Special mention goes to Dr. Gavin Reynolds and Dr. Ian Gabbott for convincing me to specialise in Granulation, and for providing me with fantastic lab training at AstraZeneca, before I started my course. And to Dr. Christine Haider for further nurturing my enthusiasm in Granulation. Thanks to Dr. Kate Pitt for her meticulous reviews and general help during the early years of my PhD. I embarked on this journey with my friends Chalak, Mohammed, Riyadh, Syed and Zhiyu, and I will always cherish the special bond we have developed over the years. I would also like to say thank you to Alessandra, Ali, Arthi, Bilal, Bob, Chiamaka, Chuan, Constantijn, Ei Leen, Feng, Jiankai, Kawther, Kimiaki, Mingzhe, Osama, Qing, Ranjit, Robert, Selassie, Sushma, Vikram, Wafaa and Xavier for making my time at Sheffield University truly wonderful.

Finally, but by no means least, thanks go to my dearest Mother, Abi, Soban and Dad for their unbelievable support. They are the most important people in my world and I dedicate this thesis to them.

List of Publications and Presentations

Journal publications:

Balashanmugam, M., Cheong, Y.S., Hounslow, M.J. and Salman, A.D., 2015. *Semi-solid paste binder dispersion in a moving powder bed*. Procedia Engineering, 102, 626-633.

Balashanmugam, M., Cheong, Y.S., Alam, Z., Hounslow, M.J. and Salman, A.D., 2016. *Dispersion of a semi-solid binder in a moving powder bed during detergent agglomeration*. Chemical Engineering Research and Design, 110, 32-42.

Conference publications/presentations:

Balashanmugam, M., Cheong, Y.S., Bayly, A. E., Hounslow, M.J. and Salman, A.D., 2013. *Semi-solid binder dispersion in detergent agglomeration*. 6th International Granulation Workshop, Sheffield, UK.

Balashanmugam, M., Cheong, Y.S., Hounslow, M.J. and Salman, A.D., 2014. *Semi-solid paste binder dispersion in a moving powder bed*. The 7th World Congress on Particle Technology, Beijing, China.

Balashanmugam, M., Cheong, Y.S., Alam, Z., Hounslow, M.J. and Salman, A.D., 2015. *Dispersion of a semi-solid binder in a moving powder bed during detergent agglomeration*. 7th International Granulation Workshop, Sheffield, UK.

Table of Contents

ABSTRACT	I
ACKNOWLEDGEMENTS	IV
LIST OF PUBLICATIONS AND PRESENTATIONS.....	V
LIST OF FIGURES	X
LIST OF TABLES	XVII
NOMENCLATURE.....	XVIII
CHAPTER 1 INTRODUCTION	1
1.1 The research problem.....	1
1.2 What is granulation?	2
1.3 Thesis structure	5
CHAPTER 2 LITERATURE REVIEW.....	6
2.1 Introduction	6
2.2 Granulation and high shear mixers	6
2.3 Detergents and surfactants	14
2.4 Classes of surfactants	16
2.5 What is a semi-solid?	18
2.6 Inorganic solid components in detergent formulations.....	18
2.6.1 Sodium carbonate.....	18
2.6.2 Zeolite	18
2.6.3 Sodium silicate.....	19
2.6.4 Sodium sulphate	19
2.6.5 Sodium tripolyphosphate	19
2.7 Detergent agglomeration process	19
2.8 Non-reactive detergent agglomeration	22
2.8.1 Changes in the bulk density and Hausner ratio	25
2.8.2 Changes in granule porosity and mean granule saturation.....	29
2.8.3 Granulation regime maps	30
2.9 Reactive detergent agglomeration using LAS acid	33
2.10 Effect of binder viscosity	41
2.11 Effect of binder droplet size	42
2.12 Effect of impeller speed	45
2.13 Effect of primary particle size.....	48
2.14 Effect of the method of binder delivery on granule properties	48
2.15 Summary of recent work and identification of knowledge gaps.....	51
2.16 Particle size	52
2.17 Particle shape	53
2.18 Particle size distributions	54
2.19 Quantification of particle size distributions	56
2.20 Modelling dispersion using a population balance approach	57
CHAPTER 3 EXPERIMENTAL METHODOLOGY AND CHARACTERISATION OF MATERIALS.....	61

Table of contents

3.1	Introduction	61
3.2	High shear mixers	61
3.2.1	10 L Roto Junior high shear mixer.....	62
3.2.2	“Mini-mixer”.....	62
3.2.3	32 L Bella B-32-XN paddle mixer.....	63
3.3	Materials.....	65
3.3.1	Zeolites	66
3.3.2	Sodium carbonate	67
3.3.3	Sodium alkyl ether sulphate paste (AE3S)	69
3.3.4	Linear alkyl benzene sulphonic (LAS) acid	70
3.4	Binder viscosity.....	71
3.5	Binder wettability.....	78
3.6	Measuring the size of particles/granules	78
3.7	Microscopy.....	80
3.8	Scanning electron microscopy	80
3.9	Powder flowability	83
3.10	Climatic chamber	84
3.11	Granule preparation.....	85
3.12	Optical imaging using a high speed camera.....	85
3.13	Thermal imaging	86
3.14	Particle image velocimetry.....	89
3.15	Measuring granule strength and powder coated binder particle (PCBP) hardness.....	90
3.15.1	Uni-axial confined compression technique	90
3.15.2	Indentation of PCBPs.....	92
3.16	Preparation of compacts	94
3.17	UV spectroscopy	94
3.18	X-ray microtomography.....	96
CHAPTER 4 EFFECT OF BINDER DELIVERY METHOD ON GRANULE GROWTH AND BINDER DISTRIBUTION.....		98
4.1	Introduction	98
4.2	Production of surfactant droplets	99
4.3	What happens at the interface between the paste and the powder?	102
4.4	Isolating the effects of shear and impact.....	102
4.5	Injecting and preloading the binder	103
4.6	Binder distribution	115
4.7	Granule strength	119
4.8	Tracking binder dispersion <i>in situ</i>	121
4.9	Conclusions	126
CHAPTER 5 SEMI-SOLID BINDER BREAKAGE		128
5.1	Introduction	128
5.2	Key stages in dispersing a viscous binder.....	129
5.3	Quantifying the adhesion between the powder and binder	131
5.4	Granulation methodology.....	134
5.5	Determining the constitution of a PCBP	136
5.6	Monitoring the rate of powder layering	139

Table of contents

5.7	Binder size reduction and breakage patterns.....	145
5.8	Qualitative analysis of PCBP surface attributes.....	150
5.9	Changes in the internal makeup of a PCBP with time	153
5.10	Changes in the mechanical properties of the PCBPs with time	154
5.11	Conclusions	160
CHAPTER 6 ASYMPTOTIC SELF-SIMILAR MODEL FOR BREAKAGE		162
6.1	Introduction	162
6.2	Probability functions	163
6.3	Particle coalescence	164
6.4	Continuous form of the PBE	165
6.5	Spatial variation – micro-distributed form.....	167
6.6	1-D PBE for granulation	168
6.7	Binder breakage	168
6.8	The breakage kernel	170
6.9	Moments.....	172
6.10	Assumptions of the present model	172
6.11	Dimensionless form of PBE.....	175
6.12	Moment equation	175
6.13	Asymptotic self-similar solution of the PBE	177
6.14	Determining the number based frequency density, q_0 , with time	181
6.15	Conclusions	182
CHAPTER 7 VALIDATION OF THE POPULATION BALANCE MODEL FOR BREAKAGE		184
7.1	Methodology for determining k	184
7.2	Fitting trend lines to the experimental data.....	184
7.3	Comparing the experimental mean length with the predicted mean length..	190
7.4	Conclusions	191
CHAPTER 8 REACTIVE GRANULATION USING LINEAR ALKYLBENZENE SULPHONIC ACID		193
8.1	Introduction	193
8.2	Paddle mixers	193
8.3	Simulating nuclei formation using droplet of binder on a static powder bed	196
8.4	Monitoring the dispersion of HLAS in situ	200
8.5	Effect of particle size on binder dispersion.....	203
8.6	Effect of impeller speed on binder dispersion	205
8.7	Conclusions	207
CHAPTER 9 CONCLUSIONS AND FURTHER WORK.....		209
9.1	Effect of the method of binder delivery	209
9.2	Semi-solid binder breakage.....	210
9.3	Modelling binder breakage	211
9.4	Online monitoring of binder dispersion in situ	212
9.5	Further work.....	213
9.5.1	Understanding the formation of wall make-up	213
9.5.2	Online near infrared (NIR) imaging for monitoring binder distribution ..	213
9.5.3	Uses of the population balance model and further improvements	214

Table of contents

REFERENCES.....	216
APPENDIX I METHOD FOR DETERMINING POROSITY FROM XRT	222
APPENDIX II INDENTATION OF PCBPS	224
II.1 Zeolite.....	224
II.2 Ground ash.....	226
II.3 Light ash	229
APPENDIX III THE DIRAC'S DELTA FUNCTION.....	232
APPENDIX IV THE MOMENT EQUATION.....	233

List of Figures

Figure 2.1. Granulation mechanism for low viscous binders (Iveson et al., 2001a).....	7
Figure 2.2. Spatial agglomeration structures - adapted from literature (Iveson et al., 2001a).....	8
Figure 2.3. Schematic of the high shear mixer.	11
Figure 2.4. Mechanisms of binder dispersion (i) distribution (ii) immersion (Schaefer and Mathiesen, 1996a).....	12
Figure 2.5. The nucleation map proposed by Hapgood et al. (2003).....	13
Figure 2.6. Granule growth regime map proposed by Iveson et al. (2001b).	13
Figure 2.7. a) structure of a surfactant molecule and b) interaction between the surfactant and water – adapted from Myers (2006).....	15
Figure 2.8. Commonly used types of surfactants and their availability – adapted from Levinson (2009).....	17
Figure 2.9. Process flow diagram for detergent agglomeration (Mort et al., 2001).....	20
Figure 2.10. Laundry detergent manufacture process (Capeci et al., 1996).	21
Figure 2.11. Change in granule morphology with time (a) powdery (90 s), (b) beginning of crumble (180 s), (c) end of crumble (240 s), (d) crumble-agglomerate (300 s), (e) agglomerate (480 s) and (f) wet agglomerate (480 s). Zeolite was granulated with LAS acid (45 wt%) in a 3 L domestic food processor at 1350 rpm, 22°C (Rough et al., 2005b).....	24
Figure 2.12. Size distribution of the granules shown in Figure 2.11 at different times (Rough et al., 2005b).	25
Figure 2.13. Bulk density against mixing time for a 45 wt% LAS–zeolite mixture (Rough et al., 2003). Dotted line indicates the beginning of the crumble regime.	26
Figure 2.14. Bulk density against scaled mixing time for a 45 wt% LAS–zeolite mixture at different impeller speeds (Rough et al., 2005b). Dotted line indicates the beginning of the crumble regime.	27
Figure 2.15. Hausner ratio against mixing time for a 45 wt% LAS–zeolite mixture. Note different scales for the Hausner ratios (Rough et al., 2003). Dotted line indicates beginning of the crumble regime.	28
Figure 2.16. Hausner ratio against scaled mixing time for a 45 wt% LAS–zeolite mixture at different impeller speeds. The scaling factor is based on ratio of Froude numbers (Rough et al., 2005b).	29
Figure 2.17. Plot of mean granule porosities (Δ) and mean percent saturation of granules (\bullet) against mixing time for a 45 wt% LAS–zeolite mixture, at an impeller speed of 1350 rpm. The dashed line marks 100% for the saturation axis (Rough et al., 2005b).....	30
Figure 2.18. (a) Plot of ρ_g/P_2 vs. mean saturation for a 45 wt% LAS-zeolite mixture (b) Plot of ρ_g/P_2 vs. mean saturation superimposed on a granulation regime map proposed by Iveson et al. (2001a) (Rough et al., 2005b).	32
Figure 2.19. The effects of neutralisation on binder rheology (Germaná et al., 2009). ‘w’ indicates that 15% water was added to the mixture by mass and the percentage gives an indication of the degree of neutralisation.....	35
Figure 2.20. “Schematic of the particle wetting technique. a) Particle–binder contact. b) Binder wets and spreads on the particle. c) Particle is detached from the liquid reservoir. d) Liquid	

List of figures

bridge ruptures and the binder redistributes, finding an equilibrium position on the particle” (Germaná et al., 2009)	35
Figure 2.21. Contact angle was measured by identifying two tangents: s (surface of the spherical particle) and t (droplet of binder) (Germaná et al., 2009).....	36
Figure 2.22. Effect of relative humidity on contact angle a) 35% RH b) 20% RH (Germaná et al., 2009)	36
Figure 2.23. Experimental set-up for reactive granulation: (a) digital drive unit, (b) drop-wise addition of HLAS acid, (c) jacketed glass vessel with impeller, (d) volumetric measurement of evolved CO ₂ (Schöngut et al., 2013).....	38
Figure 2.24. Carbon dioxide evolution (in moles) with time for variable process (a) temperature and (b) agitation (Schöngut et al., 2013).....	39
Figure 2.25. Particle size distribution with changes in (a) temperature and (b) agitation (Schöngut et al., 2013).....	40
Figure 2.26. Schematic diagram of eccentric cylinder geometry (Feigl et al., 2003).....	43
Figure 2.27. The evolution of a droplet within annular region of two eccentric cylinders. The inner cylinder rotates at two different speeds: 14 and 18 rpm (Feigl et al., 2003).....	43
Figure 2.28. Time lapse image sequence of a PEG 2000 droplet on a moving bed of powder (Chouk et al., 2009)	44
Figure 2.29. Dimensions of a typical spinning riffler tray (Litster et al., 2001).....	45
Figure 2.30. The trend of granule strength versus porosity obtained by the different methods (Rahmanian et al., 2009).....	46
Figure 2.31. “Effect of impeller speed on granule porosity for granules in the size range 1.0–1.18 mm. (a) low viscosity system, (b) high viscosity system” (Mangwandi et al., 2010).	47
Figure 2.32. “Effect of impeller speed on the granule tensile strength of granules in the size range 1.0–1.18 mm. (a) low viscosity system, (b) high viscosity system” (Mangwandi et al., 2010).	47
Figure 2.33. Size-averaged liquid to solid ratio distribution for bulk granulation sample (Reynolds et al., 2004).....	51
Figure 2.34. High shear mixer represented as a constant volume batch reactor where binder dispersion occurs.....	59
Figure 3.1. A 10 L Roto Junior high shear mixer.	62
Figure 3.2. Schematic of the “mini-mixer”	63
Figure 3.3. Image of the 100 ml “mini-mixer”.	63
Figure 3.4. Schematic of the aerial view of the 32 L paddle mixer.	64
Figure 3.5. Side view of the paddle mixer. Binder is injected (red arrows) from the bottom at certain points along the horizontal axis of the mixer.	64
Figure 3.6. Image of the aerial view of the Bella B-32-XN 32 L paddle mixer.	65
Figure 3.7. Effect of the surfactant concentration on the surface tension (KRÜSS, 2014).	68
Figure 3.8. Structure of sodium alkyl ether sulphate.	69
Figure 3.9. Chemical structure of LAS acid.	71

Figure 3.10. Velocity profile between an upper rotating plate and a lower fixed plate separated by a gap, h. The upper geometry moves with a velocity v along the x-axis – adapted from Bohlin (1994).....	72
Figure 3.11. Flow curves for various systems – adapted from Tadros (2011).....	73
Figure 3.12. 40 mm serrated upper geometry and lower plate.....	74
Figure 3.13. Velocity profile across the powder bed.	74
Figure 3.14. Change in the viscosity of the surfactant paste with increasing shear rate.....	75
Figure 3.15. Relationship between shear stress and shear rate for AE3S at 25°C. A Herschel-Bulkley model fit has been used to describe the data.	76
Figure 3.16. Change in the viscosity of HLAS with shear rate at different temperatures.	77
Figure 3.17. Schematic representation of a FTA 125 goniometer.	78
Figure 3.18. Size distribution of the primary particles.....	80
Figure 3.19. SEM images of the primary powder particles.	82
Figure 3.20. SEM of zeolite - ×1700.	83
Figure 3.21. Angle of repose measurement for primary powder particles and commercially manufactured detergent powder.	84
Figure 3.22. Schematic diagram of the set-up used to monitor binder dispersion optically.....	86
Figure 3.23. Thermal image of the paddle mixer. The bright yellow patches indicate binder rich zones.	88
Figure 3.24. Setup for determining the emissivity of a test material.	88
Figure 3.25. Example of a binary image that was imported into the PIV software.	90
Figure 3.26. Typical output from the PIVlab software. Green arrows show the direction as well as the magnitude of the velocity vectors of individual lumps of binder in the mixer.	90
Figure 3.27. Graphical representation of Adams' equation (Adams et al., 1994).	91
Figure 3.28. Zwick Roell Z0.5 compression machine.	92
Figure 3.29. (a) Set-up used for indenting PCBPs, (b) 10 N load cell fitted with an indenter and (c) key dimensions of the 60° diamond pen indenter.	93
Figure 3.30. Concept of absorbance spectroscopy.	94
Figure 3.31. Relationship between absorbance and % transmittance.	95
Figure 3.32. Principles of X-ray tomography (adapted from Jacobs et al., 1995).	96
Figure 4.1. A low viscous droplet gets drawn into a bed of powder by capillary action. The cylinders represent pores or channels in the powder bed.....	98
Figure 4.2. Sessile droplet on a solid surface.....	99
Figure 4.3. Dispensing AE3S binder using needles of different sizes.	101
Figure 4.4. Effect of heat on AE3S (a) before (b) after heating to 100°C for an hour.....	101
Figure 4.5. Images from a time-lapse video of the interface between powder and paste.	102
Figure 4.6. (a) flat-plate impeller (b) pitched impeller.	103
Figure 4.7. Mixing achieved using a flat-plate impeller at 500 rpm. (a) aerial view (b) paste embedded beneath the powder. The paste has migrated to the bottom of the bed.....	103

List of figures

Figure 4.8. Visible changes in binder dispersion in the granulator, with time, at 200 rpm – binder was preloaded as one large blob.	106
Figure 4.9. Change in the mean diameter of the granules with time at 200 rpm.	107
Figure 4.10. Change in the mean diameter of the granules with time at 400 rpm.	107
Figure 4.11. Change in the mean diameter of the granules with time at 800 rpm.	108
Figure 4.12. Mass distribution at 200 rpm - blobs vs. injected.	110
Figure 4.13. Mass distribution at 400 rpm - blobs vs. injected.	112
Figure 4.14. Images of the dry product after 75 s of wet massing (a) 400 rpm – injected and (b) 400 rpm- preloaded.	113
Figure 4.15. Mass distribution at 800 rpm - blobs vs. injected.	114
Figure 4.16. UV spectroscopy control study comparing a surfactant solution with a detergent solution.	115
Figure 4.17. Binder content of different size classes at 200 rpm, after 75 s of wet massing....	117
Figure 4.18. Binder content of different size classes at 400 rpm, after 75 s of wet massing....	117
Figure 4.19. Binder content of different size classes at 800 rpm, after 75 s of wet massing....	118
Figure 4.20. Images of the dry product after 75 s of wet massing at (a) 200 rpm and (b) 800 rpm, for the injected case.	118
Figure 4.21. Granule strength against time – 200 rpm.	119
Figure 4.22. Granule strength against time – 400 rpm.	120
Figure 4.23. Granule strength against time – 800 rpm.	120
Figure 4.24. Strength of the large granules (>2000 µm) against impeller speed at 75 s.	121
Figure 4.25. Large granules (>2000 µm) as seen under a light microscope: (a) 200 rpm (b) 800 rpm.	121
Figure 4.26. Time lapse thermal image sequence of the high shear mixer for both preloaded and injected cases at 200 rpm.	123
Figure 4.27. Variation in the binder concentration at the surface with time, at 200 rpm.	124
Figure 4.28. Time lapse thermal image sequence of the high shear mixer for both preloaded and injected cases at 400 rpm.	125
Figure 4.29. Average surface temperature of the moving bed of powder with time for both preloaded and injected cases at 400 rpm.	126
Figure 5.1. Granulation mechanism for low viscous binders.	130
Figure 5.2. Hypothesis proposed for the layering and fragmentation of paste fragments in a moving powder bed.	131
Figure 5.3. Schematic representation of the apparatus used for preparing cylindrical semi-solid binder particles of a uniform shape and size.	132
Figure 5.4. Schematic representation of the technique for determining the mass of powder that has layered at zero shear.	133
Figure 5.5. Micrographs of the cylindrical strands after coating with primary powders.	134
Figure 5.6. Mass of the PCBP after coating with primary powders.	134

List of figures

Figure 5.7. Viscosity measurement at 25°C before and after a freeze-thaw cycle.	136
Figure 5.8. X-ray scans of the raw materials. Two mean grey values have been reported for three powders - one for a loose powder bed and another for a compact made with a 3 kN compression force.	138
Figure 5.9. XRT images reveal layering is the main mechanism for powder assimilation on the surface of a binder particle (zeolite at 300 rpm).	139
Figure 5.10. Relative change in the mass of the PCPBs as a percentage of the mass of the original binder at 300 rpm.....	140
Figure 5.11. Relative change in the mass of the PCPBs as a percentage of the mass of the original binder at 600 rpm.....	141
Figure 5.12. Layering of particles of different sizes on the surface of a binder fragment.	141
Figure 5.13. Changes in the internal makeup of the granule during transition from the nucleation to the wet-agglomerate regime. Zones within the granule that are rich in binder have been highlighted (yellow ovals).	142
Figure 5.14. Volume fraction of solids in the binder with time at 300 rpm.....	143
Figure 5.15. Volume fraction of solids in the binder with time at 600 rpm.....	144
Figure 5.16. Mass fraction of the primary powder that has been used at 300 rpm.	145
Figure 5.17. Mass fraction of the primary powder that has been used at 600 rpm.	145
Figure 5.18. Size distribution of the binder particles measured using the Camsizer, $D_{v4,3} = 5817 \mu\text{m}$	147
Figure 5.19. Change in the mean diameter ($D_{v4,3}$) of the PCPBs with time at 300 rpm.	149
Figure 5.20. Change in the mean diameter ($D_{v4,3}$) of the PCPBs with time at 600 rpm.	149
Figure 5.21. Micrographs of the PCPBs at different time intervals at 300 rpm.....	152
Figure 5.22. Surface properties of the light ash PCBP at 300 rpm.	153
Figure 5.23. Changes in the structure of PCPBs containing zeolite with time at 300 rpm.....	154
Figure 5.24. The applied stress can be tensile or compressive.	155
Figure 5.25: Sample PCBP pre and post indentation (after 75 s).	157
Figure 5.26. Force vs. displacement curves for the indentation of zeolite PCPBs.	159
Figure 5.27. Force vs. displacement curves for the indentation of ground ash PCPBs.	159
Figure 5.28. Force vs. displacement curves for the indentation of light ash PCPBs.	160
Figure 6.1. Phase changes during the binder dispersion process.	169
Figure 6.2. Diagrammatic representation of binary binder breakage.....	173
Figure 6.3. Probability distribution of the size of the fragments post-breakage.	173
Figure 6.4. A square may be broken down into N^2 self-similar pieces, each with magnification factor, N (Zohuri, 2015).....	177
Figure 7.1. Experimental plot of $\ln q_0$ vs. particle diameter for zeolite at 300 rpm.....	186
Figure 7.2. Experimental plot of $\ln q_0$ vs. particle diameter for zeolite at 600 rpm.....	187
Figure 7.3. Experimental plot of $\ln q_0$ vs. particle diameter for ground ash at 300 rpm.....	187
Figure 7.4. Experimental plot of $\ln q_0$ vs. particle diameter for ground ash at 600 rpm.....	188

List of figures

Figure 7.5. Experimental plot of $\ln q_0$ vs. particle diameter for light ash at 300 rpm.....	188
Figure 7.6. Selection constant against time for zeolite, ground ash and light ash at 300 rpm..	189
Figure 7.7. Plot of selection constant against time for zeolite and ground ash at 600 rpm.....	189
Figure 7.8. Comparing the experimentally determined value for the mean size ($l_{1,0}$) with predicted mean ($l_0/(kt+1) + l_{\min}$).....	191
Figure 8.1. Cross-section through a paddle mixer indicating the location of the fluidised zone (Rodenburg, 2007).	194
Figure 8.2. Porosity of the loose compacts was determined using X-ray tomography – compression load was 500 N.	198
Figure 8.3. Mass of the nuclei - weighed after 48 hours.....	198
Figure 8.4. Spread of a droplet of LAS acid on the surface of a compact.	198
Figure 8.5. Percentage increase in the mass of the nuclei against temperature.	199
Figure 8.6. Schematic of the aerial view of the paddle mixer. The mixer was split into different zones and binder was injected in zones 3 and 4. The dashed line indicates the position of the fluidised zone.	201
Figure 8.7. (a) thermal image and (b)binary image.	202
Figure 8.8. Output from PIV analysis showing binder movement within the paddle mixer as vectors.....	202
Figure 8.9. Volume of binder injected into the mixer.....	203
Figure 8.10. Thermal images comparing the dispersion of binder in a moving bed of ground and light ash at 50 rpm.....	204
Figure 8.11. Average temperature of Zone 1 for a bed of light and ground ash at 50 rpm.....	205
Figure 8.12. Thermal images comparing the dispersion of binder in a moving bed of light and ground ash at 100 rpm.....	206
Figure 8.13. Average temperature of Zone 1 with time.....	207

Appendix figures:

Figure I-1. Slice obtained from the X-ray scanner. Air space is represented by a yellow oval.	222
Figure I-2. Histogram of number of pixels for the 8-bit grey scale image.	222
Figure I-3. Binarised XRT image of the granule.	223
Figure I-4. Histogram of number of pixels for the binary image.....	223
Figure II-1. Force vs. displacement for zeolite at 15 s.....	224
Figure II-2. Force vs. displacement for zeolite at 30 s.....	224
Figure II-3. Force vs. displacement for zeolite at 45 s.....	225
Figure II-4. Force vs. displacement for zeolite at 60 s.....	225
Figure II-5. Force vs. displacement for zeolite at 75 s.....	226
Figure II-6. Force vs. displacement for ground ash at 15 s.....	226

List of figures

Figure II-7. Force vs. displacement for ground ash at 30 s.....	227
Figure II-8. Force vs. displacement for ground ash at 45 s.....	227
Figure II-9. Force vs. displacement for ground ash at 60 s.....	228
Figure II-10. Force vs. displacement for ground ash at 75 s.....	228
Figure II-11. Force vs. displacement for light ash at 15 s.....	229
Figure II-12. Force vs. displacement for light ash at 30 s.....	229
Figure II-13. Force vs. displacement for light ash at 45 s.....	230
Figure II-14. Force vs. displacement for light ash at 60 s.....	230
Figure II-15. Force vs. displacement for light ash at 75 s.....	231
Figure III-1. Graphical representation of the Dirac's delta function (adapted from Grivet-Talocia and Gustavsen, 2015).....	232
Figure IV-1. Transforming $f(l,x)$ into $g(u,v)$	234

List of Tables

Table 2.1. Effect of speed, binder viscosity (temperature) and liquid to solid ratio on the rate at which the system progresses through the different regimes (Rough et al., 2005b).	25
Table 2.2. Geometric equivalent diameters (Figura and Teixeira, 2007).	53
Table 2.3. Definitions of particle shape (adapted from Allen, 1997).....	54
Table 2.4. Characteristics that are frequently used to represent particle size (Figura and Teixeira, 2007).	55
Table 3.1. Properties of STEOL CS-370 surfactant (Stepan, 2010).	70
Table 3.2. Properties of LAS acid (BASF, 2012).	71
Table 3.3. Herschel-Bulkley parameters for AE3S binder at 25°C.	76
Table 3.4. Typical detergent powder composition by mass (excluding surfactant binder).....	85
Table 4.1. Detergent formulation used for the binder delivery study.	104
Table 6.1. Breakage distribution functions (Hill and Ng, 2002). w is the parent particle volume and v is the child particle volume.	172
Table 6.2. Key properties of the model.....	183

Nomenclature

A	projected area
$A(v,t)$	attrition rate
a_s	surface area
B_{brea}	birth of particles of a certain size as a result of breakage
B_{coal}	coalescence birth rate
d	particle diameter
d_A	surface area equivalent sphere
D_{brea}	death of particle as a result of breakage
D_{coal}	coalescence death rate
d_p	projected area equivalent circle
d_{Pe}	perimeter circumference equivalent circle
d_v	volume equivalent sphere
$d_{v,10}$	10 th percentile of the particle size volume based distribution
$d_{v,50}$	50 th percentile (median) of the particle size volume based distribution
$d_{v,90}$	10 th percentile of the particle size volume based distribution
e	restitution coefficient
f	frequency
ff_c	flow function coefficient of the powder
Fr	Froude number
g	acceleration due to gravity
$G(v,t)$	growth/layering rate
h_l	thickness of the layer of liquid on the surface of a particle/granule
k	selection constant
l	particle length
L_T	total length of all granules
M	Mass
m_j	j th moment
$n(x,t)$	average number of particles of size x per unit volume in the discrete case.
$n(x,t)dx$	average number of particles of size between x and x+dx per unit volume in the continuous case.
N_{birth}	net rate of formation of particles of a certain size
n_i	frequency of class m
N_T	total number of particles in the particle state space being considered
Q	particle flow rate
q_0	number based frequency density
q_2	area based frequency density
q_3	volume based frequency density
R	sub-region within particle state space (S)
S	particle state space
s	granule liquid saturation
$S(u)$	selectivity of particles of size u
s_{max}	maximum granule liquid saturation
St^*	critical Stokes deformation number
St_{def}	Stokes deformation number

<i>subscript F</i>	Final
<i>subscript g</i>	granule
<i>subscript I</i>	Initial
<i>subscript l</i>	liquid
<i>t</i>	time
<i>T</i>	temperature
<i>t_p</i>	droplet penetration time
<i>u</i>	particle of volume u
<i>v</i>	particle of volume v
<i>V</i>	volume
<i>x</i>	particle size
<i>x_{area}</i>	diameter of the area equivalent circle
<i>x_i</i>	upper size class limit
<i>x_{i-1}</i>	lower size class limit
<i>x_m</i>	middle value of the size class
<i>Y_g</i>	Yield stress
<i>z</i>	Gradient

Greek characters:

α	aspect ratio
$\beta(v,t)$	nucleation rate of new granules
γ_L	liquid surface tension
ε	porosity
θ	static contact angle
μ	liquid viscosity
v	tip speed
ρ_B	powder bulk density
ρ_L	liquid density
ρ_S	solid density
ρ_t	true density
Φ	cross-sectional area
ϕ_s	solid fraction
ϕ_l	liquid fraction
Ψ	sphericity
Ψ_A	spray flux

Abbreviations:

AE3S	Sodium alkyl ether sulphate paste
CMC	Critical micelle concentration
DEM	Discrete element model
fps	Frames per second
GC	Grounds carbonate (ground ash)
LAS/HLAS	Linear alkyl benzene sulphonlic acid
LC	Light carbonate (light ash)
PBE	Population balance equation
PBM	Population balance model

Nomenclature

PCBP	Powder coated binder particle
PEPT	Particle emission positron tracking
PIV	Particle image velocimetry
PSD	Particle size distribution
rpm	revolutions per minute
XRT	X-ray tomography
Z	Zeolite

Chapter 1

Introduction

Over the last 40 years, the manufacture of laundry detergents has changed significantly with many different product forms being introduced into the market, including liquids, gels, compacts and capsules (Bayly et al., 2009). Despite an increase in the popularity of newer product forms, the powdered form still remains the most popular option.

The powder form offers many advantages over other forms of detergent in that they contain large amounts of inorganic material, which are a lot cheaper than alternatives made using petroleum derivatives. Furthermore, due to the inherently low water (moisture) content within the formulation, it is easier to incorporate other compounds that serve different functions like bleaches and enzymes and to keep such compounds stable for longer (Bayly et al., 2009). Segregation is also easier to prevent in powder formulations providing it is well managed (for example by granulation) in comparison to liquid formulations that are more prone to phase separation.

Detergent is produced either by spray drying or by granulation in a high shear mixer. The granulation process is preferred due to its lower energy consumption, and also the product from the granulation process is denser and stronger. Detergent is granulated using a binder that also functions as the surfactant in the formulation. These binders could either be active i.e. they react with the powder they are mixed into (e.g. linear alkyl benzene sulphonate acid) or inactive (e.g. semi-solid sodium alkyl ether sulphate paste).

What follows is a brief section summarising the motives for this research work. A general background to the field of granulation has also been included here, along with an outline of the structure of this thesis.

1.1 The research problem

This research focuses on understanding one key aspect of high shear granulation that is binder dispersion in a moving bed of powder. In recent years, significant research has been undertaken in order to understand the mechanisms involved in these processes and to develop mathematical models that describe the process of granulation. The majority

have focussed on studying systems using low viscous liquid binders. This research aims to extend this work to soft solid (semi-solid) and reactive surfactant binders used mainly in detergent manufacture, which are highly viscous and paste-like. One of the challenges associated with the use of a highly viscous binder is ensuring its dispersion in a moving bed of powder during the high shear wet granulation process. It is known that binder dispersion influences other aspects such as granule growth, strength and porosity. The study will focus on understanding the dispersion of the binder by mechanical action of both the impeller and powder particles. This is fundamental to understanding the detergent agglomeration process and is a key limiting factor in being able to run equipment at higher process throughputs. The study also aims to predict the behaviour of such binders. Ultimately, this will help in developing methods for improving binder dispersion in a high shear environment.

1.2 What is granulation?

Granulation is used to convert fine powders into more free flowing, easy-to-process granules. There are two different types of granulation processes: wet and dry. The wet granulation process usually involves mixing the powder with a liquid, known as a binder, in specialised process equipment, which encourages the aggregation of the fine powders and binder into larger granules.

The granulation process has the advantage of being able to alter the handling characteristics of a solid formulation without altering its chemical properties. Granulation is often done to avoid powder segregation and help maintain the uniformity of a mixture. It improves the flowability of the powder, as larger aggregates are less cohesive and also helps to minimise dust formation. Furthermore, in tabletting applications, for example, using granules instead of the primary powder in its original form helps to improve the compaction characteristics of the mixture, i.e. produce stronger tablets with a better dissolution profile. Besides the detergent manufacturing industry, the process is widely employed in a range of other industries including the food, pharmaceuticals, and agricultural chemicals (fertilizers).

Granulation refers to any unit operation that processes and changes all or some of the properties of the powdery material that is introduced into it. There are a number of different unit operations which could be used for agglomerating powders, including:

- Fluidised bed granulators – these are employed for wet granulation applications. They can be operated in either a continuous or a batch mode. These units are often equipped with spray nozzles that are used to spray the binder. The binder can be sprayed from either the top or bottom. Mixing occurs as a result of the air that is used to fluidise the powder and binder droplets within the bed. Key process parameters include air temperature and fluidising air velocity (air pressure).
- Twin screw granulators – a relatively new unit operation employed for continuous wet granulation. They are increasingly common in pharmaceutical applications. The mixer consists of a barrel and two intermeshing screws. The screw configuration is made up of two different types of elements: kneading and conveying. Kneading elements promote mixing between the binder and powder, whilst the conveying elements serve to carry the wet material. Different mechanisms will dominate various sections along the length of the screw. Key process variables include screw speed, powder feed rate, length of the screw and screw configuration.
- Roller compactors – a popular method adopted for continuous dry granulation. The equipment contains two counter rotating rollers. These rollers serve to apply a high stress to an incoming flow of powder in order to produce dense compacts called ribbons (Omar et al., 2016). These ribbons can then be milled in order to produce granules. One key advantage of this method is that it eliminates the need for a drying unit operation, as there is no liquid binder involved, thus reducing energy costs. Key process parameters include roller speed, powder feed rate and roller pressure.
- Low shear mixers - refer to rotating drums and pan granulators. Such mixers are low shear as they do not have an impeller. Therefore, the stress achieved within such mixers is a lot lower compared to high shear systems. Generally, the rotating action of the mixing vessel brings about agglomeration of the material. The

binder can be preloaded, poured, sprayed or melted-in (only for solid binders).

Granules tend to be spherical, as attrition at the boundaries smoothens any rough edges and the high centrifugal forces produce granules with high strength and low porosity.

- High shear mixers – these are the most commonly used unit operations for agglomeration. Key features of a high shear mixer include a mixing bowl and impeller that is connected to a drive shaft. A chopper may be present to enhance mixing. The rotating action of the impeller imparts shear and impact (stresses) onto the mixture, to bring about intimate mixing between the constituent elements resulting in the formation of granules. Again, as with low shear mixers, the binder can be preloaded, poured, sprayed or melted-in (solid binders). Key process parameters include impeller speed, chopper speed, binder addition method/rate, and mixing time.

Granulation is a unit operation that has been investigated over many decades. Despite the maturity of the industry as a whole, there are many aspects of granulation that still remain poorly understood. Unlike systems which involve liquids and gases (like distillation and gas absorption for example) which are not only very well understood, but are easily predicted using advanced models, at any scale, or with any variation in the processing condition, most granulation processes are not very well understood. Any models that predict them are empirical at best. Therefore, it is fair to say that our understanding of granulation still remains more of an art form than a precise science. Process understanding and product development comes from experience or trial and error, rather than a fundamental understanding of the underlying physics and chemistry. If a new granular product has to be developed, a number of experiments will have to be performed to determine which formulation properties and or process variable will give the desired granular properties.

1.3 Thesis structure

The thesis is structured in the following order:

- Chapter 2 provides a comprehensive review of the relevant literature and identifies current knowledge gaps in this area of research that this thesis aims to address.
- Chapter 3 discusses the experimental methods, measurement techniques and analytical tools that were used.
- Chapters 4-8 discuss the experimental outcomes. Chapter 4 begins by discussing the effect of the method of binder addition on binder dispersion, as well as the kinetics of the granule growth. Chapter 5 discusses how binder dispersion within the mixer was isolated and attempts to quantify binder dispersion with time. Chapter 6 discusses the development of an asymptotic self-similar model describing binder breakage. Chapter 7 uses the experimental data from Chapter 5 to validate the model that was developed in Chapter 6 to describe binder breakage. And finally Chapter 8 looks at the dispersion of a reactive binder in a paddle mixer.
- Chapter 9 discusses the overall conclusions of this research work and suggests the scope for avenues of further work stemming from this research.
- The appendix provides some supplementary information.

Each chapter begins with a brief introduction and ends with a conclusion that summarises the key findings where appropriate.

Chapter 2 Literature Review

2.1 Introduction

This research concerns the dispersion of highly viscous binders in a moving bed of powder during detergent agglomeration. Prior to discussing specific aspects of detergent agglomeration, this chapter begins by giving a general overview of the agglomeration process and more specifically the high shear wet agglomeration process. Some background will also be given into the various mechanisms that have been proposed for binder dispersion, along with regime maps that have been suggested over the years to predict the granulation process. The latter half of this chapter focuses on the literature concerning the manufacture of dry laundry powder, followed by the identification of knowledge gaps in the research along with the motivation for this research work.

This chapter also gives some background information on particle size and a brief introduction to population balance modelling. These sub-sections will be referred to later on when discussing the model that has been developed to predict the dispersion of a highly viscous binder in a moving bed of powder (Chapter 6 & Chapter 7).

2.2 Granulation and high shear mixers

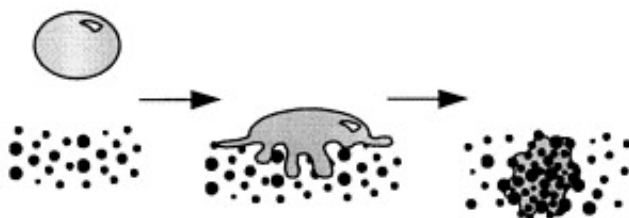
It is well known that in order to get particles to adhere, bonds have to be created between them and these bonds have to be strong enough to prevent them from breaking down as a result of subsequent processing operations. There are several different bonding mechanisms that aid this, including (Summers and Aulton, 2002):

- Adhesive and cohesive forces in immobile liquid films between individual primary particles.
- Interfacial forces in mobile liquid films within granules.
- Solid bridges that are formed after the solvent has evaporated.

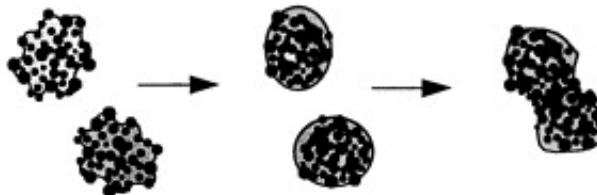
- Forces of attraction between solid particles (van der Waals forces, hydrogen bonds and electrostatic forces).
- Mechanical interlocking between particles.

The general wet granulation process can be divided into three main sub mechanisms namely **wetting and nucleation**, **consolidation and coalescence** and finally **breakage and attrition** (Figure 2.1) (Iveson et al., 2001a).

i. Wetting & Nucleation



ii. Consolidation & Coalescence



iii. Attrition & Breakage

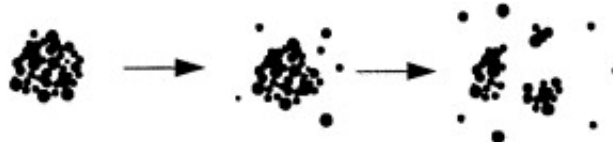


Figure 2.1. Granulation mechanism for low viscous binders (Iveson et al., 2001a).

Nucleation refers to the process of contacting the dry powder with the liquid binder. This step of the granulation process involves distributing the binder throughout the powder bed. This distribution results in the formation of primary agglomerates. Wetting of the particles takes place during the nucleation stage. The degree of particle wetting determines the number of nuclei that are formed. When two wet particles collide they may adhere as a result of the formation of a liquid bridge. The better the spread of the binder over the particles that make up the powder bed, the greater will be the bonding

and adhesion between them upon collision. During early nucleation, there is limited compaction which aids in strengthening the resultant nuclei too.

Different types of spatial structures are formed depending on the degree of binder/liquid saturation (Iveson et al., 2001a), namely pendular, funicular, capillary and droplet (Figure 2.2). In the pendular state, particles are held together by liquid bridges at their contact points. This requires the liquid saturation within the system to be low enough to let discrete bridges exist between the individual particles and their solid surfaces. The capillary structure is only found when the levels of liquid saturation in the system are higher and the resulting granular structure is saturated with liquid binder. All voids between the particles have been filled and any liquid present at the surface of the agglomerate is drawn back from the surface into its interior structure. The funicular state is an intermediate between the pendular and the capillary state, where all voids between the particles are not fully saturated. Finally, the droplet state only occurs when the particles are held within or at the surface of the structure of a droplet. All four of these states could exist during the high shear agglomeration process.

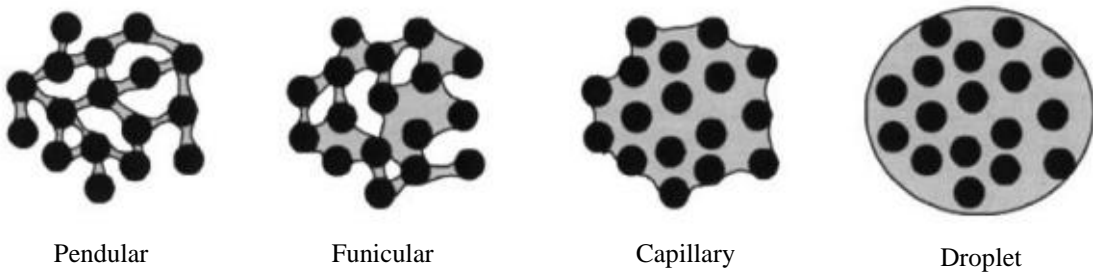


Figure 2.2. Spatial agglomeration structures - adapted from literature (Iveson et al., 2001a).

Granule growth occurs when these primary agglomerates collide and stick to each other. This process is referred to as **coalescence**. When fine particles in the powder bed stick to the surface of an existing agglomerate, this process is referred to as **layering**. As the granules start to collide against one another, as well as the surface of the equipment they gradually begin the process of **consolidation**. This refers to a reduction in the size and the porosity of the granule, as a result of the stresses that act at its surface. Generally, a reduction in the porosity of the granule makes it stronger (Iveson et al., 2001a).

Ennis et al. (1991) suggest that the kinetic energy of any two colliding particles can be dissipated by the viscous forces caused by the layer of binder on their surface. When this condition is satisfied coalescence is said to occur. The ratio of the kinetic energy to the energy of viscous dissipation is given by the dimensionless Stokes Deformation number (Equation 2.1).

$$St = \frac{4\rho_g u d}{9\mu} \quad \text{Equation 2.1}$$

where:

ρ_g is the density of the granule

u is the tangential velocity of the particle

d is the granule diameter

μ is the viscosity of the binder

They also define a critical value for the Stokes Deformation number (St^*) (Equation 2.2). If $St^* > St$, then coalescence is said to occur. The coefficient of restitution (e) is a measure of the restitution between two objects as a result of a collision. It gives an indication of the amount of kinetic energy that is available for the objects to rebound, against the amount of energy that is lost through viscous dissipation. If a thicker layer of binder (h) is present on the surface of the particle then the value of e is lowered.

$$St^* = \left(1 + \frac{1}{e}\right) \ln\left(\frac{h}{h_{asp}}\right) \quad \text{Equation 2.2}$$

where:

e is the coefficient of restitution of the colliding granules

h is the thickness of the layer of binder on the particle surface

h_{asp} is the characteristic height of surface asperities

However, a limitation of this model is that the granules are considered to be rigid bodies, therefore the effects of granule deformation are not accounted for. At higher impeller speeds, it is expected that e will reduce (due to a decrease in the porosity) and h

would increase (as more liquid gets squeezed to the surface through consolidation). Therefore, coalescence would be more prevalent as St^* increases.

A higher binder viscosity would reduce h , as less liquid is available at the surface and this in turn will increase e , therefore St^* decreases, and the rate of coalescence falls. The mixing time (to attain the required level of granule growth) can be shortened if a larger amount of binder reaches the surface of the particle as a result of compaction i.e. if the time required to attain adequate binder saturation can be shortened, then mixing time to achieve the required level of granule growth can be reduced too.

Breakage and attrition refers to the process whereby wet or even dry granules are broken as a result of the shear, impact, wear or compaction within the mixer. This could also occur post-granulation in other unit operations (for example during drying).

It is well known that the agglomeration process is a multi-scale problem. The macro-scale kinetics (granule growth), which is influenced by method of binder addition, binder dispersion and rate of mixing, all have a direct influence on micro-scale phenomena which occur during granulation including nucleation, growth, consolidation and breakage (Poon et al., 2009).

High shear mixers are commonly encountered unit operations for wet granulation applications. They are known to produce compacts that are high in strength and bulk density. Key features of a high shear mixer include a mixing bowl, impeller and a chopper (Figure 2.3). The action of the impeller fluidises material, whilst binder is added into the mixer. The binder can be preloaded, poured, sprayed or melted-in (solid binders). Critical parameters that could be varied when considering the scale-up of a high shear agglomeration process include the impeller tip speed and Froude number (Chitu et al., 2011). Froude Number is a dimensionless parameter measuring the ratio of the inertial force on an element of fluid to the weight of that element of fluid i.e. the inertial force divided by the gravitational force.

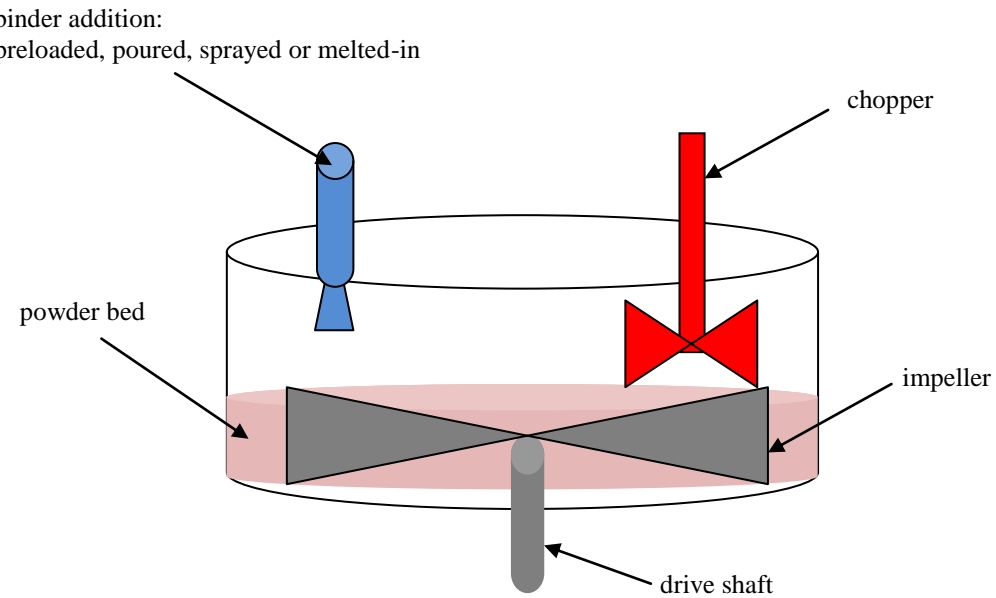


Figure 2.3. Schematic of the high shear mixer.

The initial size of the droplet of binder that is introduced into a high shear mixer and its effects on the granulation process in a high shear mixer have been investigated by Schaefer and Mathiesen (1996a) and Hapgood et al. (2002). Schaefer and Mathiesen (1996a) report that the size of the binder particles affects the mechanism of binder dispersion during melt granulation. They granulated lactose monohydrate with meltable polyethylene glycol (PEG) particles. The binder was used as flakes, coarse or fine powder. Their study revealed the existence of two distinct mechanisms of binder dispersion, which have a strong dependence on the binder size: (i) distribution mechanism or (ii) immersion mechanism (Figure 2.4).

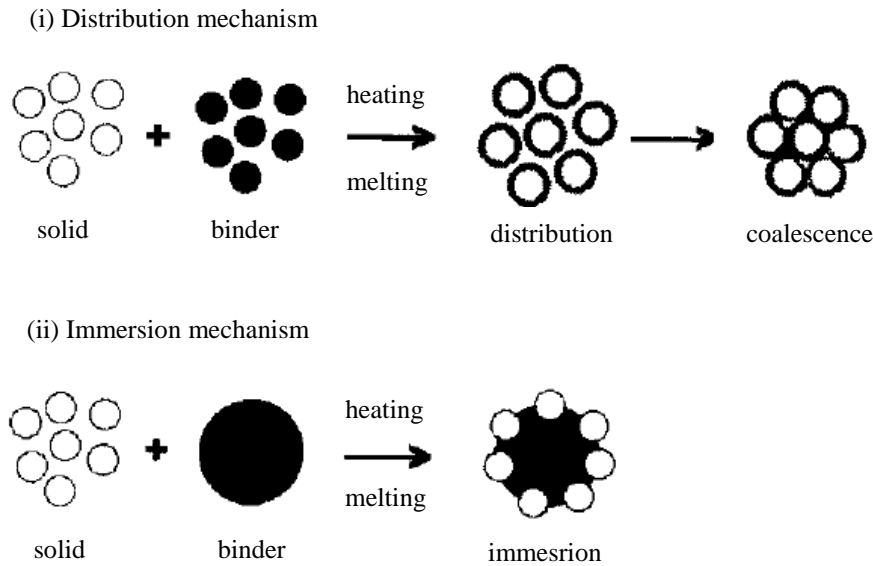


Figure 2.4. Mechanisms of binder dispersion (i) distribution (ii) immersion (Schaefer and Mathiesen, 1996a).

Hapgood et al. (2003) developed a nucleation regime map introducing two new concepts: (i) the droplet controlled regime and (ii) the mechanical dispersion regime (Figure 2.5). In the droplet controlled regime, each drop that touches the surface of the powder bed results in the formation of a nucleus. It is assumed that droplets do not land on the same area (i.e. the spray flux, Ψ_A , is low) and that the drop penetrates the powder bed really quickly (i.e. penetration time, t_p , is short). Conversely, if t_p is long, for example when considering binders that are very viscous or when the binder addition flux is high, then the mechanical dispersion regime will dominate. Seo et al. (2002) provides further evidence for the relationship between the relative size of the primary particle to the binder droplet and the mechanism by which subsequent agglomerate growth takes place. However, one study conducted by Osborne et al. (2011) has shown that pouring, pumping and spraying binder into a high shear mixer, all result in the same granule size distribution eventually.

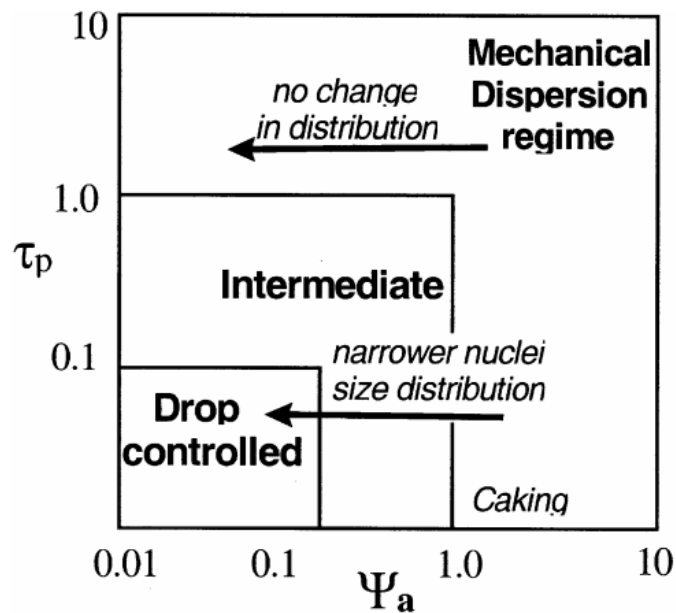


Figure 2.5. The nucleation map proposed by Hapgood et al. (2003).

A regime map has been developed by Iveson et al. (2001b) to enable granule growth to be predicted in equipment such as rotating drums and high shear mixers (Figure 2.6). These regime maps show Stokes Deformation Number varies as a function of the maximum granule saturation. Such maps are useful in predicting the final consistency of the material given a set of initial conditions.

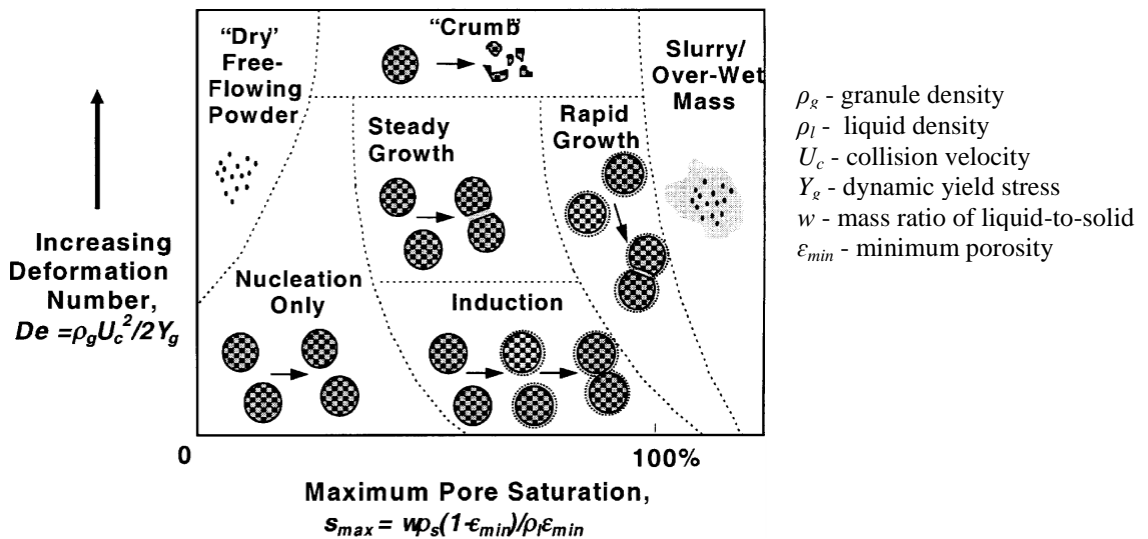


Figure 2.6. Granule growth regime map proposed by Iveson et al. (2001b).

2.3 Detergents and surfactants

The detergent industry has shifted its focus towards the manufacture of compact laundry powders in order to minimise the amount of product packaging, as well as any associated transportation costs in moving large volumes of product (Bayly et al., 2009). The manufacturing route, which involves granulation in a high shear environment is therefore, more favourable to the spray drying process, as it produces denser granules that are stronger. The detergent granulation process often employs a highly viscous surfactant as the binding substance. Many of the mechanisms outlined in Section 2.2 are not applicable when considering the dispersion of such binders in a high shear environment. Physical phenomena such as capillary action and interfacial forces have little or no influence on the dispersion process too. The dispersion of a highly viscous binder occurs entirely as a consequence of mechanical action.

From this point onwards, literature that specifically deals with detergent agglomeration will be discussed in more detail. This section begins with some general background on surfactants and the detergent manufacturing process as a whole.

Detergents are water soluble cleansing agents which interact with dirt/impurities to make them more soluble. They contain an ingredient called a surfactant. The word surfactant is short for surface-active-ingredient (Myers, 2006). These substances wet the surface of the fabric to emulsify oil and other particulates. They also serve to keep the emulsified matter in suspension to prevent them from settling onto the surface of the fabric (Yu et al., 2008). This is achieved by lowering the surface tension of water even at low to moderate concentrations. The surfactant molecule is made up of two different segments – a lipophilic (oil loving) component and a hydrophilic (water loving) component, thus making them amphiphilic (Figure 2.7). The lipophilic part is composed of a long hydrocarbon chain, whilst the hydrophilic part consists of a charged head. It is the existence of these opposing forces within the same molecule that help to suspend the dirt in water (Myers, 2006). Figure 2.7 also exhibits the bi-layer arrangement in a water-air-oil interface, with the hydrophilic tail in the air/oil phase and the hydrophilic head in water.

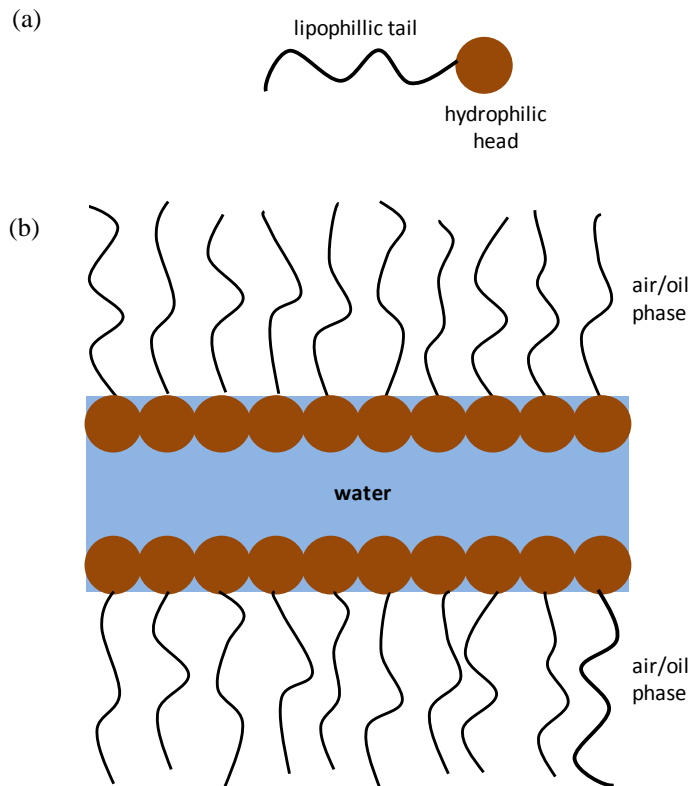


Figure 2.7. a) structure of a surfactant molecule and b) interaction between the surfactant and water – adapted from Myers (2006).

Detergents are commercially available in a wide variety of forms such as powder, liquids, gels and capsules. The most widely used product still remains detergent in its powder form. This is largely due to its lower retail cost and longer shelf-life (Bayly et al., 2009). For example, liquids can undergo phase separation post production, whereas the powder form retains its formulation consistency, provided the segregation of its constituent components is managed (through granulation for example).

A typical detergent formulation consists of four main components (Yu et al., 2008):

- Surfactant.
- “Builders” – primarily aid in softening water.
- Alkalinity sources – mainly carbonates.
- Bleaches.

The term “builder” comes from the role that these compounds play in the detergent manufacturing process. In spray dried formulations, compounds like zeolites make a key contribution towards the structure of the resultant granule – hence the name builder (CEFIC, 2000). Builders also help in preventing greying of fabrics and assist in dirt removal.

The surfactant can either be inert or active (reactive). An active binder has a lower viscosity than an inert binder. Inert binders are often soft-solids. The soft-solid binder is preferred to the thinner active binder, as it results in the production of stronger granules. It is more difficult to push out a more viscous liquid from within the internal structure of a granule than a less viscous one, therefore resulting in the formation of stronger bonds between the constituent particles. Another advantage of a soft solid binder is its ability to enable better control of the agglomeration process as a whole (Mort et al., 2001). For example, uncontrollable ball growth and deformation is prevented as the fine powders that are often present in detergent formulations need a large amount of binder. The fine particles pack closely with the soft solid, and this results in binder becoming saturated with powder. Furthermore, the high viscosity of the binder will impact its flow through the interparticle spaces, thereby, reducing the effect of growth post-consolidation. This means that there is less binder available on the surface of the granules for further particle interaction, therefore preventing uncontrolled granule growth (also known as balling). However, it is easier to disperse a low viscous binder in a moving bed of powder; thus ensuring a more even surfactant concentration in the finished laundry product.

2.4 Classes of surfactants

Surfactants are generally classified based on the electrical charge of their head group (Figure 2.7). There are several different types of surfactants (Levinson, 2009), these include:

- Anionics - negatively charged.
- Cationics – positively charged.
- Amphoteric or Zwitterionics – both positive and negative groups exist on the same head.

- Nonionics – zero (no) charge.

Of these four classes, the most commonly employed categories are anionics and non-ionic surfactants, accounting for a combined 86% of all surfactants sold globally (Levinson, 2009) (Figure 2.8). Many commonly used fabrics are negatively charged therefore anionics are ideal, as they will not be prone to adhere onto the fabric that is being cleaned. This in turn, prevents oil and other undesirable particulates from settling on to the surface of the fabric (Bayly et al., 2009).

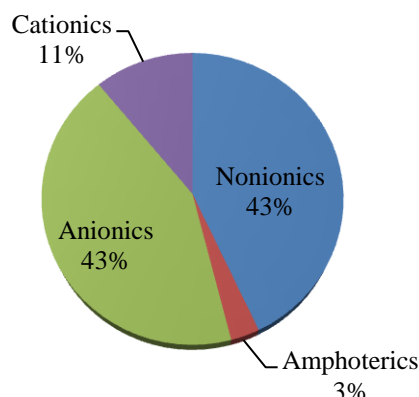
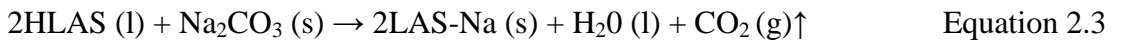


Figure 2.8. Commonly used types of surfactants and their availability – adapted from Levinson (2009).

Alkyl aryl sulfonates are the most commonly used anionic surfactants, in particular, linear alkylbenzene sulphonate (LAS acid) (Yu et al., 2008). The linear chains are preferred over the branched chains, as they are more biodegradable and therefore more environmentally friendly. Other advantages of LAS include its ease of dispersion in aqueous mediums (a gel is not formed) and its excellent thermal & chemical stability (Bayly et al., 2009). It is often neutralised using carbonates (Equation 2.3) that make up part of the detergent formulation to form a sodium salt (LAS-Na) (Germaná et al., 2009). This study involves the use of both reactive and non-reactive anionic surfactants. The non-reactive semi-solid surfactant (alkyl ethyl ethoxy sulphate or AE3S) is also anionic. It has the following chemical formula: $\text{CH}_3(\text{CH}_2)_{10}\text{CH}_2(\text{OCH}_2\text{CH}_2)_n\text{OSO}_3^-\text{Na}^+$. $[\text{CH}_3(\text{CH}_2)_{10}\text{CH}_2]$ is the hydrophobic tail, and $[-(\text{OC}_2\text{H}_4)_n\text{OSO}_3^-]$ is the hydrophilic head. It is a pale yellow opaque semi-solid paste at room temperature. More details about the surfactants used in this study are given in Section 3.3.



2.5 What is a semi-solid?

One of the surfactants used in this study (sodium alkyl ether sulphate) is a semi-solid paste at room temperature. A semi-solid refers to a substance that behaves as both a solid and a liquid. For example, semi-solids like solids are able to hold their shape and can support their own weight, however, like liquids when a stress is applied to them they start to flow.

2.6 Inorganic solid components in detergent formulations

The surfactant is often combined with several other inorganic solid components that make up a typical detergent formulation. Each powder has a specific function to play in maximising the detergency of the formulation (Bayly et al., 2009):

2.6.1 Sodium carbonate

Sodium carbonate also known as soda ash, has the chemical formula Na_2CO_3 . It is a brilliant white powder, with a true density of 2.54 g/cm^3 . The compound is basic in nature. It helps to soften water by competing with calcium and magnesium ions that are present in the aqueous medium, thus preventing them from binding with the surfactant molecule.

2.6.2 Zeolite

They refer to a diverse range of insoluble crystalline compounds and are widely used for adsorption, ion exchange and other separation processes. They have porous structures and serve as molecular sieves for other cations like Na^+ , Ca^{2+} , Mg^{2+} and K^+ . There are many different grades of the compound, the most widely used form in detergents is sodium aluminosilicate, $\text{Na}_{12}\text{O}_6\text{Al}_{12}\text{O}_{18} \cdot 12\text{SiO}_2 \cdot 27\text{H}_2\text{O}$. It is a fine white powder, with a true density of 2.24 g/cm^3 .

2.6.3 Sodium silicate

Sodium silicate is also known as water glass and has the chemical formula Na_2SiO_3 . It is available as a white solid or as an aqueous solution. The powder can be dissolved in water to produce a basic solution. It has a true density of 2.40 g/cm^3 .

2.6.4 Sodium sulphate

Sodium sulphate has the chemical formula Na_2SO_4 . It is a brilliant white powder that is insoluble in water. It is inert and does not react with acidic surfactants. It has a true density of 2.66 g/cm^3 .

2.6.5 Sodium tripolyphosphate

Sodium tripolyphosphate (STPP) has the chemical formula $\text{Na}_5\text{P}_3\text{O}_{10}$. It is used in detergent formulations to serve as a builder. It also aids in softening water by binding to calcium and magnesium ions. It has a true density of 2.52 g/cm^3 .

More information about the primary powders used in this study (zeolite and light ash) can be found in Section 3.3.

2.7 Detergent agglomeration process

One of the challenges associated with the use of a highly viscous paste is ensuring its subsequent dispersion within the granulator. To increase the performance of the detergent, the loading (concentration) of the surfactant in the detergent granules has to be maximised. To achieve this, most surfactants are added in their highly concentrated paste form. This means that diluting the binder to improve its distribution, by reducing its viscosity, is not an option for improving paste handling and dispersion. Knight et al. (1998) conducted studies using a low viscous binder and reported that shearing forces imparted by the impeller are vital for ensuring good distribution.

The general agglomeration mechanism using a conventional solvent binder or aqueous binder consists of three main steps (refer to Section 2.2). This generic mechanism is not applicable to granulation involving highly viscous surfactant binders, like LAS acid and AE3S. For example, at a shear rate of 10 s^{-1} , molten PEG 20000 has a viscosity of 27 Pa.s at 70°C , whilst AE3S has a viscosity of 800 Pa.s.

The size distribution of the resulting agglomerates depends on the method of binder addition (Mort et al., 2001). Ideally, a well atomised binder spray will result in a narrower size distribution, providing the droplet size is less than the desired agglomerate size, and the binder is added to a location where there is a sufficient powder flux. However, it is not possible to spray a semi-solid binder due to its high viscosity. Therefore binder distribution is enhanced by staging the agglomeration process across two mixers, to help narrow the size distribution, by dividing the growth transformation into more manageable segments. Commercially, the detergent agglomeration process consists of more than one stage to enable better control of the process (Figure 2.9). Mixer 1 is used to mechanically disperse the binder into the powder, whilst the second mixer is used to control the size of the resulting agglomerates.

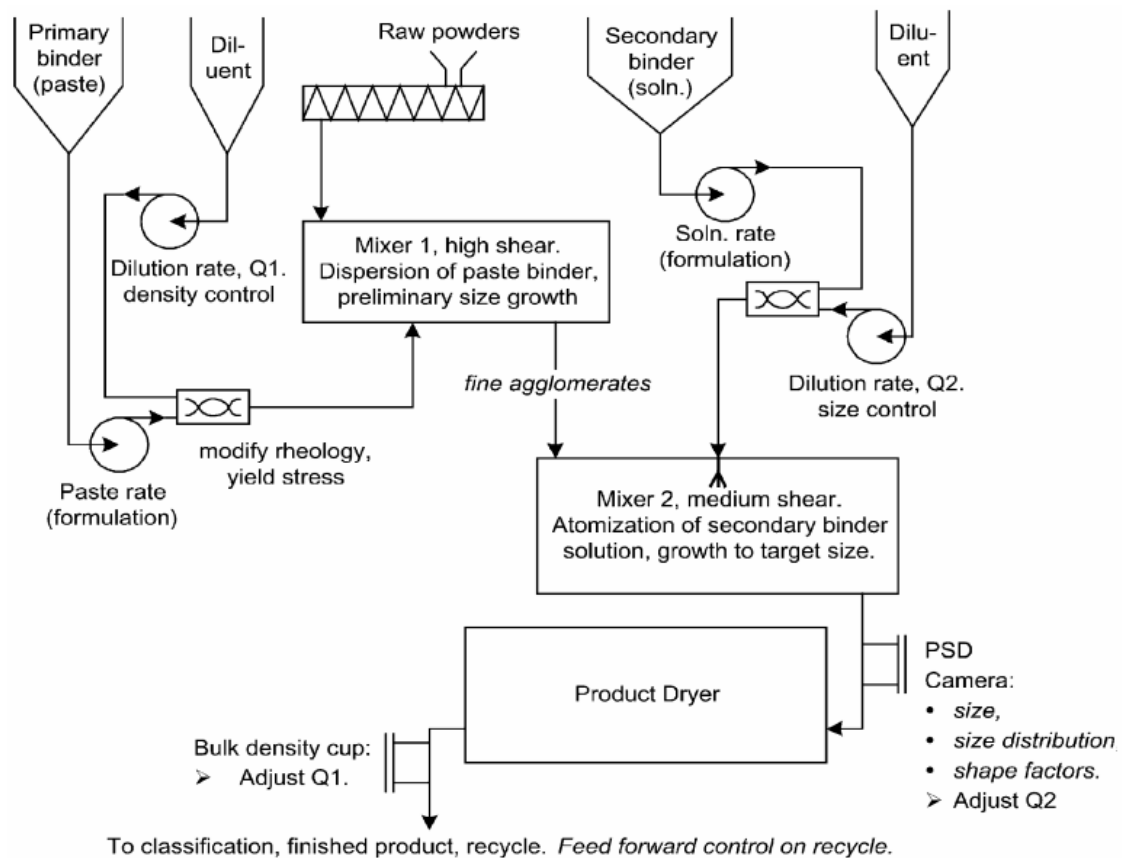


Figure 2.9. Process flow diagram for detergent agglomeration (Mort et al., 2001).

Capeci et al. (1996) outline a complete process for producing high density detergent agglomerates (Figure 2.10). This involves:

- i. Mixing/densifying – the surfactant and the dry powders in order to produce agglomerates. This stage could involve more than one mixing step as outlined in Figure 2.9.
- ii. Screening & grinding (stage 1) – separating the agglomerates into different size classes, and grinding those that are above a certain size (a milling operation).
- iii. Conditioning - this involves further downstream processing post agglomeration, such as drying and cooling (to improve granule flow). Granules below a certain size are recycled back into the mixer for further agglomeration.
- iv. Screening & grinding (stage 2) – separating agglomerates after they have been conditioned into different size classes. Agglomerates that are considered to be large are once again subjected to a size reduction process.
- v. Finishing – refers to the mixing of the selected size classes of agglomerates to produce the finished laundry product.

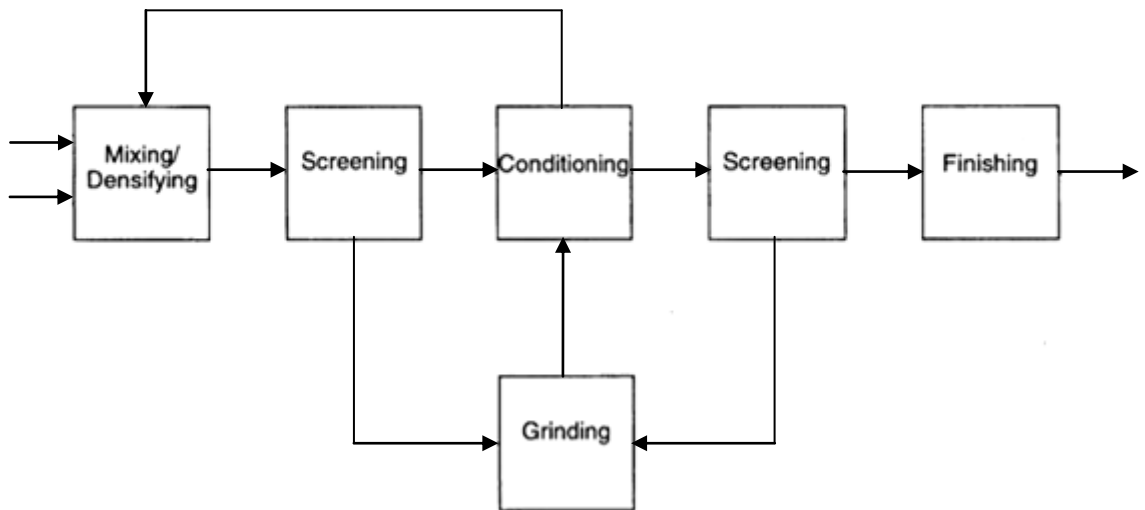


Figure 2.10. Laundry detergent manufacture process (Capeci et al., 1996).

2.8 Non-reactive detergent agglomeration

Up to this point, a general overview of the detergent agglomeration process has been given and some of the challenges associated with the use of a surfactant binder have been discussed. The rest of this section summarises the recent granulation research involving the use of a highly viscous binder. Rough et al., (2003, 2005 a-d) conducted a series of studies in a domestic food processor. They granulated fine zeolite powder with LAS paste, which is a neutralised form of LAS acid. It is a highly viscous opaque yellow semi-solid gel at room temperature.

They investigated changes in the granule morphology and size distribution and their study revealed the existence of five distinct regimes, including a powdery, crumble, agglomerate, wet agglomerate and dough state (Figure 2.11). This was a qualitative method of characterising the granules by visually examining micrographs of samples. In the powdery regime, the granules are quite fluffy and weak, and the size distribution is wider (Figure 2.12). They also claim the size of the granules starts to decrease after 180 s of wet massing. However, mean or median sizes have not been reported from their size measurements to support this claim, and the size distribution presented in their work seems to suggest otherwise i.e. an increase in the mean size with time c.f. Figure 2.12. Crumble refers to the formation of lumps of surfactant paste covered with powder. As time progresses, the samples become more homogenous and the size distribution becomes narrower. The powdery nature of the samples ceases to exist after 240 s (Figure 2.11). After 300 s some granule growth is evident.

Rough et al. (2005b) discuss the effects of three parameters, namely speed, binder viscosity and liquid to solid ratio. The rate at which the material moves from one regime to another depends on these parameters (Table 2.1). Increasing the impeller speed enhances the rate at which the various regimes were formed. They also claim that changing the impeller speed does not affect the shape of the granules in each regime (Rough et al., 2005a), however micrographic evidence was not provided to support this. It was also stated that when comparing the data obtained at 1350 rpm against the data obtained at 1650 rpm, the higher impeller speed resulted in a narrower size distribution, with a lower volume percentage of the larger granules. Again, size distributions have not been presented in support of their statement. This finding was said to be in agreement with

the study conducted by Schaefer and Mathiesen (1996a) using lactose and molten polyethylene glycol (PEG). Higher speeds could result in the breakage of some of the larger granules in the mixer. However, others (Heng et al., 2000) argue that at higher speeds, granule deformability is greater resulting in more binder being squeezed on to the surface of the granule promoting more growth i.e. enhanced granule consolidation aids growth via coalescence. In reality, it is likely to be a trade off between breakage and consolidation. Rough et al. (2005b) also report that an increase in the temperature of the binder lowers its viscosity, which enhances its distribution. A less viscous binder enables the regimes to be reached in a shorter period of time at both the impeller speeds. Also, increasing the binder to solids ratio reduces the time taken to form a given regime. The methodology adopted by Rough et al. (2005b) to determine the influence of process parameters on progression through the various agglomeration regimes relies primarily on visual inspection and a qualitative analysis of micrographs of the granular samples.

The onset of the detergent agglomeration process is very rapid at higher impeller speeds. This makes control challenging and any small variation in the process conditions could result in over or under-agglomerated product. All agglomeration processes (even low viscous systems) require a minimum level of binder to saturate the powders, before the binder becomes available for providing stickiness. Generally, the more deformable the granules are, the more readily they progress onto the agglomerate regime (York, 2003).

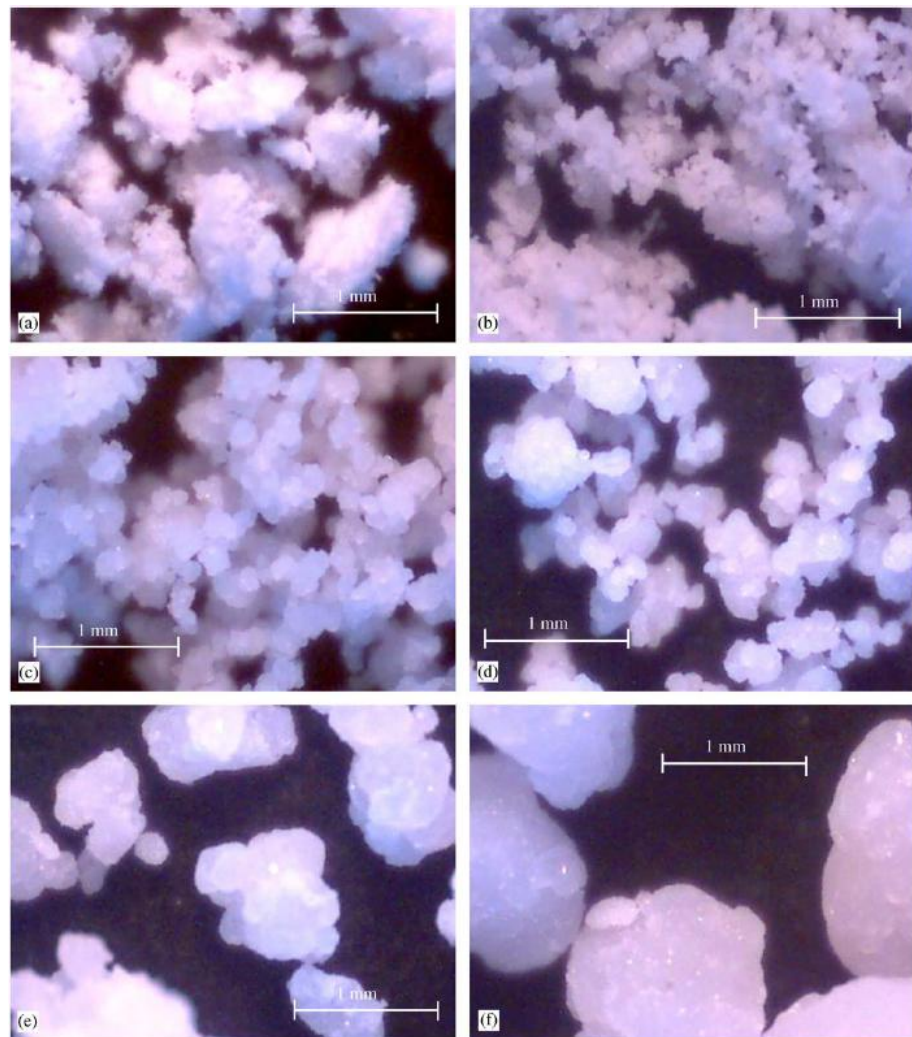


Figure 2.11. Change in granule morphology with time (a) powdery (90 s), (b) beginning of crumble (180 s), (c) end of crumble (240 s), (d) crumble-agglomerate (300 s), (e) agglomerate (480 s) and (f) wet agglomerate (480 s). Zeolite was granulated with LAS acid (45 wt%) in a 3 L domestic food processor at 1350 rpm, 22°C (Rough et al., 2005b).

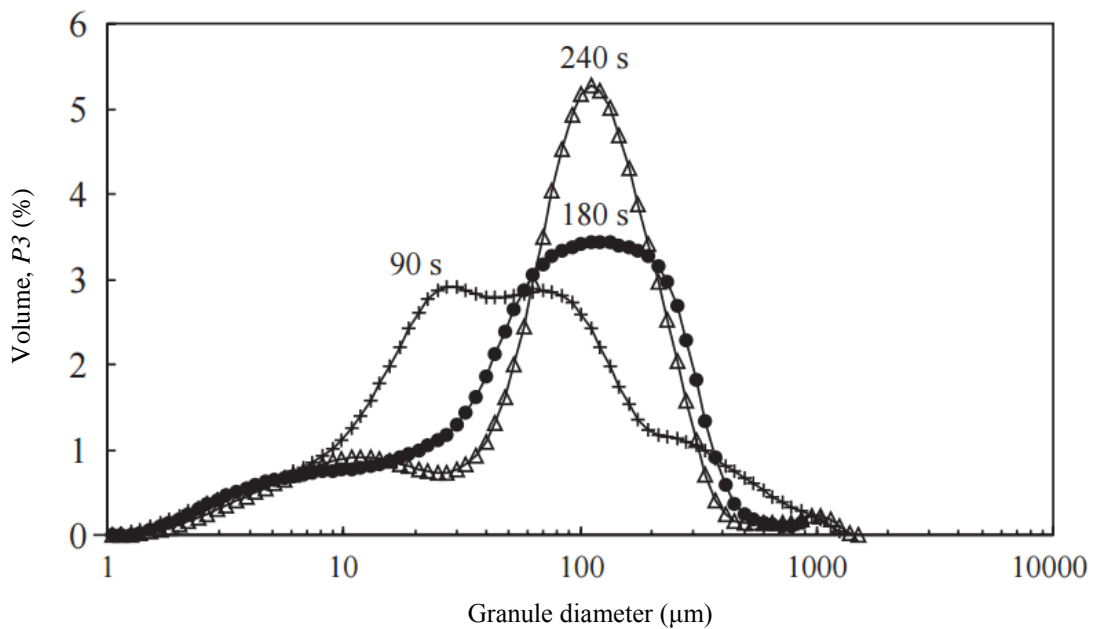


Figure 2.12. Size distribution of the granules shown in Figure 2.11 at different times (Rough et al., 2005b).

Table 2.1. Effect of speed, binder viscosity (temperature) and liquid to solid ratio on the rate at which the system progresses through the different regimes (Rough et al., 2005b).

Regime	Mixing time/s									
	22 °C, 45 wt%		1350 rpm, 45 wt%		22 °C, 1350 rpm					
	1350 rpm	1650 rpm	40 °C	55 °C	40 wt%	50 wt%	55 wt%	60 wt%	65 wt%	
Powdery	30–120	< 60	30	30	60–120	< 30	< 30	< 20		{ < 15
Powdery-crumble	150	60–90	60–120	60	180	30–60	30–45	25		
Crumble	180–240	120–180	150	90	240–600	90	60	30		
Crumble-agglomerate	270–330	210	180	120	N/A	110	70	40		
Agglomerate	360	240	210	150	N/A	120	75	50		
Wet agglomerate	420	270	240	180	N/A	150	90	60		
Smooth dough	N/A	N/A	N/A	N/A	N/A	180	105	65		

2.8.1 Changes in the bulk density and Hausner ratio

Studies conducted by Rough et al. (2003, 2005b) showed a distinctive trend in the variation of the wet bulk density (aerated density of the LAS-zeolite granules), with a decrease towards the crumble regime, and a gradual increase towards the agglomerate regime (Figure 2.13 and Figure 2.14). Their study did not investigate the densities of the wet agglomerate or dough due to the high cohesivity of the granules. According to Hibbare and Acharya (2012), who investigated detergent agglomeration using both highly

viscous non-reactive and reactive binders, an increase in binder to solids ratio results in a decrease in the bulk density of the granules (for both binders).

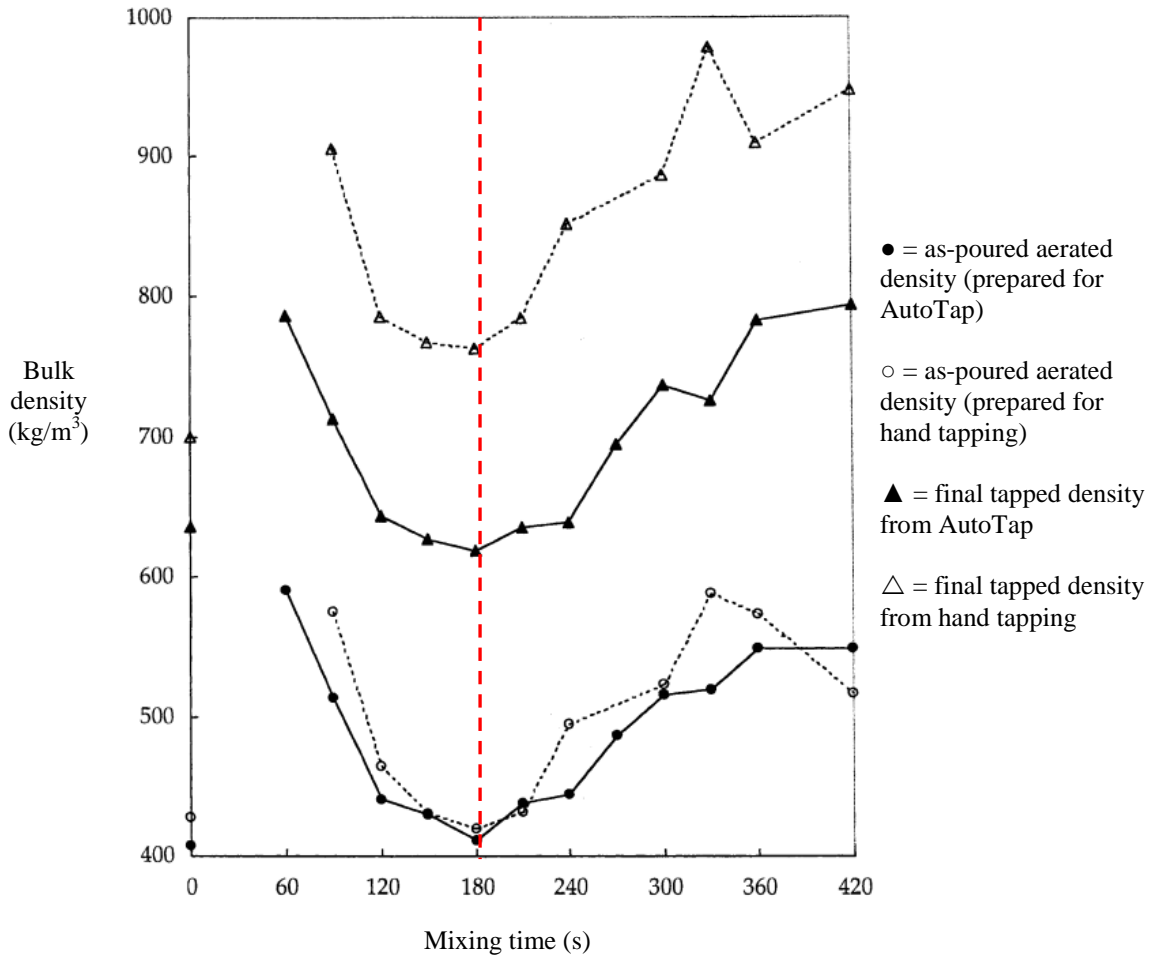


Figure 2.13. Bulk density against mixing time for a 45 wt% LAS–zeolite mixture (Rough et al., 2003). Dotted line indicates the beginning of the crumble regime.

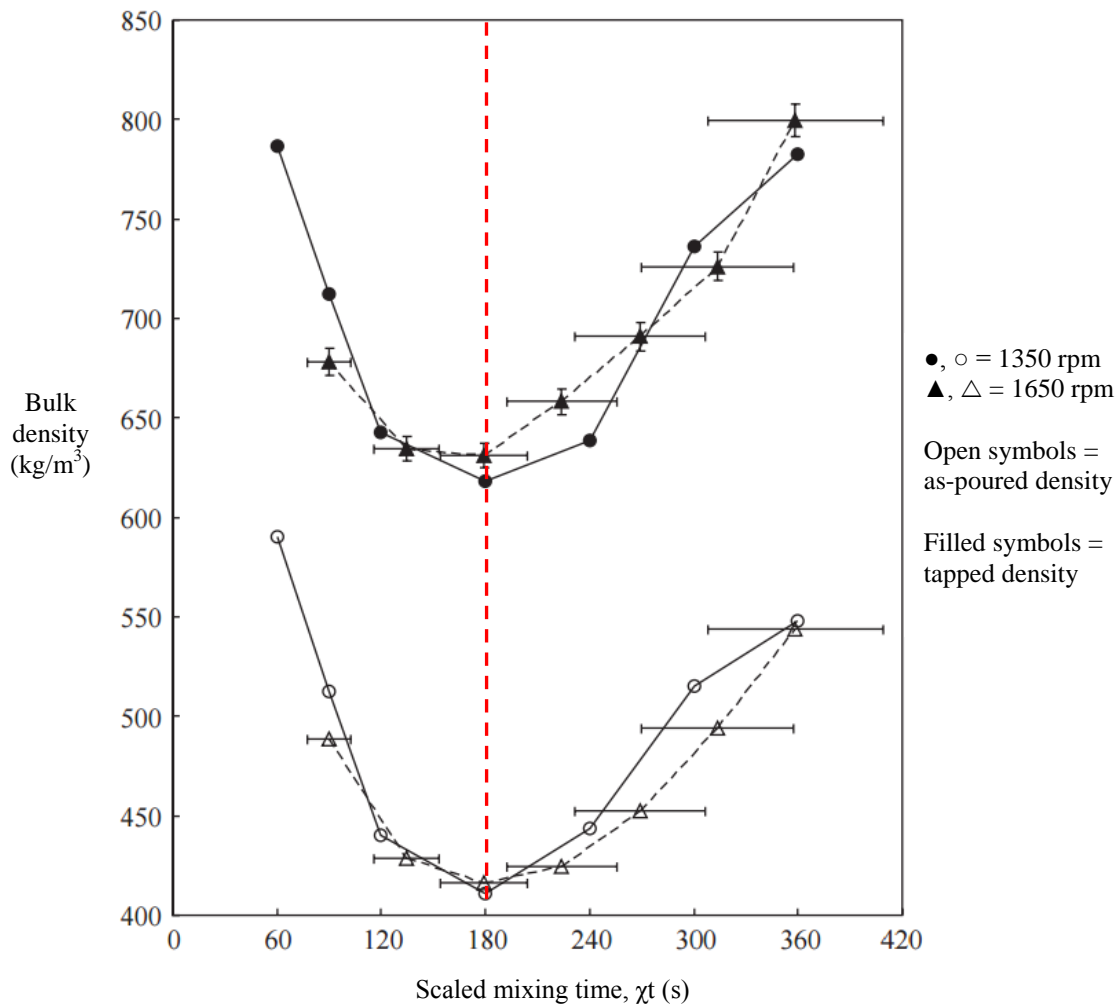


Figure 2.14. Bulk density against scaled mixing time for a 45 wt% LAS-zeolite mixture at different impeller speeds (Rough et al., 2005b). Dotted line indicates the beginning of the crumble regime.

The changes in the Hausner ratio as a function of the mixing time were monitored and used to identify the existence of different granulation regimes. The Hausner ratio is the ratio of the tapped density to the bulk density of the powder. This ratio can be related to the inter-particle friction and cohesivity of material in a moving bed of powder. Hausner ratios which are <1.25 indicate the material is free-flowing, whilst materials with a ratio >1.40 are classed as cohesive.

A plot of the Hausner ratio as a function of time for the LAS-zeolite mixture is shown in Figure 2.15. Again, two different tapping methods were investigated: hand tapping and Autotap. The Hausner ratio for unmixed zeolite powder using the hand tapping and

Autotap methods are 1.64 and 1.56 respectively. Both set of results show a similar trend with time, however, the Hausner ratio is consistently lower for the Autotap than the hand tapping method (Rough et al., 2003). The maximum Hausner ratio was found in the crumble regime indicating the material is most cohesive in this regime. Granule cohesiveness aids in promoting growth via coalescence and increases the granule size. They use the results from the Hausner ratio to explain how the properties of the sample changes as a function of mixing time. At first, the sample consists largely of a powdery mix that is inhomogeneous, with a wide size distribution and a high bulk density. With further mixing the granules that are now covered in powder, decrease in size, thus narrowing the size distribution, which results in poor packing. This corresponds to an increase in the Hausner ratio (and an increase in the inter-granular friction). As mixing proceeds, the powder particles become incorporated into the granules, making them smoother and less cohesive. Thus, the granule packing efficiency improves and the Hausner ratio becomes smaller and a local minimum is seen in the agglomerate regime. At a higher impeller speed of 1650 rpm, a similar trend was observed (Figure 2.16).

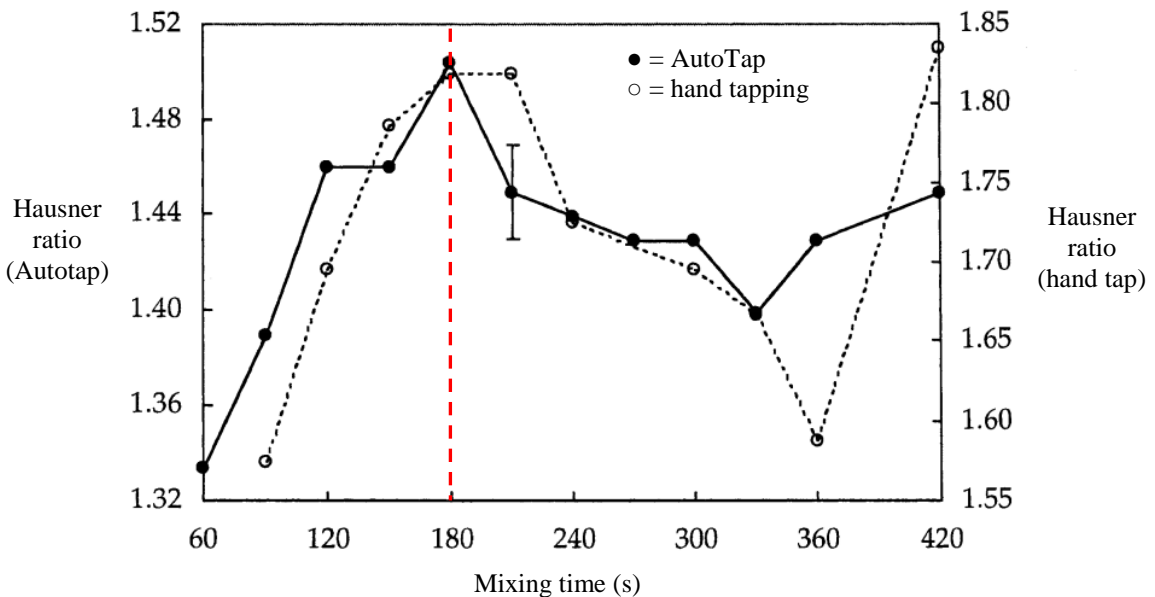


Figure 2.15. Hausner ratio against mixing time for a 45 wt% LAS–zeolite mixture. Note different scales for the Hausner ratios (Rough et al., 2003). Dotted line indicates beginning of the crumble regime.

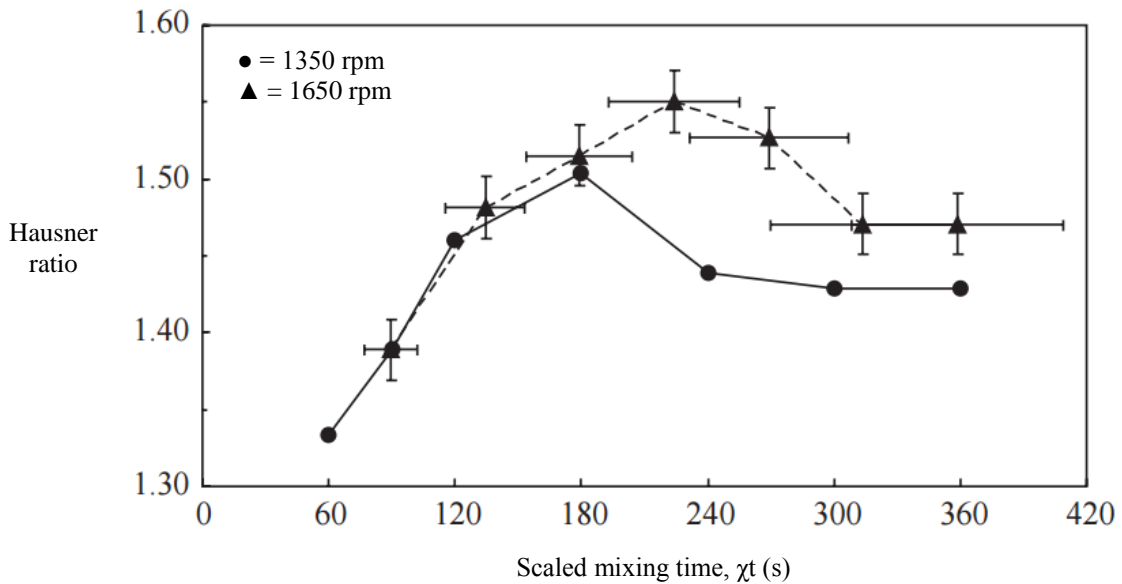


Figure 2.16. Hausner ratio against scaled mixing time for a 45 wt% LAS–zeolite mixture at different impeller speeds. The scaling factor is based on ratio of Froude numbers (Rough et al., 2005b).

2.8.2 Changes in granule porosity and mean granule saturation

Granule porosity is a ratio of intra-granular voidage against total volume of granule. The porosity of the granules was estimated using a liquid displacement method, in which a known mass of material was immersed in hexane (Rough et al., 2005b). The results (Figure 2.17) show that the porosity decreases to a minimum at 180 s (which corresponds to the crumble regime) and then increases to a maximum at 300 s (which corresponds to the crumble-agglomerate regime). They claim the increase in porosity from 180 to 300 s is due to the entrapment of air within the granule structure during coalescence. It was assumed that the level of saturation within the granules follows the opposite trend to the granule porosity (Rough et al., 2005b). The highest saturation is therefore, obtained at the crumble regime and lowest is at the crumble-agglomerate regime. This trend observed for the change in the porosity with mixing time contradicts the widely reported and well accepted trend of declining granule porosity with increasing mixing time (Schäfer and Mathiesen, 1996a, Knight et al., 1998, van den Dries and Vromans, 2002, Wauters et al., 2002, Ohno et al., 2007).

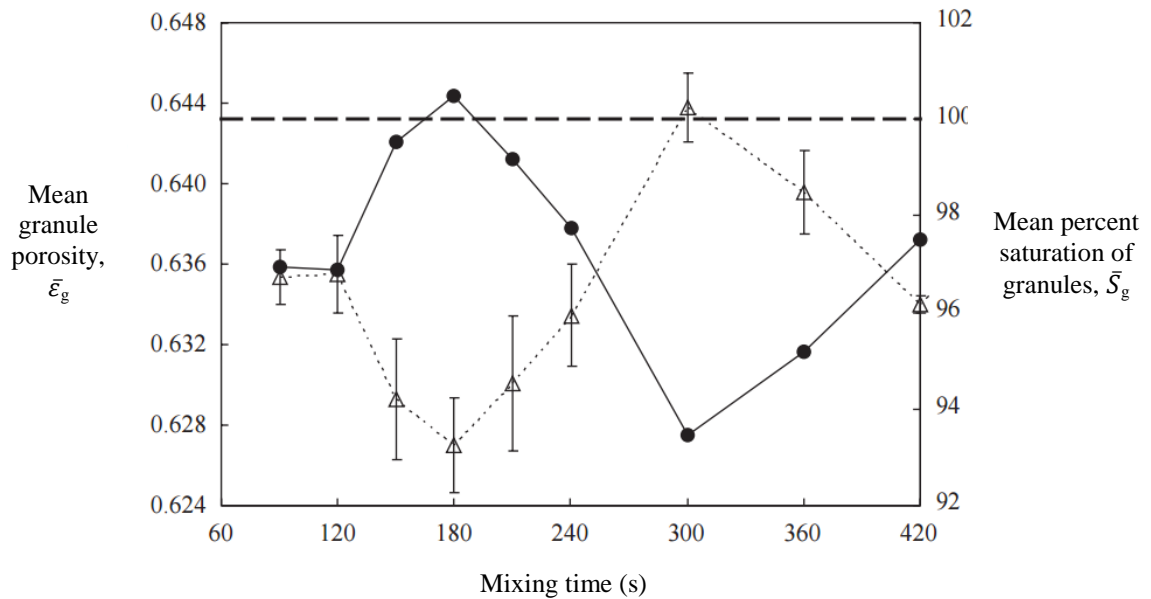


Figure 2.17. Plot of mean granule porosities (\triangle) and mean percent saturation of granules (\bullet) against mixing time for a 45 wt% LAS–zeolite mixture, at an impeller speed of 1350 rpm. The dashed line marks 100% for the saturation axis (Rough et al., 2005b).

2.8.3 Granulation regime maps

Rough et al. (2005d) also attempt to use the agglomeration regime map (Figure 2.6) proposed by Iveson et al. (2001b) to describe the agglomeration process involving a highly viscous binder. In order to relate this regime map to their experimental results the maximum pore saturation was replaced with the mean percent saturation of granules (S_g) determined from the granule porosity at a given mixing time (refer to Section 2.8.2). Also in order to obtain the Stokes deformation number (St) a value for the yield stress (Y_g) was approximated using a parameter, P_2 , obtained from the bulk tapping analysis, which they claim represents the plastic yield. More details about the parameter P_2 and how it was determined can be found in Rough et al. (2003). The results obtained from the tapping analysis have been used to determine a material property of the granules, namely the plastic yield. This is not a reliable technique as the flowability of the granules during tapping is also influenced by the size distribution of the granules and their shape – none of which have been controlled in this study. Therefore, it is not possible to elucidate the effect of tapping on the granule deformability alone. A sample with a wider size distribution may give a different value for the plastic yield than one

with a narrower size distribution, even if both the granular samples have the same constitution. In addition, the effect of size and shape, and the breakage of the wet granules during the tapping process could also influence granule flowability. This therefore, questions the validity of their approach to approximating a value of St .

A plot of the ρ_g/P_2 against mean percent saturation of granules when superimposed onto the granulation regime map, supposedly, gave an indication of the progression of a LAS-zeolite system through the regime map (Figure 2.18). It is also unclear as to how they superimposed Figure 2.18a on Figure 2.18b, as the position would influence which consistency regimes the system is going through.

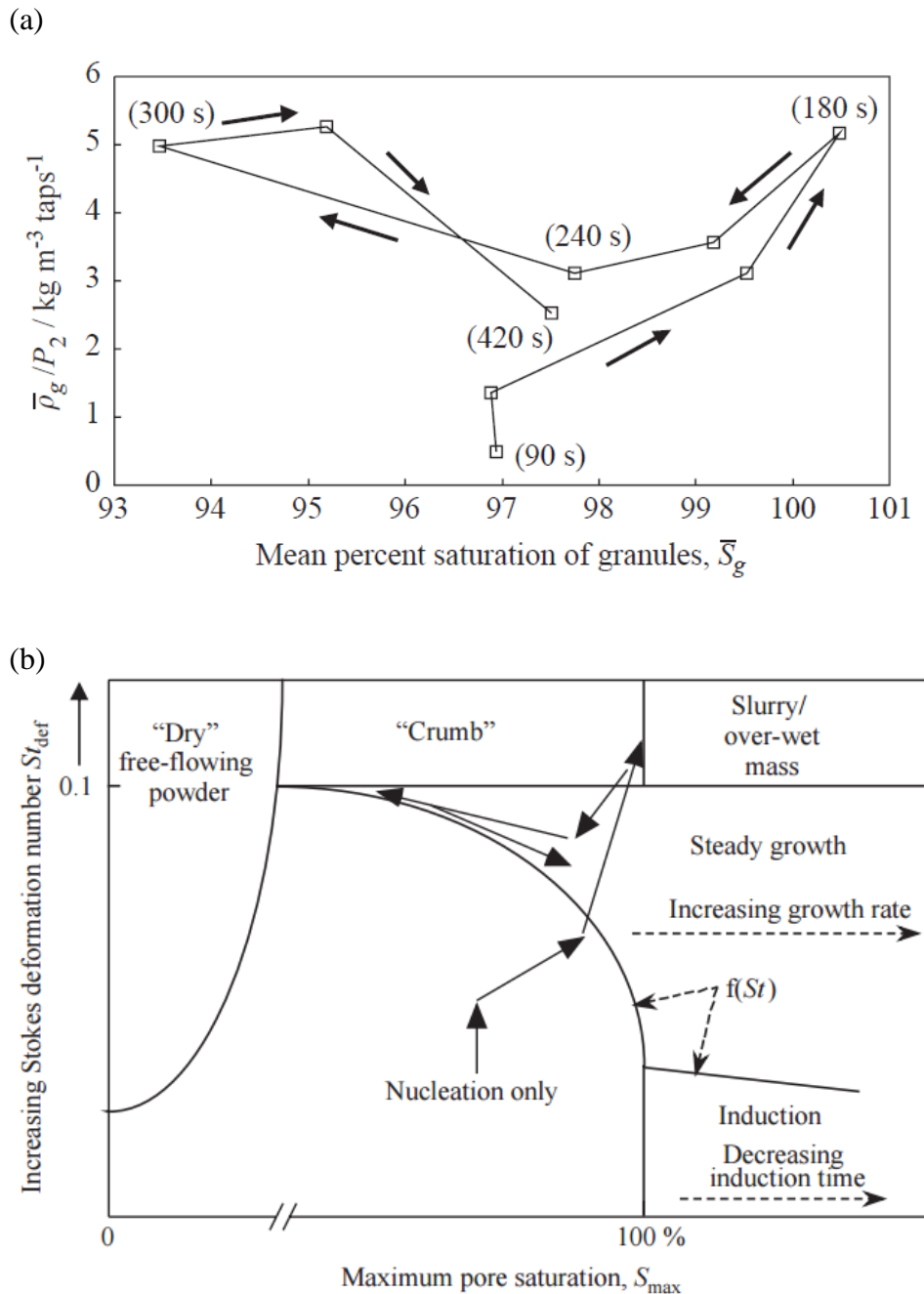


Figure 2.18. (a) Plot of ρ_g/P_2 vs. mean saturation for a 45 wt% LAS-zeolite mixture (b) Plot of ρ_g/P_2 vs. mean saturation superimposed on a granulation regime map proposed by Iveson *et al.* (2001a) (Rough *et al.*, 2005b).

2.9 Reactive detergent agglomeration using LAS acid

LAS acid is a reactive binder that is commonly used in industrial detergent agglomeration processes. Most detergent powders contain sodium carbonate, which acts as an alkaline source and reacts with the binder. This results in the formation of the surfactant anion (LAS-Na), carbon dioxide gas and water (refer to Equation 2.3 in Section 2.4). The neutralised surfactant also acts as a binder by forming physical links between the particles (Germaná et al., 2009). Other powders like zeolites and sulphates, that are present in the formulation are inert and do not react with the surfactant.

LAS acid is normally fed onto an agitated powder bed in a high shear environment. As the reaction progresses, there is an increase in the viscosity of the binder. The presence of the neutralised form of the surfactant binder results in the formation of stronger inter-particle bridges (Germanà et al., 2008). Once introduced into the mixer, changes in the viscosity of the binder (or its degree of neutralisation) is controlled to some extent by the binder-to-powder ratio, impeller speed, method of binder addition and efficiency of the binder distribution process, as a whole. The occurrence of a reaction, which forms another binder with a different viscosity to that of the original binder, makes the granulation process more complicated. There is some literature that looks into the chemistry of the reaction, and how it impacts on the resulting granule attributes (Schöngut et al., 2013, Germaná et al., 2009). These studies attempt to relate the micro-scale binder-particle interactions to certain carefully controlled macro-scale experiments, and link these to process/formulation parameters. Observing micro-scale phenomena is fundamental to understanding how liquid bridges (between the binder and the powder) change with time, as the reaction progresses. Apart from the strength of the liquid bridge, the kinetics of the reaction also influences the wetting and adhesivity, and ultimately the growth of the granules.

Enhanced wetting (or coverage of the surface) of the particle with binder will lead to a faster rate of reaction. Germaná et al. (2009) studied the wettability and adhesion behaviour during the reaction process. Viscosity measurements were conducted on LAS acid that had been pre-neutralised with sodium carbonate particles. As the reaction progresses, it causes changes in the rheological properties of the binder (Figure 2.19). In some cases, 15% water (by mass) was added to the HLAS binder before adding sodium

carbonate particles. In Figure 2.19, the letter ‘w’ indicates that water was added to the mixture and the percentage gives an indication of the degree of neutralisation. Adding water to HLAS resulted in two different trends. Samples with low percentages of neutralisation show an increase in the viscosity and shear thinning behaviour due to a transition from an isotropic phase to a more rigid lamellar phase. On the other hand, samples with higher percentages of neutralisation show a decrease in the viscosity, due to an increase in the thickness of the layer of water in the lamellar phase (Germaná et al., 2009). It is not clear how the impact of the reaction kinetics on changes in the viscosity was isolated, as increasing the solid content will undoubtedly make the mixture less flowable, with an increase in the percentage of neutralisation.

This study also investigated how environmental conditions such as relative humidity could affect the wettability of the binder-powder mixture, with a view to determining if such parameters can be varied to counteract any seasonal variations. A glass particle was wetted using the technique outlined in Figure 2.20. The contact angle was subsequently determined as shown in Figure 2.21. The influence of equilibrium relative humidity on the contact angle made on the surface of the glass particle by the binder that has undergone different levels of neutralisation is shown in Figure 2.22. By decreasing the relative humidity, the contact angle made by the binder (that has a neutralisation level below 30%) is reduced. Also, the transition from “liquid” to “sticky” occurs at low levels of neutralisation (Figure 2.22). In the sticky regime, the contact angle is not measurable as the coating assumes an irregular shape on the surface of the glass particle. Germaná et al. (2009) have shown that the state of the binder, i.e. extent of binder neutralisation, influences the particle surface coverage. They have also shown that wettability governs the size and the shape of the resulting liquid bridge that is formed between two particles. Others have shown that nucleation and subsequent granule growth can only occur if the pendular bridges between the particles are strong enough to hold them in place (Tardos et al., 1997).

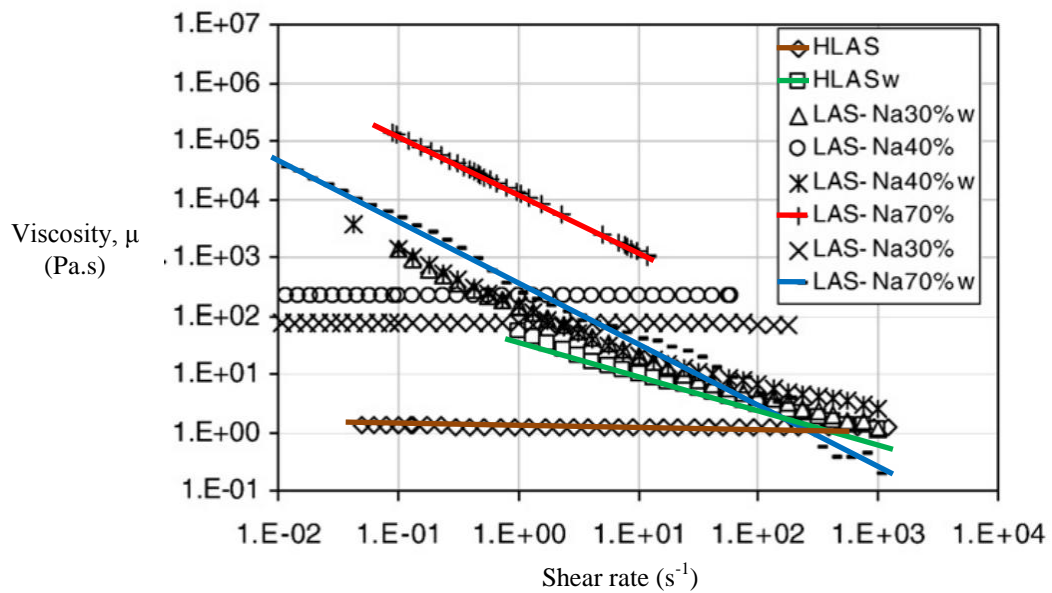


Figure 2.19. The effects of neutralisation on binder rheology (Germaná et al., 2009). ‘w’ indicates that 15% water was added to the mixture by mass and the percentage gives an indication of the degree of neutralisation.

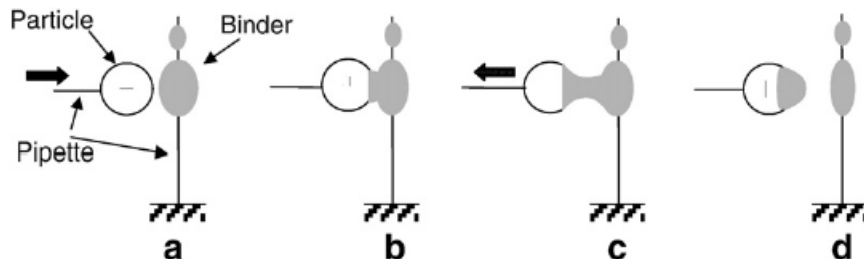


Figure 2.20. “Schematic of the particle–binder contact. a) Particle–binder contact. b) Binder wets and spreads on the particle. c) Particle is detached from the liquid reservoir. d) Liquid bridge ruptures and the binder redistributes, finding an equilibrium position on the particle” (Germaná et al., 2009).

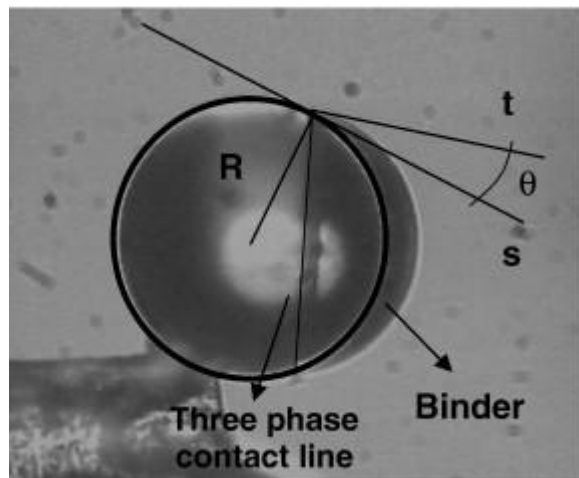


Figure 2.21. Contact angle was measured by identifying two tangents: s (surface of the spherical particle) and t (droplet of binder) (Germaná et al., 2009).

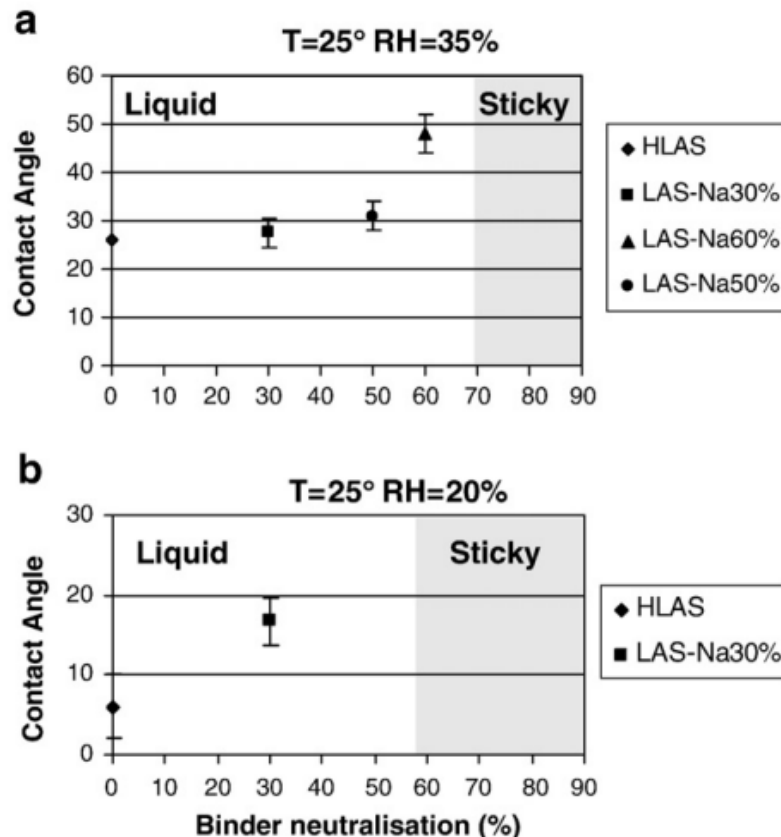


Figure 2.22. Effect of relative humidity on contact angle a) 35% RH b) 20% RH (Germaná et al., 2009).

Schöngut et al. (2013) investigated reactive granulation of sodium carbonate with a LAS acid, namely dodecyl-benzene sulfonic acid (DBSA). The set-up shown in Figure

2.23 was used to monitor the evolution of carbon dioxide as the reaction progresses. In all of their experiments a stoichiometric excess of sodium carbonate was used. Each powder bed was used twice before being discarded. Water is produced during the neutralisation process, and this forms a liquid crystalline phase with LAS-Na. LAS-Na is regarded as the solid form of the binder. It is known from non-reactive granulation that the rate at which the binder solidifies determines key properties of the resulting granules, such as dissolution (Ansari and Stepanek, 2008) and porosity (Štěpánek and Ansari, 2005). A rise in the temperature has an influence on the evolution of carbon dioxide (Figure 2.24a) and on the extent of neutralisation. An increase in the agitation also results in an increase in the rate of reaction (Figure 2.24b). This increase was attributed to the effect that added shear and impact has on exposing fresh un-reacted surfaces of sodium carbonate. Their technique for monitoring the progress of the reaction is not able to differentiate between the influence of contact area and mass transfer on the kinetics. Also as the powder beds were used twice before being discarded, any residual LAS acid that is left in the mixture may also influence the experimental outcome.

The viscosity of LAS acid decreases with increasing temperature, while the total amount and the rate of formation of the highly viscous (semi-solid) LAS-Na increases with an increase in the temperature. The former effect results in smaller granules with an increase in the temperature whilst the latter results in larger ones. Therefore, the highest mean granule size was observed at 40°C (Figure 2.25a). Again, the influence of the effects of mass transfer and contact area cannot be controlled in this experiment, as this would depend on how the LAS acid and powder interact within the mixture. When comparing the granule size distributions obtained by conducting experiments at two different speeds, and a fixed temperature of 20°C, there appears to be very little difference (Figure 2.25b). This suggests that the granule size distribution is more dependent on the physical state of the binder (which is controlled by the temperature and the rate of reaction) rather than on the impeller speed, at least within the range that was investigated (600 – 1000 rpm).

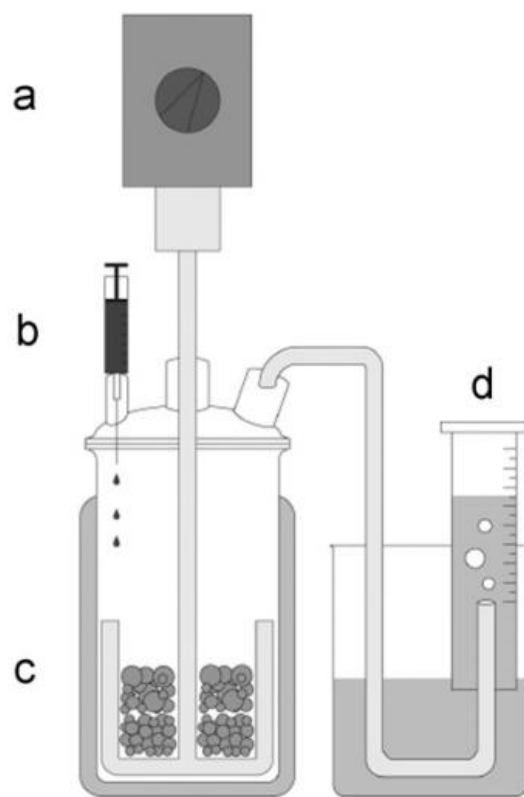


Figure 2.23. Experimental set-up for reactive granulation: (a) digital drive unit, (b) drop-wise addition of HLAS acid, (c) jacketed glass vessel with impeller, (d) volumetric measurement of evolved CO_2 (Schöngut et al., 2013).

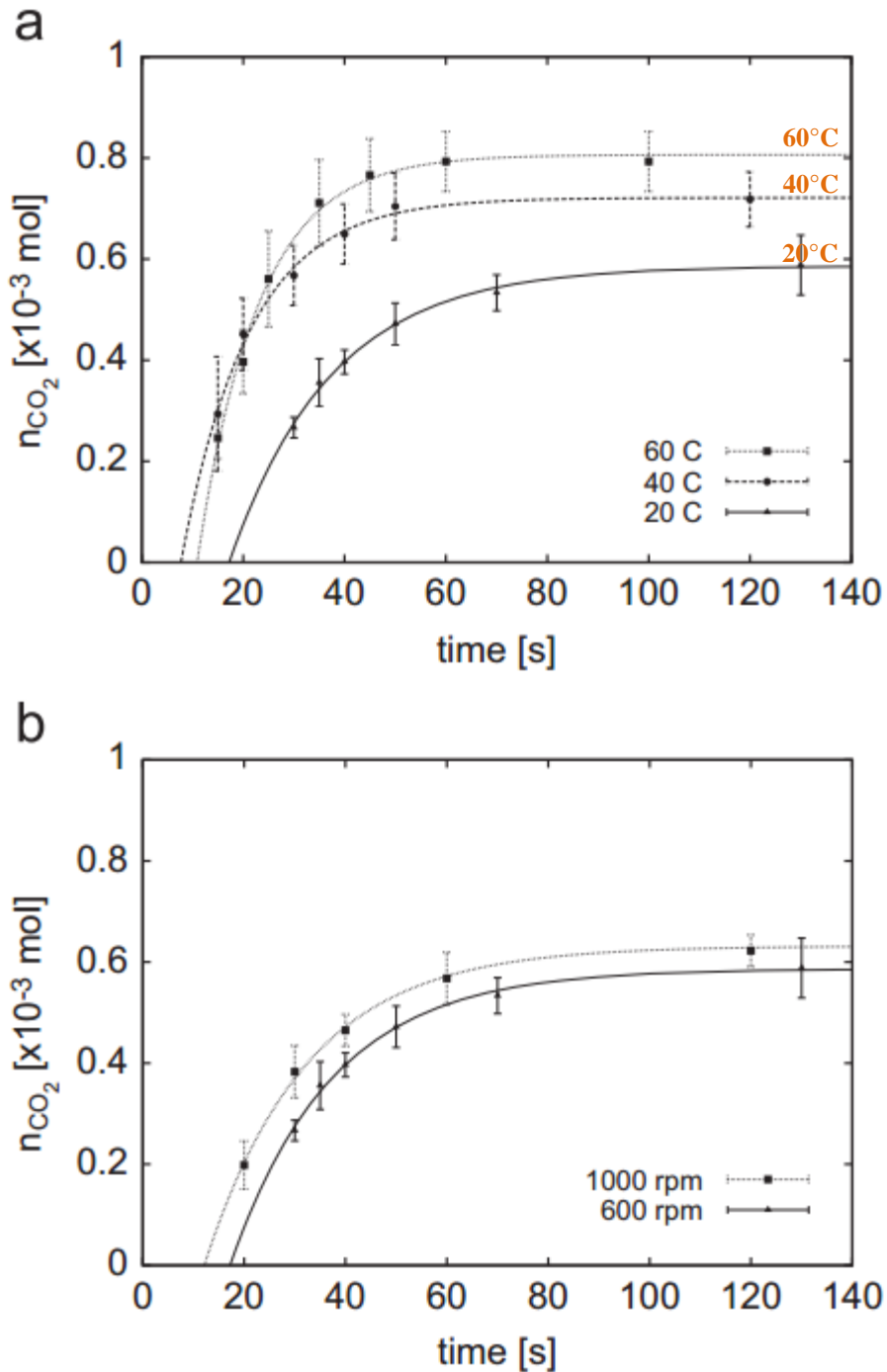


Figure 2.24. Carbon dioxide evolution (in moles) with time for variable process (a) temperature and (b) agitation (Schöngut et al., 2013).

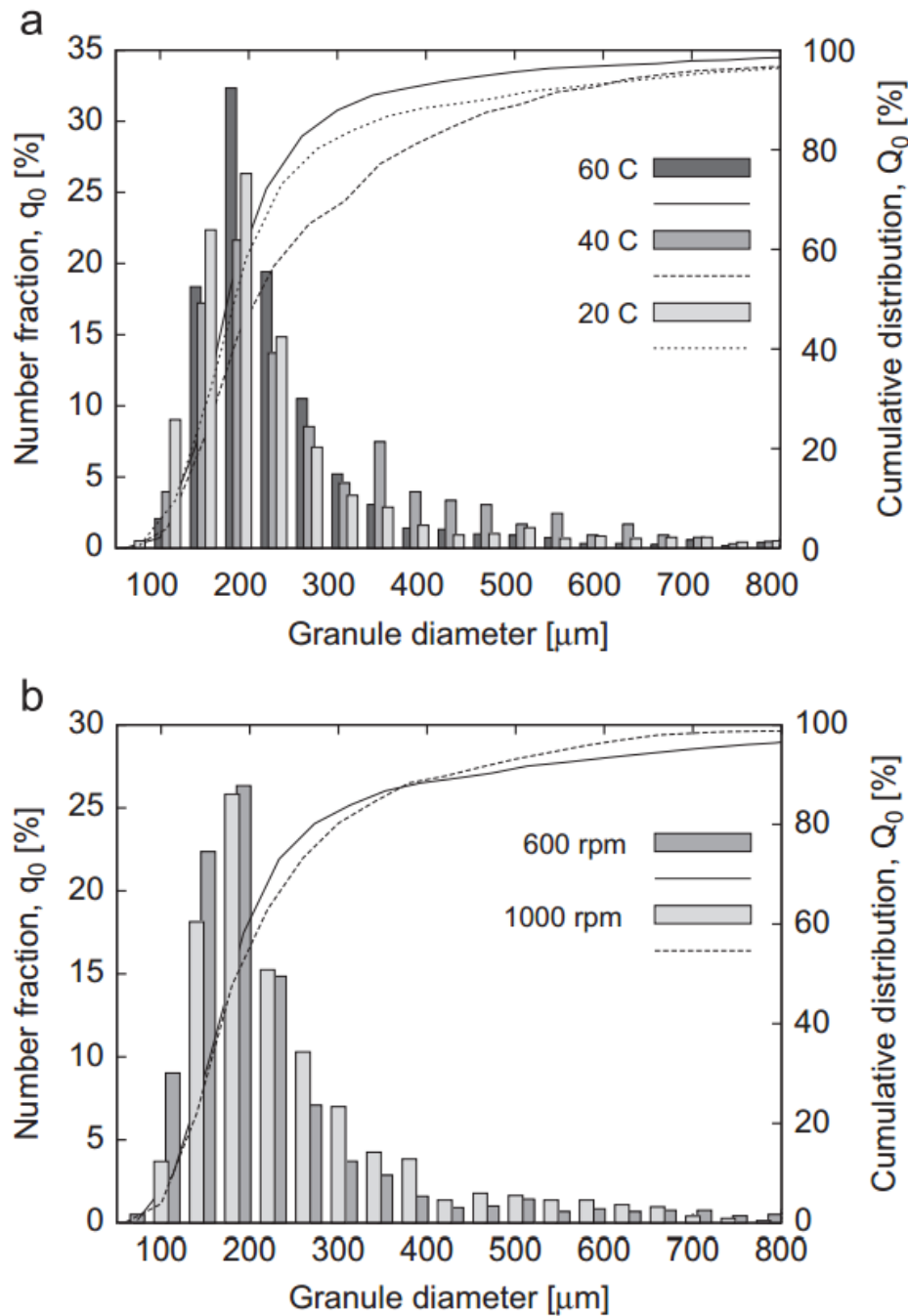


Figure 2.25. Particle size distribution with changes in (a) temperature and (b) agitation (Schöngut et al., 2013).

In summary, the literature suggests that the success of any granulation process using a reactive binder will therefore, depend upon the amount of binder that is added and the rate at which the reaction progresses. An increase in the temperature will reduce the viscosity of the binder, but will increase the rate of formation of the more viscous product

(LAS-Na) (Schöngut et al., 2013). The progress of the reaction changes the properties of the binder; it first becomes “sticky” and later too solid to partake in any further granule growth (Germaná et al., 2009). An understanding of the degree of neutralisation and the water content is therefore, necessary for controlling the transition of the binder from the liquid to the solid state, which influences binder wettability. A low water content and low relative humidity are desirable for promoting good wetting, which facilitates the formation of liquid bridges (Germaná et al., 2009).

2.10 Effect of binder viscosity

As the surfactants employed for the manufacture of dry laundry powders are generally very viscous, it is necessary to understand the role that binder viscosity plays on the granulation process. The viscosity of the binder has two major influences on the wet granulation process:

- It impacts the initial dispersion of the binder in a moving bed of powder (Schaefer and Mathiesen, 1996b, Rough et al., 2005b, Germanà et al., 2008).
- As discussed in Section 2.2, viscosity also has a direct influence on the rate of consolidation (i.e. higher the binder viscosity, poorer is the rate of consolidation) and thereby, also influencing granule growth post-nucleation (Ennis et al., 1991). However, if the binder is more viscous, the liquid bridges formed between two particles will be stronger. This facilitates more growth via coalescence (Schaefer and Mathiesen, 1996b). Therefore, when considering a binder with a higher viscosity in wet agglomeration applications, it is a trade off between poor consolidation as a result of reduced deformability, and enhanced growth as a result of stronger bridge formation during coalescence.

The influence of binder viscosity on the mean size of the granules has been previously studied by Mangwandi et al. (2010) and Chitu et al. (2011). At higher impeller speeds, both report an increase in the mean size of the granules, when the binder viscosity is higher. Mangwandi et al. (2010) also report an increase in the circularity of the granules when the binder viscosity is lower. This is in agreement with the observations made by Schaefer and Mathiesen (1996b), who claim the higher viscosity could reduce the sur-

face plasticity of the granules, thus making them more irregular in shape. However, according to Schæfer and Mathiesen (1996b), using a low viscosity binder may also lead to the formation of more elongated granules, as they are easier to deform.

Others (Schæfer and Mathiesen, 1996b, Mangwandi et al., 2010, Germanà et al., 2008, Chitu et al., 2011) have investigated changes in the granule strength with increasing viscosity of the binder. An increase in the strength of the granules with an increase in the viscosity of the binder was reported by Schæfer and Mathiesen (1996b), Germanà et al. (2009) and Mangwandi et al. (2010). However, at low impeller speeds the opposite trend has been reported by Chitu et al. (2011) and Mangwandi et al. (2010).

2.11 Effect of binder droplet size

Binder dispersion involves spreading the binder into a moving bed of powder. When the binder comes into contact with the bed of powder, the interactions between the two components determine the size, shape and strength of the resultant nuclei, and eventually the size, shape and strength of the end-product. Therefore, it is of interest to understand the effect of the initial size and shape of the binder (droplet) on the granulation process.

The motion of a droplet in a shear flow has been simulated in a liquid medium by Renardy et al. (2002), Feigl et al. (2003), and Favelukis et al. (2005). Feigl et al. (2003) simulated the motion of a droplet in the annulus between two eccentric cylinders (Figure 2.26). The flow pattern within this region is supposedly synonymous to the flow patterns generated by a rotor stator device for dispersing viscous substances. A droplet of polydimethylsiloxane (PDMS) was dispersed into a polyethylene glycol-water-ethyl alcohol mixture, which was used as the continuous liquid phase. PDMS is a Newtonian fluid. The evolution of the droplet is shown in Figure 2.27 and with time, it gets elongated and deformed. At higher rotational speeds, the droplet dissociates (gets broken up).

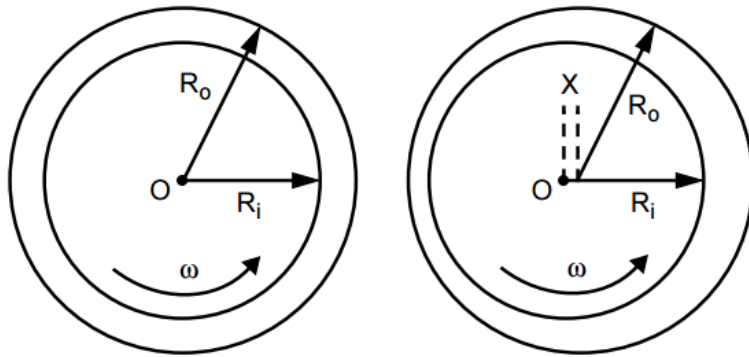


Figure 2.26. Schematic diagram of eccentric cylinder geometry (Feigl et al., 2003).

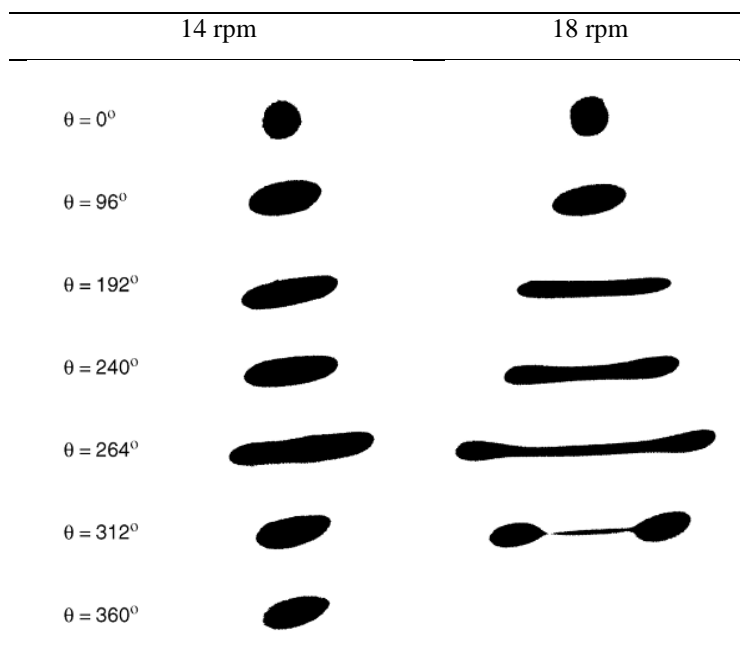


Figure 2.27. The evolution of a droplet within annular region of two eccentric cylinders. The inner cylinder rotates at two different speeds: 14 and 18 rpm (Feigl et al., 2003).

Favelukis et al. (2005) observed the evolution of a shear thinning droplet in a continuous phase. Their studies report that shear thinning droplets are harder to deform and break in comparison to Newtonian ones. The ratio of the viscosity between the dispersed and continuous phase was kept constant when making any comparisons. This suggests that droplet breakage may take longer for shear thinning binders.

Dynamic powder flows in a high shear environment are much more complex. The powder phase is also not continuous like a liquid, as some regions may be dense (closely

packed) whilst others could be less dense (more fluidised). Furthermore, the bed of powder is inclined along the base of a vertical shaft mixer (when it is operated), with the bed height at a maximum towards the walls of the mixing vessel. It is therefore difficult to infer what would happen in a moving bed of powder solely based on what is observed in a fluid medium.

The interaction between a droplet and a moving bed of powder has been investigated by Chouk et al. (2009) and Litster et al. (2001). Others have conducted droplet penetration studies using a static bed of powder (Agland and Iveson, 1999, Hapgood et al., 2002). Chouk et al. (2009) found that the movement of the binder droplet on a dynamic bed of powder was controlled by its own inertia. The droplet soon decelerates and its subsequent motion is dictated by the movements of the powder bed. They also claim that the inclination of the powder bed facilitates further deformation and breakage of the droplet. The extent of deformation also depends on the position of the droplet; deformation increases as the distance from the edge of the mixing vessel increases. This is largely due to an increase in the inclination towards the centre of the impeller, which aids in promoting the downward motion of the droplet. Figure 2.28 is a time lapse sequence of a polyethylene glycol (PEG) 2000 droplet in a moving bed of calcium carbonate powder.

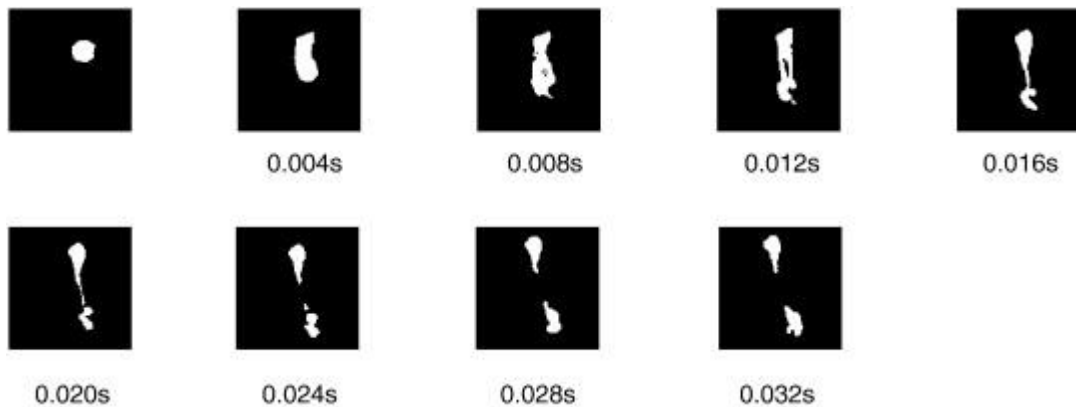


Figure 2.28. Time lapse image sequence of a PEG 2000 droplet on a moving bed of powder (Chouk et al., 2009).

Litster et al. (2001) studied the dispersion of binder in a spinning riffler (Figure 2.29). Binder was sprayed on the surface of a dynamic bed of powder. They define a dimen-

sionless parameter called a spray flux (Ψ_a), which is the ratio of the wetted area covered by the nozzle to the spray area in the nucleation zone. The spray flux controls the size and shape of nuclei. At low Ψ_a , the nuclei size distribution is narrow and the converse is true at high Ψ_a . At low fluxes, the droplet controlled regime dominates (refer to Figure 2.5), and at higher fluxes the powder bed starts to cake on the surface. Agland and Ivenson (1999) report similar results when conducting experiments on a static bed of powder. Their study focuses primarily on droplet impacts on powder surfaces. They define a critical Webber number (We_{crit}) that determines if the system begins to cake. We_{crit} appeared to increase with increasing particle size. If drops spread across the surface before sinking in, then this will increase the surface coverage and incidence of caking and nuclei coalescence.

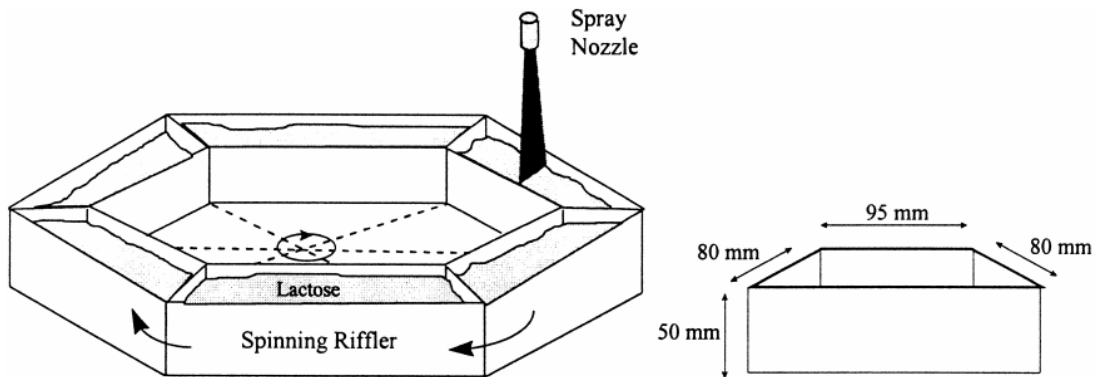


Figure 2.29. Dimensions of a typical spinning riffler tray (Litster et al., 2001).

Many of the studies conducted on droplet shape and size have been performed using liquids that are not highly viscous. In addition, the studies have been done in a liquid medium (Renardy et al., 2002, Feigl et al., 2003, Favelukis et al., 2005) or using single droplets (Chouk et al., 2009). Others have attempted to replicate the nuclei formation process in overly simplified set-ups (Litster et al., 2001). None of these studies have attempted to isolate the dispersion behaviour of a highly viscous binder in a high shear environment.

2.12 Effect of impeller speed

Impeller speed plays a paramount role in any high shear wet granulation process, as it influences every step of the granulation process (nucleation, growth and breakage). It

accelerates the time taken to progress through the different regimes, as discussed in Section 2.8.

At higher impeller speeds, an increase in the mean size of the granules is widely reported (Mangwandi et al., 2010, Knight et al., 2000). However, at very high impeller speeds, granule growth is impeded as breakage sets in (Knight et al., 2000, Vonk et al., 1997) and sometimes unmanageable granule growth is prevented by operating the mixers at such speeds (Schäfer and Mathiesen, 1996a). Vonk et al. (1997) studied the influence of impeller speed on the break-up of nuclei by agglomerating microcrystalline cellulose (MCC) and lactose, using water (as a binder). They report the break-up of large primary nuclei at impeller speeds of 50 rpm or more and this results in the formation of smaller secondary nuclei.

The impeller speed also has an influence on the granule strength (Mangwandi et al., 2010, Rahamanian et al., 2009, Hassanpour et al., 2009). Rahamanian et al. (2009) have reported a decrease in the porosity of the granules with increasing impeller speed and a corresponding increase in the strength of the granules (Figure 2.30). Mangwandi et al. (2010) report both, an increase and a decrease in the porosity and strength of the granules (depending on the viscosity of the binder) with increasing impeller speed (Figure 2.31 & Figure 2.32). An increase in the granule porosity and reduction in the granule strength is observed, with an increase in the impeller speed, when using a low viscous binder.

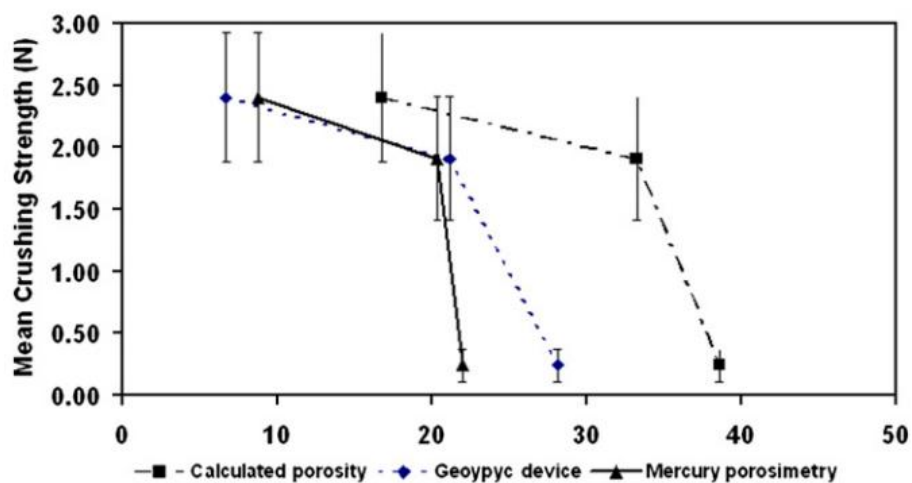


Figure 2.30. The trend of granule strength versus porosity obtained by the different methods (Rahamanian et al., 2009).

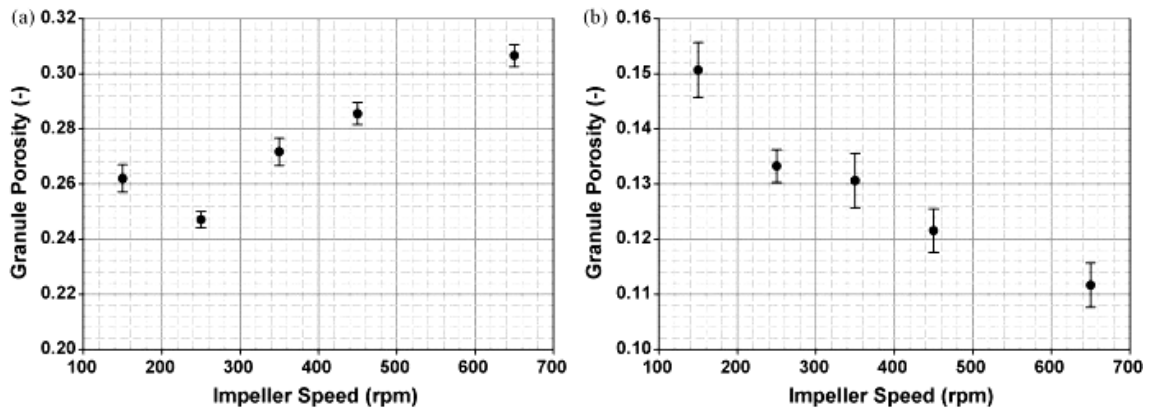


Figure 2.31. “Effect of impeller speed on granule porosity for granules in the size range 1.0–1.18 mm. (a) low viscosity system, (b) high viscosity system” (Mangwandi et al., 2010).

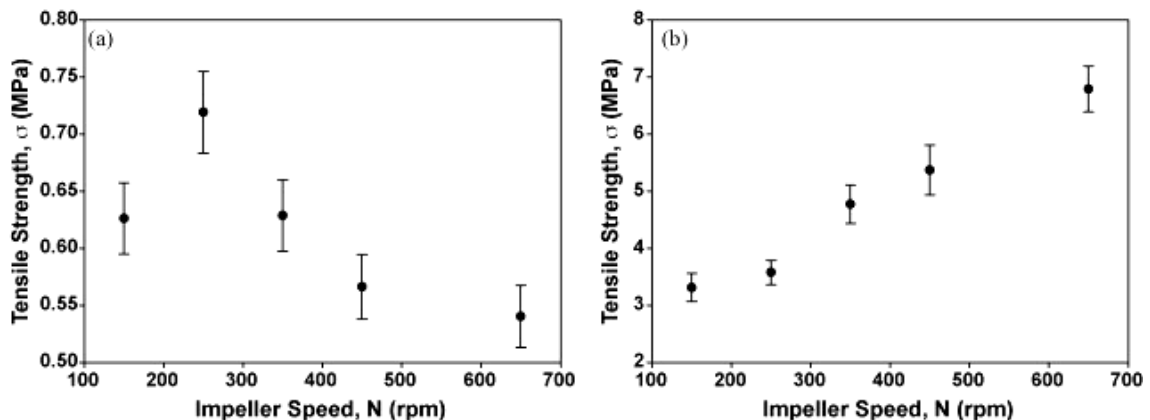


Figure 2.32. “Effect of impeller speed on the granule tensile strength of granules in the size range 1.0–1.18 mm. (a) low viscosity system, (b) high viscosity system” (Mangwandi et al., 2010).

Many (Rough et al., 2005b, Rahamanian et al., 2009, Mangwandi et al., 2010) have studied the influence of impeller speed on granule morphology too. Rahamanian et al. (2009) report an increase in the circularity of the granules with an increase in the impeller speed. They also observe that granules produced at lower impeller speeds are more elongated. However, Mangwandi et al. (2010) report the opposite trend and Rough et al. (2005b) observe that an increase in the impeller speed does not change the morphology of the granules significantly (when using a highly viscous binder).

Any disparities in the trends observed as a result of the change in the impeller speed is due to other factors such as formulation variables c.f. Mangwandi et al. (2010) report two different trends in the granule size, strength and porosity with an increase in the impeller speeds, when a low and high viscous binder are used.

2.13 Effect of primary particle size

The size of the primary particles used in any wet granulation application determines the amount of binder required to form granules. Granules are formed when primary particles adhere to one another. Adhesion between particles is as a result of the formation of liquid bridges between them. Larger particles have a smaller surface area; therefore require less binder than smaller ones to ensure complete wetting or saturation of all available surfaces. Keningley et al. (1997) report an increase in the minimum liquid to solid ratio in order to form granules with a decrease in the mean size of the primary particles. The primary particle size also determines the critical viscosity of the binder that is required to promote the formation of liquid bridges. To prevent breakage of the bridges, a higher viscosity is required when the primary particle size is larger (Keningley et al., 1997).

2.14 Effect of the method of binder delivery on granule properties

Liquid binder can be introduced into a high shear granulator in four main ways: preloading, pouring, melting and spraying. Holm et al. (1984) observed an inhomogeneous size distribution when a binder of low viscosity was not atomised (sprayed) particularly, at lower impeller speeds. Therefore, spraying the binder or reducing the size of the binder droplets leads to better binder distribution. Knight et al. (1998) investigated three different methods of binder addition pouring, melting and spraying using a single low viscous binder. For all three methods of binder addition, the resulting granule size distribution was initially bimodal, and with time they become mono-modal. They also report that spray-on and melt-in techniques yielded a lower proportion of coarse granules and had more fine material when mixed for longer compared to the pour-on method. Also, the melt-in method produced granules with the smallest $D_{v4,3}$ and the bimodality in the size distribution took longer to appear for this technique. They conclude that initially all three methods of binder addition give rise to different liquid distributions within the

powder bed. However, at prolonged mixing times, the distribution improves and differences becomes less apparent. Eventually, growth by agglomeration will be matched by breakage and attrition therefore, the size distribution will reach a steady state and becomes time independent (Michaels et al., 2009). In other words, when the stress acting on an agglomerate or granule is greater than the strength of the liquid bridge between them, breakage will occur, however if the converse is true then growth will dominate.

For the pour-on method, Knight et al. (1998) found that initially, the coarse granules consist of three distinct phases: air, liquid and solid. The binder is not evenly distributed within the structure of the granules. However, they did not investigate the internal structure (binder distribution and porosity with granule size fraction) for the granules made using the other methods of binder addition. Spraying is preferred over the other methods, as it minimises the amount of energy required to disperse the binder once it is in the mixer thereby, shortening granulation times to reach the same set point. In other words, the smaller the size of the droplet that is introduced into the mixer, the quicker will be the initial dispersion, spread and distribution of the binder into the mass of powder. The method of binder addition thus, has an effect on the kinetics of granule growth. The conclusion of their study reveals that there is non-uniformity in the distribution of the binder for all cases of binder addition. This non-uniformity is most pronounced during the early stages of the granulation process. Other literature that has focussed on the method of binder delivery also conclude that the delivery condition has an influence on the kinetics of the granulation process (Schaefer and Mathiesen, 1996a, Osborne et al., 2011).

Changing the method of binder addition, not only changes the droplet size of the liquid binder, but also the rate of binder addition. Hence, another factor that is likely to influence binder distribution is the rate of liquid addition. Knight et al. (1998) observe a larger average granule size for the pour-on method in comparison to the spray on method. Pouring all the binder into the mixer at once is likely to result in over-wetting of certain regions of the powder bed, which leads to the rapid formation of large granules or lumps. Whereas, spraying the binder more gradually does not result in the formation of lumps, as over wetting is greatly reduced. Smirani-Khayati et al. (2009) also claim that increasing the rate at which binder is added into the mixer influences the kinetics of the

granulation process, i.e. larger granules are formed earlier on in the granulation process. According to their study, when a larger quantity of binder is introduced into the mixer over a shorter period, the probability of the droplets colliding with the powder is increased therefore, the rate of nucleation is enhanced. However, the final granule size is not influenced by the rate of addition.

A commonly used approach to monitor binder distribution is to compare the binder content in different size classes. It is widely reported that there is a higher binder content in larger granules (Osborne et al., 2011, Scott et al., 2000, Reynolds et al., 2004). In order to compare the effect of the method or rate of binder addition, it is common practice to look at the binder content in a similar size class of granules (Figure 2.33). Initially, the heterogeneity in the binder content amongst the different size classes is likely to be greater, and with time this heterogeneity is greatly reduced. When the wet massing time is short, the time available for binder distribution will be short, and the resulting heterogeneity in binder distribution will be greater.

Majority of the aforementioned studies have focused on understanding the impact of binder addition on the distribution of low and moderately viscous liquids and in some cases, the distribution of a solid that is melted within a granulator at an elevated temperature. There is, however, a knowledge gap on the impact of binder addition methods on the dispersion and subsequent distribution of a highly viscous semi-solid binder.

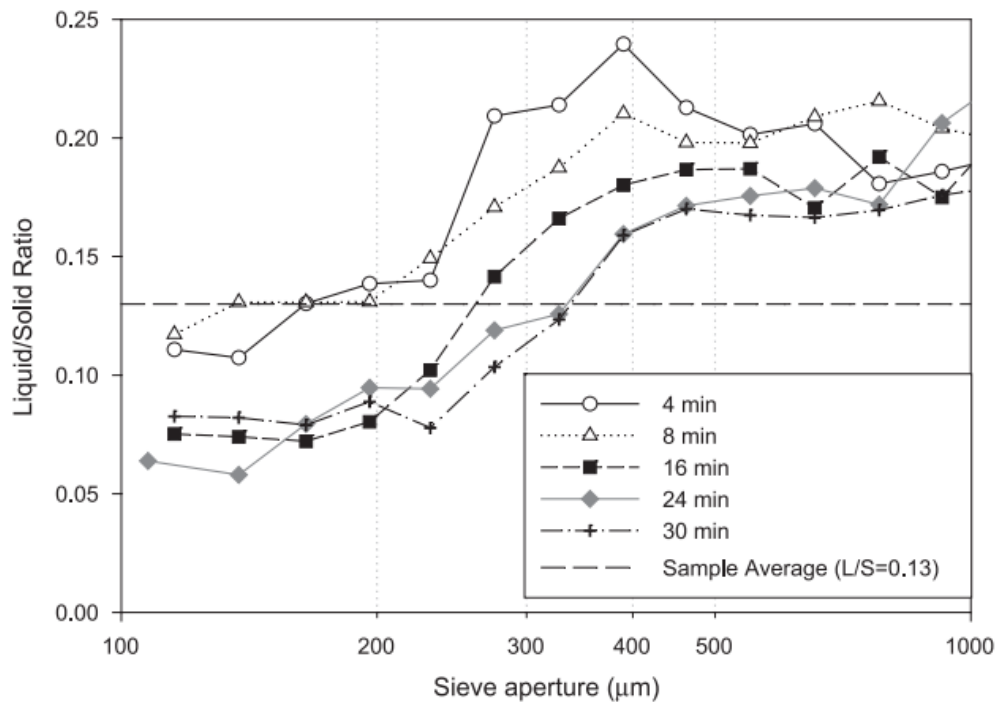


Figure 2.33. Size-averaged liquid to solid ratio distribution for bulk granulation sample (Reynolds et al., 2004).

2.15 Summary of recent work and identification of knowledge gaps

To summarise, a key difference or challenge in detergent agglomeration is handling and dispersing the highly viscous surfactant binder. In comparison to water these binders are about $\times 10^4$ more viscous. For the reactive granulation, involving LAS acids, dispersion is more complex due to changes in the viscosity as the reaction progresses.

Rough et al. (2003, 2005a, 2005b, 2005c, 2005d) have identified the existence of several distinct regimes during the agglomeration process. The rate at which the aforementioned regimes are achieved can be accelerated by increasing: the temperature of the binder, binder to solids ratio or impeller speed. All of the existing studies on soft-solid binder granulation have been done using zeolite or calcium carbonate (calcite) as the powder medium in a domestic food processor. Their research is primarily focused on the final granule attributes. Additionally, research on reactive granulation has been principally focused on the reaction kinetics, binder wettability and granule attributes like size and strength. Therefore, there is a lack of knowledge on how the initial dispersion

of the surfactant binder takes place and how this impacts on the granulation process as a whole.

The present study begins by looking into the effect of the method of semi-solid binder delivery on the kinetics of the granule growth, which has not been investigated previously. It also focuses on the distribution of a binder, with a view to isolating and quantitatively describing the dispersion of the lumps of highly viscous binder, as a function of time. This study also monitors the movement of the surfactant binder, *in situ*, to obtain useful insights concerning dispersion in a pilot scale system for detergent agglomeration – a paddle mixer.

The thesis describes a granulation operation that is not conventional – largely due to the high viscosity of the binders that are employed in detergent agglomeration applications. The process is, however, of great industrial importance. Therefore, there is also an interest in being able to predict and model high viscous binder dispersion, and to date the author is not aware of any work that has been conducted concerning this. This study uses a population balance based kinetics approach to model and describe the dispersion of a semi solid binder in a moving bed of powder.

One way of assessing the extent of binder dispersion is to monitor the size of the semi-solid binder “particles” within the granulator, as a function of time. Thus, it is essential to have a good understanding of particles size, particle size distributions and different methods of representing them. The next section starts by giving an introduction to particle size and is followed by another section that introduces population balance modeling.

2.16 Particle size

There are numerous ways in which the size of a particle can be described. It is normally given in the form of a linear dimension (such as the particle diameter or length). However they can also be reported as a volume, V , or a surface area, a_s . Describing particles that have a regular shape is easier, as they have linear dimensions which are clear-cut (Hounslow, 2005). An example of this would be a sphere, which can be defined by its

radius or diameter. Its volume and surface area can also be easily calculated using well known equations.

Most particles are not regular in shape making it difficult to assign a single linear dimension to describe its size. To make uneven shapes easier to describe it is convenient to define a volume-equivalent sphere diameter. Area equivalent diameters are defined similarly. These equivalent particle sizes are hypothetical dimensions that could be assigned to a model particle (that is usually spherical) with the same volume or surface area (Table 2.2).

When measuring the particle size of a sample it is often good practice to ensure that the sample you are measuring is representative of the bulk. This process is referred to as powder sampling. A chute splitter or rifle sampler can be used for this purpose. This is a device that contains many v-shaped channels, which split a sample into two equal halves. The process is repeated until the desired sample size is achieved. This reduced sample can then be used for size analysis.

Table 2.2. Geometric equivalent diameters (Figura and Teixeira, 2007).

Equivalent diameter	Equation	Measured quantity
Volume equivalent sphere	$d_v = \sqrt[3]{\frac{6V}{\pi}}$	volume, V
Surface area equivalent sphere	$d_A = \sqrt{\frac{A}{\pi}}$	surface area, a_s
Projected area equivalent circle	$d_p = \sqrt{\frac{4S}{\pi}}$	projected area, S
Perimeter circumference equivalent circle	$d_{Pe} = \frac{U}{\pi}$	perimeter of the projected area, U

2.17 Particle shape

The shape refers to the location of the particle surface as a function of two independent variables (Figura and Teixeira, 2007). It can also influence properties such as flowability of the powders and its packing. There are several different qualitative terms which can be used to describe the shape of a particle (Table 2.3).

Table 2.3. Definitions of particle shape (adapted from Allen, 1997).

Description	Definition
Acicular	Needle shaped
Angular	Sharp-edged
Crystalline	Of variable geometric shape
Dendritic	Having a branched crystalline shape
Fibrous	Thread-like (can be regular or irregular)
Flaky	Plate like
Granular	Having approximately an equidimensional irregular shape
Irregular	Lacking in symmetry
Modular	A rounded irregular shape
Spherical	Global shape

Two numbers are often used to describe the shape of a particle: sphericity and aspect ratio. Sphericity is an example of a form factor that can be used to describe how similar a particle's shape is to a perfect sphere (Hounslow, 2005). This is normally determined by comparing the surface area of a perfect sphere to the surface area of the particle (Equation 2.4). As the value of the sphericity approaches a unity, the particle starts to resemble a perfect sphere.

$$\text{Sphericity, } \Psi = \frac{\text{surface area of the volume equivalent sphere}}{\text{surface area of the particle}} \quad \text{Equation 2.4}$$

The other important form factor is the aspect ratio. It is the ratio of the breadth to the length of the particle:

$$\text{Aspect ratio, } \alpha = \frac{\text{breadth}}{\text{length}} \quad \text{Equation 2.5}$$

2.18 Particle size distributions

In a given mixture, the constituent particles can vary widely in size. Therefore, to get an indication of the size of the particles, a large number of them have to be measured. Once these measurements have been made the results are often sorted into bins or size classes. These results are then presented in the form of a histogram, called a particle size distribution, where the horizontal axis represents different sizes that have been observed for the particles and the vertical axis is used to plot the frequency. The vertical axis would

depend largely on the characteristic (Table 2.4) that was chosen to represent the particle size.

Table 2.4. Characteristics that are frequently used to represent particle size (Figura and Teixeira, 2007).

Characteristic	Index r	How commonly are they used?
Number	r = 0	Very often
Length	r = 1	Seldom
Area	r = 2	Often
Volume	r = 3	Often
Mass	r = 3	Very often

Particle sizing may be done by sieving. This technique involves measuring the quantity of powder that falls through the openings of a sieve screen. Sieves are normally stacked so that the openings become progressively smaller from the top to the bottom. The powder is normally loaded on the largest screen at the top, and vibrated over period of time to aid the passage of the particles through the stack. After this time, the stack of sieves is disassembled and the mass of the powder on each screen is weighed. On each sieve, only material small enough to fall through the sieves above it, rest. In other words, material remains on the sieve because it is too large to pass through it (Figura and Teixeira, 2007).

The particles resting on each sieve have a size smaller than the sieve above it (the upper limit of the size class, x_i) and a larger size than the sieve below it (the lower limit of the size class, x_{i-1}). Based on this, a mass distribution can be constructed, where the vertical axis would be the relative mass fraction of the various size classes (Equation 2.6). The resolution of a particle size distribution is influenced by the width of these size classes, and the smaller the width of the size classes the greater the resolution.

$$Q_3(x_i) = \frac{\text{mass fraction } (x_{\min} \text{ to } x_i)}{\text{mass fraction } (x_{\min} \text{ to } x_{\max})} \quad \text{Equation 2.6}$$

There are two ways of representing a size distribution graphically:

- Frequency distribution: where the frequency (f_x) is plotted against the particle size (x).
- Cumulative frequency distribution: where the cumulative frequency (F_x) is plotted against x . F_x represents the quantity of particles of a size less than x .

2.19 Quantification of particle size distributions

Some key statistical parameters that are of paramount importance when describing any size distribution are summarized below:

Mode: particle size corresponding to the maximum frequency on a frequency versus particle size plot. It indicates the particle size that occurs most frequently. For example, if $r = 0$ (refer to Table 2.4), the mode would correspond to the particles size class with the highest count, and if $r = 3$ the mode would correspond to the size class which has the largest relative mass/volume fraction (Hounslow, 2005).

Median: is the middle value of a range of values for a particular characteristic. Median can also be determined by listing all the values in ascending order, and determining which value lies in the middle of that sequence. The median therefore divides a population into two equal parts, it is thus given the symbol x_{50} or D_{50} (Figura and Teixeira, 2007). If there are even numbers of particles in a population then, there would be two values in the middle, in which case the median would be the average of these two values. This quantity is often used to describe size distributions, as it is robust to single extreme values in a population. It is easier to determine the D_{50} from a cumulative frequency distribution than from a frequency distribution (Hounslow, 2005).

Average particle size (integral mean): also referred to as the arithmetic mean or average. The average particle size is determined by dividing the sum of all the individual particles sizes by the total number of particles in that sample. In contrast to the median and mode, the average is affected by size of each individual particle (Figura and Teixeira, 2007).

The method used to determine the mean would again vary depending on the characteristic chosen to represent the sample (number, length, area, volume or mass). The number based mean is determined using Equation 2.7.

$$X[1,0] = \frac{\sum n_i x_m}{\sum n_i} \quad \text{Equation 2.7}$$

Where x_m is the mid-value of the size class, which can be determined by taking the average of the lower size class limit (x_{i-1}) and the upper size class limit (x_i), and n_i is the frequency of size class m .

Similarly, the area and volume based mean sizes are determined from Equation 2.8 and Equation 2.9 respectively.

$$X[3,2] = \frac{\sum n_i x_m^3}{\sum n_i x_m^2} \quad \text{Equation 2.8}$$

$$X[4,3] = \frac{\sum n_i x_m^4}{\sum n_i x_m^3} \quad \text{Equation 2.9}$$

The area based mean is sensitive to the presence of many small particles due to their high surface area, and the volume based mean is sensitive to the presence of large particles due to their larger volume.

2.20 Modelling dispersion using a population balance approach

Within the field of chemical engineering, there has always been a strong interest in being able to model and simulate processes like granulation and milling. Most models try to link what is seen on a macro-scale to what happens on a micro-scale. When analysing particulate systems, the main objective is to be able determine ways in which populations of particles behave, based solely on the behaviour of a few particles in localised settings (Ramkrishna, 2000).

These populations of particles can be described by the density of a suitable extensive variable such as particle number, area, volume and mass per unit volume. The usual transport equations which express conservation laws for material systems apply to the

behaviour of these individual particles too (Ramkrishna, 2000). Most notably, the law of conservation of mass which states that when considering a closed system, the total mass of that system cannot change with time. In other words, mass cannot be created or destroyed.

One way of accounting for all the materials that enters, leaves and accumulates within the system is through a mass balance. In essence, a mass balance accounts for all the material that goes in and out of a specific system boundary. Mass balances can be done for two different conditions including (Levenspiel, 1999):

- Dynamic systems – where the mass changes with time (for example, if the flow rate of a certain material changes with time)
- Steady state systems – where the flow of a stream does not change with time and the system is in equilibrium.

A dynamic system is more difficult to model mathematically. Most batch granulation processes and the population balance models used to describe them, look at steady state problems, where the output rate is the sum of the input rate and the rate of reaction (Equation 2.10).

$$\text{Input rate} = \text{output rate} - \text{reaction rate} \quad \text{Equation 2.10}$$

In this study, the “reaction rate” refers to the change in the size of the binder particles with time. Therefore, there are no flows into or out of the high shear mixer once granulation commences. Any changes in the particle density within the mixer occur as a result of the binder dispersion.

The entire process can be modelled as a batch operation, which as the name suggests, is a non-continuous and a perfectly mixed closed vessel where variations in the local particle density occur. Providing the volume (V) of the mixer is known, then the initial concentration or density (n_0) of the particles can be determined. The total mass of the material in the mixer will therefore be $M_T = n_0V$. With time, the concentration of the

particles within the mixer will change, and this can be quantified by using Equation 2.11 (Metcalfe, 1997).

$$\text{Accumulation} = \text{Mass In} - \text{Mass Out} + \text{Generated} - \text{Consumed} \quad \text{Equation 2.11}$$

For the system shown in Figure 2.34, Equation 2.11 becomes Equation 2.12:

$$Q \cdot n_{in} - Q \cdot n_{out} - \int_V^0 r dV = \frac{dm}{dt} \quad \text{Equation 2.12}$$

where Q refers to the flows into and out of the batch mixer and r is the rate of binder dispersion. For a batch process $Q = 0$, and as the volume of the mixer is constant, it therefore follows that:

$$\frac{dm}{dt} = \frac{d(n \cdot V)}{dt} = V \cdot \frac{dn}{dt} = rV; r = \frac{dn}{dt} \quad \text{Equation 2.13}$$

where $n = n(t)$ is the particle density inside the mixer at any time.

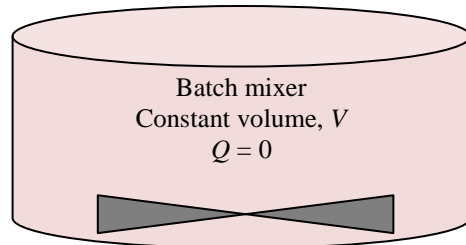


Figure 2.34. High shear mixer represented as a constant volume batch reactor where binder dispersion occurs.

To reiterate, population balance models are macroscopic models that can be used to describe the rate of change of the particle number density (or any other extensive variable) as a function of time. These equations are consistent with the law of conservation of mass. They also have a wide range of applications including dispersed phase systems (gas-liquid, gas-solid and liquid-liquid dispersions) (Ramkrishna, 2000).

Key features of any population balance model include the existence of a number density at every point in the particle state space (Ramkrishna, 2000). The number of particles can be determined by integrating the number density over the desired region. So in es-

sence, the population balance model accounts for the various ways in which the particles could either form in or disappear from a particular region in the system, as any mass balance would.

Any process that results in the generation or consumption of particle of a certain size need to be accounted for, these could include the “birth” of new particles (referred to as birth processes) and “death” of existing particles (referred to as death processes). Birth could occur as a result of the death of larger particles (by breaking or splitting), nucleation and aggregation processes. Death could occur as a result of the larger particles breaking into smaller ones or aggregation with other particles to form larger ones. When any processes that does not change the total number of particles (in a given particle state space) occurs (i.e. no births or deaths) then, these terms are collectively known as convective processes. When the birth, death and convective process terms are combined, it results in the formation of a population balance equation, which could be used to describe a real-life granulation process. Chapter 6 outlines a model that describes binder dispersion in a high shear batch granulation process.

Chapter 3 Experimental Methodology and Characterisation of Materials

3.1 Introduction

In this chapter details of the experimental methods employed, analytical tools used and other measurements techniques have been elaborated.

They have been presented in the following order:

- Description of the high shear mixers used in this study.
- Description of the various materials that have been used in this study (primary powders and binders).
- Description of the methods that have been used to characterise the raw materials (primary particle size measurements, scanning electron microscopy, binder viscosity measurements, etc.).
- Description of the methods that have been adopted to determine various properties of the granules (size, strength, binder content, porosity, etc.).

Some of the materials used and experimental procedures that have been conducted have also been introduced and explained in the individual chapters.

3.2 High shear mixers

A range of different granulation equipment that are relevant to the detergent industry were used in this study. This includes a 10 L vertical shaft Roto Junior high shear mixer, a custom made 100 ml vertical shaft high shear mixer, and a 32 L horizontal shaft Bella B-32-XN paddle mixer. All of these are batch mixers.

The 100 ml custom made mixer is a scaled down replica of the 10 L Roto Junior high shear mixer. It was used to quantify the dispersion of the semi-solid binder in a moving bed of powder.

3.2.1 10 L Roto Junior high shear mixer

A 10 L Roto Junior high shear mixer from Zanchetta & C. s.r.l., Italy, was used for conducting lab scale experiments (Figure 3.1). The mixer is cylindrical and has a vertical drive shaft. The mixing bowl is 0.28 m in diameter and 0.18 m in height. The impeller has a radius of 0.14 m and its speed can be varied from 10 – 850 rpm. It also has a water jacket that enables the temperature of the system to be varied from 25 – 80°C. It is equipped with a chopper and a binder spraying pot too. There is a pneumatic cleaning system to minimise the accumulation of powder in the clearance between the impeller and the mixing bowl.

The mixer comes equipped with a variety of different blades with different angles ranging from 27 – 45°. The higher the pitch of the blade, the greater its impact on the powder bed upon collision. The blade with a 45° pitch was used to investigate the effect of different methods of binder delivery on the kinetics of binder dispersion and granule growth. There is also a flat plate impeller available to isolate and study the effect of shear alone.



Figure 3.1. A 10 L Roto Junior high shear mixer.

3.2.2 “Mini-mixer”

A small 100 ml custom made high shear mixer was used in this study (Figure 3.2 - Figure 3.3). The impeller has a radius of 4.2 cm. The mixer is cylindrical. The bowl is 8.5 cm in diameter and 5 cm in height. The impeller speed can be varied from 0 – 600 rpm.

The impeller's three blades are pitched at an angle of 45° (same pitch as the blade used with the 10 L Roto Junior high shear mixer) and the angle between the blades is 120°. The clearance between the impeller and the bottom of the wall of the mixing vessel is negligible i.e. the clearance is too small for material to accumulate beneath the impeller.

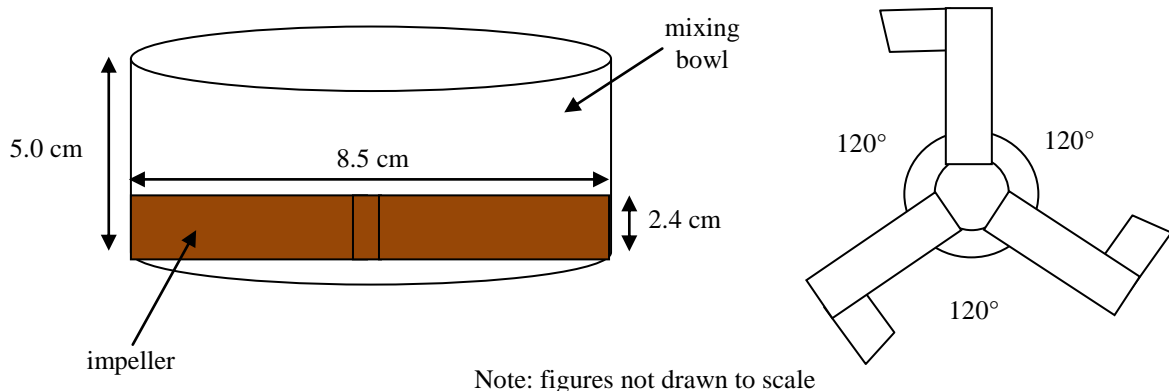


Figure 3.2. Schematic of the “mini-mixer”.

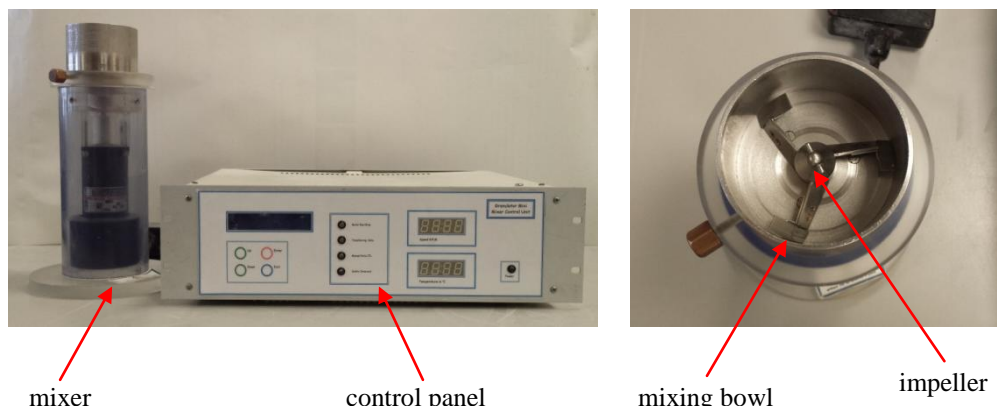


Figure 3.3. Image of the 100 ml “mini-mixer”.

3.2.3 32 L Bella B-32-XN paddle mixer

A horizontal twin-shaft 32 L Bella B-32-XN batch paddle mixer by Dynamic Air Conveying Systems, USA was used to monitor the dispersion of a reactive binder in a moving bed of powder (Figure 3.4 - Figure 3.6). The shafts are counter rotating and intermeshing. The paddles have a radius of 9.5 cm. Material is charged from the top of the mixer, and discharged through two large bomb bay doors located at the bottom of the mixer. Sufficient material was added to cover the paddles and the shafts (fill level \approx

40%). The air space directly above the paddles aids in fluidising the material during operation. The paddles lift material along the centre of the mixer, where most of the mixing is believed to take place. This section is referred to as the fluidised zone, as material is suspended momentarily, in a weightless state. Binder is injected from the bottom of the mixer in to the fluidised zone. Transport of the materials is axial and bidirectional.

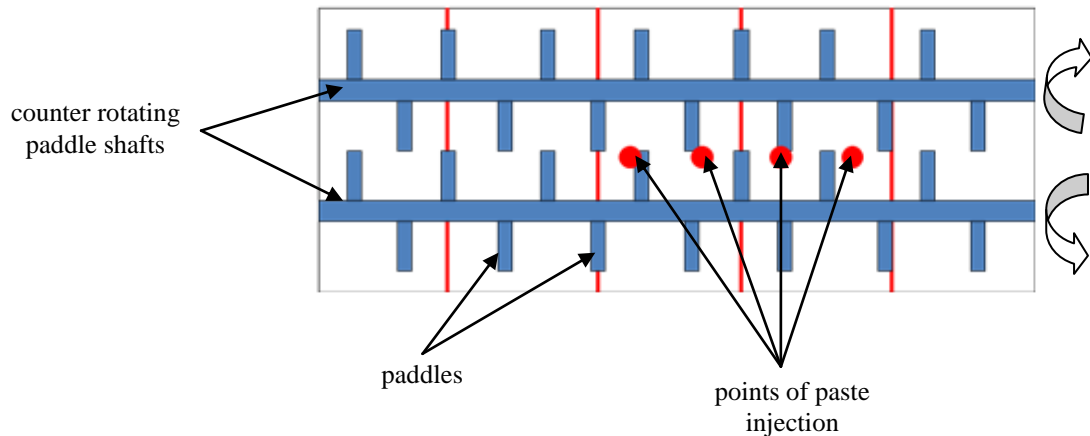


Figure 3.4. Schematic of the aerial view of the 32 L paddle mixer.

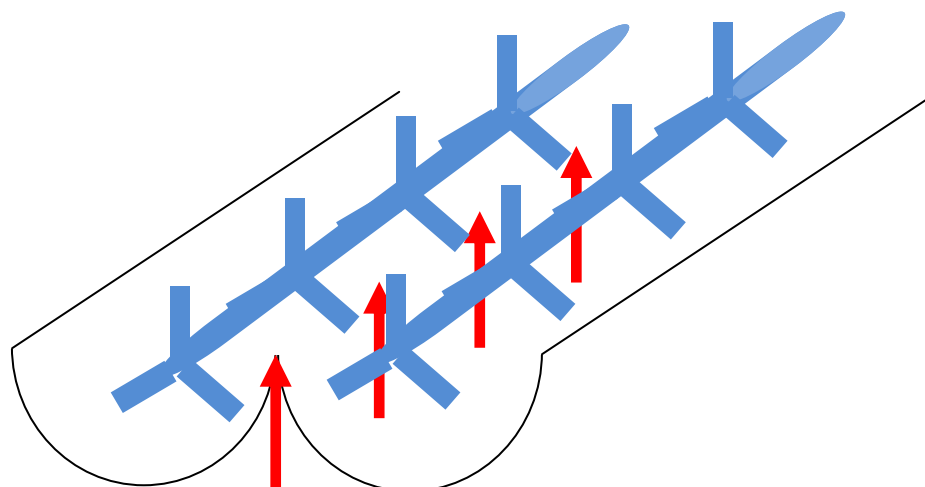


Figure 3.5. Side view of the paddle mixer. Binder is injected (red arrows) from the bottom at certain points along the horizontal axis of the mixer.



Figure 3.6. Image of the aerial view of the Bella B-32-XN 32 L paddle mixer.

3.3 Materials

As discussed in Section 2.3, the main components of any detergent formulation are surfactants, builders, bleaching agents and special additives such as enzymes. Surfactants help remove grease, dirt and oil from fabrics. However, their effectiveness is impaired by the presence of magnesium and calcium ions in areas that contain hard water. Therefore builders that compete with these ions are often added into modern formulations to counteract their effect and help increase the detergency of the formulation. Zeolite and sodium carbonate are two examples of commonly employed builders. Zeolites help improve the detergency by ion exchange and sodium carbonate improves detergency by precipitating magnesium and calcium ions (CEFIC, 2000).

Components such as bleaches and enzymes are present in detergent formulation in much smaller quantities (Bayly et al., 2009). Therefore, the effect of their presence on granulation process has not been investigated. Three different powders (primary particles) were used in this study, including light sodium carbonate (light soda ash), ground sodium carbonate (ground soda ash) and zeolite. This section discusses general structural features, properties and areas of application of each of the materials studied in this thesis.

3.3.1 Zeolites

Zeolites are naturally occurring compounds found originally in rocks of volcanic origin (CEFIC, 2000). Zeolite is derived from Greek and loosely translates to a “stone that boils”. In 1756, it was observed by a Swedish mineralogist Baron von Cronstedt that when the rocks of zeolite are heated rapidly they released water and appeared to boil (Friedman, 2004).

Nowadays, it refers to crystalline aluminium silicates of natural and synthetic origin. They have the following general formula: $M_{x/n}[(AlO_2)_x(SiO_2)_y \cdot zH_2O]$. M is generally a cation with an interchangeable valency n , and y refers to the number of SiO_2 molecules in its structure. Zeolites are composed of several SiO_4^{4-} and AlO_4^{4-} tetrahedrons, which are linked by so-called secondary building units to form a three dimensional network (Friedman, 2004). More than 50 natural and 200 synthetic zeolites have been classified to date. A common property of all zeolites is their ion exchange capability, and for this reason they are sometimes referred to as “molecular sieves”. They are used in a variety of different industrial processes and products, including fluid catalytic cracking, waste water treatment, construction materials, paper manufacturing, animal feeds and in cat litter (CEFIC, 2000).

Three different varieties of zeolite are available for use in detergent applications; these are Zeolite A, Zeolite P and Zeolite X. All three varieties have significantly different structures. Zeolite A, also referred to as Zeolite NaA or Zeolite 4A has a cavity which is known as an α -cage, which has a diameter of 0.42 nm and can therefore, be permeated by calcium ions. The smaller magnesium ions are impeded as they have a hydrate shell - $[Mg(H_2O)_6]^{2+}$. At higher temperatures, the hydrate gradually disintegrates, thus making the zeolite more permeable to magnesium ions as well. Zeolite P has a higher value of y and its pore size is smaller (0.30 nm), it therefore binds to calcium ions strongly. Zeolite X (the latest introduction) has the largest pore diameter of 0.74 nm, making it the most porous. Its ability to act as an ion binding agent is therefore far better compared to the Zeolite A and P varieties (Friedman, 2004).

Zeolite A powder (sodium aluminosilicate, $\text{Na}_{12}\text{O}_6\text{Al}_{12}\text{O}_{18} \cdot 12\text{SiO}_2 \cdot 27\text{H}_2\text{O}$) supplied by PQ Corporation, USA was used in this study. It is a fine white powder that is insoluble in water (true density: 2240 kg/m^3).

3.3.2 Sodium carbonate

Sodium carbonate or soda ash makes up a large proportion of a typical detergent formulation as they are the cheapest builders. There is, however, one disadvantage of using a builder that precipitates out other poorly soluble salts, in that it leads to the incrustation of inorganic deposits on to the fibres on the surface of the fabric. This is minimised by adding compounds known as polycarboxylates (Friedman, 2004).

Sodium carbonate improves the detergency by increasing the pH of the washing medium. This is done by lowering the surfactant's critical micelle concentration (CMC). In colloid and surface chemistry, CMC is defined as the concentration above which micelles form (KRÜSS, 2014). At lower surfactant concentrations, the surfactant molecules arrange on the surface of the aqueous medium. When more surfactant is added, the surface tension drops even further, as more surfactant molecules are available on the surface. The point at which the surface of the aqueous medium gets saturated with surfactant molecules is known as the critical micelle concentration (Figure 3.7).

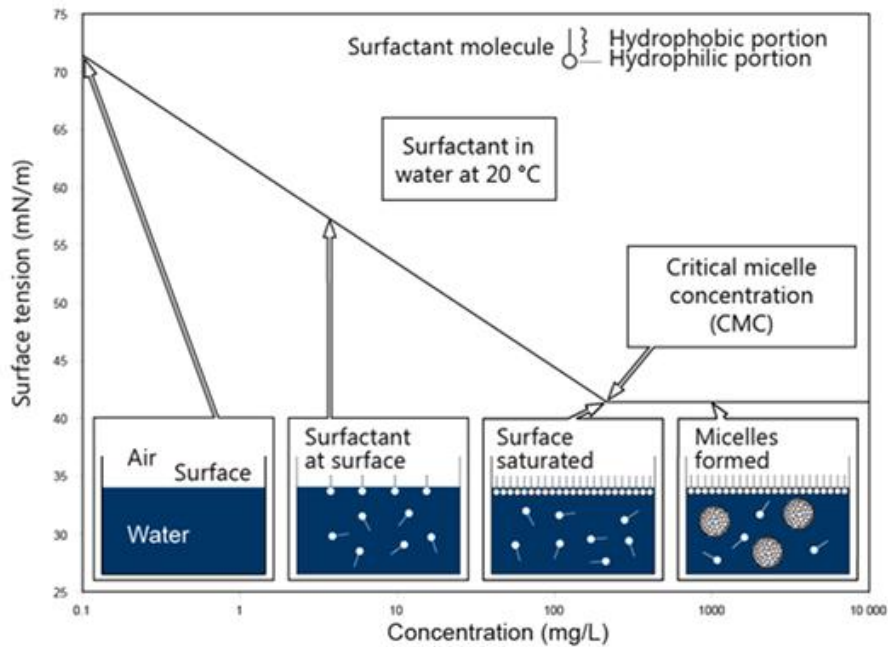


Figure 3.7. Effect of the surfactant concentration on the surface tension (KRÜSS, 2014).

Two different sizes of sodium carbonate were used in this study. Light ash (sodium carbonate, Na_2CO_3) supplied by Tata Chemicals, UK, is a coarse white powder that is soluble in water (true density: 2540 kg/m^3). Ground ash is obtained by micronising light ash using a pin mill. The milling process was carried out by Procter & Gamble at their Technical Centre in Newcastle and the exact details of this size reduction operation is proprietary information.

3.3.3 Sodium alkyl ether sulphate paste (AE3S)

The surfactant used in this study is sodium alkyl ether sulphate (also known as sodium laureth sulphate or sodium lauryl polyoxyethylene ether sulphate). It is an anionic surfactant (refer to Section 2.4 for the classification of surfactants based on their charge). Its chemical structure is shown in Figure 3.8.



Figure 3.8. Structure of sodium alkyl ether sulphate.

STEOL CS-370 surfactant paste supplied by Stepan GMBH, Germany, was used in this study. It is an aqueous concentrated sodium lauryl ether sulphate. It is a highly viscous semi-solid paste that is opaque and pale yellow in colour. The binder has a water content of around 30%, a viscosity of around 9 Pa.s at 25°C and a shear rate of 10 s⁻¹. The density of the paste is 1085 kg/m³ at 25°C. The binder was dyed with anionic Monazol blue BV from Brenntag, Germany, to give good contrast against the brilliant white powders during microscopy. The concentration of the dye in the paste was 0.1 g/dm³. The blue dye was dissolved in 1 ml of water and mixed into 2 L of the detergent paste. The paste was then stirred at 1500 rpm for 30 mins using an overhead stirrer. This binder is different from the HLAS binder used in reactive granulation. It is a **neutral in pH** and there is **no reaction** between the binder and the basic powders that are present in the detergent formulation.

This specific compound is synthetically derived from fatty alcohols and is ethoxylated to an average of 3 moles. Ethoxylation is the process by which ethylene oxide is added to a fatty acid alcohol, to create the deteritive properties of the surfactant molecule. Also, the higher the ethoxylation the less irritating it is to the skin and the more soluble the surfactant is in water. After ethoxylation the molecule is sulphated using sulphur

trioxide gas. Besides dry laundry powder, this substance is also used in manufacturing hand soaps, shampoos and bath products. The manufacturer states the product can be thickened if required by using salts, betaines or amides. Betaines and amides also serve to enrich foaming when mixed with water (Stepan, 2010). Some of the other key properties of the compounds are summarised in Table 3.1. The percentage of active gives an indication of the amount of water present in the surfactant. The cloud point refers to the temperature below which a waxy substance forms a cloudy appearance.

Table 3.1. Properties of STEOL CS-370 surfactant (Stepan, 2010).

Property	Description
Active, %	70
Density, g/cm ³	1.09
Moles of EO	3
Physical state/form at 25°C	Paste
Surface tension, mN/m	32
CMC, mg/l	183
Melting/freezing point, °C	6
Cloud point, °C	11

3.3.4 Linear alkyl benzene sulphonic (LAS) acid

Linear alkyl benzene sulphonic acid (LABSA, HLAS or LAS acid) is the reactive binder used in this study. It is also known as dodecylbenzene sulphonic acid. They are derived from linear alkyl benzenes (LAB) (BASF, 2012). It has the chemical formula C₁₆₋₁₉H₂₆₋₃₂O₃S (Figure 3.9). LAB is reacted with sulphur trioxide (SO₃) gas to make LAB sulphonic acids. LAS is primarily used for the manufacture of detergents (washing and cleaning products). Key benefits of using LAS include its comparatively low cost and good wettability. At room temperature (25°C), it is a dark brown viscous liquid. Some other properties of LAS acid are summarised in Table 3.2. TensaAryl SBLA LAS acid made by TensaChem, Belgium was used in this study.

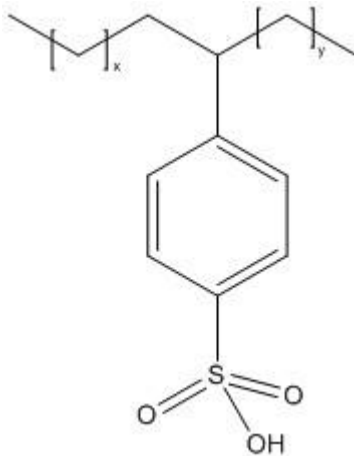


Figure 3.9. Chemical structure of LAS acid.

Table 3.2. Properties of LAS acid (BASF, 2012).

Property	Description
Active, %	96
Physical state/form at 25°C	Liquid
Melting/freezing point, °C	6.35
Boiling point, °C	189

3.4 Binder viscosity

The viscosity is defined as follows:

$$\text{Viscosity} = \frac{\text{Shear stress } (\sigma)}{\text{Shear rate } (\dot{\gamma})} \quad \text{Equation 3.1}$$

Consider a thin layer of material between two parallel plates to which it adheres, such that a shear stress is applied via the plates (Figure 3.10). The deformation of a material as a result of the force acting on it depends on the force per unit area; this quantity is referred to as the shear stress (σ) and has the units Pa. The shear rate ($\dot{\gamma}$) refers to the change of strain with time i.e. the velocity profile (Equation 3.2) and has the units s^{-1} (Tadros, 2011).

$$\dot{\gamma} = \frac{\delta\gamma}{\delta t}$$
Equation 3.2

When the flow is linear, a layer at a distance l from the reference layer moving with a velocity v (Figure 3.10) will travel a distance $\delta l = v\delta t$, so that (Tadros, 2011):

$$\dot{\gamma} = \frac{\delta}{\delta t} \left(\frac{\delta l}{l} \right) = \frac{v}{l} = \frac{ms^{-1}}{m} = s^{-1}$$
Equation 3.3

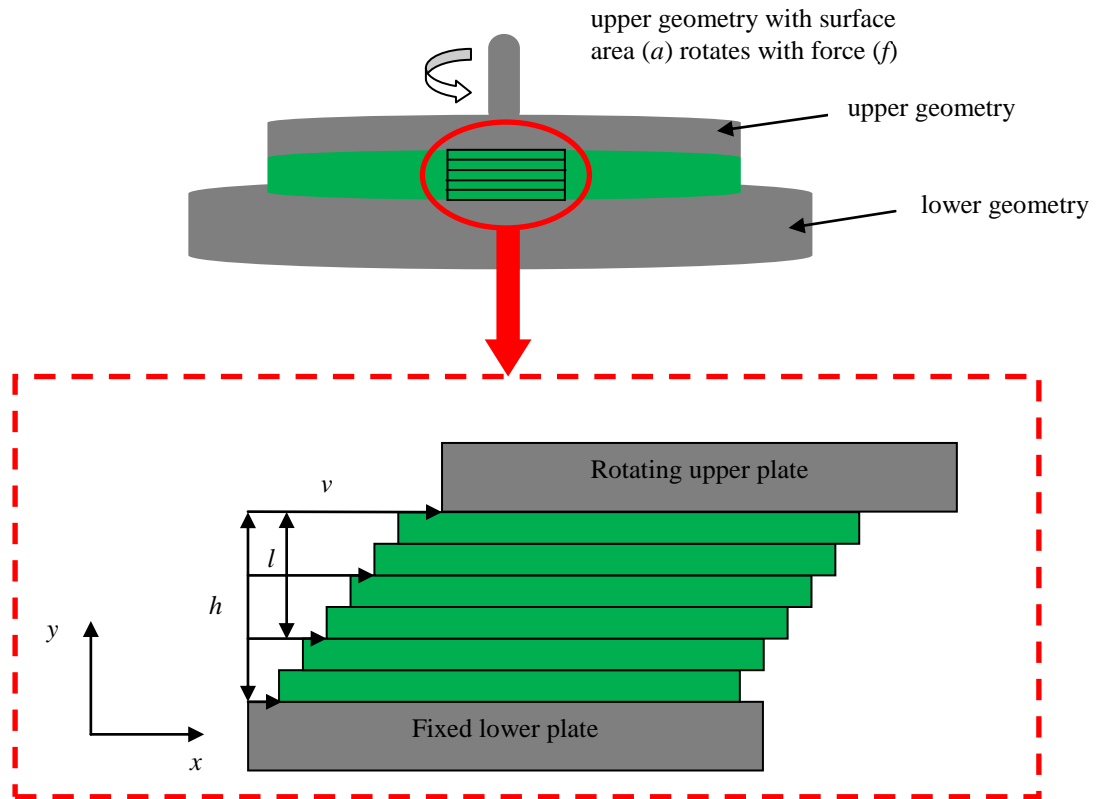


Figure 3.10. Velocity profile between an upper rotating plate and a lower fixed plate separated by a gap, h . The upper geometry moves with a velocity v along the x -axis – adapted from Bohlin (1994).

A plot of the shear stress against the shear rate enables one to determine the properties of the liquid. The characteristic stress-strain rate relationships for different systems are summarised in Figure 3.11.

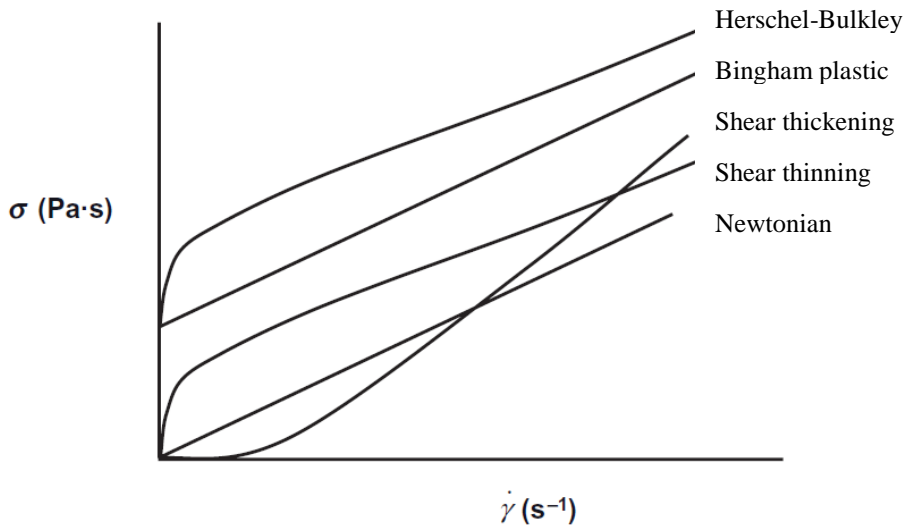


Figure 3.11. Flow curves for various systems – adapted from Tadros (2011).

The rheological properties of the liquid were measured using a Kinexus Pro rheometer by Malvern, UK. It is important to select the appropriate measuring geometry for any rheological measurement. For most applications, there are three commonly used types of geometries including (1) the cone and plate, (2) parallel plates and (3) the cup and bob. For highly viscous material, it is recommended to use the cone and plate or parallel plate (Bohlin, 1994). As the material is highly viscous, there is likely to be some wall slip at higher shear rates, therefore, the parallel plate geometry with serrated edges was selected (Figure 3.12). A 40 mm serrated plate was used and the gap between the plates was fixed at 1 mm. The material was carefully loaded onto the Peltier plate using a spatula (to avoid pre-shearing the paste) and subsequently trimmed. It is known that under or over-loading the geometry with sample can cause significant differences (up to 30%) in the results (Bohlin, 1994).

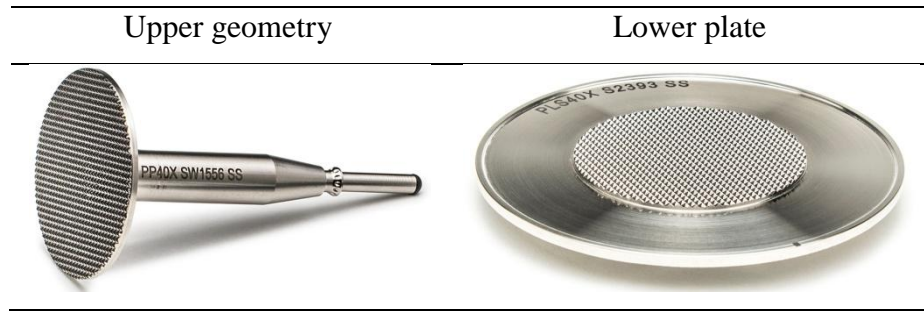


Figure 3.12. 40 mm serrated upper geometry and lower plate.

An isothermal viscometry experiment was conducted at 25°C and the shear rate was varied from 0.1 s⁻¹ to 500 s⁻¹. Shear rates within the mixer vary spatially. A simplified approach for approximating the shear rates within the mixer is to consider a cross-section of a powder bed (Figure 3.13). The shear rate will be at a maximum towards to edge of the impeller. During operation the fill level for both the vertically shafted high shear mixers used in this study is approximately 40%. The maximum tip speed of the 10 litre Roto Junior and “mini-mixer” is 11.7 and 2.52 m/s respectively. The velocity at the surface of the powder bed was determined (using PIV – refer to Section 3.14) to be 1.4 m/s for the 10 L Roto Junior and 0.30 m/s for the mini-mixer. The shear rate was subsequently calculated using Equation 3.4, where ΔV is the difference in the velocity at the surface of the powder bed and the edge of the impeller, and Δh is the height of the powder bed. The shear rates were determined to be 286 s⁻¹ for the 10 L Roto Junior and 110 s⁻¹ for the mini-mixer.

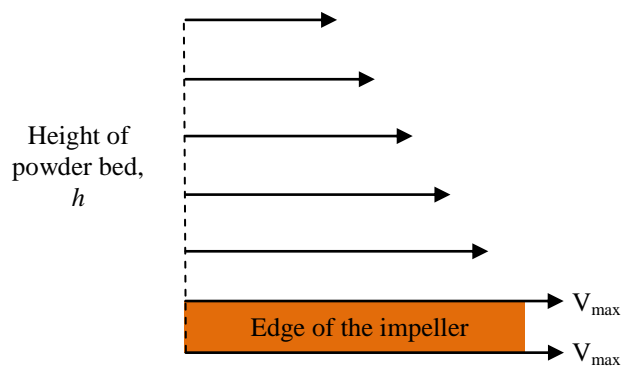


Figure 3.13. Velocity profile across the powder bed.

$$\dot{\gamma} = \frac{\Delta V}{\Delta h} \quad \text{Equation 3.4}$$

The binder exhibits shear thinning behaviour (Figure 3.14). A power law can be used to describe shear thinning and shear thickening fluids (Equation 3.5), where n is the power law index and it is less than 1 for shear thinning fluids and greater than 1 for shear thickening fluids. Furthermore certain liquids may behave as solids when subjected to smaller stresses. For such materials flow or permanent deformation is only observed when the stresses acting on it exceed a critical value - and this value is often referred to as the yield stress (σ_y). As AE3S exhibits shear thinning behaviour a Herschel-Bulkley (HB) model (Equation 3.6) may be used to describe the variation in the shear stress with shear rate (Figure 3.15), where σ_y^{HB} is the unique notation for the characteristic yield stress obtained using this model. The HB parameters for AE3S binder at 25°C are summarised in Table 3.3.

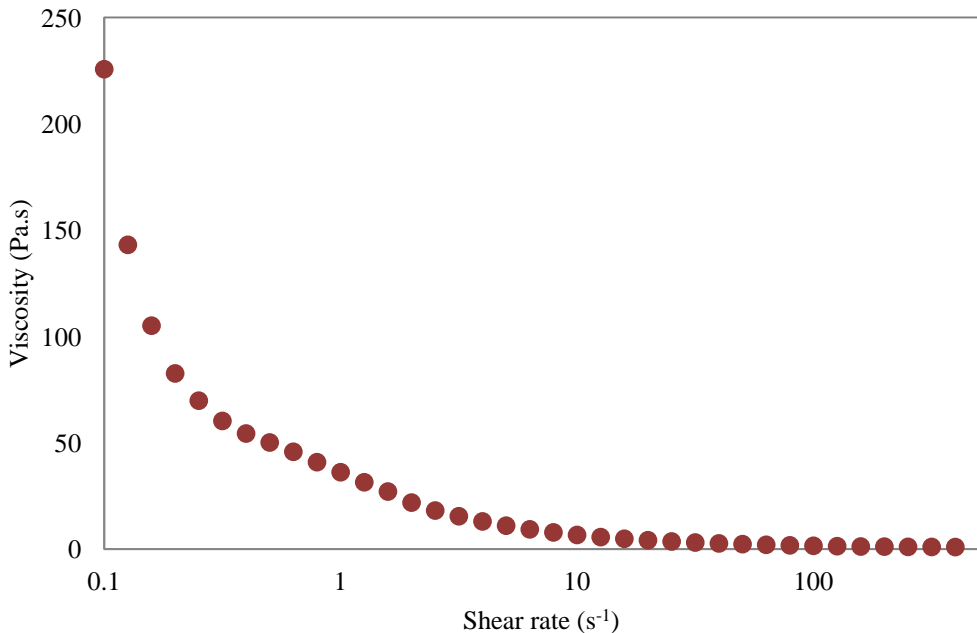


Figure 3.14. Change in the viscosity of the surfactant paste with increasing shear rate.

$$\sigma = K\dot{\gamma}^n$$

Equation 3.5

$$\sigma = \sigma_y^{HB} + K\dot{\gamma}^n$$

Equation 3.6

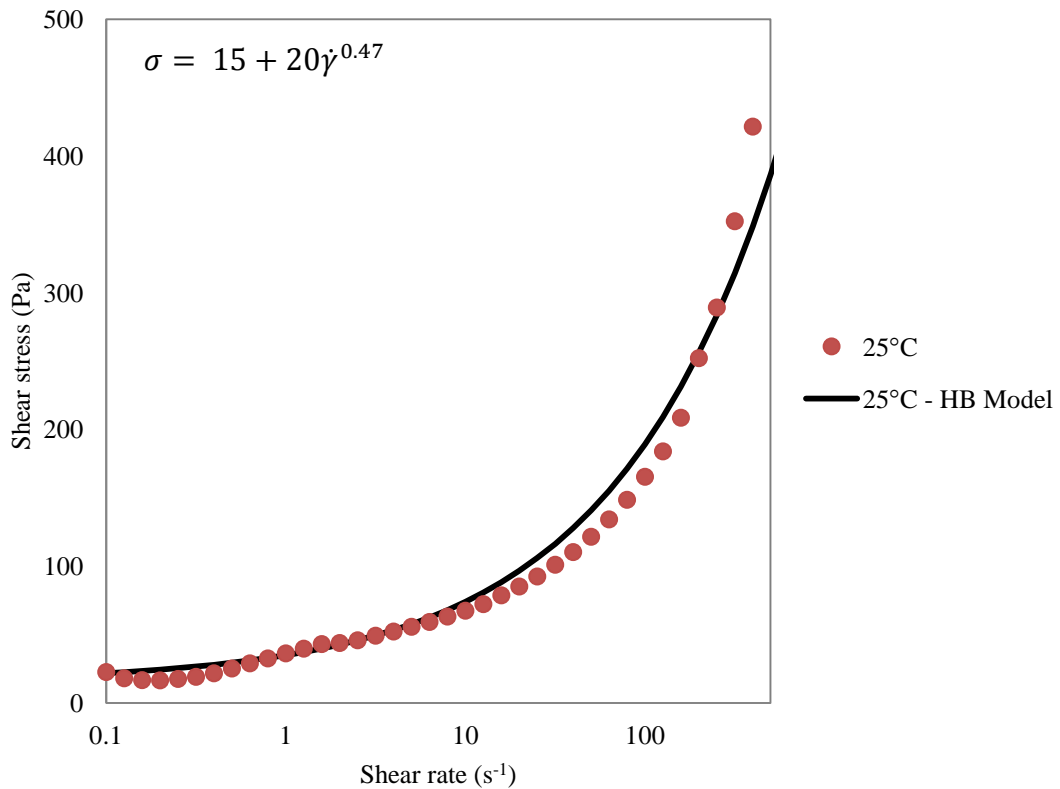


Figure 3.15. Relationship between shear stress and shear rate for AE3S at 25°C. A Herschel-Bulkley model fit has been used to describe the data.

Table 3.3. Herschel-Bulkley parameters for AE3S binder at 25°C.

Parameter	
σ_y^{HB}	15 Pa
K	20
n	0.47

The same geometry was used to determine the viscosity of reactive binder HLAS as well. As the reaction progresses during granulation heat is released, therefore, the shear viscosity was measured as a function of the shear rate at different temperatures. HLAS

exhibits Newtonian behaviour (Figure 3.16). There is also a decrease in the viscosity of the binder with an increase in the temperature. At 20°C, the binder has a viscosity of 1.5 Pa.s and this reduces by a factor of 10 at 70°C (to 0.15 Pa.s).

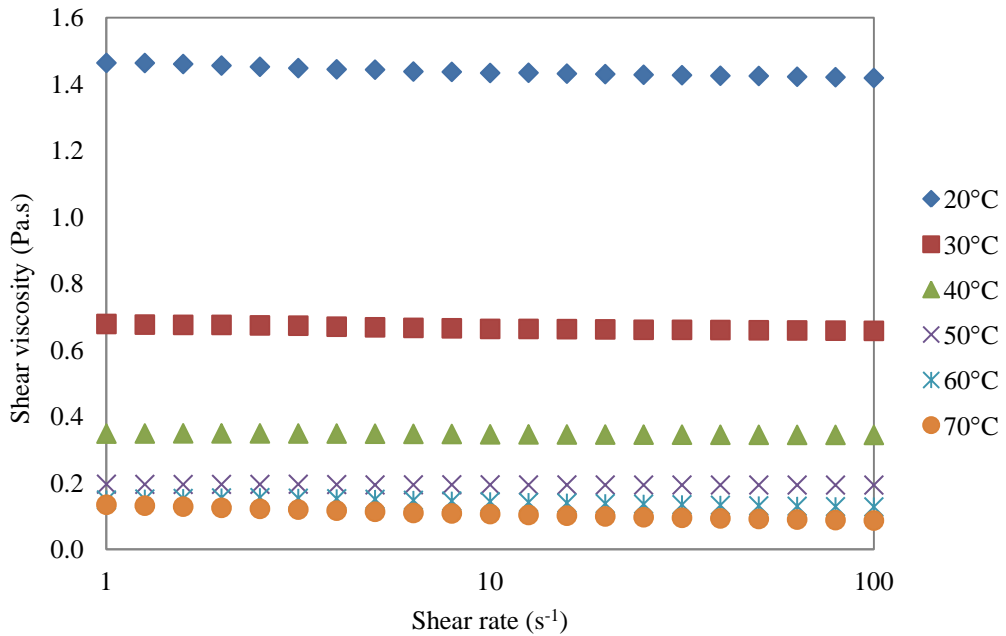


Figure 3.16. Change in the viscosity of HLAS with shear rate at different temperatures.

3.5 Binder wettability

An attempt was made to determine the wettability of both the binders used in this study. A *FTA125* goniometer from First Ten Angstroms, USA, was used (Figure 3.17). Multiple measurements were conducted for each test condition to obtain a more reliable average.

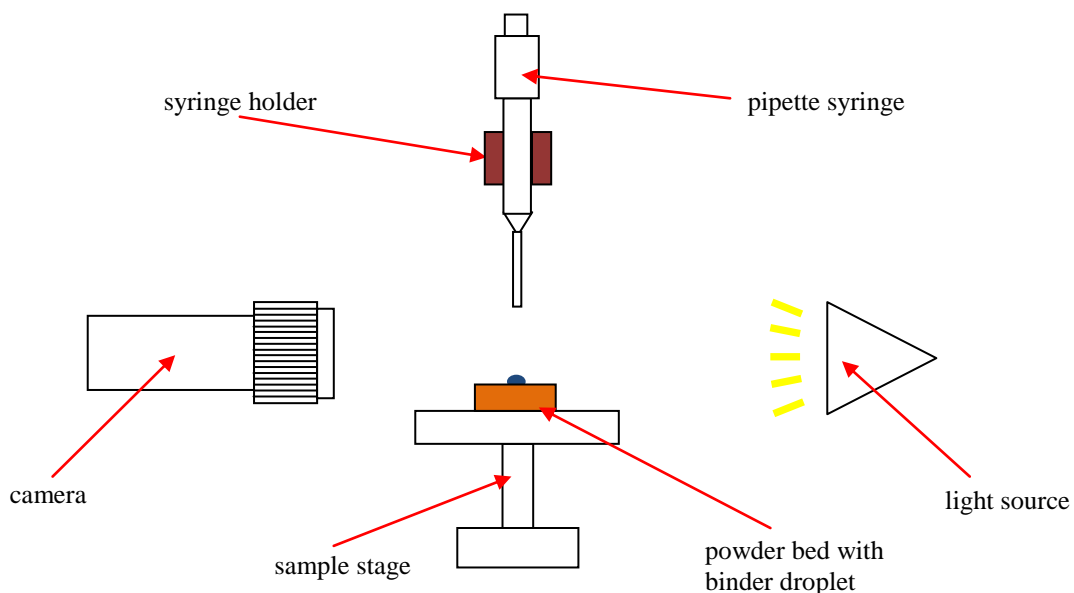


Figure 3.17. Schematic representation of a *FTA 125* goniometer.

3.6 Measuring the size of particles/granules

Particle sizes can be measured using several different techniques including sieve analysis, laser diffraction and static or dynamic image analysis.

As outlined in Section 2.18, particle size can be measured using sieves. Sieves from Retsch, Germany, were used to construct the mass based size distributions of the batches made using the 10 L Roto junior high shear mixer for the method of binder delivery study (Chapter 4). Sieves were also used to separate the powder coated binder particles (PCBPs) from the residual primary powder for the binder “breakage” study (Chapter 5).

A Camsizer P4 by Retsch, Germany, was used to measure the size of the binder fragments. It is a device that employs dynamic image analysis to measure the size distribution of a sample that is fed through it. It is equipped with dual cameras: a basic camera and a zoom camera. The basic camera detects larger particles whilst the zoom camera detects smaller ones. The complete size range of particles is therefore captured by both cameras. A vibratory chute feeds the sample into the Camsizer and the feed rate is adjusted, so that each particle falls through the field of measurement as an individual entity. The manufacturer claims this device is suitable for measuring particles that range from 20 µm to 30 mm.

When using highly cohesive particles that are smaller in size the vibration from the feeder alone is not capable of separating particles out as individual entities. The Camsizer XT is another system that is commercially available for measuring the size distribution of particles that are fine and more cohesive. It also has a dual camera system (basic and zoom). The XT is equipped with a dispersion unit that has an adjustable air pressure and variable nozzle geometries. This helps separate out fines and presents them as individual entities. The system is capable of determining particles that range from 1 µm to 3 mm.

The Camsizer XT was used to determine the volume based mean size ($D_{v4,3}$) of all three powders. A dispersion pressure of 200 kPa was selected and three runs were performed for each powder. In all cases, the results showed excellent repeatability. Light ash, ground ash and zeolite have a mean size of 130, 11 and 9 µm respectively. The size distributions of the primary powders are shown in Figure 3.18.

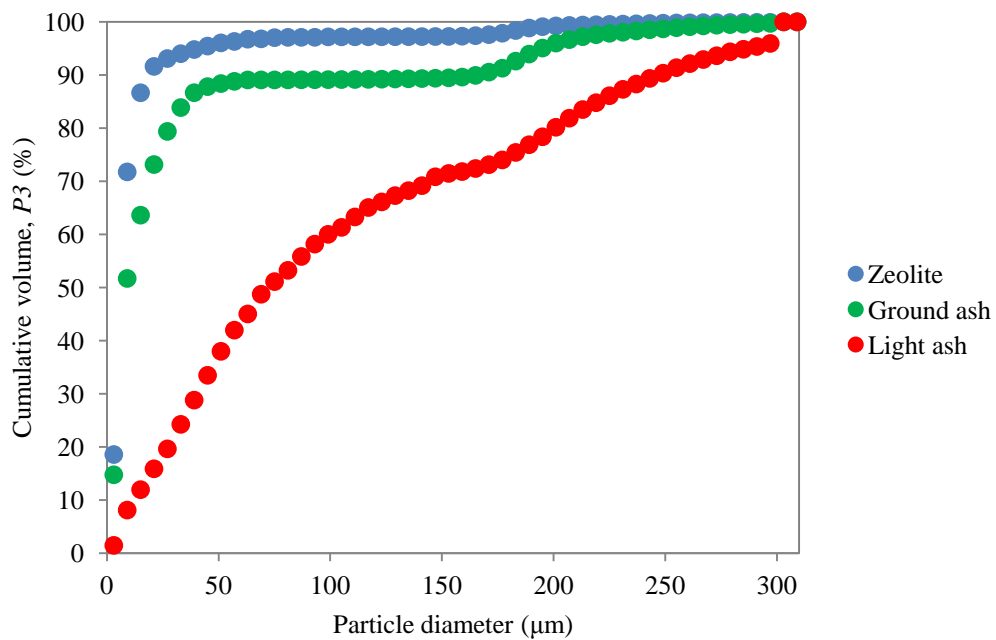


Figure 3.18. Size distribution of the primary particles.

3.7 Microscopy

Images of the material studied were taken using a VHX-5000 Digital Microscope by Keyence Corporation, Japan. Unlike a conventional microscope this system has a large depth of field. It also has the added advantage of being able to freely observe samples from various angles. The microscope is equipped with a lens that is capable of magnifications ranging from $\times 20$ to $\times 200$.

3.8 Scanning electron microscopy

SEM images of the primary particles were taken using a JSM-650 by Jeol, USA. Samples were placed on a standard 12.5 mm metal stub and were subsequently coated for 1 minute using a sputter coater that deposits gold on to the surface of the sample. This gold coating helps improve the conductivity of the sample, thereby making surface features more visible.

The powders have different morphologies, as seen from the SEM images (Figure 3.19). Light ash consists of needle shaped sub-primary particles that are combined into one porous structure. Ground ash is also composed of sub-primary particles; however

they are smaller in size. It is apparent that there are fewer needle shaped entities in ground ash. This could be a direct consequence of the milling process, where elongated primary particles are prone to undergo more attrition. The zeolite particle consists of a structure made of more circular sub-primary particles when compared to light and ground ash (Figure 3.20). Therefore, in comparison to zeolite, the light & ground ash particles are rougher.

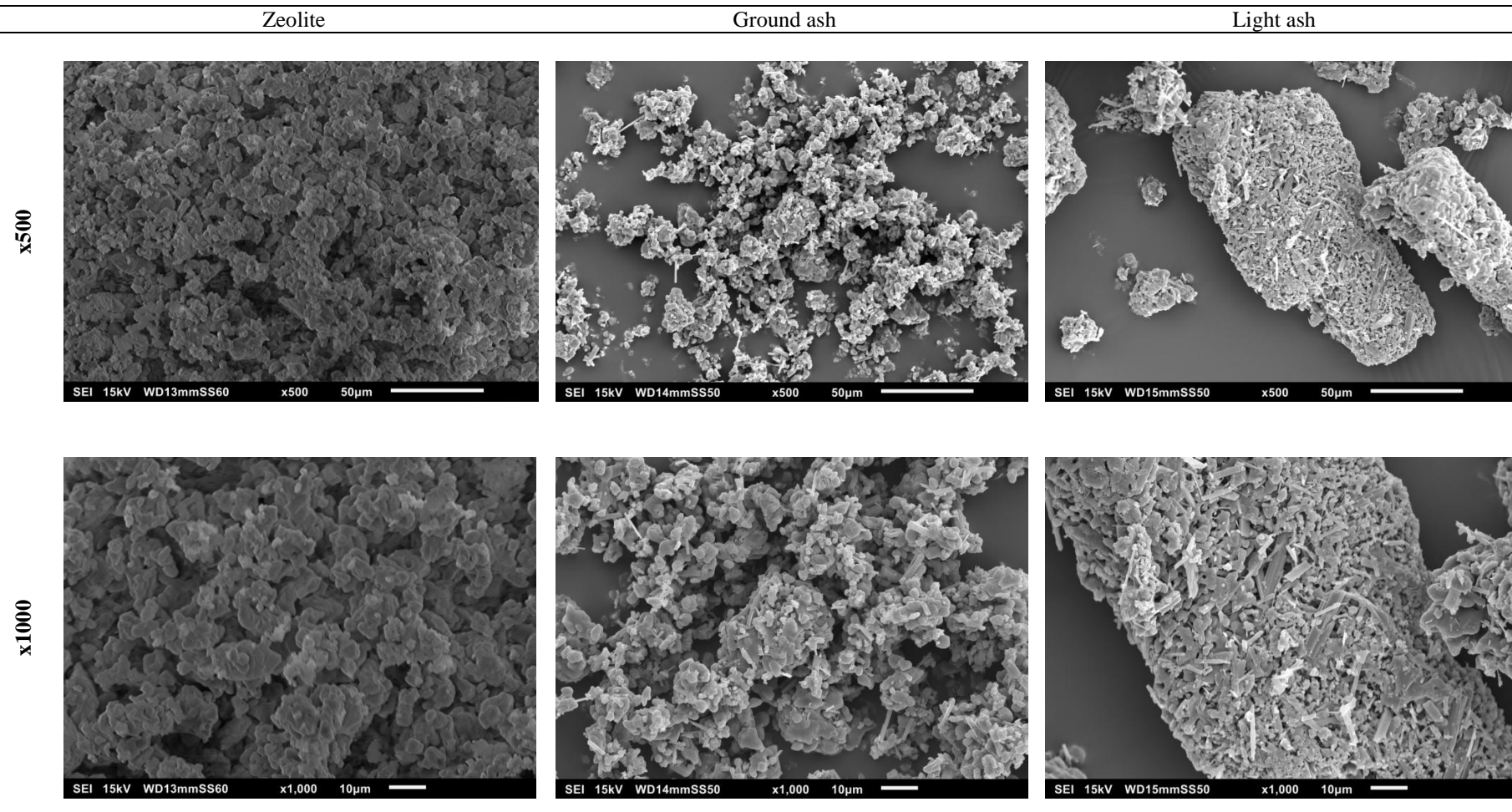


Figure 3.19. SEM images of the primary powder particles.

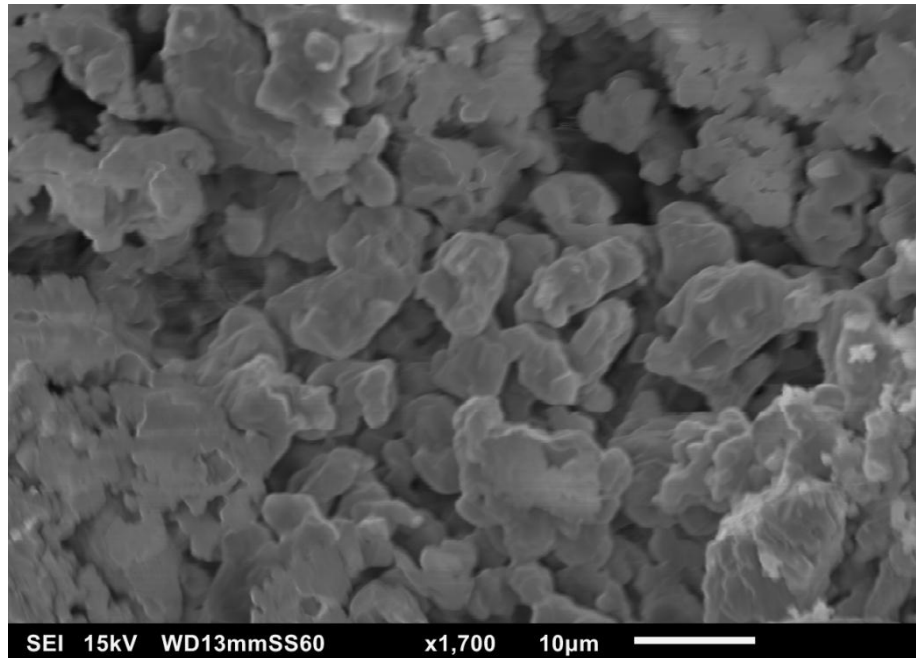


Figure 3.20. SEM of zeolite - $\times 1700$.

3.9 Powder flowability

Powder flowability is a factor that is likely to influence the rate at which the binder gets coated and fragmented within the mixer. The flow behaviour of powders is affected by particle size and shape (roughness). Therefore, changes in the composition of the detergent formulation, result in changes in the flowability of the mixture too.

The flow properties of the primary powders were measured using a ring-shear cell tester RST-XS.s by Dr. Dietmar Schulze, Germany. The powder flowability was described by the flow function coefficient (ffc). The ffc of the powder is calculated by dividing the consolidation stress of the corresponding yield locus by the unconfined yield strength. The flow property was measured at three different stress levels, 1500, 2750 and 4000 Pa, with maximum allowable stress being 5000 Pa. The lowest stress was equal to 30% of the maximum stress. A stress higher than 5000 Pa was not used to prevent the formation of a cake and also to limit the deformation of the particles. According to Jenike (1964), powders have an extremely poor flowability when $ffc \leq 1$, very poor for the range of 1-2, poor between 2-4, fair between 4-10 and a good flowability > 10 . The flow factors of zeolite, ground ash and light ash are 3.5, 1.12 and 6 respectively.

In addition to the ring shear test, repose angle measurements were done too, and used as an indication of the material flowability. An angle of repose below 30° indicates good flowability, 30-45° indicates some cohesiveness, 45-55° indicates true cohesiveness, and above 55° sluggish or very high cohesiveness (Carr, 1965, Carr, 1970, Ennis et al., 2008). According to Geldart et al. (2006), an angle below 40° indicates the powder is free-flowing. Measurements were conducted on light ash, ground ash and zeolite (Figure 3.21). For each material, twenty repetitions were performed. Ground ash has the poorest flowability (or largest angle of repose), as it is smaller in comparison to light ash and rougher in comparison to the more circular zeolite particles. Light ash particles are already “free flowing” according to Geldart’s criteria. Also, note the flowability of light ash is not very different to that of the commercially available detergent product (DAZ by Procter & Gamble, UK). Both the ring-shear cell tests and angle of repose measurements show good agreement.

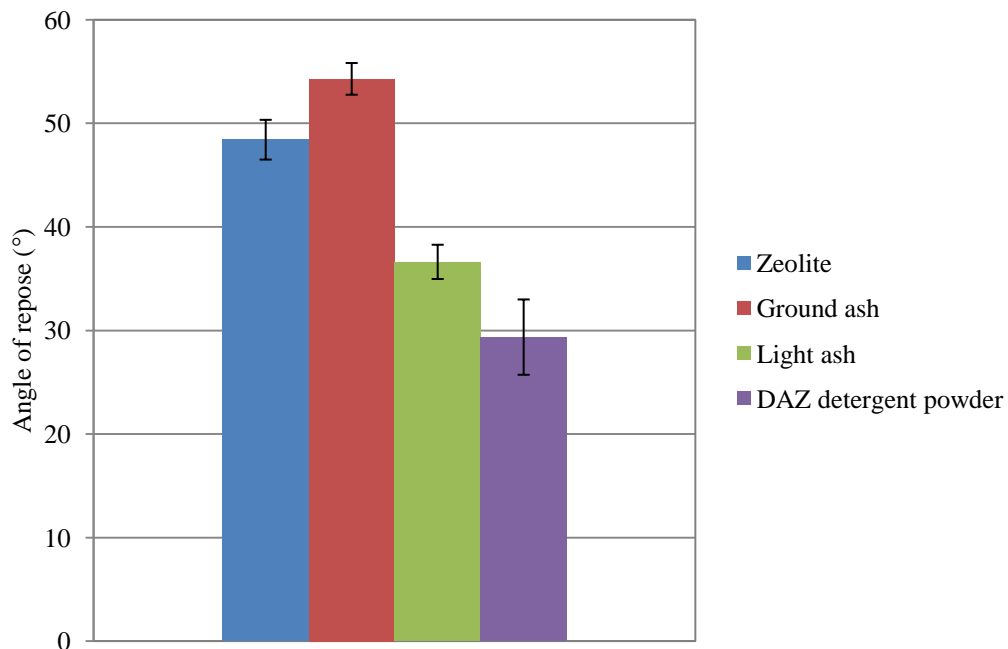


Figure 3.21. Angle of repose measurement for primary powder particles and commercially manufactured detergent powder.

3.10 Climatic chamber

A KMF240 I climatic chamber by Binder, Germany, was used for equilibrating the primary powders at 25°C and 40% RH, for 48 hours prior to conducting the granulation

experiments. It has a temperature test range from 10 to 90°C ($\pm 0.1^\circ\text{C}$) and a humidity test range from 10 to 90% ($\pm 0.1\%$).

3.11 Granule preparation

Detergent granules were prepared using a 10 L Roto Junior high shear mixer. The detergent composition is listed in Table 3.4. This mixture of powders reflects the typical composition of a commercially manufactured dry laundry powder. The two different sizes of carbonates used in the mixture leads to different interaction properties with the binder. Furthermore, the larger light ash particles may act as seeds for the finer particles (ground ash and zeolite) to attach. The powder was granulated with the semi-solid binder: sodium alkyl ether sulphate. The product of this granulation process was analysed to determine the effect of different methods of binder addition on the kinetics of granule growth, binder content and strength.

The total size of the batch was limited 1 kg (on a wet basis) to ensure the fill level was kept constant for all experiments i.e. 650 g of powder was granulated using 350 g of surfactant (semi-solid binder AE3S). After drying the wet mass, it yielded approximately 900 g of dry product.

Table 3.4. Typical detergent powder composition by mass (excluding surfactant binder).

Powder	Manufacturer	Composition (%)	$D_{v,4,3}$ (μm)
Light sodium carbonate	TATA Chemicals	20	130
Ground sodium carbonate	TATA Chemicals	55	11
Zeolite	PQ Corporation	25	9

3.12 Optical imaging using a high speed camera

An optical imaging technique was used to track the movement of the semi-solid paste in a moving bed of powder during the initial stages of granulation. A Photron FASTCAM 1024C fitted with the Navitar Zoom 700 c-mount lens was used for this purpose (Figure 3.22). At higher frame rates (>125 fps), additional illumination was required to be able

to visualise the contents of the mixer. The shutter speed was also varied to enhance the sharpness of the images.

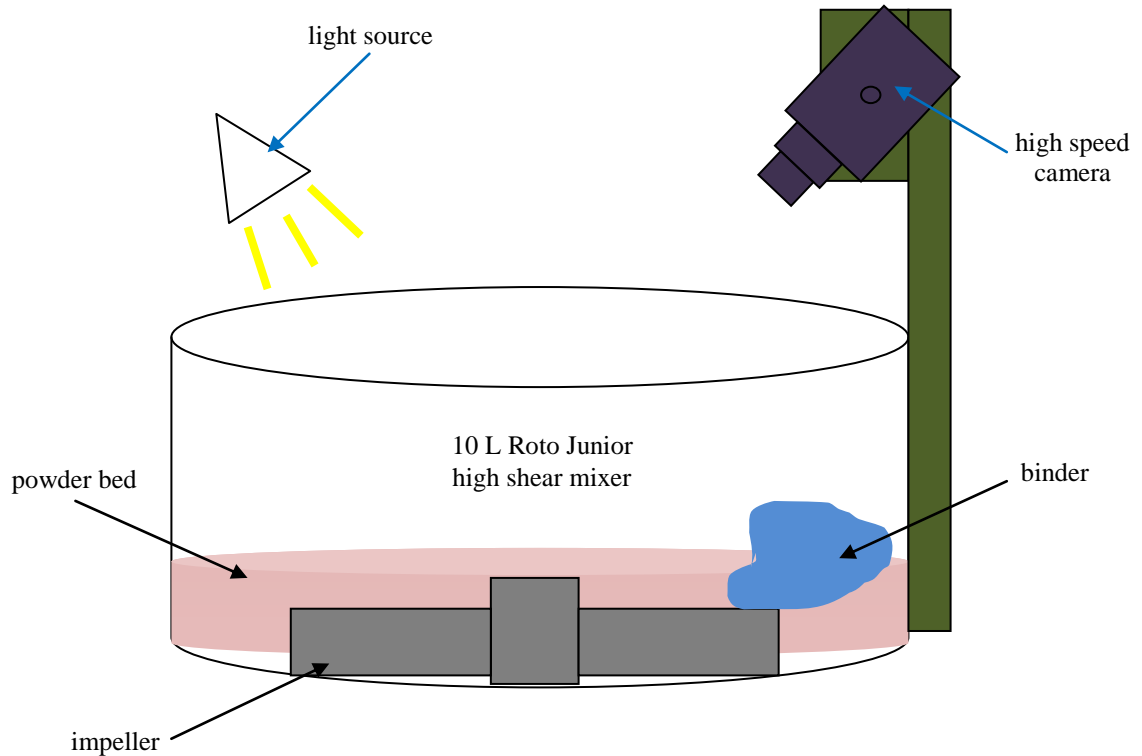


Figure 3.22. Schematic diagram of the set-up used to monitor binder dispersion optically.

3.13 Thermal imaging

Optical and high speed images of the high shear mixer only provide limited information as to how the paste disperses into the powder bed, as a function of time. The paste becomes coated by the powder, making it indistinguishable from the bulk. In this study, thermal imaging has been introduced for the first time as a technique for visualising the movement of the paste in a moving bed of powder. The paste was heated to a higher temperature than the powder for the non-reactive binder. For the reactive case, the exothermic reaction between the binder and the powder (upon contact) enables binder rich zones to be traced (Figure 3.23).

A FLIR A655sc thermal camera was used to capture images of the high shear mixer at 50 fps. At this frame rate, the full frame is made up of 640×480 pixels. The 32-bit col-

our images that are produced by the thermal camera are converted into 8-bit binary images prior to processing, using the PIVlab software (Section 3.14).

Emissivity is a material property that has to be considered when taking thermal images. Emissivity refers to the ability of a surface to emit infrared energy. It is a ratio that compares the amount of radiation that has been emitted by an object to the energy emitted by a black body (Equation 3.7). Therefore, a blackbody has an emissivity of 1.

$$\text{Emmisivity} = \frac{\text{Energy radiated by an object}}{\text{Energy radiated by a black body}} \quad \text{Equation 3.7}$$

The thermal imager detects infrared radiation (energy) and converts the detected radiation into a temperature. It is important to determine the emissivity of the surfactant paste to ensure that the temperatures measured by the software are accurate. A thermocouple was used to determine the actual temperature of the paste that was placed on a hot plate which was heated to 50°C (Figure 3.24). The FLIR R&D analysis software has an in-built function that can determine the emissivity, based on the known temperature (binder temperature recorded using the thermocouple) and the shown temperature (as measured by the thermal camera). The emissivity of the paste and powder were determined to be 0.98 and 0.85 respectively. This suggests both materials are good emitters of infrared radiation like most non-metals. Therefore, a thermal imager can be used to monitor the temperature of both materials *in situ*.

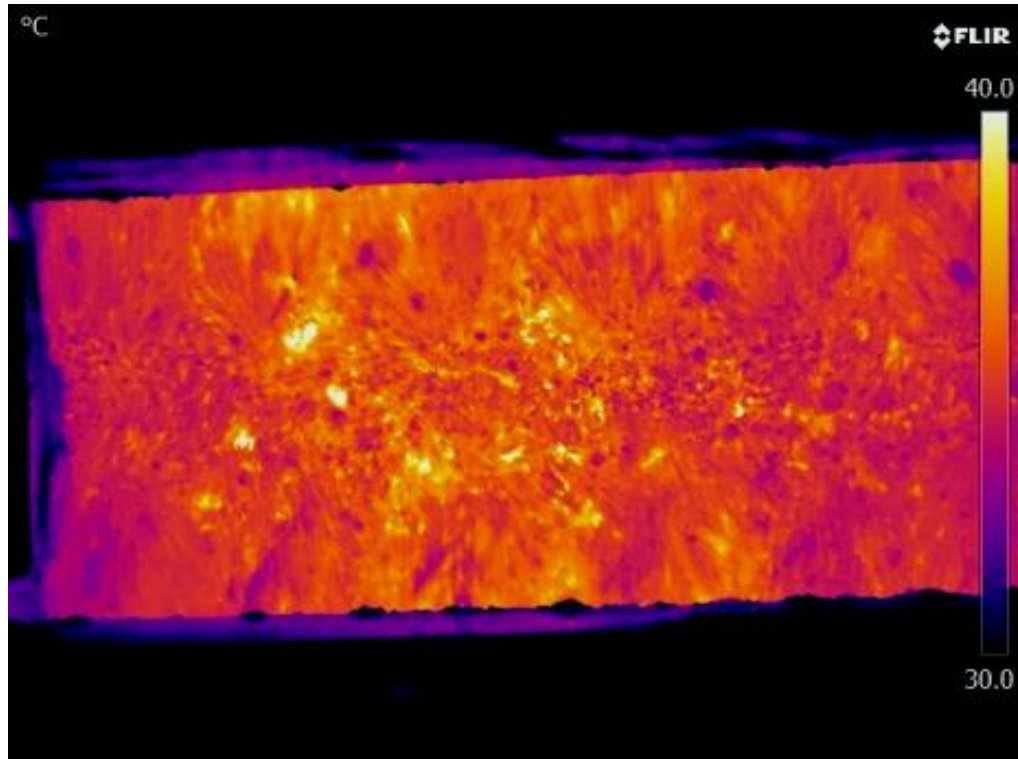


Figure 3.23. Thermal image of the paddle mixer. The bright yellow patches indicate binder rich zones.

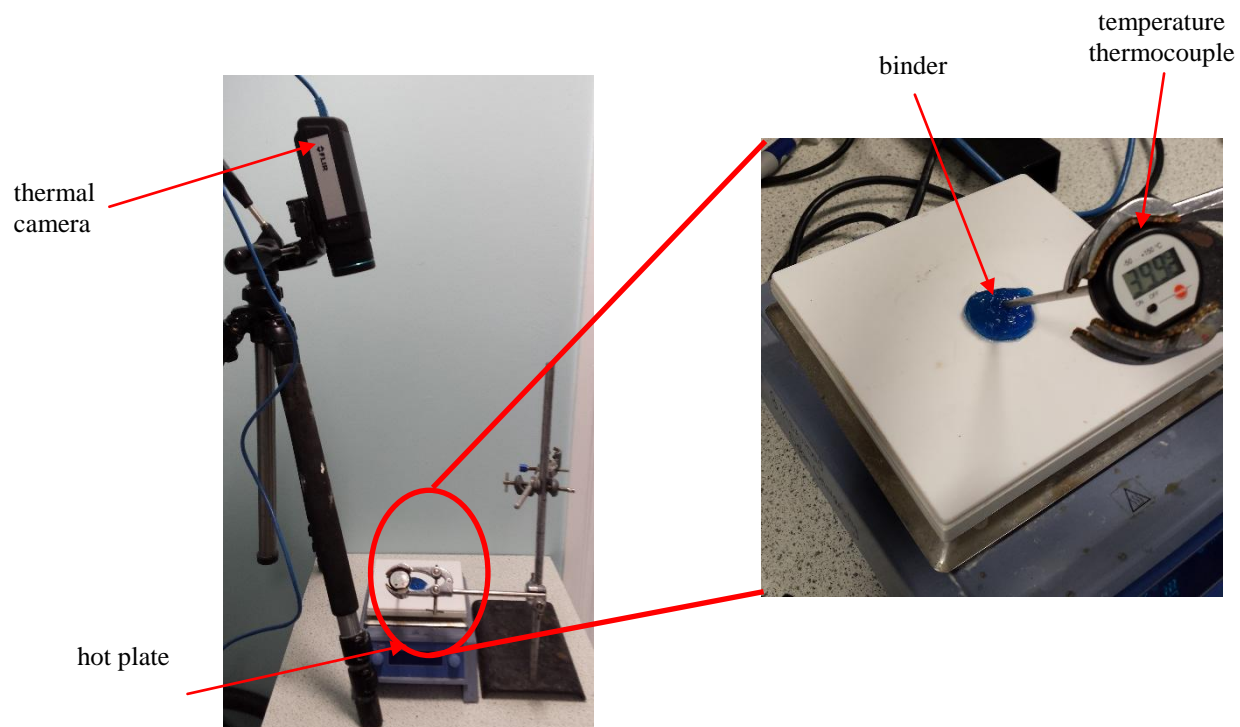


Figure 3.24. Setup for determining the emissivity of a test material.

3.14 Particle image velocimetry

The thermal images that capture the movement of a viscous binder in an agitated bed of powder were analysed using a particle image velocimetry (PIV) software. The PIVlab code developed by William Thielicke (for use with the MATLAB software) was used in this study. It is a graphical user interface (GUI) based tool for pre-processing, analysing, validating, visualising and simulating PIV data. This tool was used to determine the surface velocity of the binder in a moving bed of powder from the thermal images. As discussed in Section 3.13, the exothermic reaction between the powder and the binder results in a visible heat pattern that can be detected using a thermal imager. Frames from the thermal video can be used to obtain useful insights concerning the movements, as well as the interaction between the binder and powder. After importing images onto the software, an area of interest is defined (Figure 3.25). The PIVlab software divides the image into a series of interrogation areas, and a cross correlation algorithm (Equation 3.8) is employed to determine the displacement and velocity vectors between successive images in an interrogation area. A and B in Equation 3.8 refer to two interrogation areas in two consecutive images. When the two signals match each other, the amplitude reaches its maximum value. This enables the coordinates and therefore, the displacement of the particle from the first image to the second image to be found. More details about the cross correlation algorithm can be found in the literature (Huang et al., 1997, Thielicke and Stadhuis, 2014, Raffel et al., 2013). The velocity can in turn be determined, if the time difference between the consecutive images is known. In order to determine the real velocity, the images were calibrated against a known distance. An example of the typical output generated by the software is shown in Figure 3.26.

A PIV analysis was used to produce a vector field depicting the movement of binder in a paddle mixer (refer to Section 3.2 for more details about the mixer) and also to locate binder rich zones within the mixer. These mixers are more recently being employed in detergent granulation applications. The flow field within such mixers is different from the toroidal motion that is observed in vertical shaft high shear batch mixers (Ramaker et al., 1998). The results are presented in Section 8.4.

$$C(m, n) = \sum_i \sum_j A(i, j)B(i - m, j - n) \quad \text{Equation 3.8}$$



Figure 3.25. Example of a binary image that was imported into the PIV software.

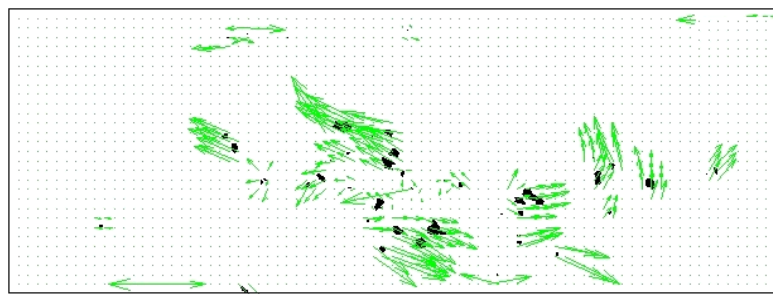


Figure 3.26. Typical output from the PIVlab software. Green arrows show the direction as well as the magnitude of the velocity vectors of individual lumps of binder in the mixer.

PIV was also used to determine the surface velocity of the powder in order to approximate the shear rates within the mixer which varies spatially (discussed in Section 3.4).

3.15 Measuring granule strength and powder coated binder particle (PCBP) hardness

3.15.1 Uni-axial confined compression technique

The strength of the dry granules was determined by using the uni-axial confined compression technique on a small bed of granules. The force-displacement data was recorded to determine the load at the time of fracture. The compression model proposed by Adams et al. (1994) is commonly used to approximate the granule strength from the average granule bed strength and this method of testing is often preferred to testing the strength of individual granules due to the large variation in the structure and composition of granules within the same batch.

The force is converted into a stress (P) and the displacement into a strain (ε_n). The Adams' equation was used to determine granule strength (Equation 3.9), where τ is the single particle strength (MPa), and α is a pressure coefficient.

$$\ln P = \ln \left(\frac{\tau}{\alpha} \right) + \alpha \varepsilon_n + \ln (1 - e^{-\alpha \varepsilon_n}) \quad \text{Equation 3.9}$$

At high values of natural strain the last term $\ln (1 - e^{-\alpha \varepsilon_n})$ is negligible, and the equation becomes linear:

$$\ln P = \ln \left(\frac{\tau}{\alpha} \right) + \alpha \varepsilon_n \quad \text{Equation 3.10}$$

This equation can be rearranged in the form $y = mx + c$; the slope gives α and the intercept gives $\ln \left(\frac{\tau}{\alpha} \right)$ (Figure 3.27).

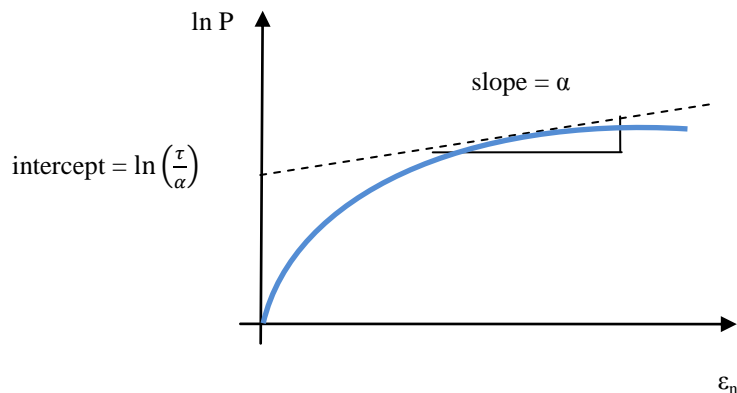


Figure 3.27. Graphical representation of Adams' equation (Adams et al., 1994).

The compression test was carried out using a Zwick Roell Z0.5 compression machine (Figure 3.28). The machine was equipped with a 500 N load cell for applying forces with an accuracy of 0.001 N. A crosshead moves the punch vertically with an accuracy of 0.2 μm . The punch and die are both 10 mm in diameter. The die has a maximum fill depth of 10 mm. The bed was tapped prior to applying a force to ensure good packing. The punch was then lowered and the maximum load was limited to 450 N.

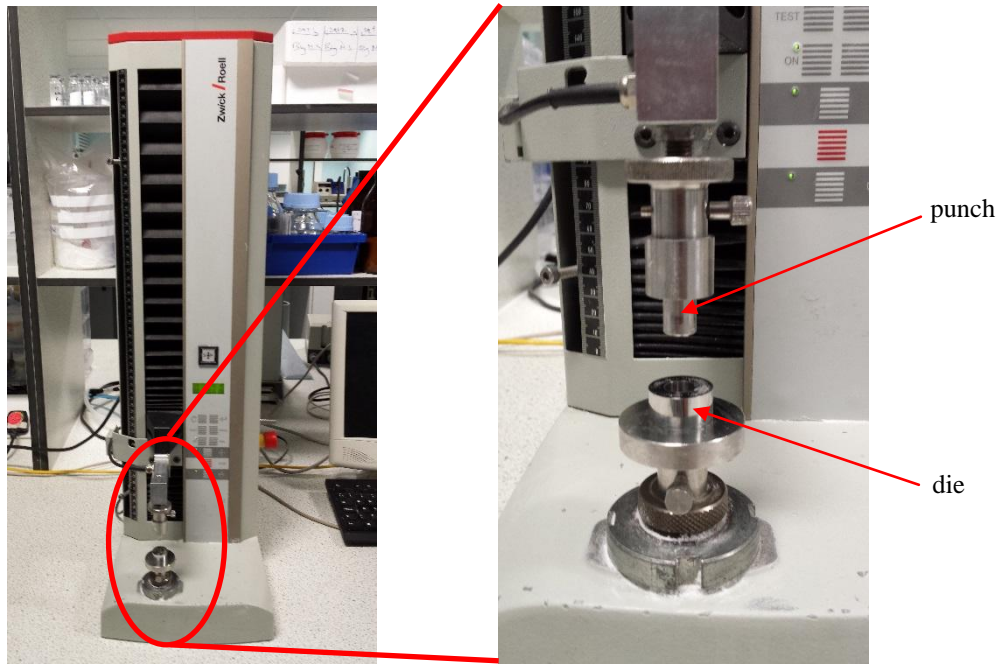


Figure 3.28. Zwick Roell Z0.5 compression machine.

3.15.2 Indentation of PCBs

A Zwick Roell Z0.5 tensile tester equipped with a 10 N load cell was used to conduct indentation type strength measurements (Figure 3.29a). The 10 N load cell had to be modified with a purpose built adaptor, in order to accommodate an indentor (Figure 3.29b). The indentor tip used for this study is a sharp 60° diamond pen by Shanghai Yiyuan Diamond Co., Ltd., China, which has a diameter of 6.3 mm (Figure 3.29c). The normal force acting on the load cell is measured as the indentor tip penetrates the surface of a PCB. The speed of the upper punch was maintained at 1 mm/min, and the maximum allowable compression force was limited to 9 N and the maximum strain to 1 mm. A preload condition was set to ensure the system starts recording the stress when the detected load exceeds 0.01 N. For each test condition (granulation time point), ten measurements were taken. In between repeat measurements, the platen and indentor tip were cleaned thoroughly, ensuring no material from the previous test influenced results. A single granule was indented at a time for each test.

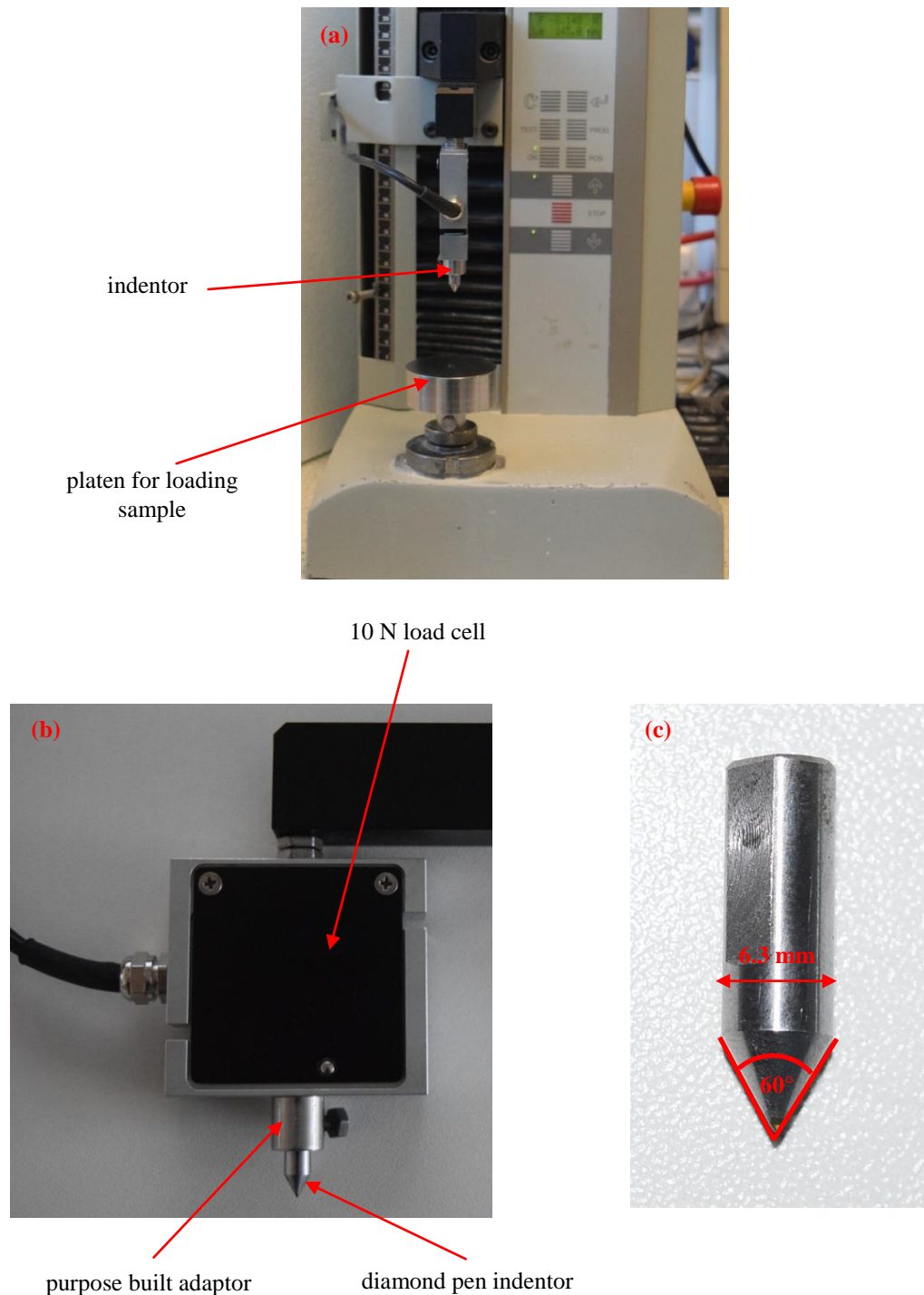


Figure 3.29. (a) Set-up used for indenting PCBPs, (b) 10 N load cell fitted with an indenter and (c) key dimensions of the 60° diamond pen indenter.

3.16 Preparation of compacts

Compacts of the primary powders were made for droplet penetration studies and XRT analysis, using an Instron 3367 tensile tester by Instron, UK. In each case, 5 g of the powder was weighed out and compressed in a die (inner diameter of 30 mm and height of 25 mm). A punch was used to apply a 500 N load to the powder contained within the die and the speed of compression was limited to 1 mm/min. A low speed of compression gives sufficient time for the powder particles within the compacts to arrange themselves. This in turn ensures the compacts are reproducible.

3.17 UV spectroscopy

UV spectroscopy is a commonly used technique for determining the binder content of granules (Osborne et al., 2011). All compounds absorb/interact with UV radiation and a UV spectrophotometer quantifies this absorbance. The principle of analysis is based on the Beer-Lambert law. A beam of radiation with radiant power P_0 leaves the sample with a reduced power P , after absorption has taken place (Figure 3.30).

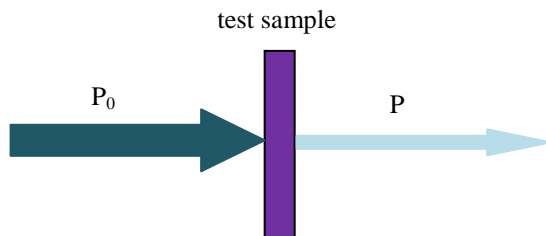


Figure 3.30. Concept of absorbance spectroscopy.

The amount of radiation absorbed may be reported as either an absorbance (A) or a transmittance (T) (Equation 3.11 - Equation 3.12) (Burns, 1993):

$$T = \frac{P}{P_0} \quad \text{Equation 3.11}$$

$$A = \log_{10} \frac{P_0}{P} = \log_{10} \frac{1}{T} \quad \text{Equation 3.12}$$

Therefore the relationship between % transmittance and absorbance is as follows (Equation 3.13, Figure 3.31):

$$A = \log_{10} \frac{100}{\%T} = 2 - \log_{10} \%T \quad \text{Equation 3.13}$$

The spectrometer measures the transmittance and converts the measured value into an absorbance. Figure 3.31 shows that above 40%, a change in the transmittance results in a small change in the absorbance. The equipment is, therefore, most sensitive and accurate when the absorbance is below 0.5.

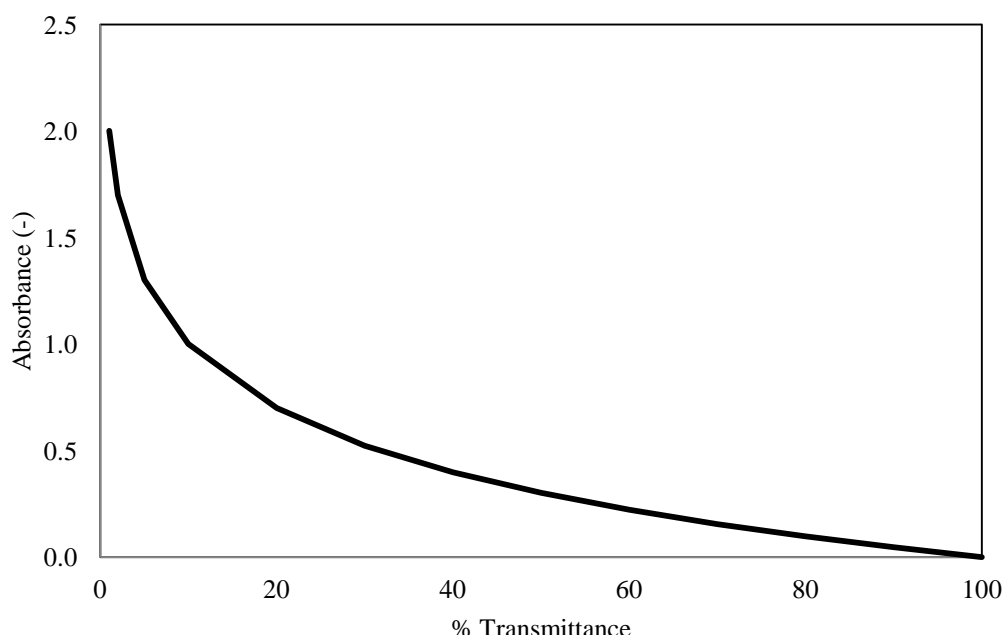


Figure 3.31. Relationship between absorbance and % transmittance.

A Genesys 6 spectrophotometer by ThermoSpectronics, Germany, was used for UV measurements. The greater the concentration of the colouring pigment in the sample, the higher the absorbance measured by the spectrometer. The aim of this experiment was to determine the binder concentration of different size classes. Batches were sampled down using a manual sample splitter. 1 g of the representative sample was then dissolved in 19 g of deionised water. The solution was then left in a water bath at 45°C for 2 hours (a higher temperature was selected to increase the rate of detergent dissolution).

Sodium carbonate has a solubility of 30.7 g/100 g of water at 25°C (Lide, 2010), therefore 19 g of deionised water will completely dissolve all the carbonates. Zeolite A, on the other hand, is poorly soluble (<1 mg/100 g of water) (Gode, 1983). For this reason, the solution was left to stand so any un-dissolved material would settle to the bottom of the vial. The clear solution was then decanted into 4 ml cuvettes for analysis. The effect of the method of binder delivery on the distribution of binder in various size classes was assessed.

3.18 X-ray microtomography

X-ray microtomography is a non-destructive technique that generates a 3D reconstruction of the specimen by obtaining a series of X-ray images/projections (Figure 3.32). Again, the principle of analysis is based on the Beer-Lambert law (refer to Section 3.16). Computerized tomography (CT) scanners generate cross-sectional images, that are referred to as slices, through the object that is being studied. Projections are obtained at many different angles as a series of slices, which are subsequently reconstructed by a back projection algorithm (Jacobs et al., 1995).

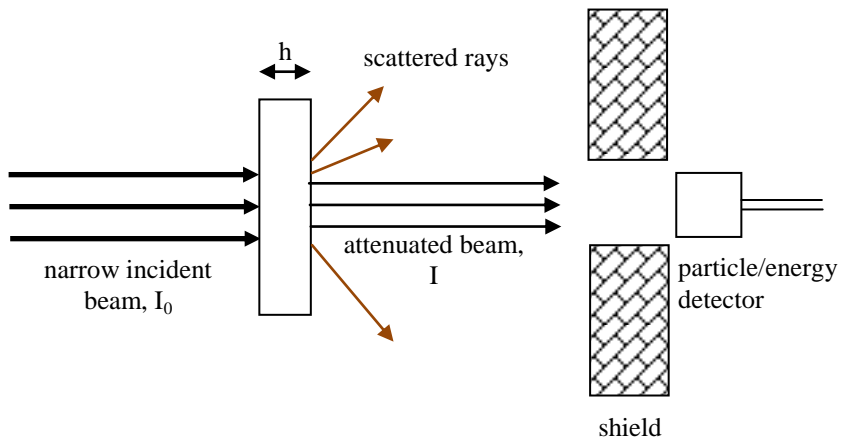


Figure 3.32. Principles of X-ray tomography (adapted from Jacobs et al., 1995).

A μCT 35 by Scanco Medical, Switzerland, was used to scan samples of the PCBPs. Absorbance of X-ray increases with increasing atomic number and mass density of the material. The density is important when analysing powder material, as air spaces or voidages within the powder matrix could result in poor distinction between different constituents in a sample. Low energy rays (45 kVp) were used. The lower energy fraction is preferentially absorbed, whilst the higher energy fraction is more penetrating. For the

purpose of XRT, samples less than 7 mm in diameter were chosen. It is therefore, safe to assume that a false increase in the contrast near the surface was avoided (due to the size of the sample).

XRT was used as a non-invasive technique to identify binder rich zones in a PCBP. This was in turn, used to assess the effect of particle type and wet massing time on the internal makeup of a PCBP. It was also used to determine the porosity of some loose compacts used in this study. The procedure for determining the porosity from the slices obtained from the XRT is outlined in Appendix I.

Chapter 4 Effect of binder delivery method on granule growth and binder distribution

4.1 Introduction

Binder distribution is an important aspect of any wet granulation process. Industrial detergent granulation processes often have very short processing times, therefore ensuring adequate and efficient distribution of the binder is crucial. Distribution of binder occurs when it is introduced into a moving bed of powder.

When considering the use of a low viscous binder for granulation, firstly, the binder starts to penetrate the powder bed due to capillary action and in some cases solubilisation of the particles aids further distribution. The binder is drawn into the pores that are present in a bed of powder, as a result of the interfacial tension. The powder bed in this case can be considered as a sponge with many pores or channels into which the water/liquid binder gets drawn (Figure 4.1). Another factor, and by far the most important driver for binder distribution is mechanical action of the impeller (mixing).

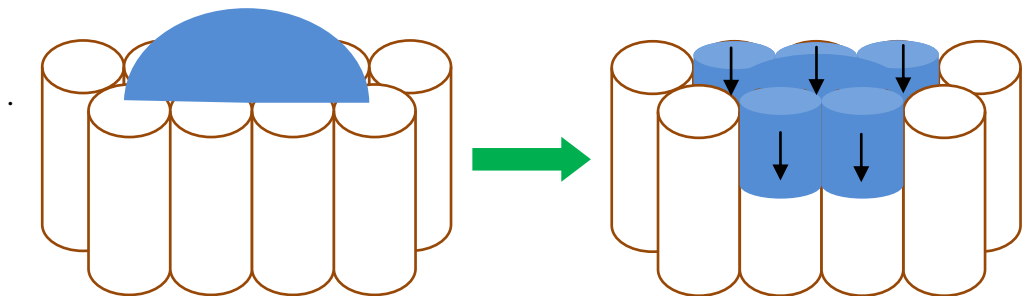


Figure 4.1. A low viscous droplet gets drawn into a bed of powder by capillary action. The cylinders represent pores or channels in the powder bed.

When considering granulation involving the use of a highly viscous binder, on the other hand, surface effects such as interfacial tension do not aid binder distribution. Therefore, distribution occurs solely due to mechanical action.

In addition to these factors, the method of binder delivery is also likely to influence binder distribution. Again, when considering a low viscous binder, the method of addi-

tion influences the size of the binder droplet; this in turn will have an impact on the mechanism of dispersion. It is well known that when the droplet is small in comparison to the primary particles, the distributive mechanism dominates and when the converse is true, the immersion mechanism dominates (refer to Section 2.2 for more details about the two mechanisms). Binder can be continuously delivered into the mixer (using a pump), sprayed, added as a solid or pre-loaded into the mixer prior to the start of the granulation process. An investigation into the effect of the method of binder addition on the dispersion of a highly viscous binder has not been conducted before. Two different methods of binder delivery (preloading and injecting) and their influence on both binder distribution and the kinetics of the subsequent granule growth have been investigated in this study.

4.2 Production of surfactant droplets

A preliminary attempt was made to assess the wettability of the semi-solid binder (AE3S) and to produce droplets of it. The Sessile drop method was adopted to determine the apparent contact angle made by the binder on a powder bed using a FTA125 goniometer (refer to Section 3.5). Sessile drop refers to the standard arrangement that is used when optically measuring the contact angle by droplet shape analysis (Figure 4.2). Contact angles are defined geometrically as the angle formed between the solid-liquid and liquid-vapour interfaces of a three phase (solid-liquid-vapour) system.

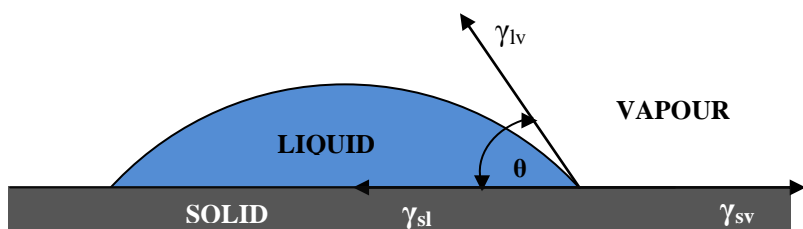


Figure 4.2. Sessile droplet on a solid surface.

Initially, experiments were conducted at room temperature (25°C). A 24 gauge needle (inner diameter = 0.31 mm) was used to produce a droplet of the binder. It was not possible to produce droplets of the material using this needle size, due to high material viscosity. A steam/jet of liquid was ejected from the needle. Subsequently, larger needle

sizes of 21 gauge (0.51 mm) and 20 gauge (0.60 mm) were used (Figure 4.3), and again it was not possible to make droplets.

Increasing the binder temperature lowers its viscosity making it easier to produce droplets. The FTA125 goniometer is not equipped with a syringe heater; therefore drop penetration experiments were conducted, instead, in an oven. The powder beds were produced by filling a Petri dish with ground ash ($D_{v4,3} = 11 \mu\text{m}$) and levelling its surface using the flattened end of a spatula. A lump of the paste was carefully placed on the surface of the powder bed. The Petri dishes were equilibrated in the oven for an hour and the binder was heated to the same temperature. Experiments were conducted at 40, 60, and 80°C. The plates were inspected every 5 mins soon after the lump of paste was placed on the surface of the powder. The paste does not penetrate the powder, thus demonstrating that increasing the temperature does not cause a significant change in the viscosity of the paste to facilitate binder penetration. When a small lump of the paste is placed on a loosely compacted powder bed, it remains on the surface indefinitely, without penetrating the bed, thus demonstrating that the viscous effects far outweigh capillary forces and diffusion.

However, when the binder was heated to a higher temperature of 100°C for an hour, it was noticed that the semi-solid paste turned into a free-flowing liquid (Figure 4.4). Upon cooling, the clear blue liquid retained the same physical properties; it does not revert back to a semi-solid. This suggests that heating the paste above this temperature results in its decomposition, i.e. an irreversible reaction that changes its physical state from semi-solid to liquid. Therefore, heating the paste to reduce its viscosity is not an option for improving binder dispersion.

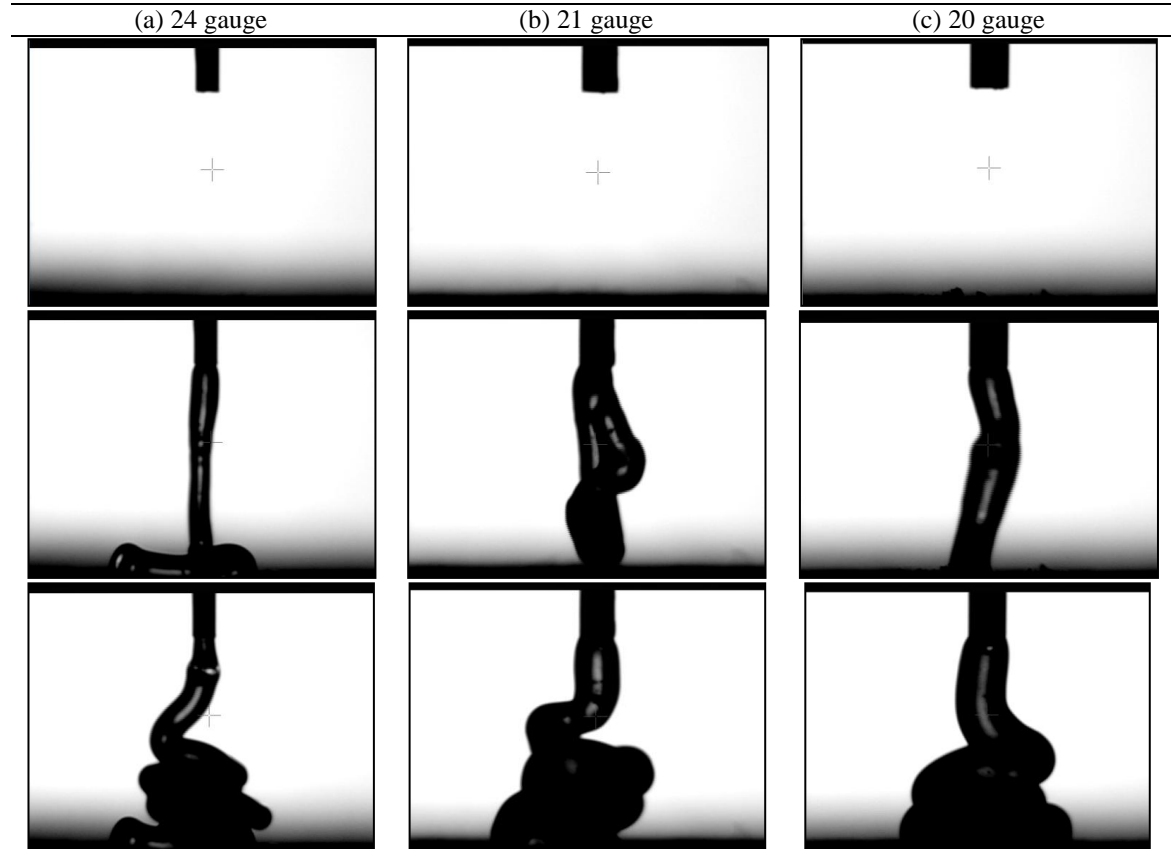


Figure 4.3. Dispensing AE3S binder using needles of different sizes.

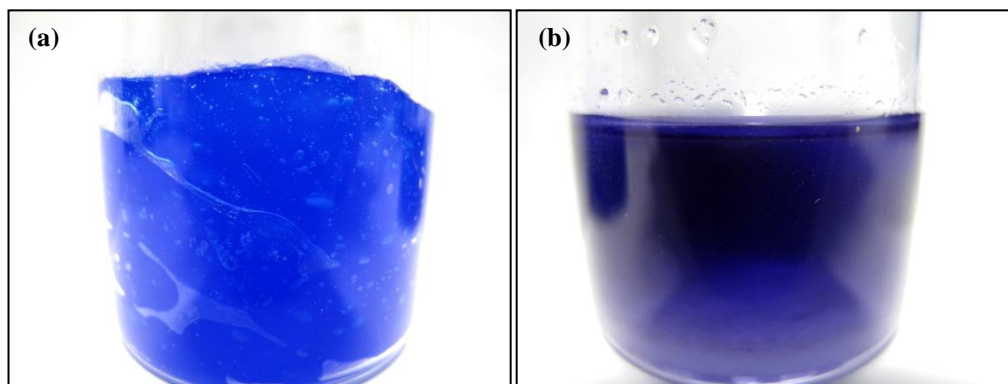


Figure 4.4. Effect of heat on AE3S (a) before (b) after heating to 100°C for an hour.

4.3 What happens at the interface between the paste and the powder?

Some experiments were conducted using the VHX-5000 Digital Microscope System, to closely inspect what happens at the interface between the semi-solid binder and powder. It would be useful to determine if there is any movement and/or dissolution of the powder in the paste.

Some powder was introduced on to the surface of the paste. A time lapse image sequence was then recorded (Figure 4.5). Images were taken every minute over a period of five hours. It can be seen that there is no visible movement or dissolution of the powder on the surface of the binder with time. The only observable change is the formation of a crust, as a result of prolonged exposure to air (due to the loss of water).

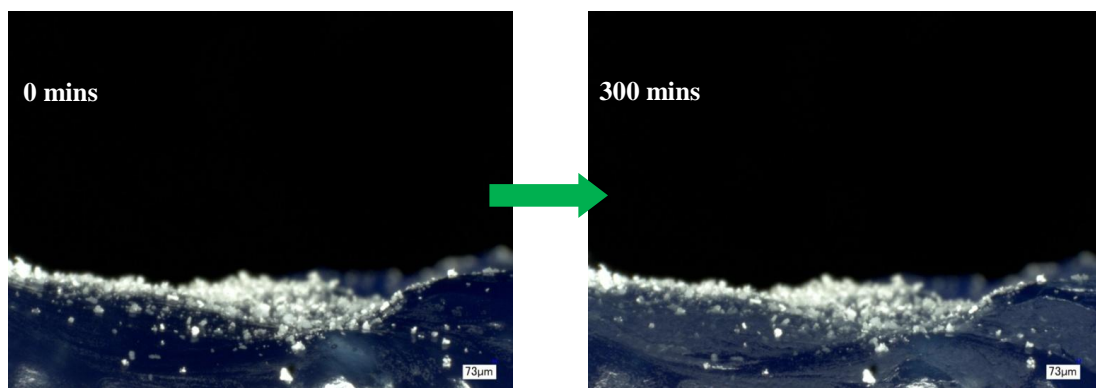


Figure 4.5. Images from a time-lapse video of the interface between powder and paste.

4.4 Isolating the effects of shear and impact

So far the meso-scale studies have been conducted on a loose bed of powder. It would also be interesting understand how the binder disperses in a moving bed of powder in a high shear mixer. The mechanical action of the impeller in any high shear granulation process imparts both shear and impact forces. In an attempt to isolate the effect of shear on the initial dispersion of the binder, some preliminary experiments were conducted using the flat plate impeller (Figure 4.6). The mixer was operated at 500 rpm. The binder and powder (refer to Table 3.4 for the composition of the powder bed) were maintained at room temperature (25°C) and the total batch size was 1.0 kg (L/S ratio = 0.5). The binder was preloaded into the mixer as one large blob.

When the flat plate impeller was used (in place of a pitched impeller), mixing was very poor. The paste migrates towards the bottom of the mixer (Figure 4.7). A possible explanation for the migration of binder to the bottom of the mixing vessel could be a difference in the density between the binder and the bed of powder (bulk density). This work demonstrates that the pitch of the blade has an important influence on the dispersion of a semi-solid binder.

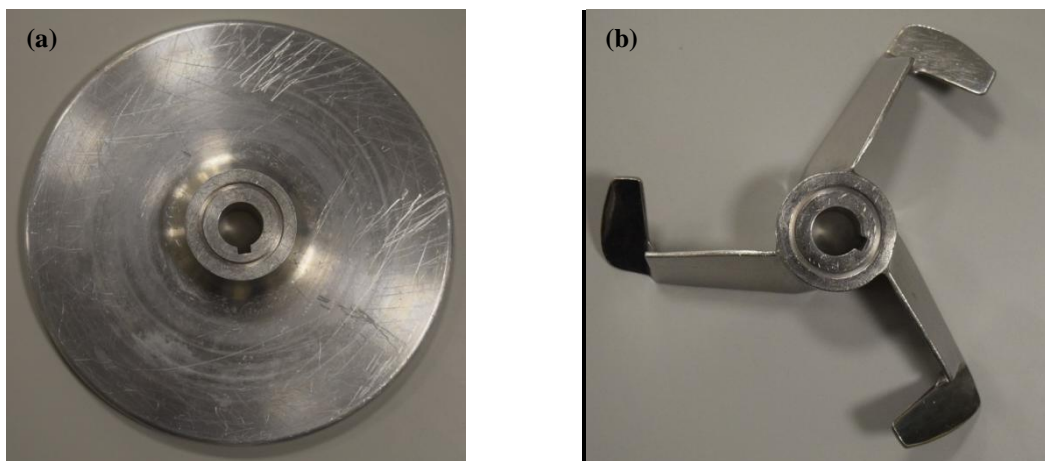


Figure 4.6. (a) flat-plate impeller (b) pitched impeller.

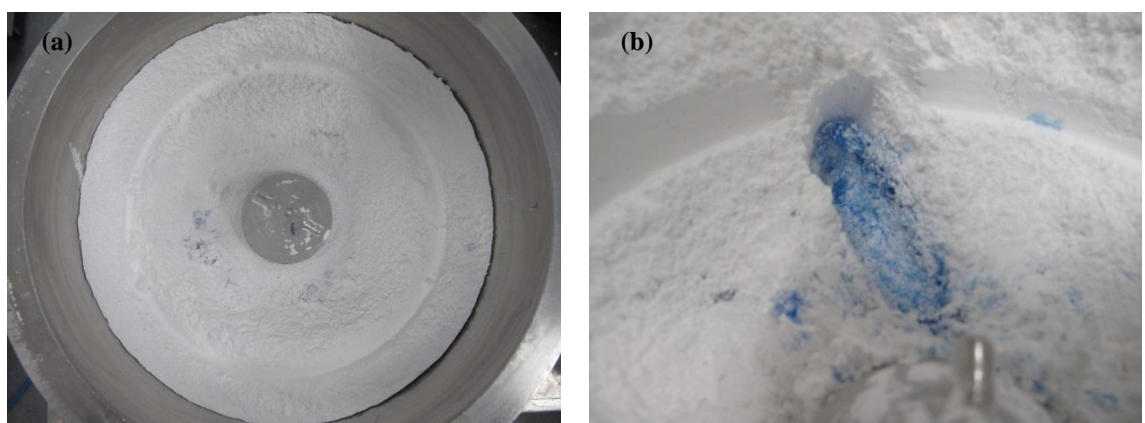


Figure 4.7. Mixing achieved using a flat-plate impeller at 500 rpm. (a) aerial view (b) paste embedded beneath the powder. The paste has migrated to the bottom of the bed.

4.5 Injecting and preloading the binder

It is hypothesised that the manner in which the binder is delivered into the mixer will influence binder distribution and granule growth. In the case of a semi-solid surfactant binder, improving dispersion by spraying is not an option due to its high viscosity.

Therefore, continuous injection and preloading (adding all binder into the mixer as one large blob) were investigated, as alternative methods of binder delivery. Also, as the semi-solid binder does not form droplets, small quantities of the binder will be referred to as “binder particles”. A powder composition that is similar to that of a typical detergent formulation was used (Table 4.1).

Table 4.1. Detergent formulation used for the binder delivery study.

Material	Composition (wt%)
AE3S (binder)	35
Light ash	13
Ground ash	36
Zeolite	16

As discussed in the Section 4.1, the smaller the size of the droplet that is introduced into the mixer, the quicker will be the initial dispersion, spread and distribution of the binder into the powder bed. Also, in most granulation processes, there will be a non-uniformity of binder content amongst granules of different sizes. Good binder distribution is often characterised by the lack of fines and any unused primary powder in the product.

Literature that has dealt with the influence of the method of binder delivery on various granule attributes was discussed in Section 2.14. In summary, Knight et al. (1998) investigated three different methods of binder addition using a single low viscous binder. This included a pour-on, melt-in and spray-on technique. The conclusion of their study reveals that there is a non-uniformity in the distribution of the binder for all cases of binder addition. This non-uniformity is most pronounced during the early stages of the granulation process. This larger difference in the binder content explains the bimodality in the size distributions that was observed at earlier times. Spraying is preferred over other methods, as it minimises the amount of energy required to disperse the binder once it is in the mixer, thereby shortening granulation times to reach the same set point. Both the spray-on and melt-in methods yielded a lower content of coarse granules than the pour-on method. Also the melt-in method produced granules with the smallest $D_{v4,3}$. The method of binder addition therefore, has an effect on the kinetics of granule growth.

Many other studies also conclude that delivery conditions have an influence on the kinetics of the granulation process (Schaefer and Mathiesen, 1996a, Osborne et al., 2011).

Increasing the rate at which binder is added into the mixer also influences the growth kinetics, as larger granules are formed earlier on (Smirani-Khayati et al., 2009). When a larger quantity of binder is introduced into the mixer over a shorter period of time, the probability of the droplets colliding with the powder is increased; therefore rate of nucleation is enhanced. However, the final granule size is usually not influenced by the rate of addition. Also with increasing time, eventually growth by agglomeration will be matched by breakage and attrition, therefore the size distribution will reach a steady state and becomes time independent (Michaels et al., 2009). In other words, when the stress acting on an agglomerate or granule is greater than the strength of the liquid bridge between them, then breakage will occur. However, if the converse is true then growth will dominate.

A commonly used approach to monitor binder distribution is to compare the binder content in different size classes. It is widely reported that there is a higher binder content in larger granules (Knight et al., 1998, Osborne et al., 2011, Scott et al., 2000, Reynolds et al., 2004). In order to compare the effect of the method or rate of binder addition, it is common practice to look at the binder content in a similar size class of granules. Initially, the heterogeneity in the binder content amongst the different size classes is likely to be greater, and with time, this heterogeneity is greatly reduced. When the wet massing time is short, the time available for binder distribution will be short and the resulting heterogeneity in binder distribution will be greater.

A majority of the aforementioned studies have focused on understanding the impact of binder addition on the distribution of low viscous and moderately viscous liquids and in some cases, the spread of melt. There is however, a lack of understanding on the impact of binder addition methods on the dispersion and subsequent distribution of semi-solid binders. This chapter attempts to address this knowledge gap.

Experiments were conducted in a 10 L Roto Junior high shear mixer (refer to Section 3.2 for more details about the granulator). Alkyl ethoxy ether sulphate (AE3S) was used as the binder (refer to section 3.3 for more details about the material). The binder con-

tains approximately 30% water by weight. It was dyed with Monazol Blue from Brenntag, UK. The concentration of the dye in the paste was 0.1 g/dm^3 . The raw materials were conditioned in a climatic chamber at 25°C and 40% relative humidity. The total size of the batch was limited to 1 kg (on a wet basis) and after drying, it yielded approximately 890 g of product.

The first method involved preloading the binder onto the surface of a stationary powder bed, as one large blob (Figure 4.8) and its subsequent dispersion was monitored with time. The second method involved injecting the binder into the mixer using six 50 ml syringes. For the injection method, the process was timed when binder injection commenced. Manual binder injection takes approximately 10 s. These batches were then analysed to determine their size, binder content and strength. Each of these granule attributes were monitored offline as a function of time. Trials were performed at a low (200 rpm, $v = 2.9 \text{ m/s}$), medium (400 rpm, $v = 5.9 \text{ m/s}$) and high (800 rpm, $v = 11.7 \text{ m/s}$) speed. A grab sampling technique was not adopted for this analysis, as starting and stopping the mixer could affect the kinetics of the granulation process. Furthermore, withdrawing samples from the mixer would result in a reduction in the fill level, which is another parameter that is known to influence the process (Hassanpour et al., 2011). Therefore, individual batches were made to study the influence of wet massing time. To ensure reproducibility, the experiments were repeated three times.

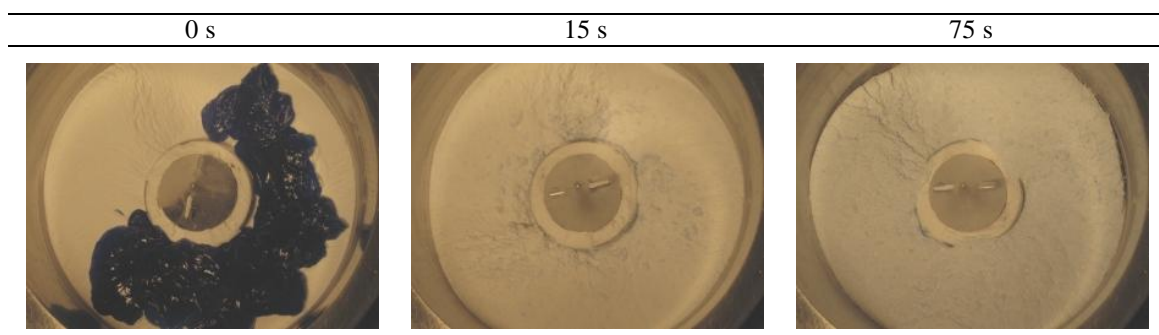


Figure 4.8. Visible changes in binder dispersion in the granulator, with time, at 200 rpm – binder was preloaded as one large blob.

The volume based mean size ($D_{v4,3}$) of the particles at all three impeller speeds was determined using the Camsizer P4 (Figure 4.9 - Figure 4.11). With increasing wet massing time, growth of the granules is evident. This is true at all three impeller speeds. However, this is most pronounced at the highest impeller speed of 800 rpm. At the lower

speeds of 200 and 400 rpm, it is also evident that granule growth is greater when the binder is injected into the mixer, as the final mean size after 75 s of wet massing is higher.

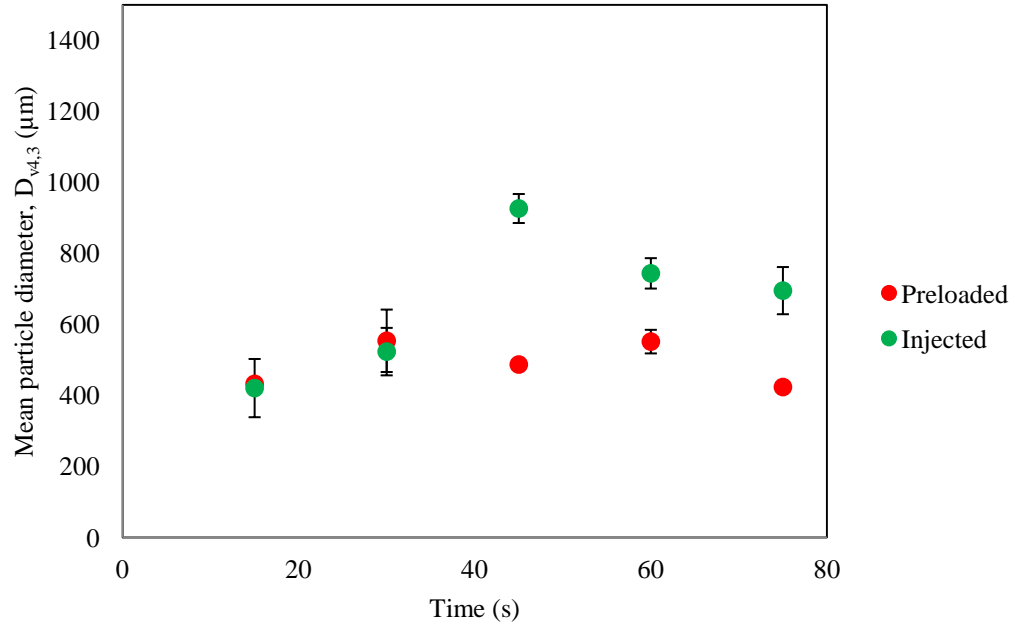


Figure 4.9. Change in the mean diameter of the granules with time at 200 rpm.

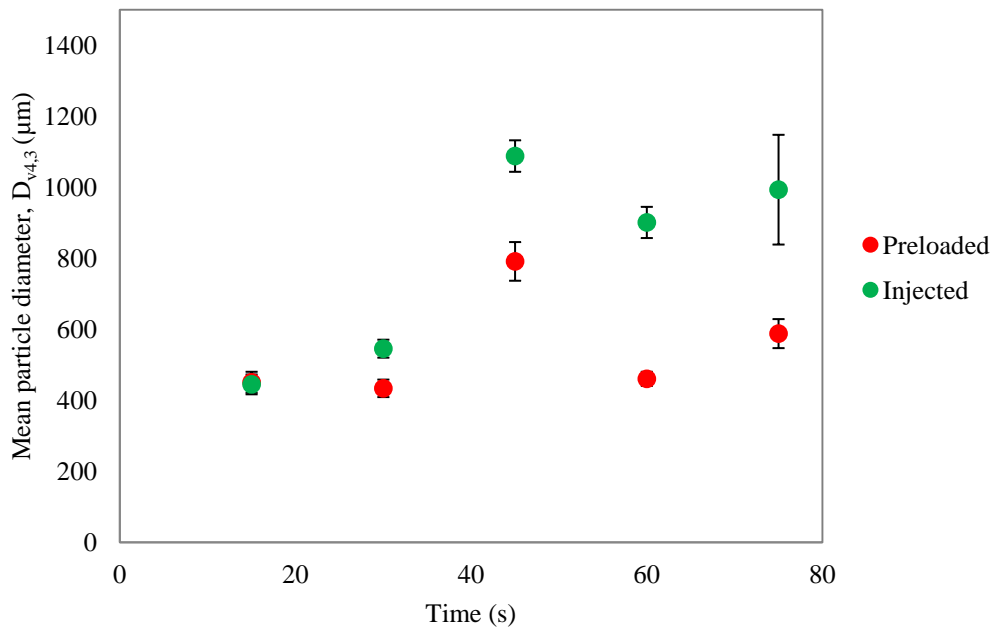


Figure 4.10. Change in the mean diameter of the granules with time at 400 rpm.

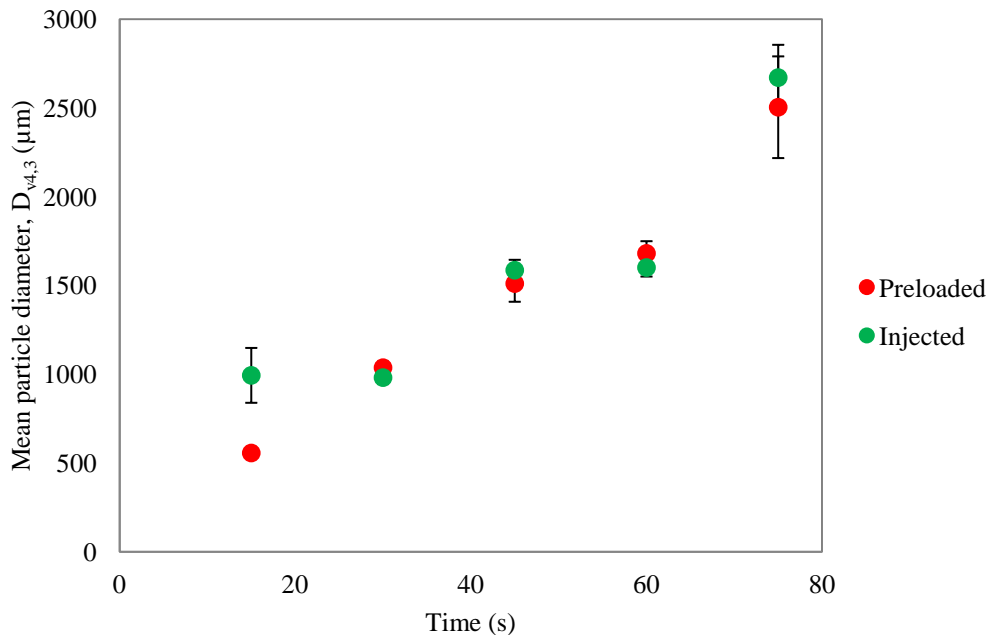


Figure 4.11. Change in the mean diameter of the granules with time at 800 rpm.

The results show that the change in the $D_{v4,3}$ mean size of the particles depends on the impeller speed and the manner in which binder is introduced in to the mixer. It is also of interest to look at the changes in the relative amounts of granules of different sizes within a batch. This may give some useful insights about the mechanistic processes that occur during granulation. Therefore, the granules were sieved and separated into three different size classes and their relative masses were compared as a function of time. In order to obtain these mass based size distributions, 500 and 2000 μm sieves were used to separate the granules. For making comparisons between the two binder delivery methods, three different classes of granules were defined as follows: **small (<500 μm)**, **medium (500 μm – 2000 μm)** and **large (>2000 μm)**. The size classes were selected by comparing the particle size distribution of the commercially manufactured detergent DAZ by P&G, UK. The D_{10} , D_{50} and D_{90} were determined to be 460, 1220 and 2046 μm respectively. The change in the mass of the different size classes with time, at different impeller speeds, are shown in Figure 4.12 - Figure 4.15.

At 200 rpm (Figure 4.12), the mass of the large granules is very small and remains constant with time for both the injected and preloaded cases. In the first 15 s, any large

lumps of binder could be reduced to medium sized lumps. The mass of the medium sized granules decreases with time for both cases too. There is no increase in the mass of the large granules, due to the low stresses acting on the moving bed of powder. Growth normally occurs by coalescence or layering, both of which require binder to be squeezed from within the granules in order to increase their cohesiveness. Therefore, it appears that breakage is the more dominant mechanism at this impeller speed. With time, the dispersion of the paste into the powder is enhanced; therefore any large powder coated binder particles will get broken down into smaller fragments. It is likely that the granules that get broken in the medium size class are binder rich nuclei. There is some evidence suggesting an enhanced distribution of binder for the injected case, when considering the mass of the small particles with time, as it is higher for the preloaded case.

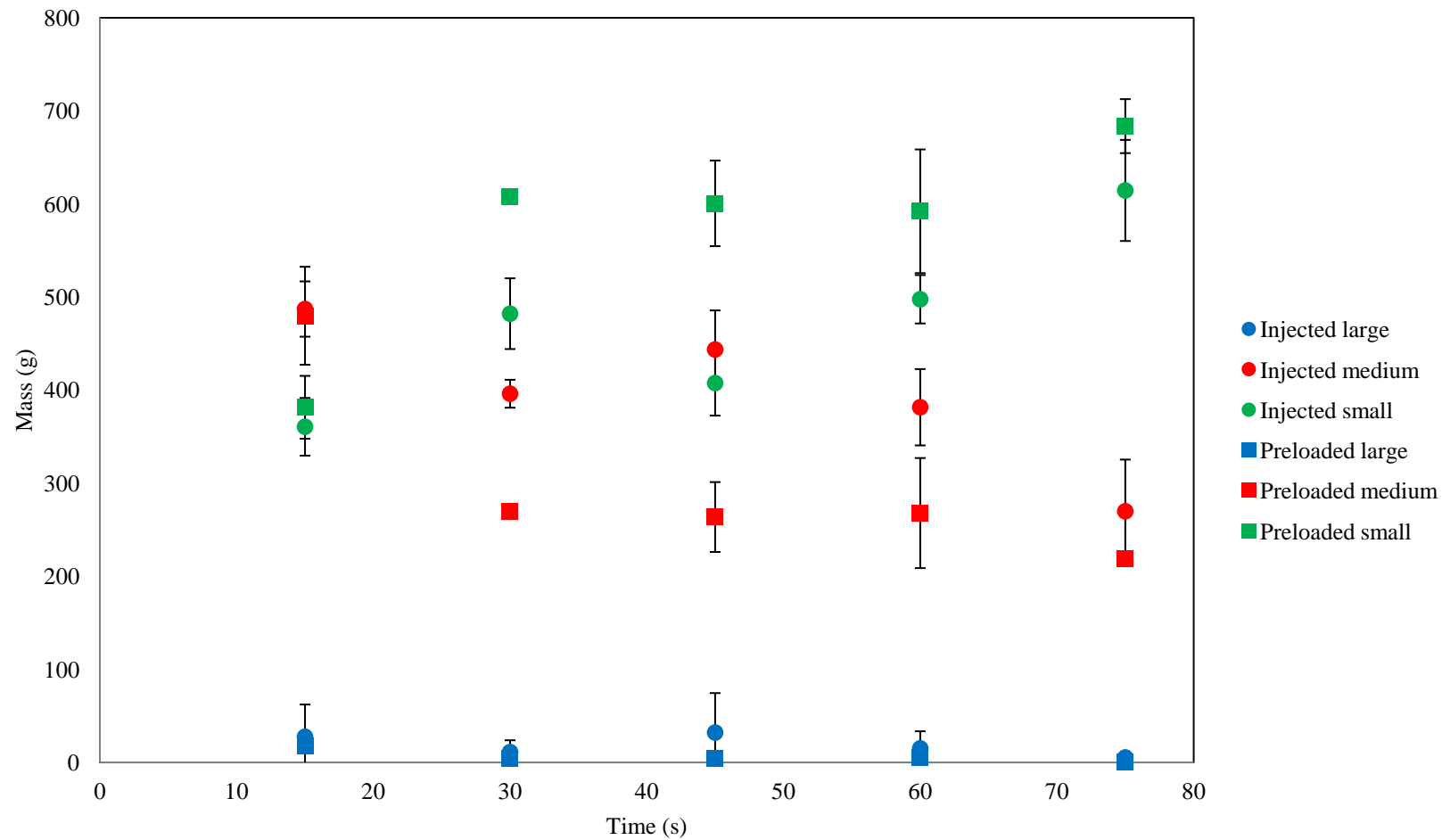


Figure 4.12. Mass distribution at 200 rpm - blobs vs. injected.

At 400 rpm (Figure 4.13), an increase in the mass of the large particles is observed when compared to the experiments that were done at a lower speed of 200 rpm. For the injected case, a sharp increase in the mass of the large particle is seen after 45 s of wet massing, whereas the mass of the large particles for the preloaded case remains constant with time. There is an increase in the mass of the medium sized particles for the pre-loaded case. For the injected case, the medium sized particles reaches a peak at 45 s, after which the mass starts to drop. This peak corresponds to the increase in the mass fraction of the large particles after 45 s. This suggests that injecting the binder into the mixer helps to speed up granule growth. When considering the small size class of particles, there is more in the preloaded case than the injected case, at all times. A minimum level of binder saturation is required to facilitate the formation of granules. Therefore, the existence of a greater quantity of small particles in the preloaded experiments, demonstrates dispersion of the binder into the powder bed is poorer with time. This trial also indicates that the method of binder addition does have an influence on the kinetics of granule growth. Adding the binder in the form of large blobs means more time is required to redistribute the binder evenly, thus reducing the time available for granule growth. Images of the dried granules after 75 s of wet massing also indicate faster growth for the injected case (Figure 4.14).

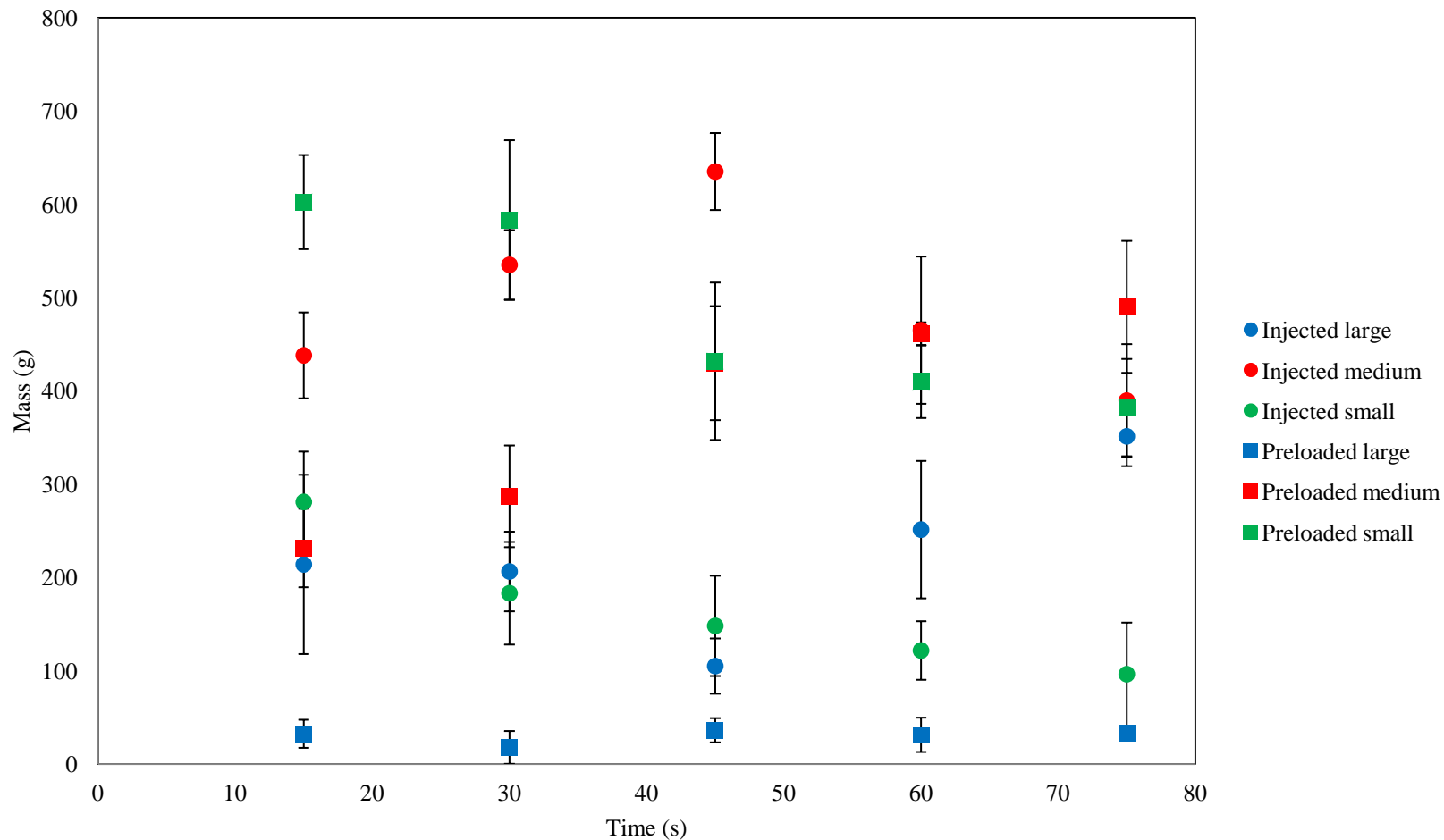


Figure 4.13. Mass distribution at 400 rpm - blobs vs. injected.

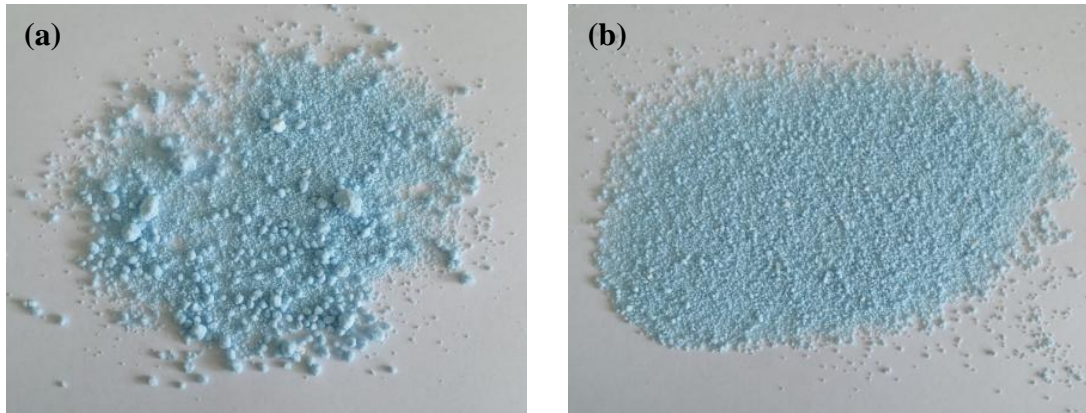


Figure 4.14. Images of the dry product after 75 s of wet massing (a) 400 rpm – injected and (b) 400 rpm- preloaded.

At an even higher impeller speed of 800 rpm, the difference between the two cases is not very clear after 15 s of wet massing (Figure 4.15). At 15 s, it can be seen that the preloaded case consists of more small granules than the injected case. After 15 s, the lack of any clear differences between the two methods of binder addition could be attributed to the very high shear and impact stresses that act on the material, thereby evenly dispersing all the binder. Another notable observation is the sharp increase in the mass of the large granules from 60 to 75 s. At this speed, the granules may easily deform, leading to rapid growth by coalescence and layering.

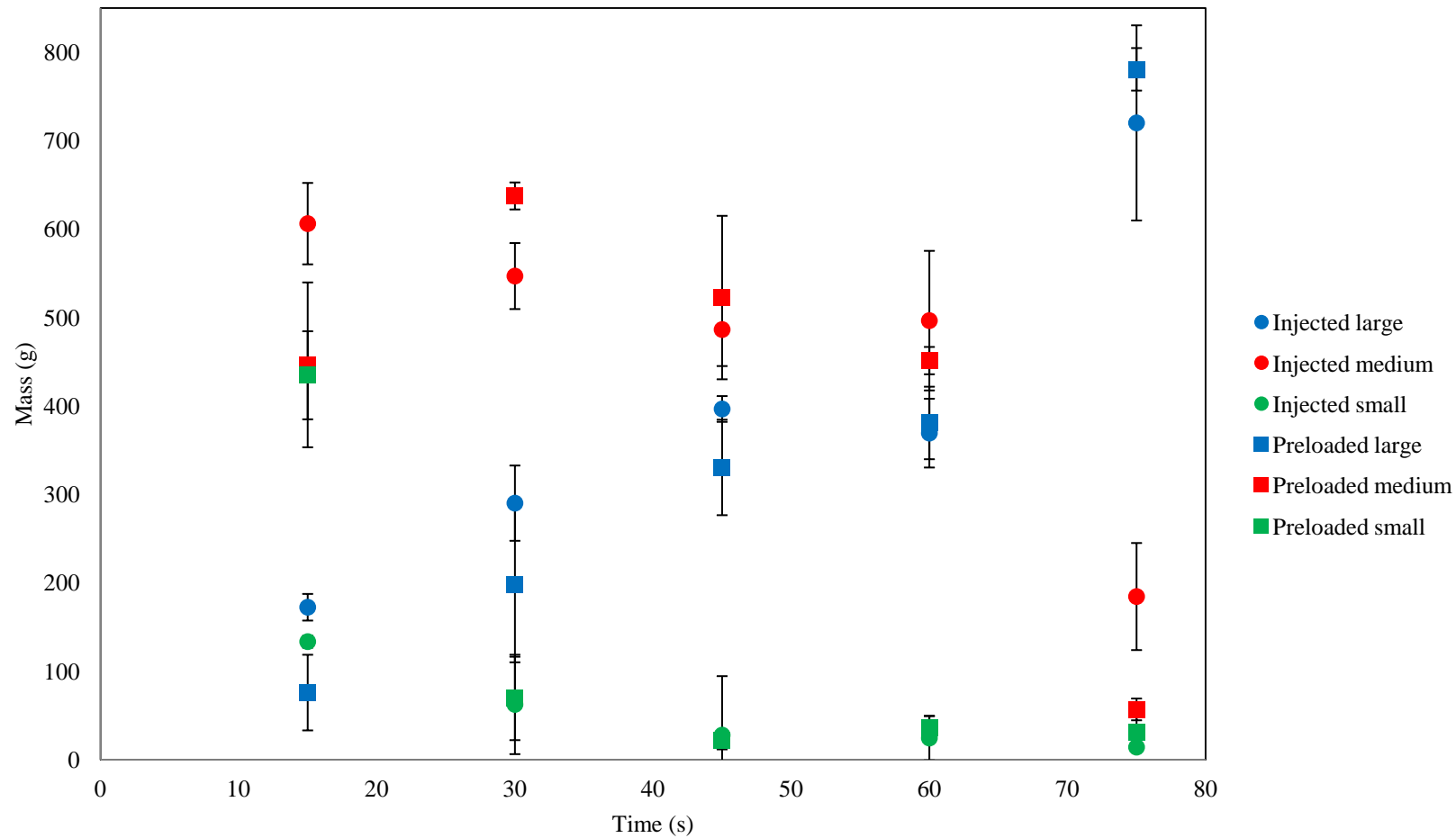


Figure 4.15. Mass distribution at 800 rpm - blobs vs. injected.

4.6 Binder distribution

Ultra-violet (UV) spectroscopy was used to determine the binder distribution amongst the various size classes in a batch of granules. Section 3.16 outlines the technique used to determine the concentration of the binder in the granules. To ensure the powder components in the detergent granules do not interfere with the UV measurements, a control experiment was performed. The control experiment compares the absorbance recorded for the surfactant solution and the detergent solution. The detergent contains the surfactant paste and powder (refer to Table 4.1 for the composition of the detergent granules). Measurements were taken at a wavelength of 285 nm. Figure 4.16 demonstrates that the addition of sodium carbonate and zeolite does not change the absorbance of UV radiation, as there is no significant difference in the measured absorbance for both cases.

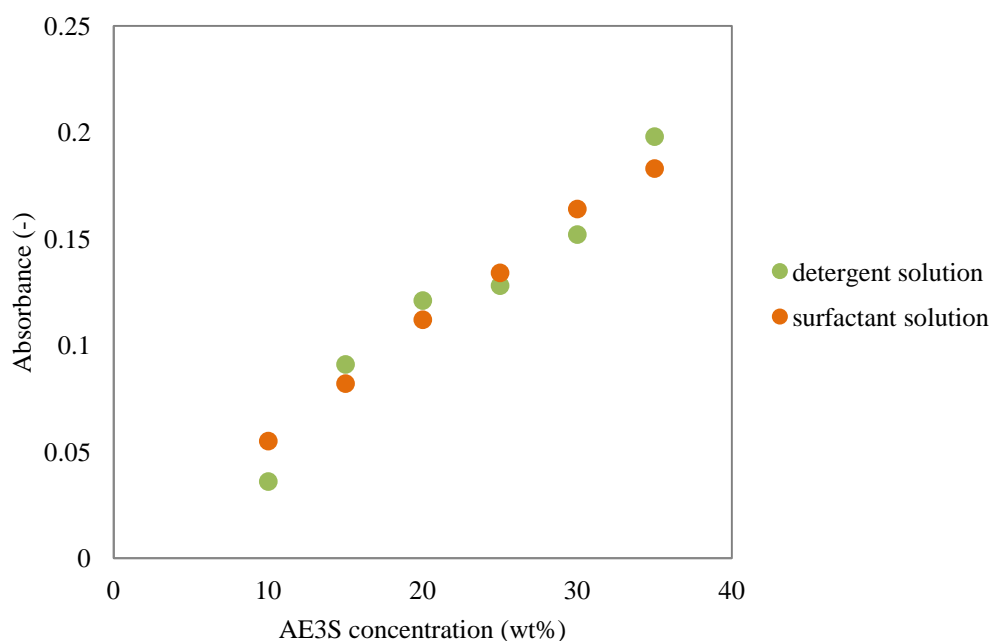


Figure 4.16. UV spectroscopy control study comparing a surfactant solution with a detergent solution.

Granules were separated into narrow size classes prior to measuring their binder content. Size classes ranging from 90 – 1000 µm were obtained using sieves from a fourth-root-of-two progression series (90, 125, 180, 250, 355, 500, 710 and 1000 µm). The results from the UV experiments are summarised in Figure 4.17 - Figure 4.19. The theoretical average value of the binder content should be 27 wt% on a dry basis. This corre-

sponds to an absorbance of 0.145. Some sources (Tan et al., 2014, Osborne et al., 2011, Knight et al., 1998, Reynolds et al., 2004) report that the average binder loading has a direct influence on granule growth. It is therefore, expected that larger granules would have more binder than smaller ones. This trend is evident from the data set obtained at all three impeller speeds: 200, 400 and 800 rpm.

At 200 rpm (Figure 4.17), the heterogeneity in the binder content amongst the different size classes is most pronounced. This is largely due to the presence of lumps of surfactant paste that have not been dispersed fully in the large size class. Images of the dry powder also give an indication of the extent of binder dispersion and at 200 rpm, the resulting product contains a significant amount of unbound primary particles (Figure 4.20a). At 400 and 800 rpm (Figure 4.18 - Figure 4.19), there are more subtle differences in the binder content between different size classes. However, again a similar trend is observed, in that, the large granules have a higher binder content. Interestingly, the span in the values of the absorbance also reduces with an increase in the impeller speed. At higher impeller speeds, the product is more granular and less powdery (Figure 4.20). This explains the smaller span in the absorbance between different size classes at higher speeds. This also suggests that the homogeneity in the binder content can be improved by granulating at higher speeds.

The results obtained from the UV analysis can be used to quantify the binder dispersion process as a whole. The difference in the binder content between the largest and smallest size of granules can be determined to give an indication of the homogeneity in the binder content of granules in different size classes. A large value would indicate poorer binder dispersion, whilst a smaller value indicates greater homogeneity i.e. better binder dispersion.

The different methods of binder addition, however, do not seem to have a significant effect on the binder content, at all three impeller speeds. This method is not able to distinguish between binder that is evenly distributed and binder that is not. For example, a powder coated binder fragment (which has a binder rich core) and a wet agglomerate (which has the binder spread out evenly throughout its internal structure) could still give the same absorbance, providing both have the same mean concentration of binder. This

could be a possible reason for the lack of an apparent difference between the two methods of binder addition.

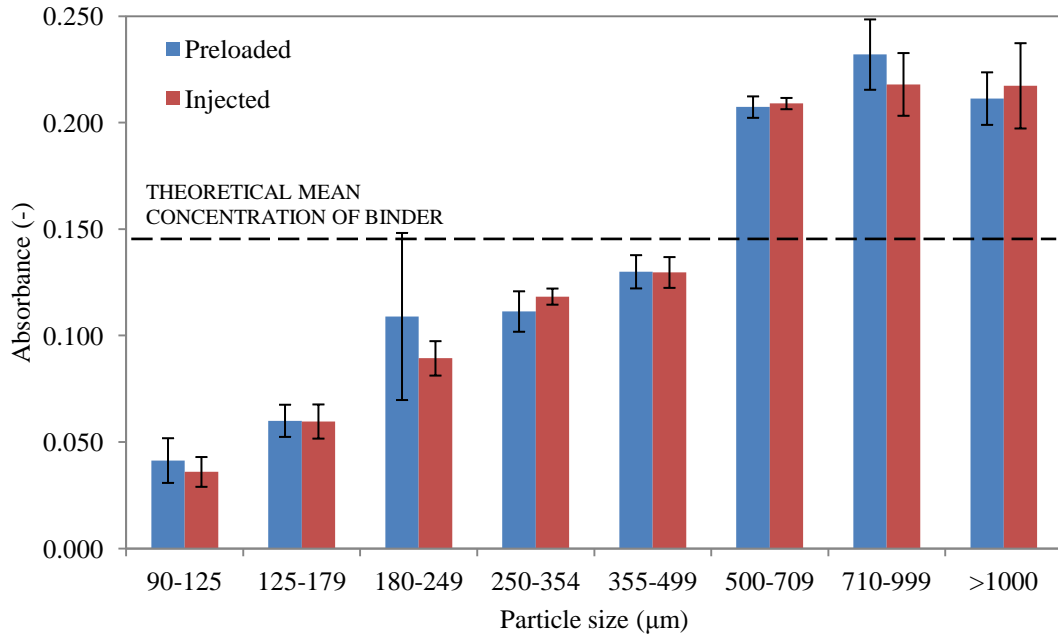


Figure 4.17. Binder content of different size classes at 200 rpm, after 75 s of wet massing.

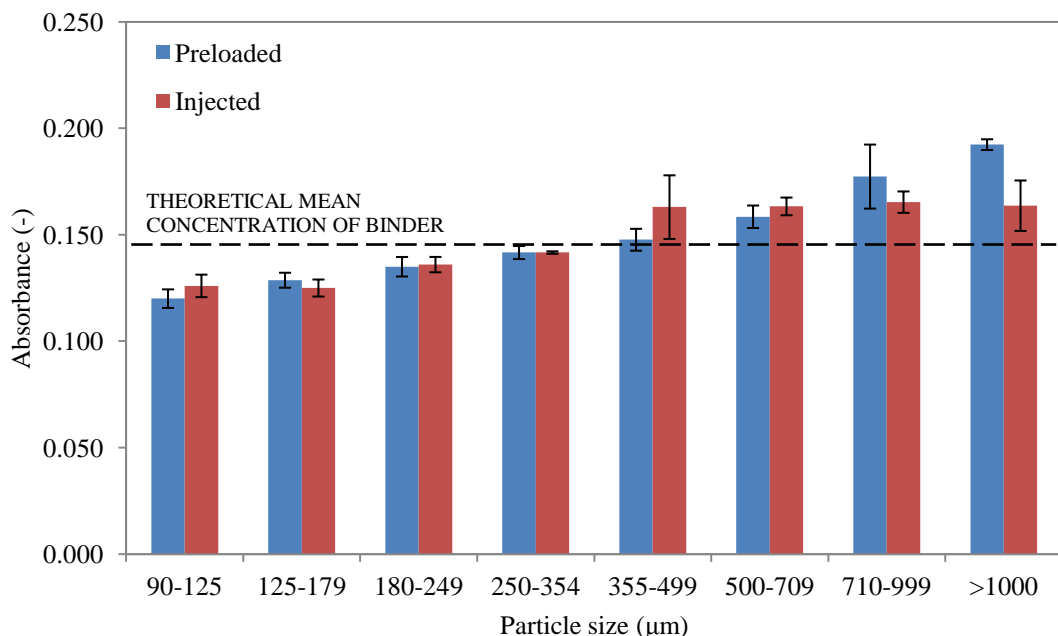


Figure 4.18. Binder content of different size classes at 400 rpm, after 75 s of wet massing.

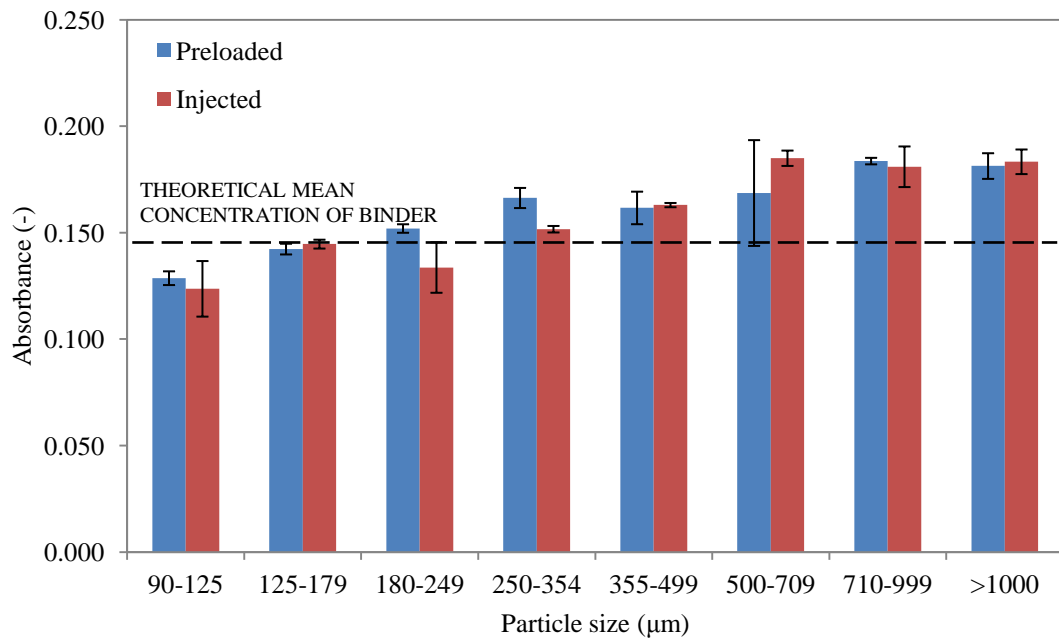


Figure 4.19. Binder content of different size classes at 800 rpm, after 75 s of wet massing.

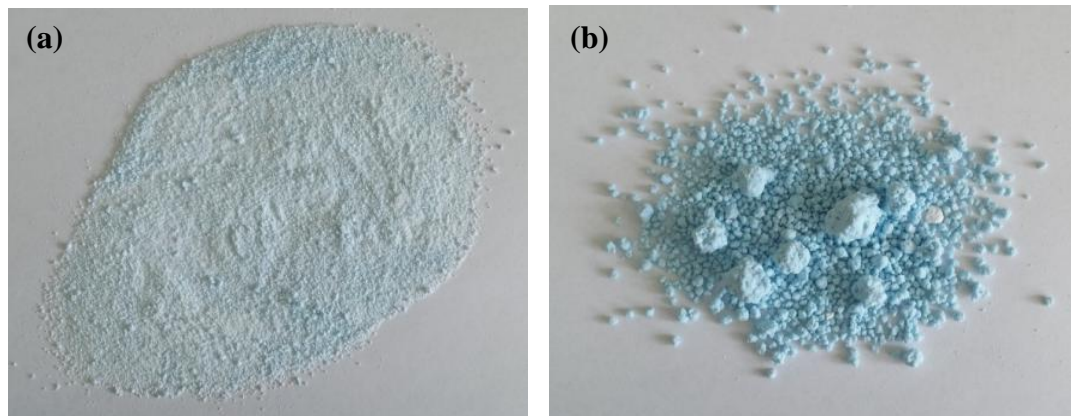


Figure 4.20. Images of the dry product after 75 s of wet massing at (a) 200 rpm and (b) 800 rpm, for the injected case.

4.7 Granule strength

Granule strength was determined using the uni-axial confined compression technique outlined in Section 3.15.1. Granules were separated into large, medium and small size classes as outlined in Section 4.5. The granules produced at a low impeller speed do not show a significant variation in strength with time, for all size classes that were analysed (Figure 4.21). This is different from the granules produced at higher speeds (400 and 800 rpm). At higher speeds, the large granules are around four times stronger than the small and medium sized granules (Figure 4.22 & Figure 4.23). At higher speeds, the consolidation process may be occurring much earlier leading to the formation of stronger granules with time. Again, there is no significant difference in granule strength as a result of the method of binder delivery.

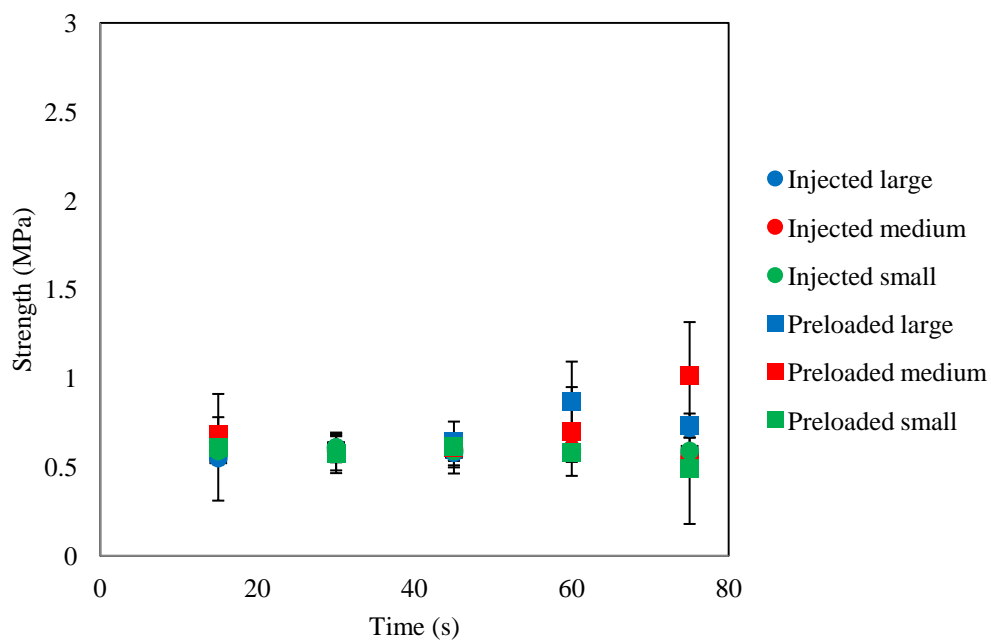


Figure 4.21. Granule strength against time – 200 rpm.

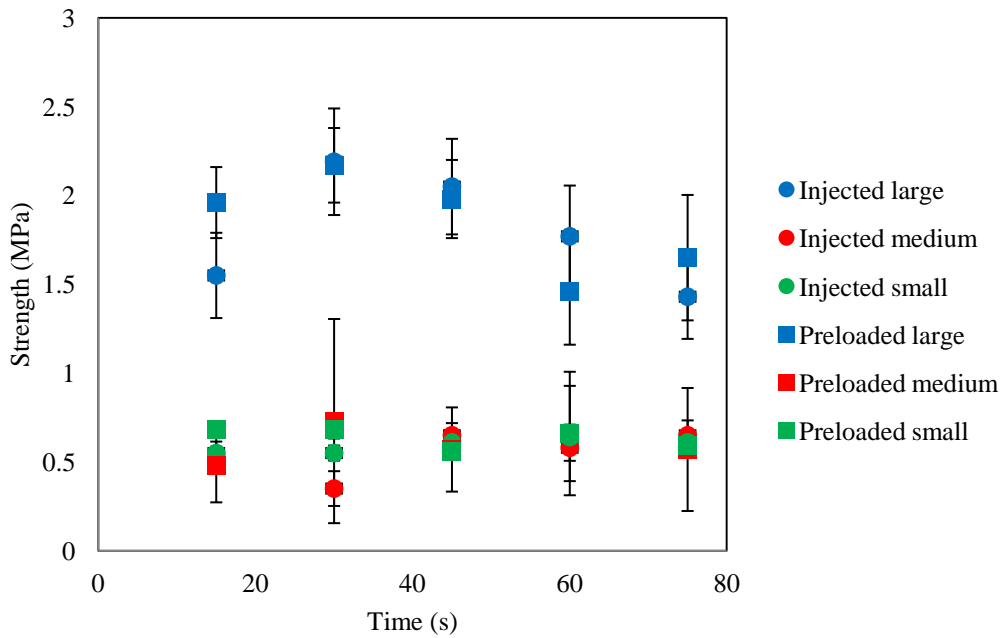


Figure 4.22. Granule strength against time – 400 rpm.

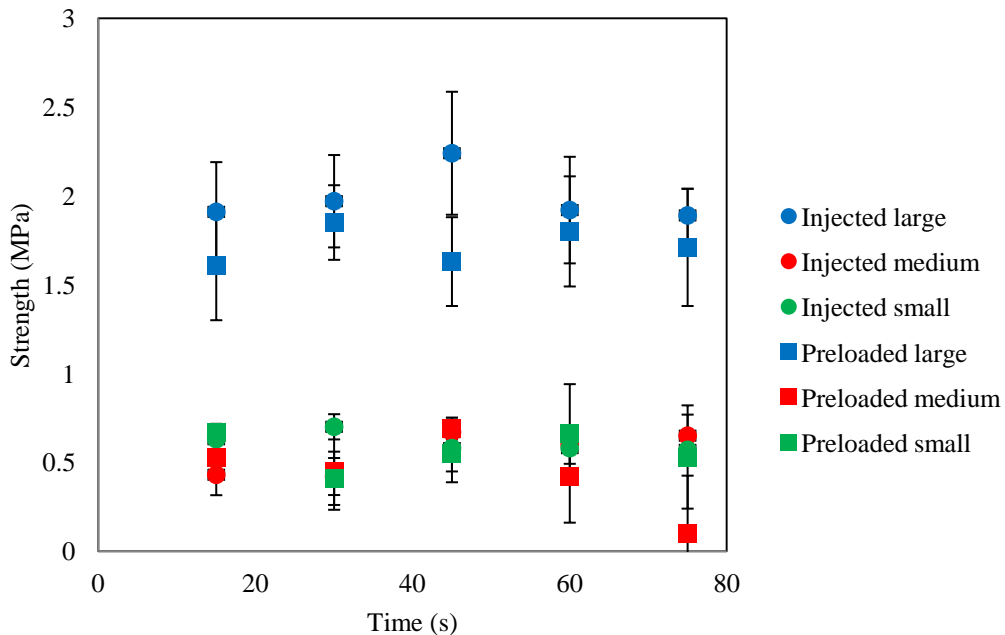


Figure 4.23. Granule strength against time – 800 rpm.

Figure 4.24 demonstrates that granules made at 400 and 800 rpm are stronger than those made at 200 rpm. Furthermore, observing micrographs of the granules (Figure 4.25) seems to suggest that at lower impeller speeds, granules have not undergone much consolidation. At 200 rpm, the large size class consists of loosely coated lumps of binder.

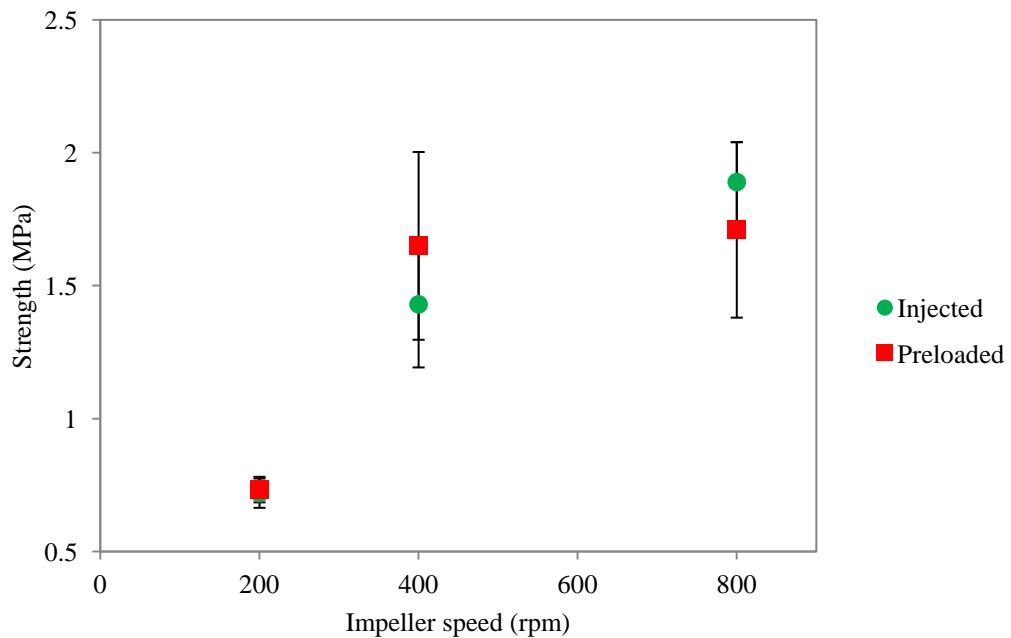


Figure 4.24. Strength of the large granules ($>2000 \mu\text{m}$) against impeller speed at 75 s.

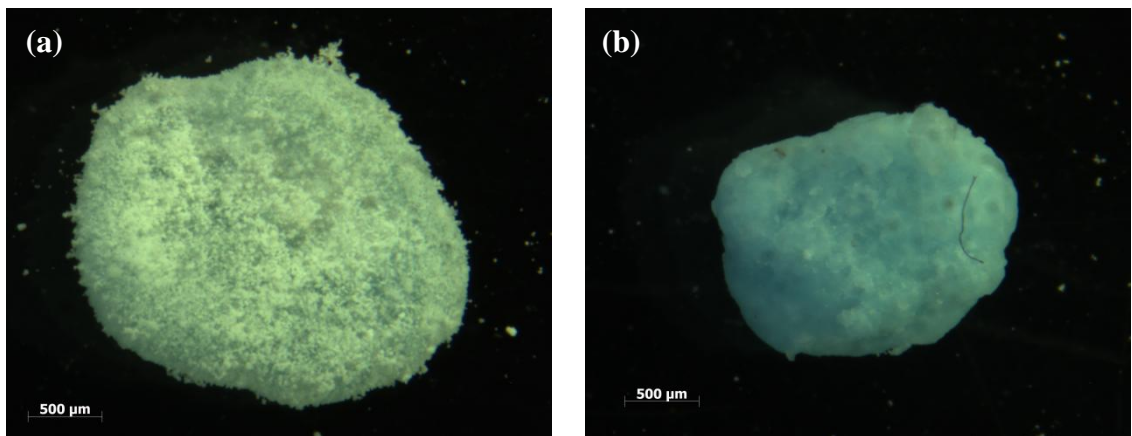


Figure 4.25. Large granules ($>2000 \mu\text{m}$) as seen under a light microscope: (a) 200 rpm
(b) 800 rpm.

4.8 Tracking binder dispersion *in situ*

A thermal camera was used to track the dispersion of the semi-solid binder in a moving bed of powder. The binder was heated to a temperature of 50°C, whilst the powder was maintained at room temperature (25°C). For more details about the thermal imaging technique refer to Section 3.13. As before, binder was delivered into the mixer either by injection or by preloading (as one large blob). Experiments were conducted at three different speeds: 200, 400 and 800 rpm. All other conditions were kept the same, during

granulation, as outlined in Section 4.5. At the higher speeds, a sheet of black polythene had to be placed over the mixer to contain the material within it. Infrared radiation is able to travel through the sheet of polythene; therefore it has a minimal effect on the resulting image quality.

The thermal images that were obtained for both the preloaded and injected case, at 200 rpm, are presented in Figure 4.26. The 32-bit colour images were converted into 8-bit grey scale images. Subsequently, appropriate threshold limits were applied to identify regions where the temperature exceeded 30°C. After binarizing, these regions appear as white spots on the image. The total area of the white regions was calculated as a function of time to enable binder dispersion to be quantified. For the preloaded case, the results indicate that the binder first settles into the bed of powder and starts to resurface with time (Figure 4.27). For the injection experiment, the binder does not settle into the powder, instead it remains on the surface and gets mixed into the powder gradually. After 60 s of wet massing, it is also evident that there are more hot spots for the preloaded case than the injected case. Injecting the paste increases the surface area of paste-powder contact, thereby, enhancing the rate at which binder and powder mix. Ideally, the binder should be distributed evenly throughout the bed. Therefore, the presence of a large quantity of binder on the surface is undesirable, as is the presence of no binder on the surface. For the injected case, it can be seen that the binder concentration at the surface reaches a steady state sooner and the concentration is much lower at the surface compared to the preloaded case (Figure 4.27). For the preloaded case, the concentration of binder at the surface is greater, as the larger lumps of paste have more kinetic energy and resurface more often. The binder distribution therefore, takes longer to reach a steady state for the preloaded case when compared with the injected case. This study further confirms that better binder distribution can be achieved by injecting the binder into the mixer.

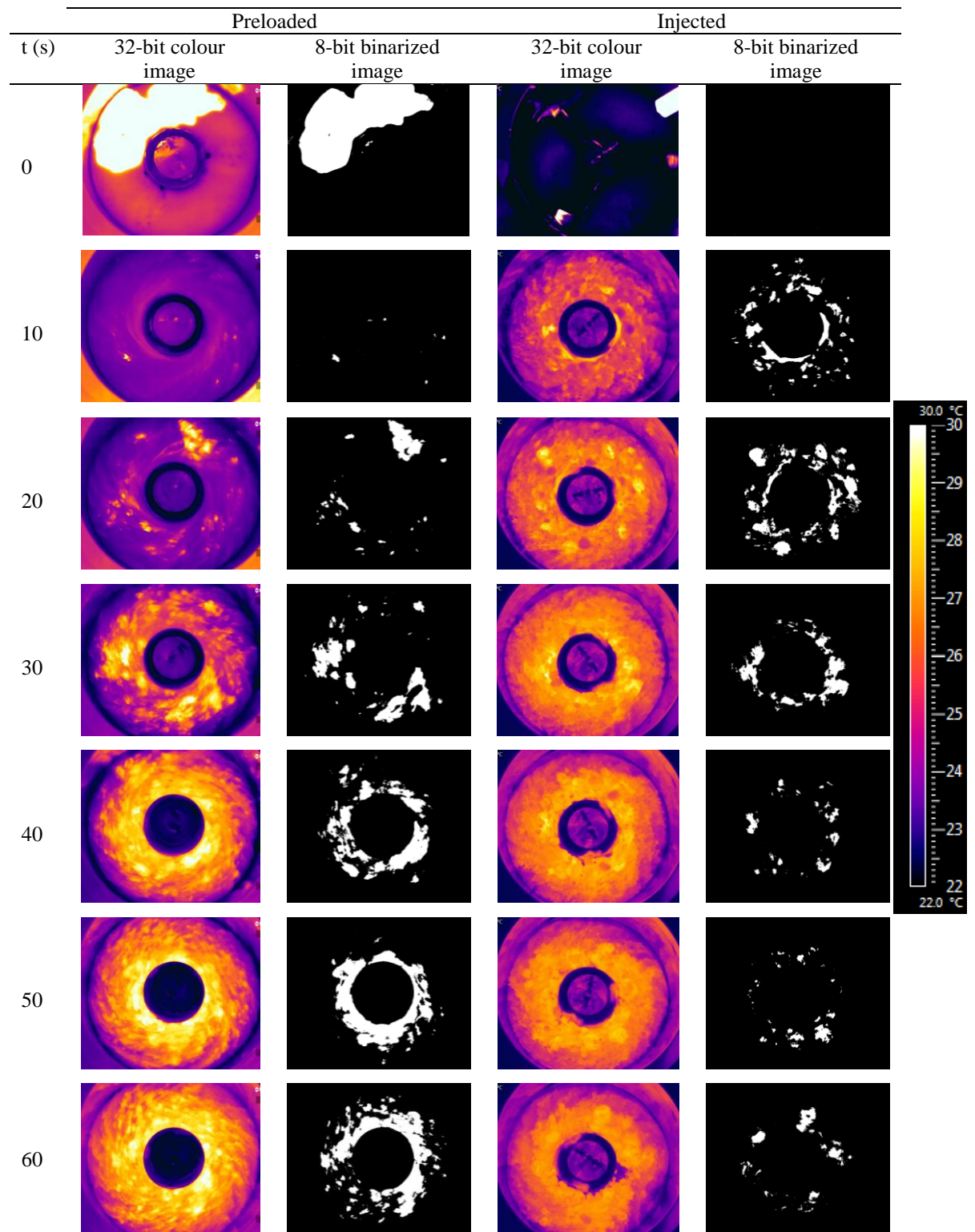


Figure 4.26. Time lapse thermal image sequence of the high shear mixer for both pre-loaded and injected cases at 200 rpm.

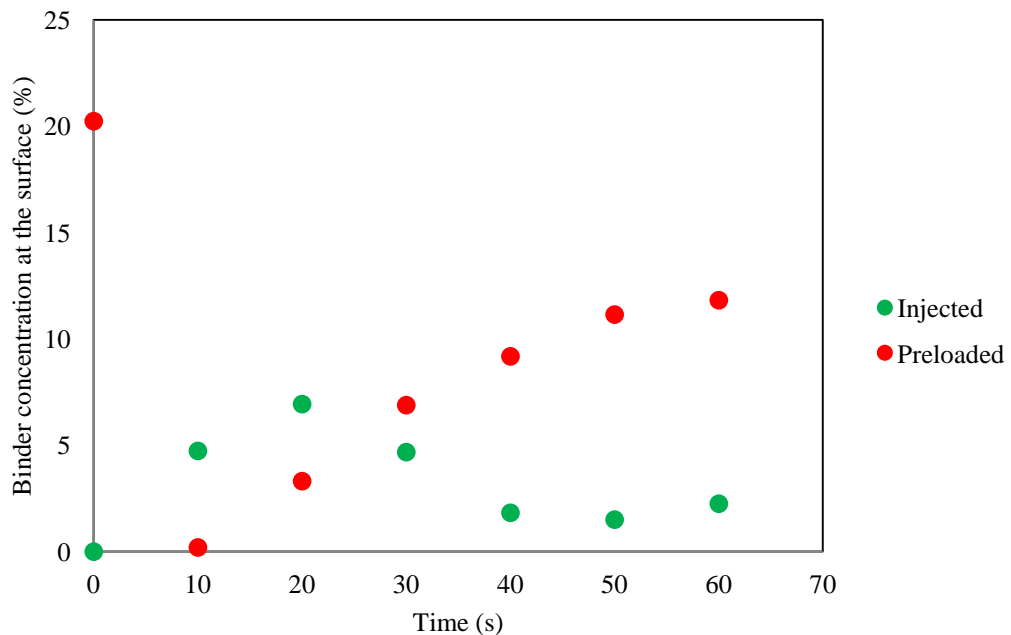


Figure 4.27. Variation in the binder concentration at the surface with time, at 200 rpm.

The thermal camera can capture up to 50 frames per second at maximum resolution (480×640 pixels). At speeds of 400 rpm and higher, it is not possible to see individual lumps of binder that surface within the moving bed of powder, as the frame rate is not high enough (Figure 4.28). At 400 rpm, there is however, a distinct difference in the average temperature of the moving bed of powder for the injected and preloaded cases (Figure 4.29). Ideally, good binder distribution would result in rapid distribution and even mixing of the binder and the powder. As the binder is warmer than the powder, mixing the two components together should result in an average temperature between 22 – 50°C. At 400 rpm, it takes longer for the temperature of the moving bed of powder to reach steady state when the binder is preloaded, compared to when it is injected (Figure 4.29). This further confirms that an even distribution of the binder can be reached sooner if the binder is introduced into the mixer as a smaller entity (i.e. as a thin stream or jet instead of one large blob). When attempting to conduct a similar analysis at the highest speed of 800 rpm, it was found that the heat generated by the moving bed of powder interferes with the results. At low to moderate speeds, it is therefore possible to elucidate the effect of the method of binder delivery using a thermal camera.

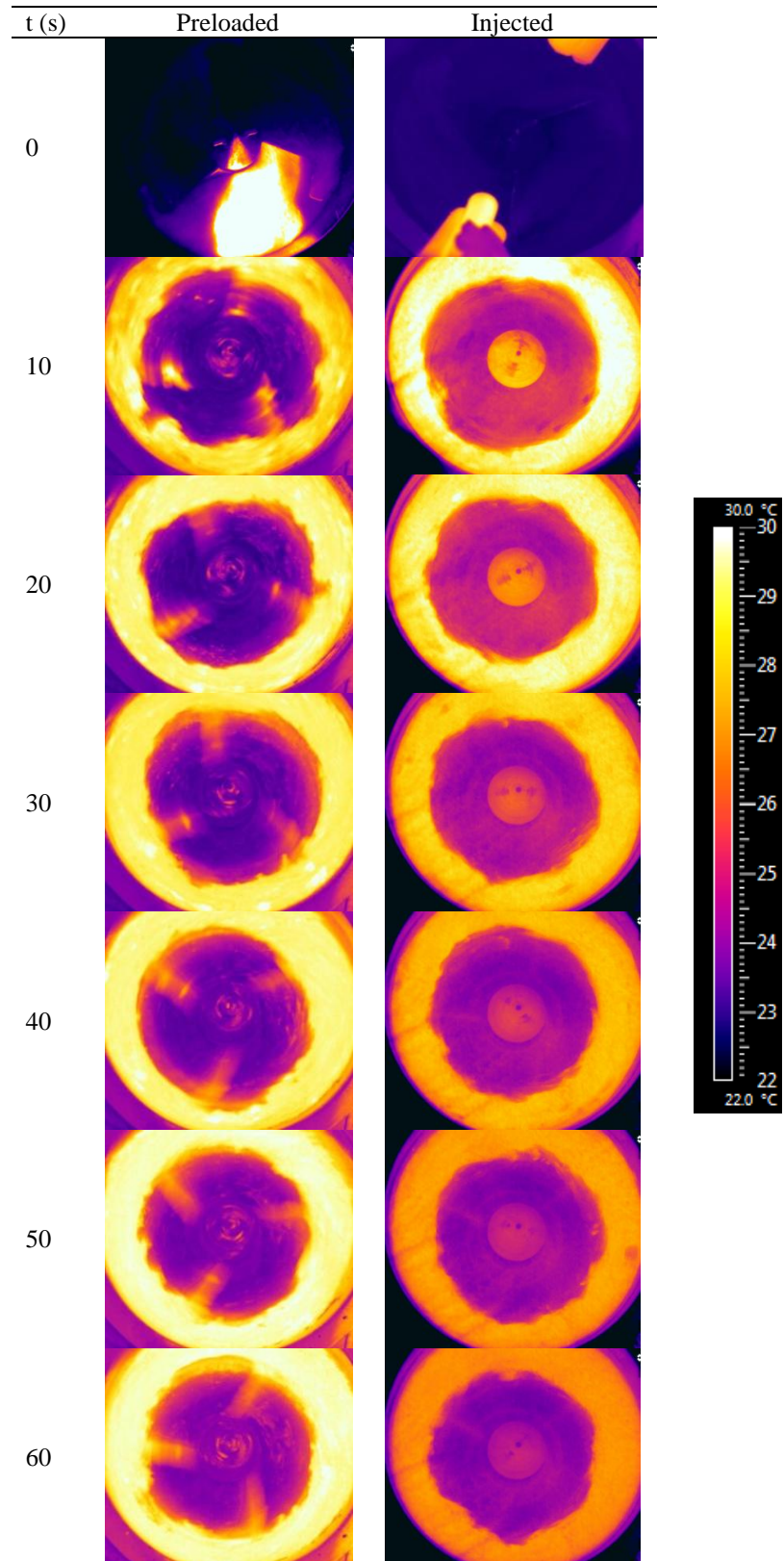


Figure 4.28. Time lapse thermal image sequence of the high shear mixer for both pre-loaded and injected cases at 400 rpm.

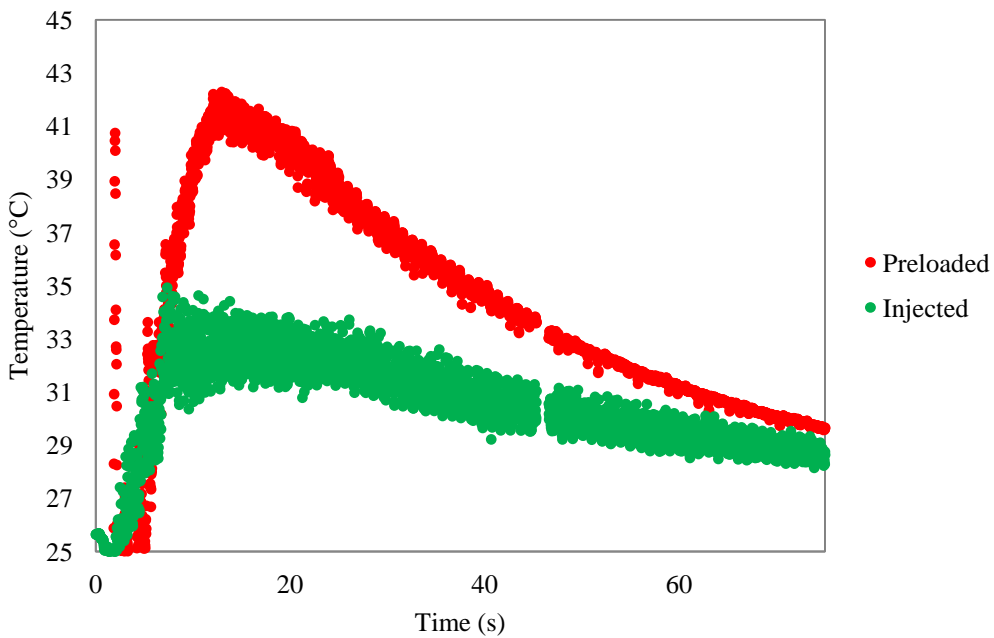


Figure 4.29. Average surface temperature of the moving bed of powder with time for both preloaded and injected cases at 400 rpm.

4.9 Conclusions

This chapter focuses on understanding the impact of the method of binder delivery on the kinetics of granule growth, binder distribution and granule strength. The semi-solid binder was either injected into the mixer or preloaded as one large blob. Experiments were conducted at three different impeller speeds: 200, 400 and 800 rpm.

At low to moderate impeller speeds (200 – 400 rpm), injecting the binder into the mixer enhances the kinetics of granule growth. Adding the binder into the mixer as a smaller entity (i.e. as a continuous stream instead of one large blob) reduces the amount of time required to distribute the binder, thus providing more time for granule growth. However, there was no apparent impact on the binder content and granule strength, as a result of the method of binder addition - both methods showed similar trends (at all speeds).

For a low viscous binder, Knight et al. (1998) report an increase in the mean size of the granules when the rate of binder addition is greater. Their study suggests an increase in the rate of binder addition results in certain regions of the powder bed becoming over-wet, and this leads to the formation of larger granules. Others (Wauters et al., 2002,

Smirani-Khayati et al., 2009) also report similar finding when using a binder of a low viscosity. However, the present study reveals that increasing the rate of addition (by preloading all the binder into the mixer at once) for a highly viscous binder results in a decrease in the mean size of the granules. This behaviour can be attributed to the high viscosity of the binder, which does not spread and wet the primary particles until it has been completely dispersed into the moving bed of powder. Therefore, a more gradual addition (by injecting for example) is better for achieving faster granule growth kinetics.

An increase in the stresses within the granulator (impeller speed) increases the rate at which material progresses through the various stages of the granulation process (nucleation, growth, consolidation and coalescence). At low impeller speeds (200 rpm), breakage (binder dispersion) is the dominant mechanism, and at higher impeller speeds granule growth begins. The heterogeneity in the binder content amongst granules of different sizes is also reduced at higher impeller speeds, and this suggests that binder distribution is better at higher agitation intensities. Furthermore, the large granules are stronger at 400 and 800 rpm. This could be due to the consolidation process occurring much earlier leading to the formation of stronger granules with time.

Furthermore, thermal imaging was used to successfully visualise the movement of the binder within the mixer. There was a clear difference in the movement of the binder within the mixer for the injected and preloaded case at the lower speed of 200 rpm. For the injected case, it can be seen that the binder concentration at the surface reaches a steady state sooner and the concentration is much lower at the surface compared to the preloaded case. This supports the argument that better binder distribution can be achieved by injecting the binder. At a higher impeller speed of 400 rpm, it was not possible to see individual lumps of binder; however the temperature of the mixer reached a steady state sooner for the injected case. Again, this suggests mixing is better when the binder is injected.

Chapter 5 Semi-solid binder breakage

5.1 Introduction

The previous chapter considered the effect of the method of binder delivery on granule growth. Results suggest that the initial size of the semi-solid binder particles influence the growth kinetics. It is also of interest to understand how the binder gets dispersed in a high shear environment. In this chapter, a mechanism for the initial dispersion of a semi-solid binder has been outlined, which involves the breakage of lumps of binder. An experimental method for isolating binder breakage was subsequently devised, and the breakage is quantified by monitoring changes of both the size and mass of the binder particles.

Once introduced into the mixer the binder gets coated with powder. They are subsequently referred to as **powder coated binder particles (PCBPs)**. Dispersion of the binder occurs during the nucleation step of the agglomeration process. The mechanism of binder dispersion is in some ways consistent with the immersion mechanism that was proposed by (Schaefer and Mathiesen, 1996a). The immersion mechanism is dominant when the binder droplet is relatively large in comparison to the size of the primary particles that constitute the moving bed of powder. The particles will initially, adhere to the surface of the large droplet and gradually start to spread. In the case of a low viscous binder, powder particles may be drawn into the core of the liquid droplet (as a result of surface tension at the liquid-particle-air interface). The semi-solid binder is a non-Newtonian fluid, with a viscosity that is $\times 10^4$ greater than that of water. Hence, surface tension will not facilitate particle penetration into the core of the binder, due to its high viscosity. Therefore, powder ingress into the core of the binder is unlikely to occur in the absence of any external forces.

After the binder is introduced into the mixer, the action of both shear and impact delivered to the contents of the mixer, by the motion of the impeller, will initially break large lumps of the binder in to smaller lumps. It is also hypothesised that the type of primary particle and the impeller speed influences the rate at which this binder breakage occurs.

This chapter discusses the following in more detail:

- Determining powder-binder adhesion in the absence of any shear or impact stresses.
- The standard method adopted for making the binder particles of a uniform size.
- The technique used for isolating the PCBPs from the unused free powder in the granulator.
- Monitoring the powder assimilation into the binder particles/fragments with time.
- Monitoring the breakage of the PCBPs with time.
- Analysing the internal structure of the PCBPs with time.
- Observing and understanding reasons for the changes in the breakage patterns, as well as the mechanical properties of the PCBPs with time.

The chapter concludes by discussing the effects of various process parameters and formulation variables on the breakage of the semi-solid binder in a moving powder bed. Some recommendations for enhancing the distribution of a semi-solid binder in a moving bed of powder have also been suggested.

5.2 Key stages in dispersing a viscous binder

As discussed in Section 2.2, the granulation process can be divided into several different stages including wetting and nucleation, consolidation and coalescence and finally breakage and attrition. To reiterate, the nucleation and wetting step involves distributing the binder into a moving bed of powder. It is in this stage that nuclei are formed, which act as seeds for further granule growth. This investigation primarily concerns the formation of these nuclei, and attempts to describe how they evolve with time in a granulator.

Figure 5.1 describes nucleation for a granulation process that involves the use of a low viscous binder. Once the droplet lands on the surface of the material, it penetrates the bed by capillary action. This results in the formation of a weak, wet nucleus. For a

highly viscous binder, the mechanism of binder dispersion is different, as the binder is too viscous to penetrate a bed of powder by capillary action. Instead, the powder layers on the surface of the binder by adhesion. Dispersion of the binder is a result of the combined action of the impeller and the moving bed of powder. The mechanical action facilitates further layering of powder onto the surface of the binder (Figure 5.2).

During the dispersion of a highly viscous binder, the powder coated binder particles are likely to resemble a **powdery-crumb** like state to begin with. These PCBPs will then undergo a size reduction process with time and eventually, all the binder will become well distributed into the bed of powder. Once this stage has been reached granule growth begins and the resulting granules will resemble that of a **wet-agglomerate**. As this study focuses primarily on the dispersion and distribution of a binder during the nucleation stage of the granulation process, all experiments have been conducted up to and excluding the point where wet agglomerates are formed. More details about how these structures were identified are discussed later.

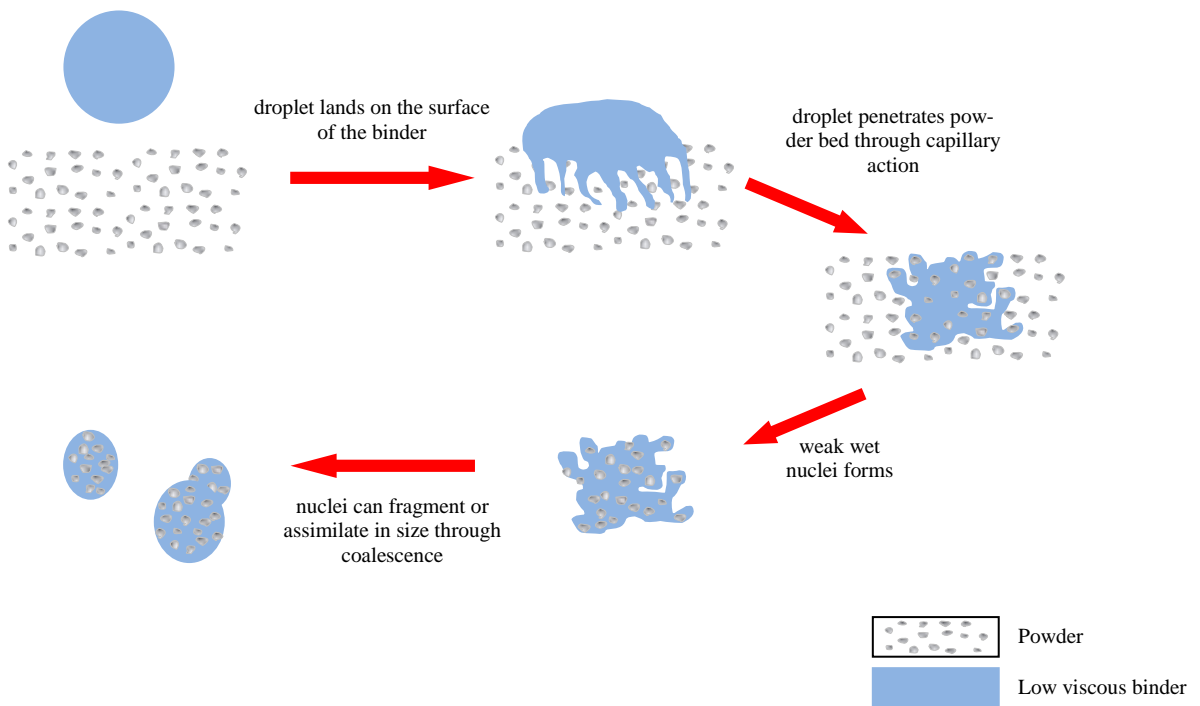


Figure 5.1. Granulation mechanism for low viscous binders.

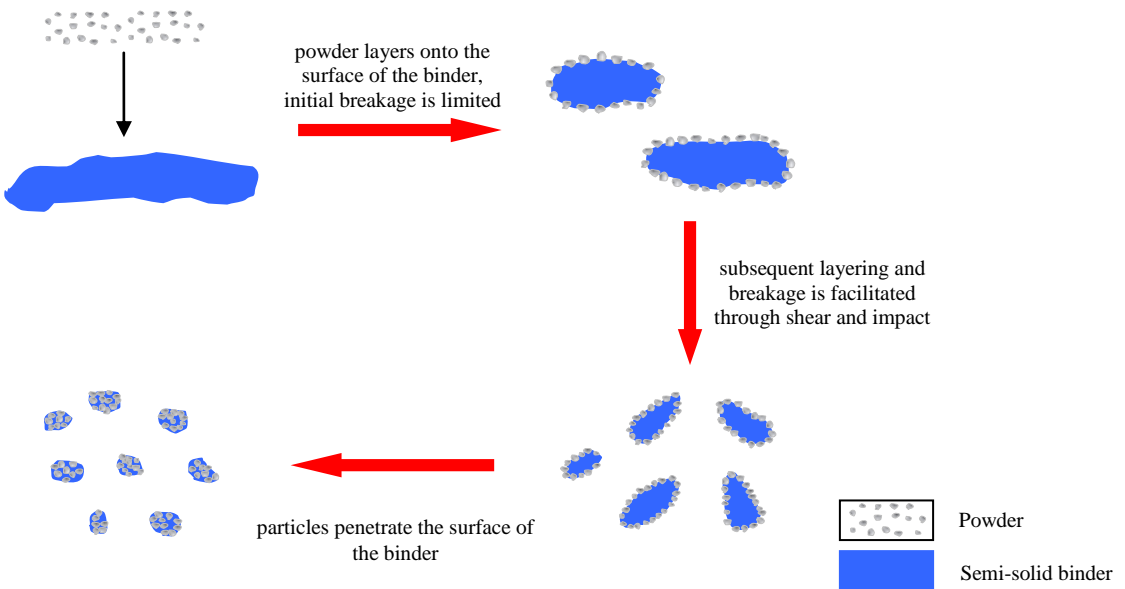


Figure 5.2. Hypothesis proposed for the layering and fragmentation of paste fragments in a moving powder bed.

5.3 Quantifying the adhesion between the powder and binder

One of the properties that is likely to influence the rate at which powder layers onto the surface of the binder is the adhesive force between them. A convenient method of quantifying the adhesion between the powder and binder is to bring them into contact under controlled conditions. In order to achieve this, “binder particles” of a uniform size need to be produced. This ensures each binder particle has the same surface area to begin with. Ideally, if the binder particle is cylindrical, it can then be made to roll over the surface of a loose powder bed and thereby, mimic powder layering at zero shear (no mixing).

The first stage of this study involved devising a method for producing binder particles or fragments of a uniform size and shape. This was achieved using the setup shown in Figure 5.3. A Watson Marlow 501u peristaltic pump equipped with an 8 mm ID silicone tube was used to pump the semi-solid binder. One end of the silicone tubing was attached to the barrel of a 20 ml syringe, which has a needle hub that is 2 mm in width. This acts as a die through which the semi-solid binder can be extruded. The binder was extruded on to microscope glass slides that have a width of 2.5 cm. The product is cy-

lindrical in shape, and is 2.5 cm long with a diameter of 2 mm. Each strand has a mass of approximately $0.110 \text{ g} \pm 0.001\text{g}$.

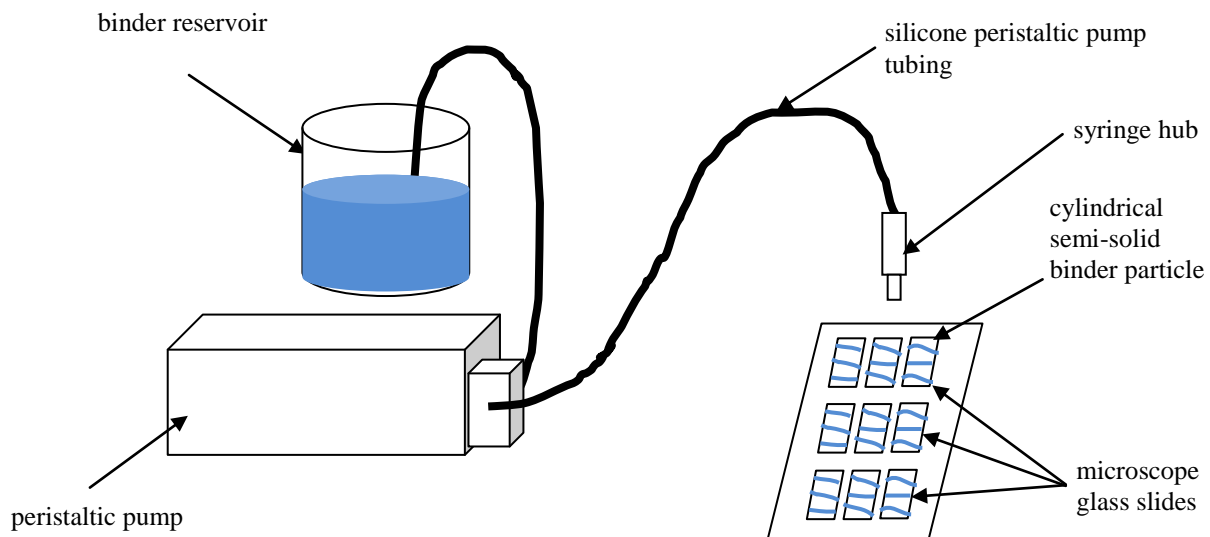


Figure 5.3. Schematic representation of the apparatus used for preparing cylindrical semi-solid binder particles of a uniform shape and size.

The cylindrical strands on the microscope glass slides were frozen at 0°C for 1 hour. Cooling them down to this temperature makes the paste less flowable and helps it retain its shape prior to being immersed in to a pool of liquid nitrogen (-196°C). At cryogenic temperatures, the cylindrical strands separate from the glass slides. Each binder particle was then placed on to the surface of a loose powder bed on a Petri dish and allowed to equilibrate to room temperature (25°C), prior to being rolled over the surface of the said powder bed (Figure 5.4). Rolling was carried out by tilting the Petri dish to an angle of 50° .

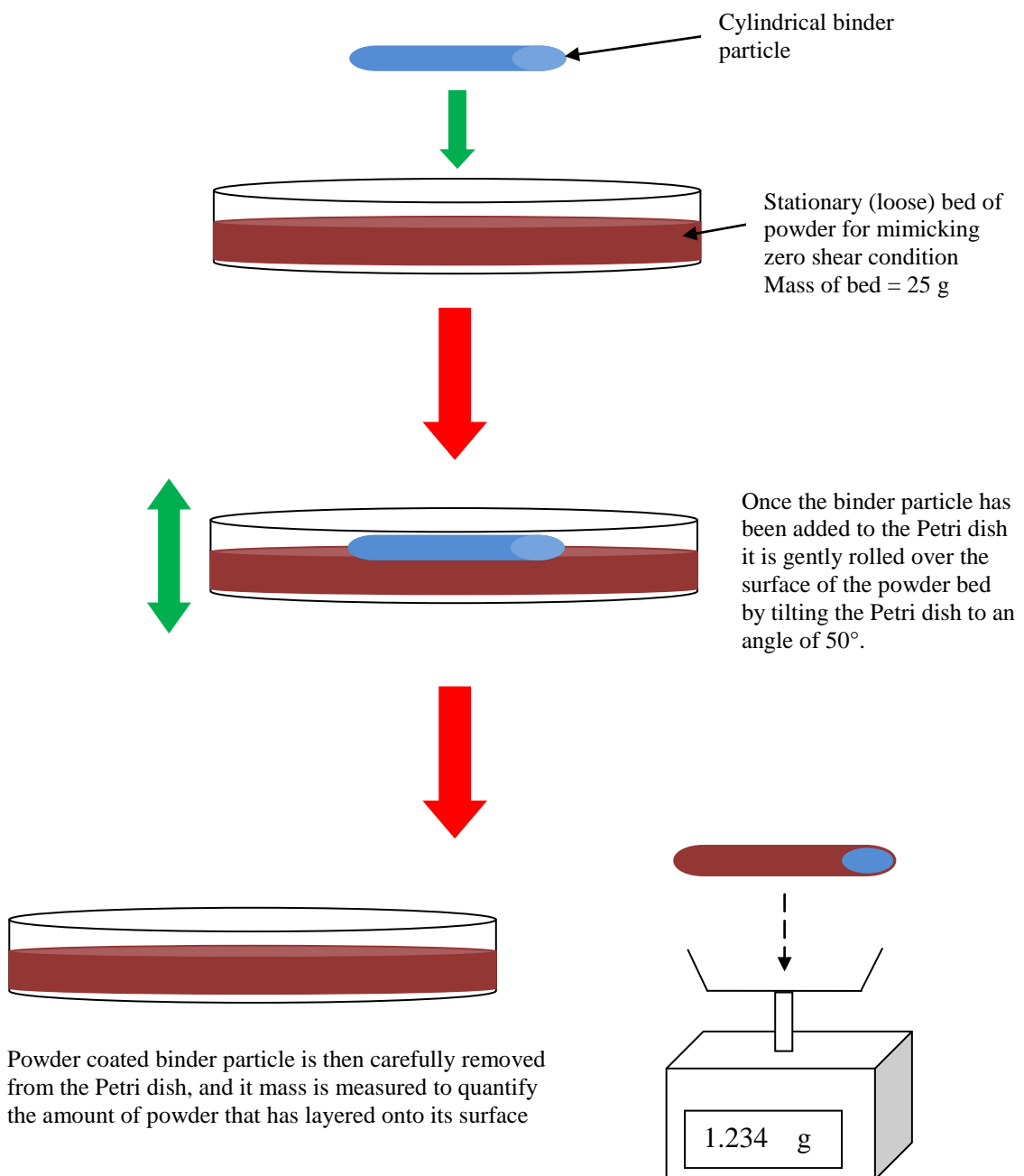


Figure 5.4. Schematic representation of the technique for determining the mass of powder that has layered at zero shear.

Micrographs of the cylindrical strands of binder (after they have been rolled over the surface of a loose bed of powder) demonstrate the various extents to which different powders are able to coat the surface of a strand of binder (Figure 5.5). Figure 5.6 shows the change in the mass of the PCBPs after being rolled over a loose bed of powder.

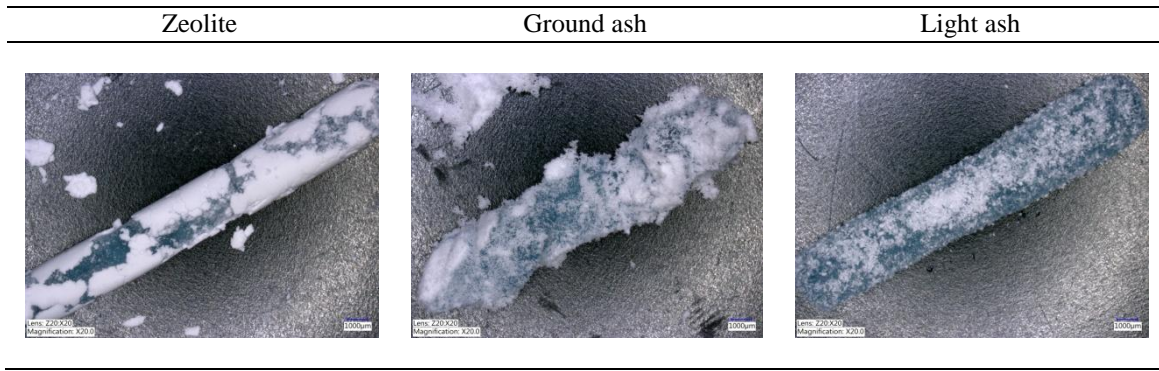


Figure 5.5. Micrographs of the cylindrical strands after coating with primary powders.

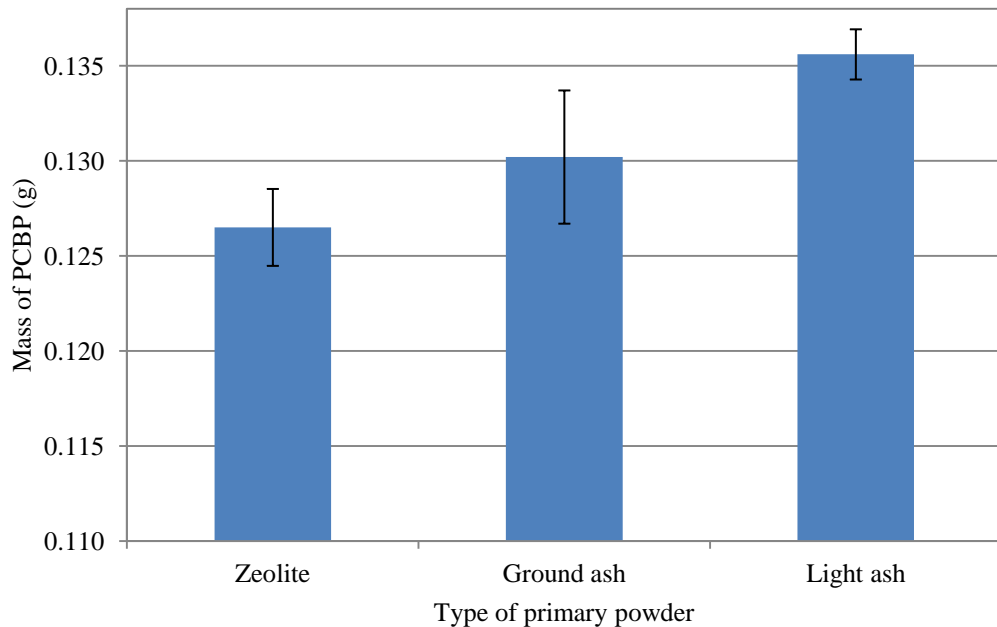


Figure 5.6. Mass of the PCBPs after coating with primary powders.

5.4 Granulation methodology

Granulation experiments were conducted in a 100 ml mixer (refer to Section 3.2 for more details about the granulator). A smaller mixer was chosen in order to conduct experiments at a lower tip speed ($v_{max} = 2.5$ m/s), which enables binder dispersion to be observed and understood in more detail. Experiments were conducted at a lower impeller speed of 300 rpm and at a maximum impeller speed of 600 rpm. All other conditions were identical to the granulation technique outlined in Section 4.5. As before, the liquid to solids ratio was kept constant at 0.5 (25 g of powder was granulated using 12.5 g of

binder). The binder particles were prepared using the technique outlined in Section 5.3; 110 strands were produced for each granulation experiment (to give a total mass of 12.5 g). The total batch size is 37.5 g. Experiments were conducted for 180 s (as opposed to 75 s in the previous study discussed in Chapter 4), as the maximum tip speed of this mixer is lower than that of the 10 L Roto Junior high shear mixer. Mixing time was recorded using a stopwatch to the nearest second.

25 g of ground ash and zeolite have a fill level of approximately 50%, whilst light ash, which has a higher bulk density, has a fill level of approximately 40%. The typical fill level when operating larger-scale granulators compares to this (Oka et al., 2015). At both speeds, the vessel operates in the roping regime. At speeds lower than 300 rpm, the mixer transitions to the bumping regime. Most industrial operations use aggressive conditions when granulating laundry powder (Mort et al., 2001), therefore binder breakage when operating in the bumping regime was not investigated.

Once added to the powder bed, strands were allowed to reach room temperature, before the mixer was operated. For all experiments, the temperature was within the range 20–25°C. After granulation, the PCBPs were carefully separated (using a 200 µm sieve - by tapping gently) and were frozen using liquid nitrogen. The mass of the PCBPs was then weighed. The rate of layering (i.e. percentage increase in mass of 12.5g of binder with time) of the three different materials was monitored. After recording the mass, the size distributions of the cryogenically frozen PCBPs were also measured using the Camsizer P4. Each experiment was conducted using a fresh batch of raw materials, as starting and stopping the granulation process, together with prolonged handling of the PCBPs could influence results.

A test was also performed to determine the viscosity of the binder after it was frozen, to ensure the freeze-thaw cycle does not influence its rheological properties. 33 ml of binder was immersed into a pool of liquid nitrogen and left to freeze into a solid for 10 mins. The binder was then removed from the liquid nitrogen and allowed to thaw, at 25°C for an hour, prior to conducting further tests. Viscosity measurements taken before and after the freeze-thaw cycle show a very similar profile (Figure 5.7).

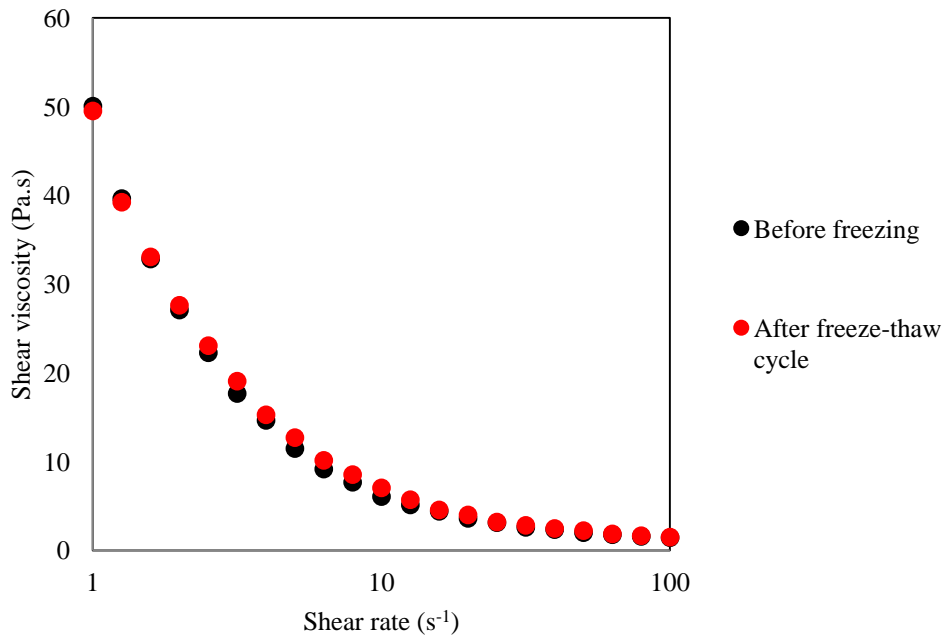


Figure 5.7. Viscosity measurement at 25°C before and after a freeze-thaw cycle.

5.5 Determining the constitution of a PCBP

As discussed in Section 5.2, with time the system progresses from the nucleation regime into the growth regime. All PCBPs in the system get destroyed and the resulting mixture resembles that of a wet-agglomerate; once it transitions into the growth regime. Breakage and dispersion of the PCBPs occurs up until the mixture resembles a crumb-like state. The different regimes can be identified by observing changes in the internal structure of the granules using XRT.

A μ CT 35 X-ray scanner by SCANCO Medical was used to scan samples of the PCBPs (refer to Section 3.18 for more details about the equipment). Final contrast between the air, semi-solid paste and powder in a sample are generally influenced by the grey values that are assigned to the said components. For each slice, a histogram can be generated, and it indicates how many pixels in the image have the same grey value. The digitisation will also influence the maximum grey-value of the image. As the scan data were converted into 16-bit images, the grey scale ranges from 0 to 65536. Therefore, each pixel in the image can take a value from 0 to 65536. This enables different elements of a PCBP to be differentiated. As air is the least dense material present in any sample, it has

the lowest grey-scale and appears black on a scan. In this study, the primary purpose of the X-ray tomography was to track the ingress of each powder into the binder fragment. Therefore, being able to distinguish between the binder and the powder is crucial. XRT proved to be a method that is capable of distinguishing between the semi-solid binder and the powders, and a convenient method of tracking the ingress of a powder into a lump of binder.

For the three powders, two scans were done, the first scan was on a loose powder bed and the second was on a compact (a 3 kN compression force was applied to 5 g of the material in a 30 mm die, using the Instron 3367 tensile test machine). X-ray scans of all raw materials are presented in Figure 5.8, along with their mean grey values. Within a granule or PCBP, the porosity of the powder rich zones is likely to be between that of the loose powder bed and a compact. A compact of the primary powder was made using a compression load of 3kN, to quantify the impact of porosity on the mean grey value. The compaction force within a high shear mixer will not exceed 3 kN, and the grey value is likely to be much closer to that of a loosely packed powder bed (as compression forces are very low during wet massing). A force of 3 kN corresponds to a stress of approximately 1 MPa.

Chan et al. (2013) determined the normal components of the stress acting on the blade, as a result of the impacting granules for the 10 L vertical shaft Roto Junior high shear mixer used in this study. An expression (Equation 5.1) was developed to correlate the granule bed properties and impeller geometries, where ρ_b is the bulk density of the granule bed, $H_{g,r}$ is the height of the granule bed, v_{rel} is the relative velocity of the granule bed, θ_I is the blade angle and h_I is the blade inclined height. The subscripts I and g denote the impeller and the granule bed respectively. A maximum value ($\sigma_{max,r}$) for the stress acting on the blade for the 100 ml mini-mixer was found using Equation 5.1. The v_{rel} was replaced with the maximum tip speed, $H_{g,r}$ was replaced with the height of the mixing bowl, and ρ_b was replaced with the true density of the primary particles in order to obtain a maximum value ($\sigma_{max,r}$) of the stress acting on the blades. The calculated approximation for the maximum stress acting on the blade is far less than 1 MPa (Equation 5.2).

$$\sigma_{i(r)} = \frac{\rho_b H_{g,r} v_{rel}^2 (1 - \cos\theta_l)}{h_l} \quad \text{Equation 5.1}$$

$$\sigma_{max(r)} = \frac{2250 \times 0.045 \times 2.52 \times (1 - \cos 45)}{0.024} = 3113 \text{ Pa} \quad \text{Equation 5.2}$$

The two scans enabled the effect of voidage (air spaces) on the grey value to be quantified. The three different powders, **in contrast with the binder**, show different grey values. It is therefore, reasonable to state that the three different materials can be easily identified, as the grey value of the binder is 4017, whilst zeolite ranges from 5464-6189, ground ash ranges from 4307-5369, and light ash ranges from 4583-5122 (Figure 5.8). Even though light ash and ground ash are chemically identical, they have different grey values, as light ash always produces a more porous structure when compacted under the same load. Also note that each PCBP scanned in this study contains only one primary powder.

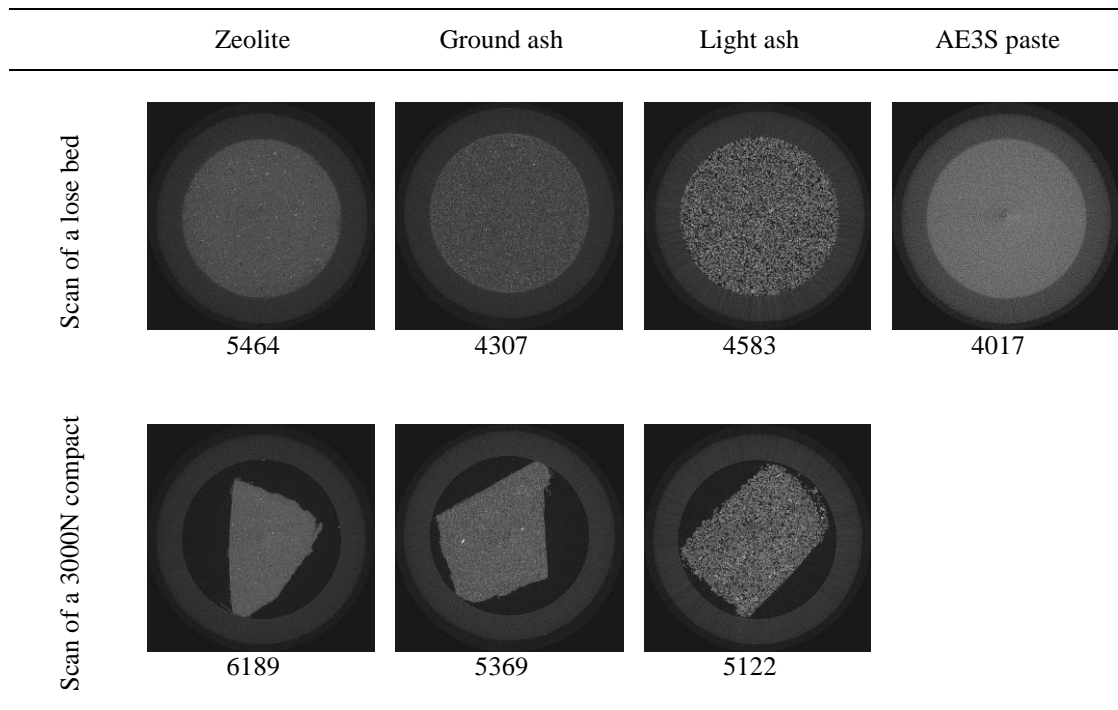


Figure 5.8. X-ray scans of the raw materials. Two mean grey values have been reported for three powders - one for a loose powder bed and another for a compact made with a 3 kN compression force.

XRT images (Figure 5.9) of the granules that were taken at different time points suggest layering is the main mechanism of powder assimilation during binder dispersion. The changes in the structure of the PCBPs with time are discussed in more detail in Section 5.9.

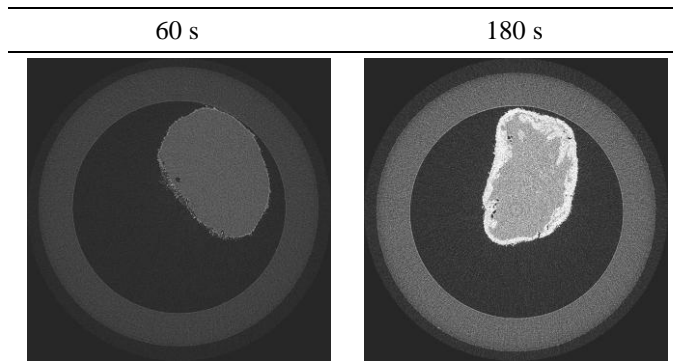


Figure 5.9. XRT images reveal layering is the main mechanism for powder assimilation on the surface of a binder particle (zeolite at 300 rpm).

5.6 Monitoring the rate of powder layering

The change in the mass of the PCBPs, as a percentage of the mass of the original binder was determined (Figure 5.10 and Figure 5.11). At both impeller speeds the mass of the PCBPs increases steadily at first, and after some time reaches an asymptote. The initial increase in the mass is linear and so the data suggest that layering of the powder on to the binder occurs steadily (at a constant rate) to begin with.

At both impeller speeds (300 and 600 rpm - Figure 5.10 and Figure 5.11 respectively), it is evident that light ash layers onto the binder more rapidly, whilst zeolite exhibits the poorest rate of layering. As light ash particles are larger than zeolite particles, they have a smaller surface area. Therefore, a larger mass of light ash is required to saturate all available binder surfaces. Zeolite, on the other hand, is a cohesive powder that consists of very fine particles that are more circular (refer to Section 3.8 for SEM images), thus explaining its poorer rate of layering compared to light and ground ash. In other words, larger particles which are rougher are more likely to penetrate the surface of a lump of binder, whilst smaller ones are better at covering the surface of the binder, but their penetration is limited (Figure 5.12).

At 600 rpm (Figure 5.11), for the ground ash system, the product resembles that of a wet-agglomerate after 90 s of wet massing, and for light ash the same phenomenon is observed after 15 s of wet massing. X-ray tomography was used to confirm this (Figure 5.13). As discussed earlier in the introduction to this chapter, the nucleation step involves breaking and dispersing fragments of the binder into the powder. This breakage and dispersion will mainly occur at the beginning of the powdery regime until the end of the crumb regime. Once the system has transitioned into the wet-agglomerate regime, PCBPs are no longer present in the mixture i.e. nucleation has ended. Therefore the mass of the PCBPs have only been recorded up to 90 s for ground ash, and up to 15 s for light ash.

At a higher impeller speed (600 rpm - Figure 5.11), there does not appear to be a significant increase in the final mass of the PCBPs (when compared to the trial done at 300 rpm - Figure 5.10), instead the time taken to reach the asymptote or steady state is shortened for all three powders, and for light and ground ash the lifespan of the PCBPs in the granulator are shortened significantly.

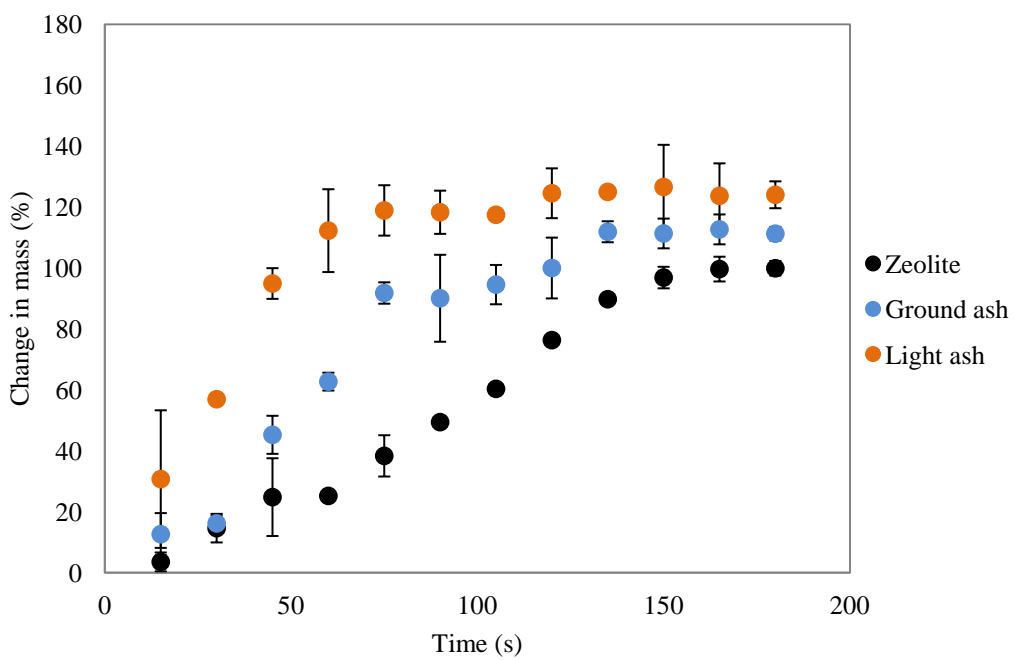


Figure 5.10. Relative change in the mass of the PCBPs as a percentage of the mass of the original binder at 300 rpm.

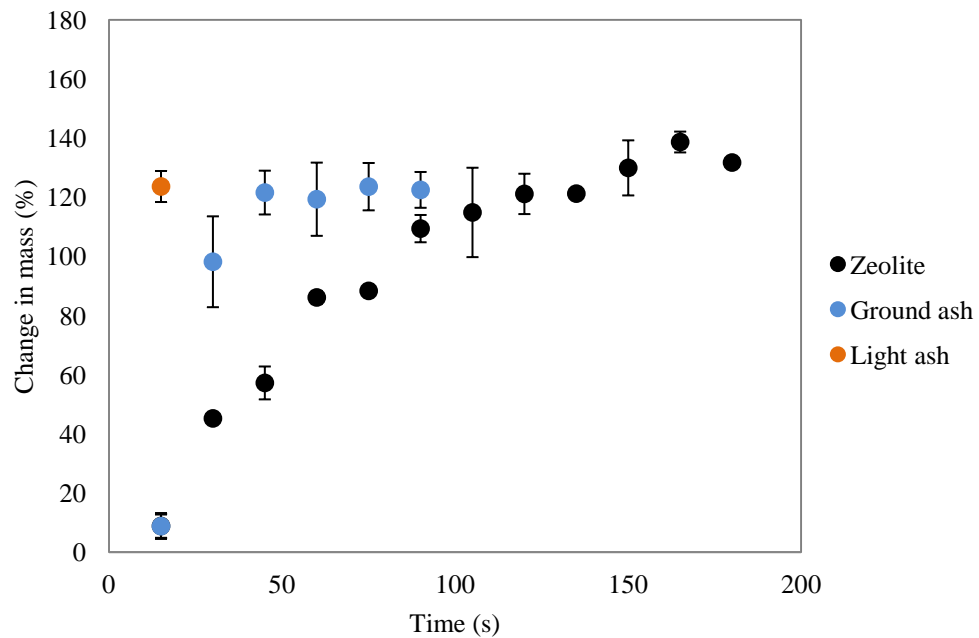


Figure 5.11. Relative change in the mass of the PCBPs as a percentage of the mass of the original binder at 600 rpm.



Figure 5.12. Layering of particles of different sizes on the surface of a binder fragment.

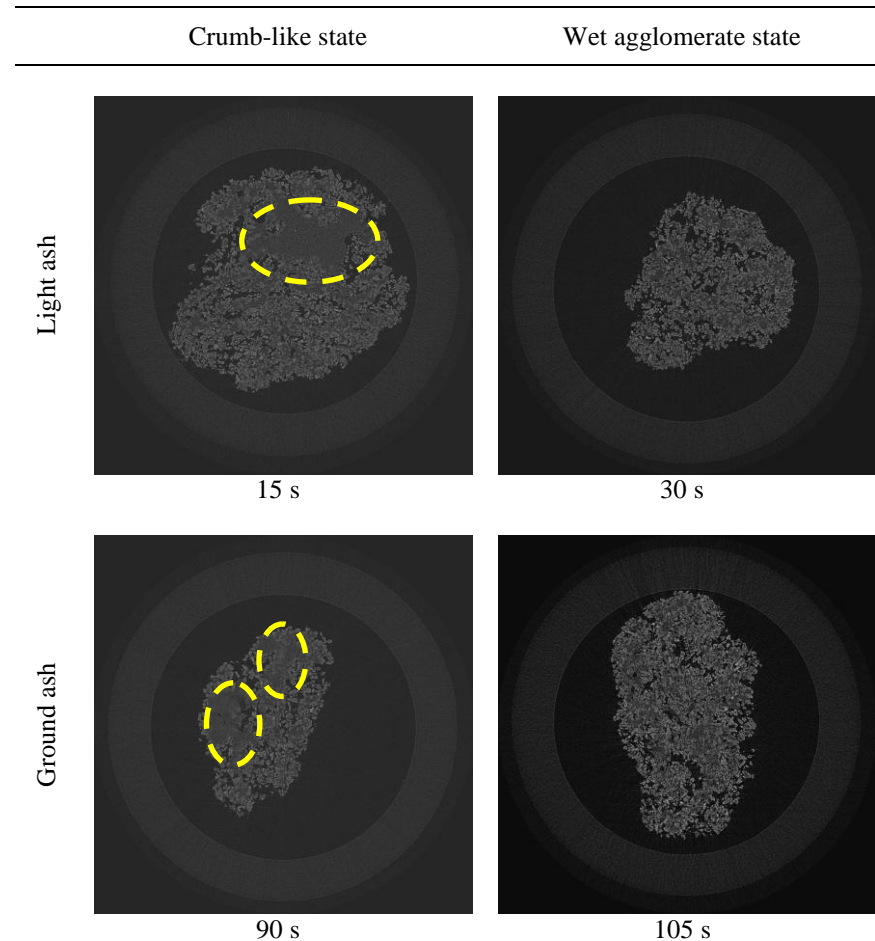


Figure 5.13. Changes in the internal makeup of the granule during transition from the nucleation to the wet-agglomerate regime. Zones within the granule that are rich in binder have been highlighted (yellow ovals).

For all materials, at both impeller speeds, the maximum percentage increase in the mass does not exceed the range 120-140% (Figure 5.10 & Figure 5.11). After this maximum is reached either the mixture transitions into the wet-agglomerate regime at higher impeller speeds for certain powders (light and ground ash), or remains in the crumb regime with no further increase in the mass at lower impeller speeds. This suggests that there is a finite volume of powder the binder can accommodate during the initial layering process. After the binder has gathered this amount of powder, depending on the amount of energy within the system, it either progresses further into another granulation regime or remains in the crumb state.

To verify this hypothesis, the volume fraction of the powder in the PCBPs was determined. The volume fraction of the solids in the PCBP was calculated using Equation

6.4. It was assumed that the individual powder particles were completely engulfed by the binder in a PCBP. Therefore the true density of the powders was used (instead of the bulk density) when determining the volume fraction of the solids. The rate of layering reaches an asymptote when the volume fraction is between 0.30 – 0.35 (Figure 5.14 - Figure 5.15). This indicates the existence of a critical volume fraction of powder that the binder is able to accommodate, after which layering stops.

$$\text{Volume fraction, } \phi = \frac{(M_{F(\text{PCBP})} - M_{I(\text{PCBP})})/\rho_s}{((M_{F(\text{PCBP})} - M_{I(\text{PCBP})})/\rho_s) + M_{I(\text{AE3S})}/\rho_l} \quad \text{Equation 5.3}$$

where:

ρ_s – powder density (g/cm^3)

ρ_l – liquid density (g/cm^3)

M – mass (g)

subscript F – final

subscript I – initial

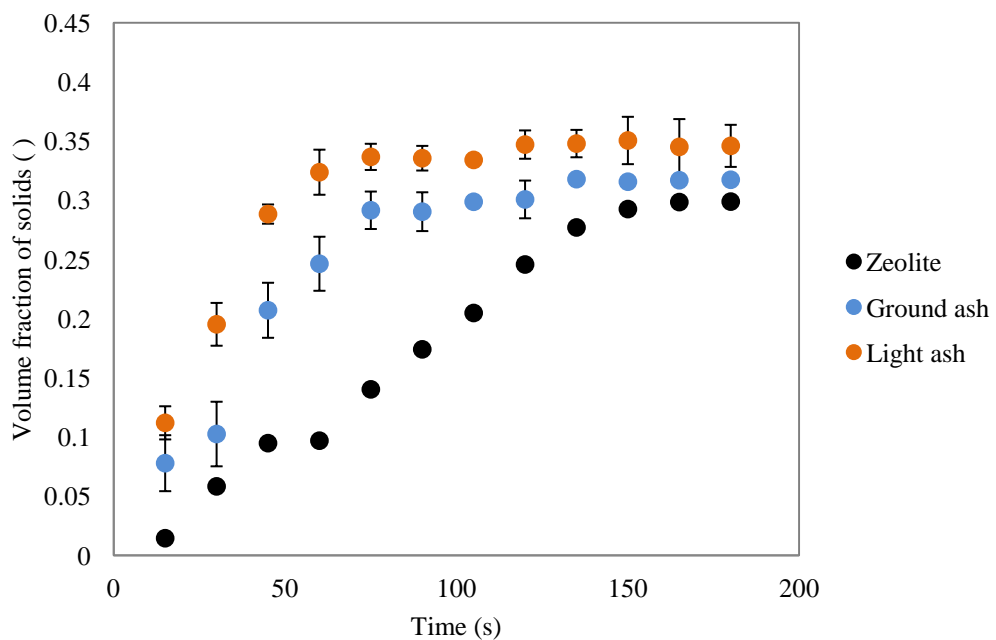


Figure 5.14. Volume fraction of solids in the binder with time at 300 rpm.

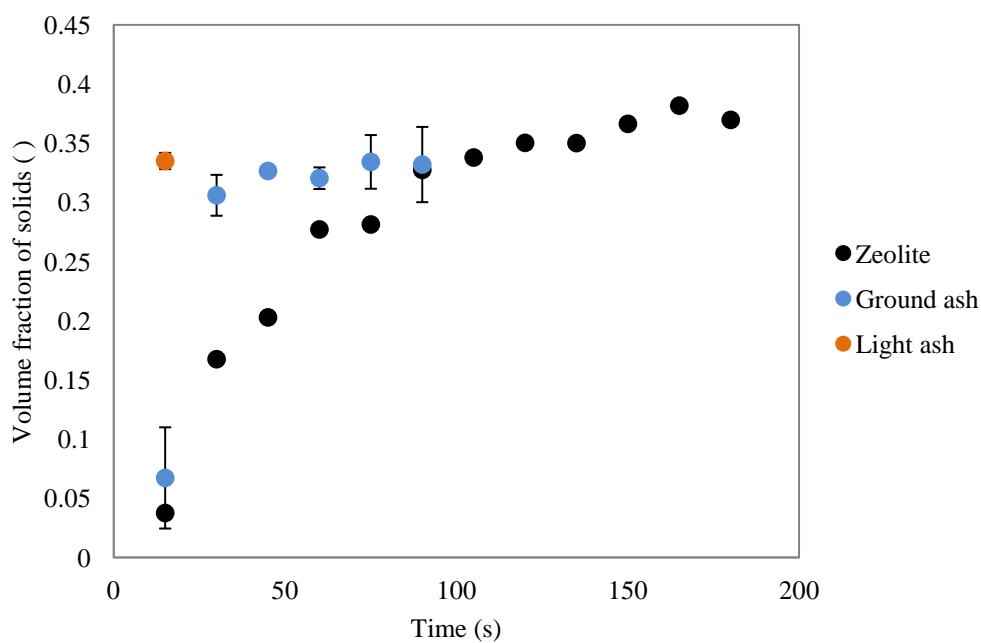


Figure 5.15. Volume fraction of solids in the binder with time at 600 rpm.

Another method of assessing the overall efficiency of the layering process is to determine the mass fraction of the primary powder that has been used up during wet massing (Figure 5.16 & Figure 5.17). At lower impeller speeds, all three powder systems have a significant quantity of unused primary powder. To reiterate, it is suggested that layering is the dominant mechanism that consumes powder during nucleation. At lower impeller speeds, most of the binder is still present in its unused form in the core of a PCBP (again XRT was used to confirm this and the results will be discussed later in this chapter). At higher impeller speeds, for light and ground ash systems all of the powder gets used up eventually and the system progresses into the wet-agglomerate regime. As discussed in Section 2.2, the higher impeller speed may help to squeeze out binder from within the agglomerates, thereby facilitating the layering of more primary particles. As a result, all the primary powder gets assimilated into the structure of the agglomerate.

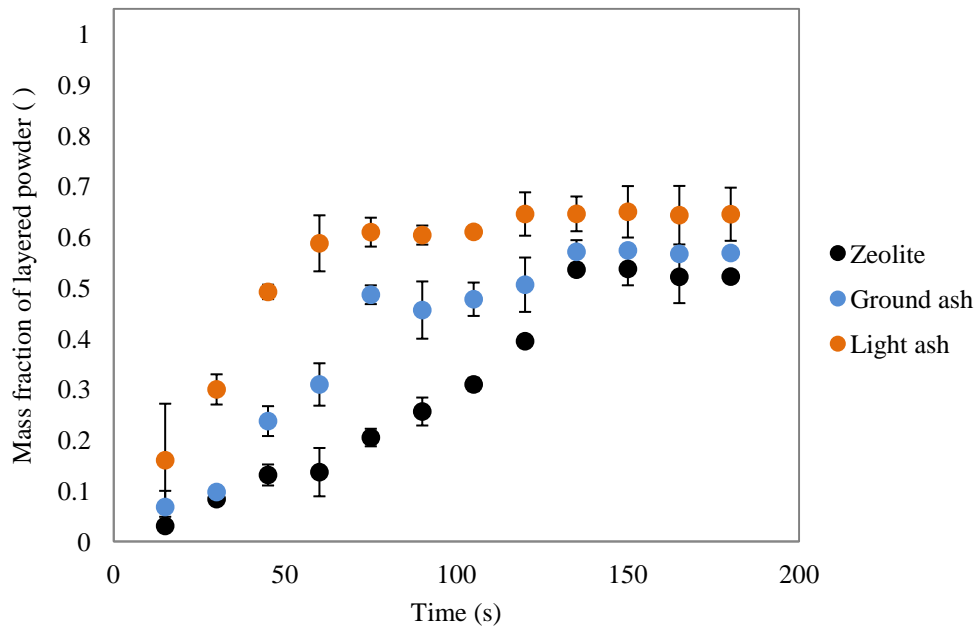


Figure 5.16. Mass fraction of the primary powder that has been used at 300 rpm.

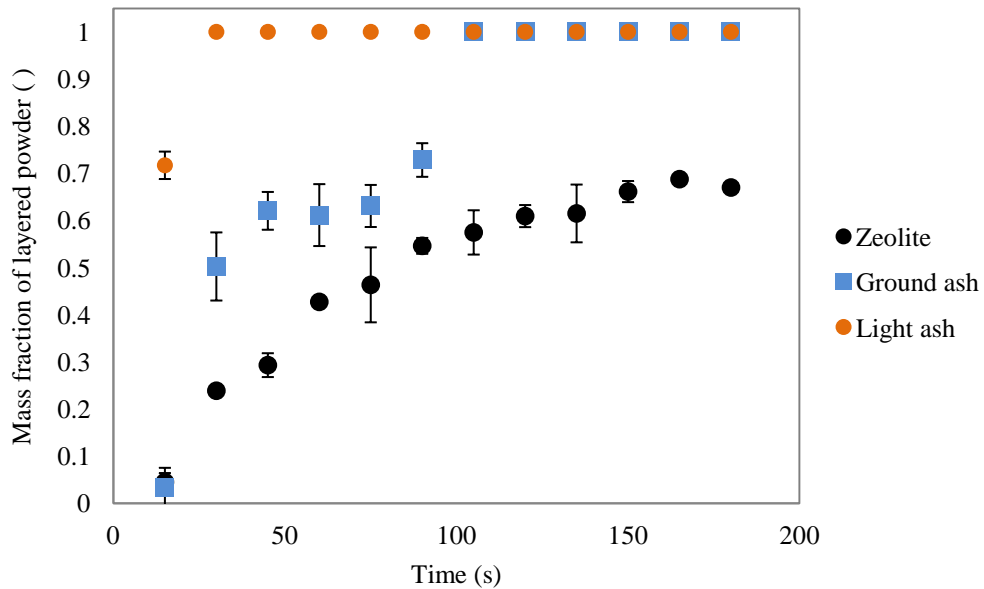


Figure 5.17. Mass fraction of the primary powder that has been used at 600 rpm.

5.7 Binder size reduction and breakage patterns

It is necessary to determine the initial size distribution of the binder particles used in this study. The initial size of the binder particles are well defined i.e. the starting materials are 2.5 cm long cylinders with a diameter of 2 mm. However, when compared with

the measurements obtained from the Camsizer, there is a significant difference (Figure 5.18). An equivalent diameter is defined by the Camsizer based on the area of particle projection (Equation 5.4); therefore the measured values are somewhat different from the predefined values. It is known that the specific orientation of the cylindrical strands of binder when presented to the Camsizer will influence the magnitude of the projected area that is determined by the device (Brown et al., 2005).

$$x_{area} = \sqrt{\frac{4A}{\pi}} \quad \text{Equation 5.4}$$

where:

A – projected area (mm^2)

x_{area} – diameter of the area equivalent circle (mm)

Based on the dimensions of the cylindrical binder particles, the maximum size the Camsizer should detect must not exceed 8 mm, when $L = 25 \text{ mm}$, $D = 2 \text{ mm}$ (Equation 5.5). From Figure 5.18, it is evident that the Camsizer detects area equivalent particle diameters between 3.5 – 7.5 mm.

$$x_{area} = \left(\frac{4}{\pi} LD\right)^{0.5} = \left(\frac{4}{\pi} \times 25 \times 2\right)^{0.5} = 7.97 \text{ mm} \quad \text{Equation 5.5}$$

where:

L – length of the cylindrical strand of binder (mm)

D – diameter of the cylindrical strand of binder (mm)

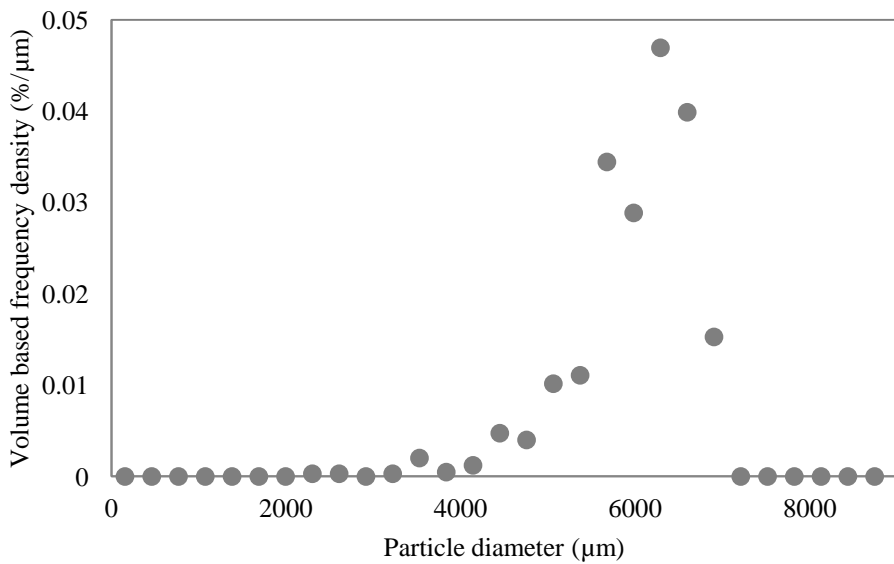


Figure 5.18. Size distribution of the binder particles measured using the Camsizer, $D_{v4,3} = 5817 \mu\text{m}$.

The size distribution of the PCBPs was measured as a function of time (refer to Section 3.6 for more details about the measurement techniques). The volume based mean diameter ($D_{v4,3}$) was determined from the size distributions. $D_{v4,3}$ was chosen as it is more sensitive to the presence of larger particles and less sensitive to the fines shed from the PCBPs. At 300 rpm (Figure 5.19), it is evident that the mean PCBP size increases, from 0 s to 15 s, for all three primary powders. This could be due to the binder particles adhering to each other at very short wet massing times, when binder dispersion process is at its early stages. At a high impeller speed of 600 rpm (Figure 5.20), an increase in the mean size is not observed at 15 s.

After 15 s, however, it is apparent that the mean particle size gradually decreases with time until 100 s (Figure 5.19 - Figure 5.20). Note that when the size of the PCBPs levels off with time, so does the change in the mass with time (Figure 5.10 - Figure 5.11). As discussed earlier, the binder may have gathered a critical volume fraction of powder and the PCBP will not undergo further layering. The fragmentation process for light ash and ground ash is more rapid compared to zeolite (at both speeds). The zeolite system has the largest mean PCBP diameter at 60 s, compared to light and ground ash. Zeolite powder is more likely to coat the binder quicker than any other powder, due to its finer size. A thin layer will cover the binder fragment, which will then gather further layers of zeolite that may protect the binder from deformation. Light and ground ash

particles have rougher surfaces with needle like particle morphology and are therefore, more likely to break and penetrate the surface of the coated binder particles. Further evidence for this was gathered from optical microscopy, which will be discussed later. From Figure 5.19 - Figure 5.20, it is apparent that after 180 s, there are a larger number of smaller light and ground ash PCBPs, whilst zeolite has the largest mean PCBP diameter. At a higher impeller speed (compare Figure 5.20 with Figure 5.19), it is evident the fragmentation process is more rapid. The final size of the PCBPs is also smaller. The higher stresses (energy) within the system may facilitate more breakage of the powder saturated PCBPs, at higher impeller speeds.

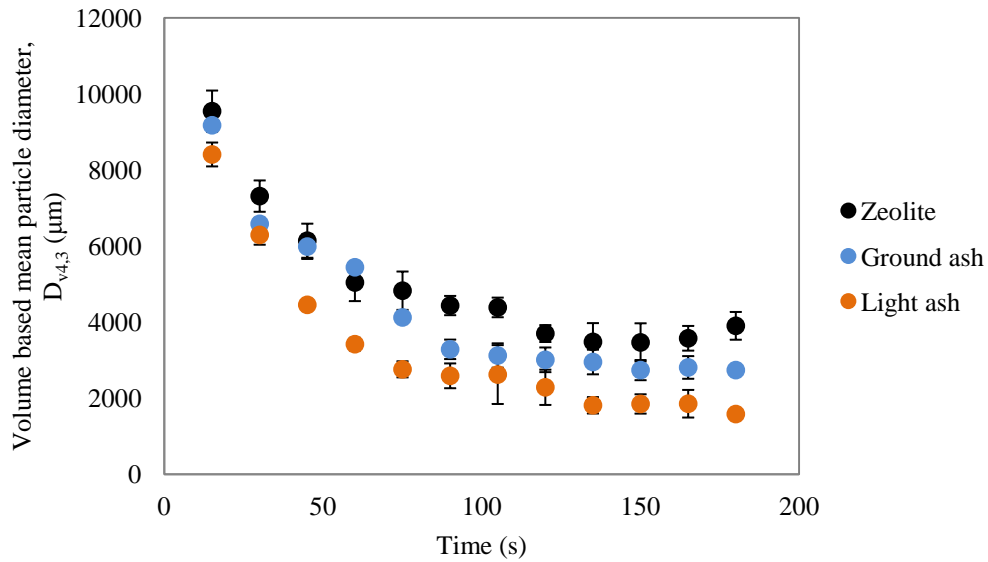


Figure 5.19. Change in the mean diameter ($D_{v4,3}$) of the PCBPs with time at 300 rpm.

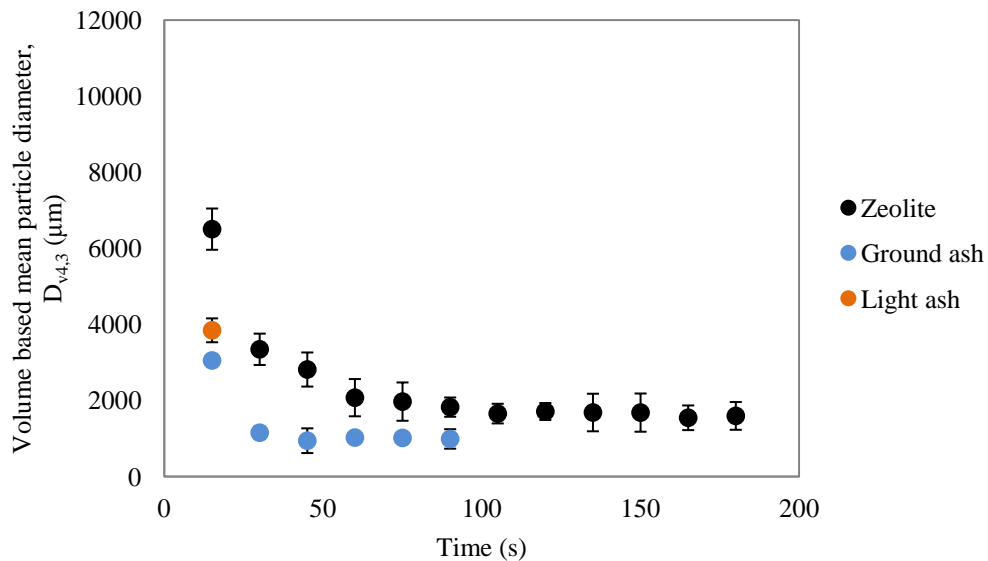


Figure 5.20. Change in the mean diameter ($D_{v4,3}$) of the PCBPs with time at 600 rpm.

At both speeds, an increase in the mass of the powder coated binder particles is observed with time (Figure 5.10 & Figure 5.11), whilst their size decreases (Figure 5.19 & Figure 5.20). This suggests that PCBPs assimilate in mass due to the exposure of fresh, uncoated surfaces of binder, as a result of breakage.

5.8 Qualitative analysis of PCBP surface attributes

Surface features of the PCBPs were analysed optically using a VHX-5000 Digital Microscope (for more details about the equipment refer to Section 3.7). A qualitative analysis of the breakage patterns was also done as a part of this study. Figure 5.21 provides micrographs of the PCBPs at different time points, for the three different powder systems, at the lower impeller speed of 300 rpm. For the zeolite system, the layering of powder onto the surface of the binder appears to be rapid with time. Zeolite coats the binder quicker than the other powders, due to its finer size and high cohesivity. After 60 s, it is evident that the binder is completely layered with powder. It can also be seen that powder has a tendency to adhere to zones that have already been coated. A thin layer will cover the binder fragment, which will then gather more layers of zeolite that may protect it from further deformation. This could be due to the cohesive nature of zeolite, causing the fine particles to adhere to material that is already on the surface of the binder.

It has been established that the PCBPs undergo breakage gradually. It is therefore of interest to understand how this breakage may occur. Breakage patterns of solids can be described as brittle, semi-brittle or ductile. The brittle breakage refers to solids that fracture without showing any noticeable plastic deformation. In contrast, ductile breakage shows considerable plastic deformation of the parent PCBP. Semi brittle fractures refers to some degree of brittle fracture taking place at the boundaries of a region of (limited) plastic deformation (Salman et al., 2007). For the zeolite system, after 60 s, deformation is likely to be mainly plastic and may become progressively semi-ductile, as the PCBPs are smaller, but still elongated, and retain a more regular oval shape, post-breakage (see zeolite at 180 s in Figure 5.21).

In the case of light ash, the breakage of the fragments is much more rapid (Figure 5.21). A closer inspection of the surface of the granules indicates the coating is thinner, in comparison to zeolite. The coating also appears to be an even monolayer. This could be attributed to the needle shaped light ash crystals, which are able penetrate the surface of the binder and probe their way into the core of the PCBP more rapidly, thus preventing the aggregation of powder on the surface. The larger particle size also makes the powder less cohesive. The PCBP appears to reach the brittle state after 2 mins of wet mass-

ing and this is evident from the presence of cracks/flaws on its surface (Figure 5.22). It is believed that this facilitates the rapid reduction in the size of the binder fragments with time.

The behaviour of the ground ash mixture is somewhat similar to that of light ash. This is an indication that surface properties and particle morphology both play an important role in binder dispersion. At a higher speed of 600 rpm, the fragmentation process is very similar, but takes place on a much shorter time scale. Conclusions drawn from visually inspecting the micrographs are in agreement with the mass and size change trends that were discussed earlier.

It is hypothesised that as the solid fraction within the binder fragment increases, its deformability reduces. Some indentation experiments were conducted to investigate this further (discussed in Section 5.10).

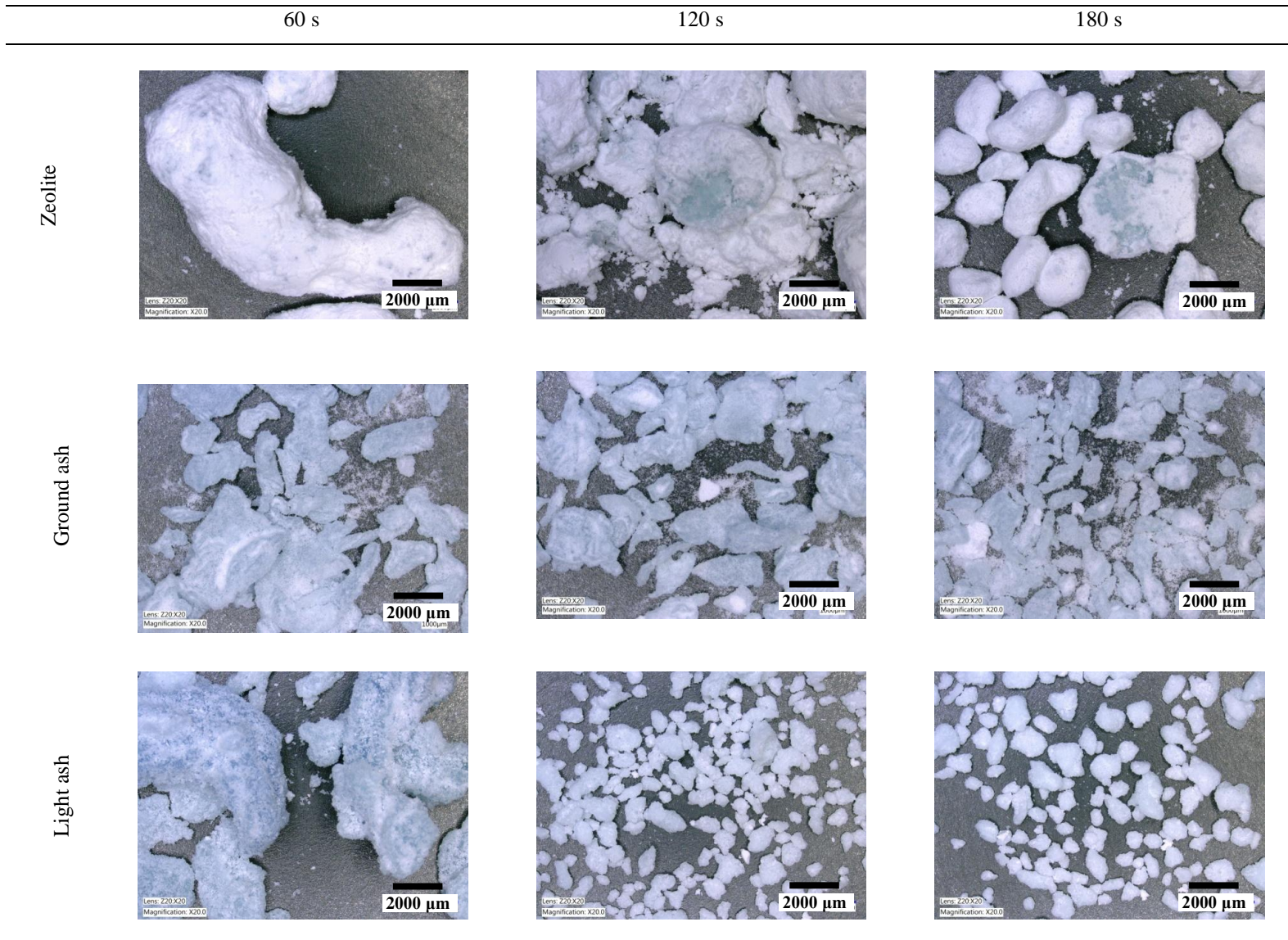


Figure 5.21. Micrographs of the PCBPs at different time intervals at 300 rpm.

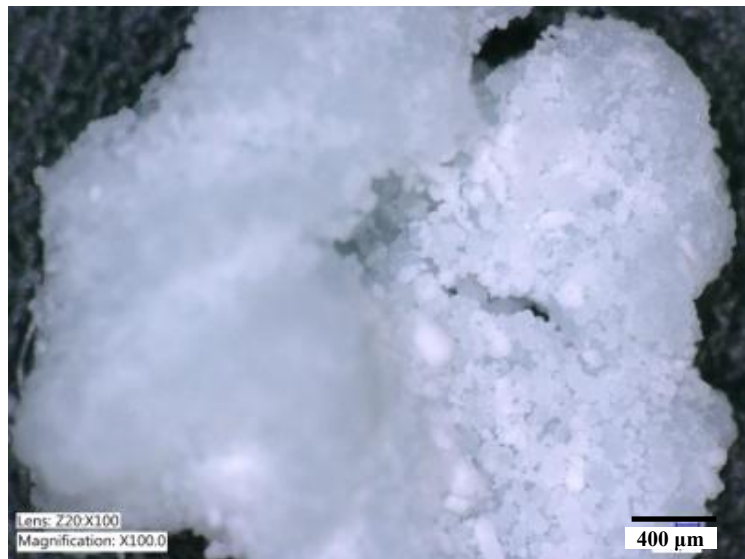


Figure 5.22. Surface properties of the light ash PCBPs at 300 rpm.

5.9 Changes in the internal makeup of a PCBPs with time

X-ray images of the PCBPs also reveal that the powder layers gradually onto the surface of the binder at 300 rpm (Figure 5.23), and at a higher impeller speed of 600 rpm, again a similar pattern is observed, but on a much shorter time scale. By visually inspecting the slices obtained from XRT, it is clear to see that the mass fraction of the powder in a PCBPs increases with time. For zeolite, the layering of the powder is mainly on the surface of the PCBPs. There appears to be limited ingress of the powder into the core of the binder, however the thickness of the layer of powder surrounding the binder increases with time. For ground and light ash, the ingress of powder into the core of the binder is much more evident and the powder layering process appears to be more rapid. This observation is in agreement with the results reported earlier that show a more rapid increase in the volume fraction of powder in a PCBPs (Figure 5.14) and a reduction in the size of the PCBPs (Figure 5.19) for the carbonates in comparison to zeolite.

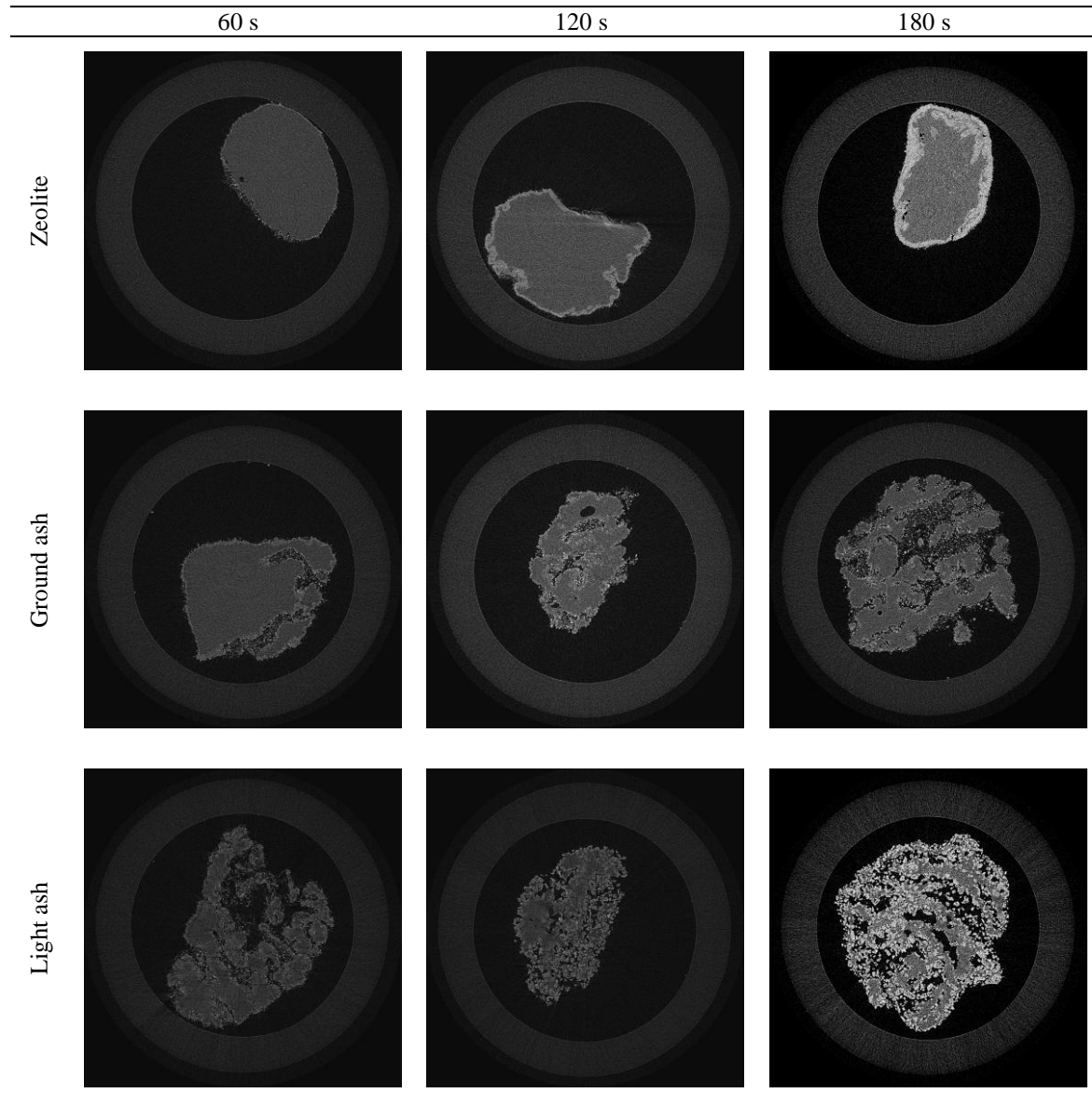


Figure 5.23. Changes in the structure of PCBPs containing zeolite with time at 300 rpm.

5.10 Changes in the mechanical properties of the PCBPs with time

Section 5.8 provides limited qualitative evidence for the changes in the mechanical properties of the PCBP with time, based on the visible presence of surface flaws. As the mass fraction of the powder contained within the binder fragments starts to increase, there is a corresponding increase in the visible presence of cracks on the surface of the PCBP (Figure 5.22). This seems to suggest that there may be a change in the mechanical properties of the PCBP with time. It is hypothesised that as more powder layers onto

the surface the PCBP, it becomes more brittle, and therefore breaks into fragments more easily under the action of shear and impact.

The strength of a material and how a material responds to the forces it is subjected to, determine its mechanical properties. Strength of a material can be divided into two kinds: compressive and tensile (Figure 5.24). In all cases the strength refers to the maximum load a material can withstand when a load is placed upon it, and it is found by dividing the load acting on the material by its cross-sectional area. It indicates the resistance of a material to undergo fracture. In other words, when a stress equal to the tensile/compressive strength developed within the material it will break.

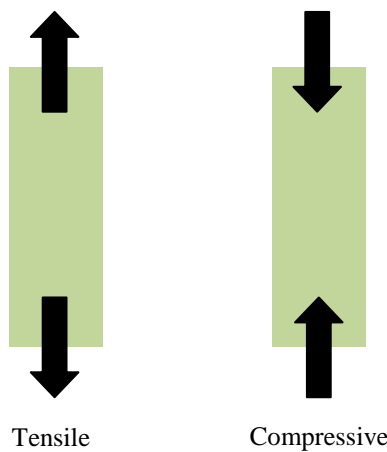


Figure 5.24. The applied stress can be tensile or compressive.

Indentation hardness is somewhat different to measuring the tensile strength, in that it describes the local plasticity of the material. This hardness can be described as the ability of a sample or material to resist plastic deformation. It is determined by measuring the amount of deformation caused by a hard indenter being pressed against a surface. There are several different methods which could be adopted to conduct this form of test. One such method uses a pendulum which is used to strike the material from a known distance or an indenter is allowed to fall under gravity onto the surface of the material leaving an indent on its surface. The size and shape of the indent are all good indicators of the material hardness (Tabor, 2000).

A Zwick/Roell Z tensile tester equipped with a 10 N load cell was used to indent the PCBPs. The indentor tip used for this study is a sharp 60° Diamond Pen. For more details about the equipment used to indent the PCBPs refer to Section 3.15. The normal force acting on the load cell is measured, as the indentor tip penetrates the surface of a PCBP. The speed of the upper punch was maintained at 1 mm/min. Also, the maximum compression force was limited to 9 N and the maximum strain to 1 mm. A preload condition was set so that the system starts recording the stress when the detected load exceeds 0.01 N. For each test condition (granulation time point), 10 measurements were taken. In between repeat measurements, the platen and indentor tip were cleaned thoroughly ensuring no material from the previous test influenced results. For each test a single PCBP was indented at a time.

A preliminary examination on a PCBP indicates that under certain conditions indentation leads to the propagation of cracks and fragmentation (Figure 5.25). This technique therefore, proves to be an effective method of determining the stiffness of a PCBP. Tests were conducted on the PCBPs made at 300 rpm. The indentation technique was chosen over a compression technique as the mechanical properties of the PCBPs evolve with time from plastic deformation to brittle behaviour. When compressing a bed of particles or a single particle, it is not possible to visually identify and isolate breakage, or to distinguish between the different types of mechanical responses. In other words, compression on its own cannot isolate the breakage; instead PCBPs will deform, fracture, then form a compact within the confines of a die, especially when considering a bed of particles. Indentation using a sharp pen was, therefore, chosen in order to be able to observe a drop in the load when cracks propagate within the structure of a PCBP and to distinguish between the different types of mechanical responses.

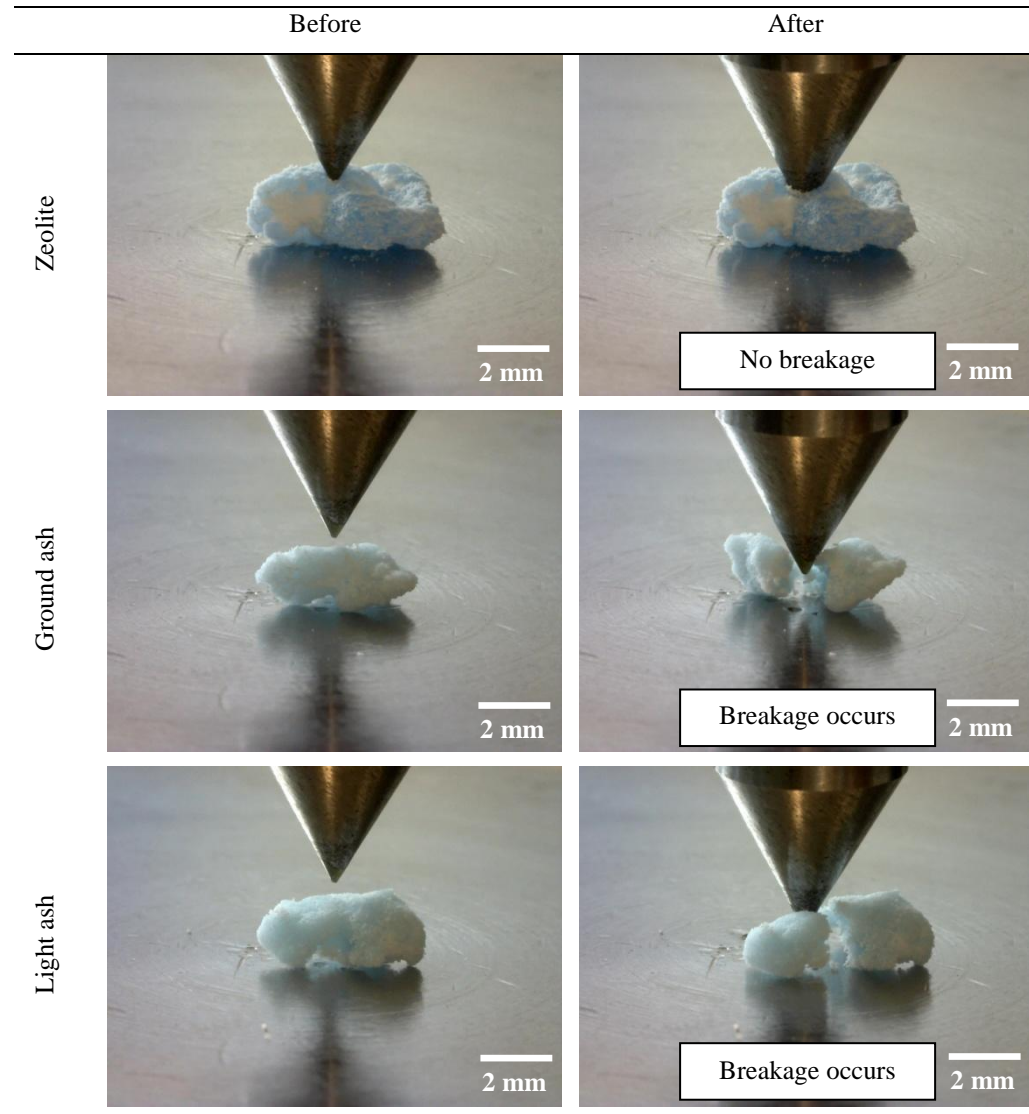


Figure 5.25: Sample PCBP pre and post indentation (after 75 s).

Images of the PCBPs taken during indentation, coupled with the force vs. displacement graphs, show how this transition occurs with time. Refer to Appendix II for force vs. displacement graphs of the three different materials. It was observed that PCBPs which are richer in binder undergo plastic deformation when indented, and the gradual penetration of the particles into the PCBPs makes them semi-brittle and eventually, brittle. These experiments aim to further explain why the rate of the size reduction process changes when a different powder is used. The average values of the force were determined for the raw data presented in Appendix II, and the gross mechanical behaviour of all the materials is presented in Figure 5.26 - Figure 5.28, at different time points. For zeolite, (Figure 5.26), it is evident that the fracture of the PCBP does not take place.

Better dispersion is achieved when the binder gets coated and breaks more rapidly within the granulator. Dispersion through plastic deformation of the PCBPs is likely to take more time compared to dispersion as a result of brittle fracture. So, from a dispersion point of view, if the material reaches this brittle state faster, binder distribution into the powder bed can be improved. Zeolite does not exhibit a brittle response even after 75 s of wet massing, whereas light and ground ash show signs of brittle breakage within 15 s and 75 s of wet massing respectively (Figure 5.27-Figure 5.28).

Once again, upon analysing the gross behaviour of the raw data presented in Appendix II, there is clear difference in the force vs. displacement curves for the three different powders. For zeolite, there is a linear relationship between the measured force and displacement, and for light ash there is a sudden drop in the force with increasing displacement. This drop in the load coupled with photographic evidence (Figure 5.25) provides proof for brittle fracture. For ground ash, the load is higher at first, but it drops with time, and more importantly, there is a change in the shape of the curve. For light ash, the drop in the load is evident even after just 15 s of wet massing. These behaviours can be explained using the results from the XRT analysis, i.e. more penetration of larger particles makes the light ash PCBP brittle on a shorter time scale. For zeolite, on the other hand, there is some loose powder coating on the surface of the PCBP, which does not provide rigidity, therefore they deform plastically.

The indentation analysis therefore links the change in the mechanical properties of the PCBP to the amount of powder held within its internal structure, i.e. with increasing mass fraction of powder in a PCBP, there is a greater likelihood for brittle fracture to occur. This suggests that a change in the mechanism of binder breakage occurs with time during wet massing, mainly as a result of changes in the composition of the PCBP with time.

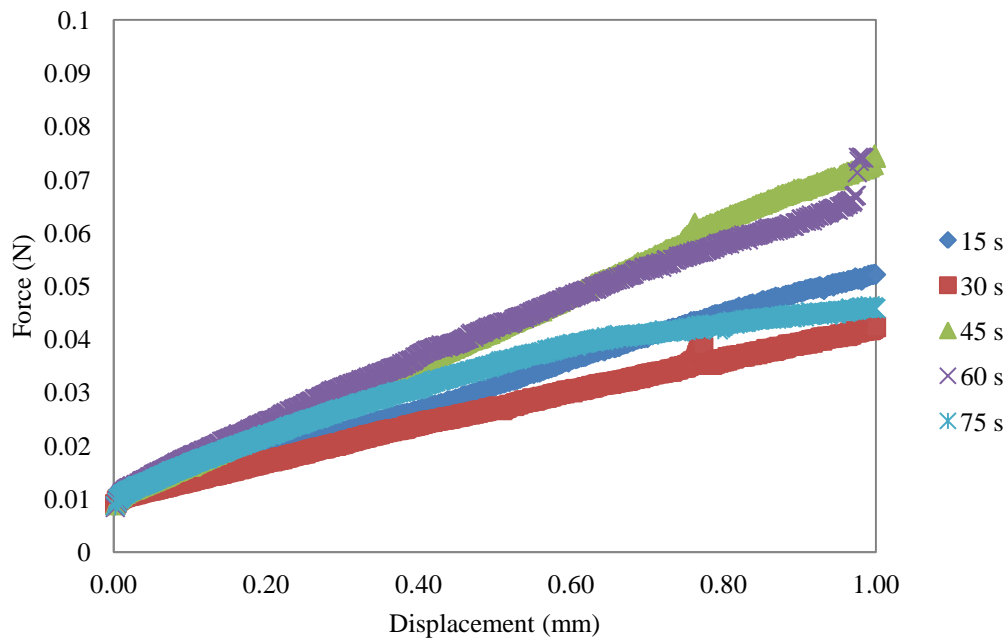


Figure 5.26. Force vs. displacement curves for the indentation of zeolite PCPs.

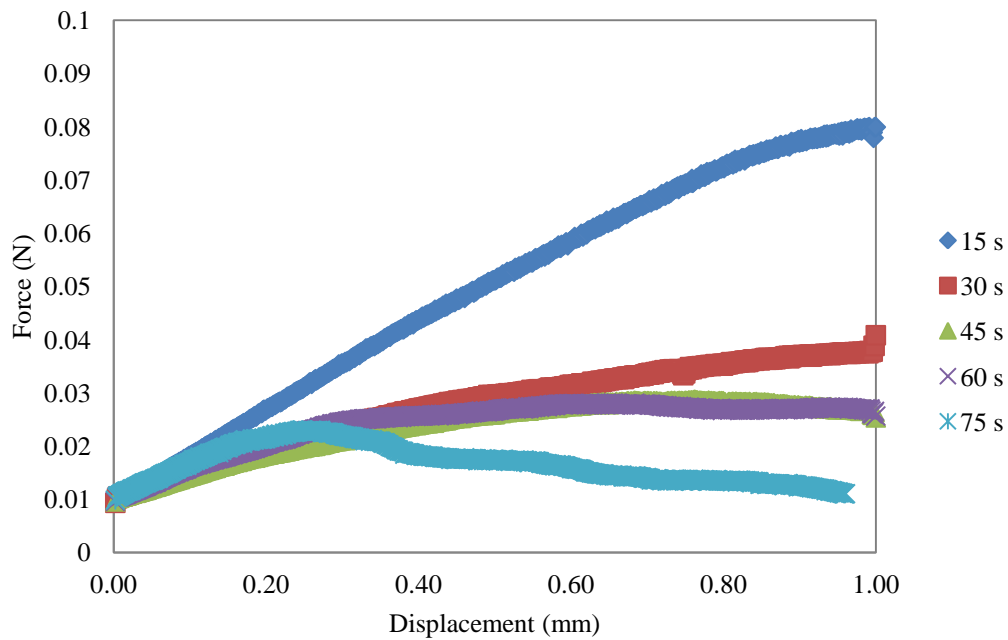


Figure 5.27. Force vs. displacement curves for the indentation of ground ash PCPs.

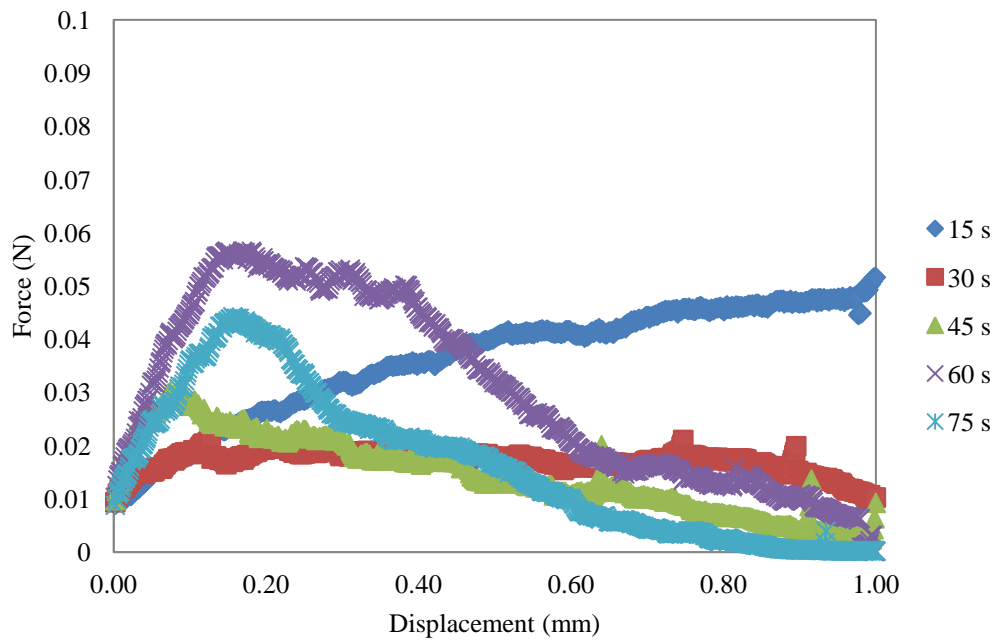


Figure 5.28. Force vs. displacement curves for the indentation of light ash PCBPs.

5.11 Conclusions

Some useful insights have been gained on the initial dispersion of a highly viscous surfactant binder in a moving bed of powder. A mechanism has been proposed for the initial dispersion during nucleation, which involves the layering of powder onto the surface of the binder and breaking large lumps into smaller fragments, through mechanical action. This is the first study to introduce the concept of “breakage” when describing the dispersion of a semi-solid binder in a moving bed of powder. The coated semi-solid binder is subsequently referred to as a powder coated binder particle (PCBP).

This study has developed a method for isolating and observing the breakage of PCBPs. A technique has also been developed for the quantifying the powder layering process, by monitoring the variation in the mass and size of the PCBPs with time. The effect of both particle type and impeller speed on the breakage of the PCBPs was investigated. Results suggest that larger and rougher particles are able to break and disperse the PCBPs more rapidly, in comparison to smaller and more circular ones. Binder dispersion is also enhanced at higher impeller speeds, due to the higher stresses acting within the granulator.

There is also some evidence that suggests the mechanical properties of the PCBPs changes with time, as its composition starts to change. The rate of powder loading into a binder particle has a direct influence on the mechanical response it exhibits, and this in turn influences the rate of binder breakage. When the rate of powder layering is faster, the PCBP exhibits brittle behaviour sooner. It was found that PCBPs containing light ash reach this brittle state on a much shorter time scale, in comparison to those that contain ground ash and zeolite.

Chapter 6 Asymptotic self-similar model for breakage

6.1 Introduction

Section 2.20 gives a brief introduction to population balances. Population balance models (PBM) are continuous simulations that can be used to describe the dynamic behaviour of a system, usually, by adopting a set of coupled equations. A continuous model in mathematical terms refers to the application of a model to continuous data, which has an infinite number of divisible attributes. Differential equations are used to describe such models. The alternative to a continuous model is a discrete one. Key aspects of the modelling process include the development of a model, followed by the testing of its validity. It is also important to understand the limitations of such models.

There are two different types of population balance models:

1. A one dimensional model – focuses on a single aspect which in most cases is the particle size.
2. A multi-dimensional model – deals with multiple aspects in the model including size, shape, porosity and binder content.

For most models generally, the current state of the system, rate of change and the input at present time are known and the next collocation point is approximated using a predicted rate of change. In probability theory, a process that satisfies the Markov Theory is one where predictions can be made of the future state, based on the present state or on process history (Dynkin, 1961). Such models are deterministic, as there is no random variation in the process (i.e. for the same starting point and processing condition the model will always give the same outcome).

The core or what is commonly referred to as the kernel of a population balance model is often based on a physical model, knowledge of the process/formulation variables, purely empirical observation, or in some cases on some form of mechanistic insight into an agglomeration process (Abberger, 2007).

One of the key challenges associated with any population balance equation (PBE) is finding its solution. When birth and death terms are integrated it often results in an output that takes the form of an integro-partial differential equation (Ramkrishna, 2000). Various processes can be described in a PBE, including nucleation, aggregation and breakage.

As experimental data is often used to validate a PBM, there is a need to extract the underlying rate laws from such experimental data. This is referred to as the inverse problem (Wright and Ramkrishna, 1992). This may include aggregation frequencies, breakage constants, etc. As the rate laws are often based on the behaviour of single particles, it is often difficult to link this to the understanding of the behaviour of several particles in the granulation mixture obtained from the experimental results. Therefore the model is often limited by the quality of the experimental data. In certain cases, to adequately specify such models parameter estimation may be required.

Sections 6.3-6.9 provide some essential background information on population balance models, including equations that describe mechanisms such as coalescence and breakage. This is followed by sections that describe the present model that predicts the breakage of PCPs.

6.2 Probability functions

Particle size is a property that varies within a distinct population of particles (Ramkrishna and Borwanker, 1973). Such distributions can either be discrete or continuous. At time, t , there exists densities, $n(x,t)$, defined by:

- $n(x,t)$ – average number of particles of size x per unit volume in the discrete case.
- $n(x,t)dx$ – average number of particles of size between x and $x+dx$ per unit volume in the continuous case.

The total number of particles is therefore given by:

$$N_{tot}(t) = \int_0^{\infty} n(x, t) dx \quad \text{Equation 6.1}$$

When a large number of particles are moving collectively within an enclosed volume it is expected that some will collide to make bigger particles, others may rebound off the wall or each other, whilst certain large particles may undergo breakage to yield smaller particles. The coalescence and breakage process will result in a change in the total number of particles within the mixer, and is therefore a time dependant process.

6.3 Particle coalescence

Consider the existence of two distinct particle sizes x and y . The probability of a collision between particles x and y is proportional to the product $n(x, t) \cdot n(y, t)$. As the collision between x and y is the same as the collision between y and x this probability is divided in 2.

Other additional factors also influence the fate of a collision between two particles i.e. will they coalesce or rebound. This includes the velocity at the time of particle collision. This is accounted for by incorporating an additional factor $\beta(x, y)$ into the general PBE. Therefore, the generalised form for coalescence now becomes Equation 6.2 (Sastry and Gaschignard, 1981).

$$\iint \frac{1}{2} n(x, t) n(y, t) \beta(x, y) dx dy \quad \text{Equation 6.2}$$

Population densities of particles may be described by their number, mass or volume. Most commonly they are expressed as a number based distribution of size x at a certain time (t), x can be the particle length (l), particle diameter (d) or particle volume (v). For studies focussing on particle growth, using v is recommended as this parameter is additive (providing any changes in the porosity of the daughter particle during growth are disregarded).

6.4 Continuous form of the PBE

In the continuous form, Equation 6.3 describes the formation of particles of volume fraction between v and $v+dv$ by successful collisions and coalescence of particles whose total volume is v . This is known as coalescence birth. Therefore, if one of the particles has a volume u , the other colliding particle must have a corresponding volume of $v-u$, so that the total volume remains as v , i.e. volume is conserved throughout.

$$N_{birth} = B_{coal}dt = \frac{1}{2} \int_0^v \beta(v-u, u)n(v-u, t)n(u, t)du \times dv dt \quad \text{Equation 6.3}$$

where B_{coal} is the coalescence birth rate.

The loss of particles of volume fraction between v and $v+dv$ as a result of binding through successful collisions is similarly represented by a death term D_{coal} . N_{death} is therefore given by:

$$N_{death} = D_{coal}dt = \int_0^\infty \beta(v, u)n(v, t)n(u, t)du \times dv dt \quad \text{Equation 6.4}$$

The accumulation of particles in the size fraction between v and $v+dv$ will therefore be given by:

$$\frac{\partial}{\partial t} [n(v, t)dv]dt = N_{birth} - N_{death} \quad \text{Equation 6.5}$$

Combining equations Equation 6.3 and Equation 6.4, allows the equation for the net rate of formation of particles of volume fraction between v and $(v+dv)$ to be obtained (Müller, 1928):

$$\begin{aligned} \frac{\partial}{\partial t} [n(v, t)dv] &= -D_{coal} + B_{coal} \\ &= - \int_0^\infty \beta(v, u)n(v, t)n(u, t)dudv \\ &\quad + \frac{1}{2} \int_0^v \beta(v-u, u)n(v-u, t)n(u, t)dudv \end{aligned} \quad \text{Equation 6.6}$$

Equation 6.6 can be rewritten to represent the change in the number of particles of a specific volume, v . In this case the left hand side (Equation 6.7) should represent the

rate of change of the number of particles with volume v (term dv is therefore lost). This form of the equation is referred to as the Smoluchowski equation (Schellander, 2013).

$$\begin{aligned} \frac{\partial}{\partial t} [n(v, t)] = & \\ - \int_0^{\infty} \beta(v, u) n(v, t) n(u, t) du & \\ + \frac{1}{2} \int_0^v \beta(v-u, u) n(v-u, t) n(u, t) du & \end{aligned} \quad \text{Equation 6.7}$$

Equation 6.7 is usually supplied with some initial conditions. Generally, these are in the time and size domain. This initial condition is normally the starting size distribution:

$$n(v, 0) = n_0(v) \quad \text{Equation 6.8}$$

And the boundary conditions are:

$$n(0, t) = n(\infty, t) = 0 \quad \text{Equation 6.9}$$

In essence, these conditions means that no particles of size zero exist, and all particles have a finite size. Other boundary conditions may apply depending on the assumptions on which the PBE is built.

Some other key assumptions that are subsumed into this model include (Abberger, 2007):

- The system is diluted so that merging of two particles is not influenced by neighbouring particles.
- Fluctuations around the mean for any given particle size are ignored.
- The mechanical and thermodynamic nature of inter-particle interactions and their potential influence on the spatial correlation are ignored.
- The shape of the aggregating particles is ignored. In most cases, the particles are assumed to be spherical.
- More specifically, Equation 6.7 assumes that coalescence is the only mechanism of growth (nucleation, breakage, etc. are not considered).

Almost all PBEs only describe some average behaviour of the underlying mechanisms through its kernel. Despite numerous assumptions (which make the model seem rather simplistic to be of practical use), it is important to observe that the details of the local motion and coalescence which arise from the physics of inter-particle interactions are in most cases, subsumed into the model by using experimental data to validate such equations.

The Smoluchowski equation was expanded to a general PBE in order to (Abberger, 2007):

- Account for more mechanisms or processes, other than coalescence causing an accumulation of particles in a size class.
- Account for the distribution of other properties other than size alone – for example in multidimensional PBEs.
- Be able to deal with particulate processes where restrictions on spatial homogeneity over the entire process volume cannot be assumed.

6.5 Spatial variation – micro-distributed form

Population balance model can be made relevant to a finite space/region within the entirety of the mixer. This requires a sub-region, R , and a particle state space, S , to be clearly defined. The PBE in the arbitrarily chosen fixed sub region, R_1 , is therefore:

$$\frac{d}{dt} \int_0^{R_1} n(R, t) dR = \int_0^{R_1} (B - D) dR \quad \text{Equation 6.10}$$

It is known that Accumulation = Input – Output + Generation – Consumption. The input and output terms in this case accounts for the inflow and outflow of materials within the defined sub-region. Generation/consumption of a specific size class will depend on the difference in the birth and death rate of the said size class. This form is only used when describing poorly mixed systems.

6.6 1-D PBE for granulation

Across the entire mixer considering the macroscopic case the general equation is as follows (Ennis et al., 2008):

$$\frac{\partial n(v, t)}{\partial t} = \frac{Q_{in}}{V} n_{in}(v) - \frac{Q_{out}}{V} n_{out}(v) - \frac{\partial(G(v, t) - A(v, t)n(v, t))}{\partial v} + \beta_{nuc}(v, t) + \beta_{coal}(v, t) - D_{coal}(v, t) \quad \text{Equation 6.11}$$

The first two terms on the right hand side represent flows into and out of the control volume respectively. $G(v, t)$ and $A(v, t)$ are the growth and layering attrition rates respectively. $\beta(v, t)$ is the nucleation rate of new granules of size v due to the addition of binder. Additional terms may be added to account for breakage.

6.7 Binder breakage

Most models only look at the growth phase of the granulation process. Therefore, nucleation and breakage terms are not included in many working models of granulation. Others have also mentioned the difficulties in modelling the processes that take place in the liquid distribution stage (Holm et al., 1985). Little progress has been made in modelling the nucleation stage. This work proposes a model that describes binder dispersion (breakage) during the nucleation stage of the granulation process.

It is necessary to clarify that the term “breakage” used in this study does not refer to the breakage of a single primary particle or the breakage of a granule within the mixer, instead it concerns how a binder fragment or PCBP undergoes size reduction, during the wetting and nucleation stage of the granulation process. Once introduced into the mixer the binder particles get coated with powder and are broken up into smaller fragments gradually. Figure 6.1 represents the change in the constitution of a binder particle as a result of wet massing, and this is consistent with the experimental observation reported in Chapter 5. In Figure 6.1, the phase change is, however, over-simplified by assuming the ratio of volume of solids to liquids (V_S/V_L) remains constant throughout the breakage process.

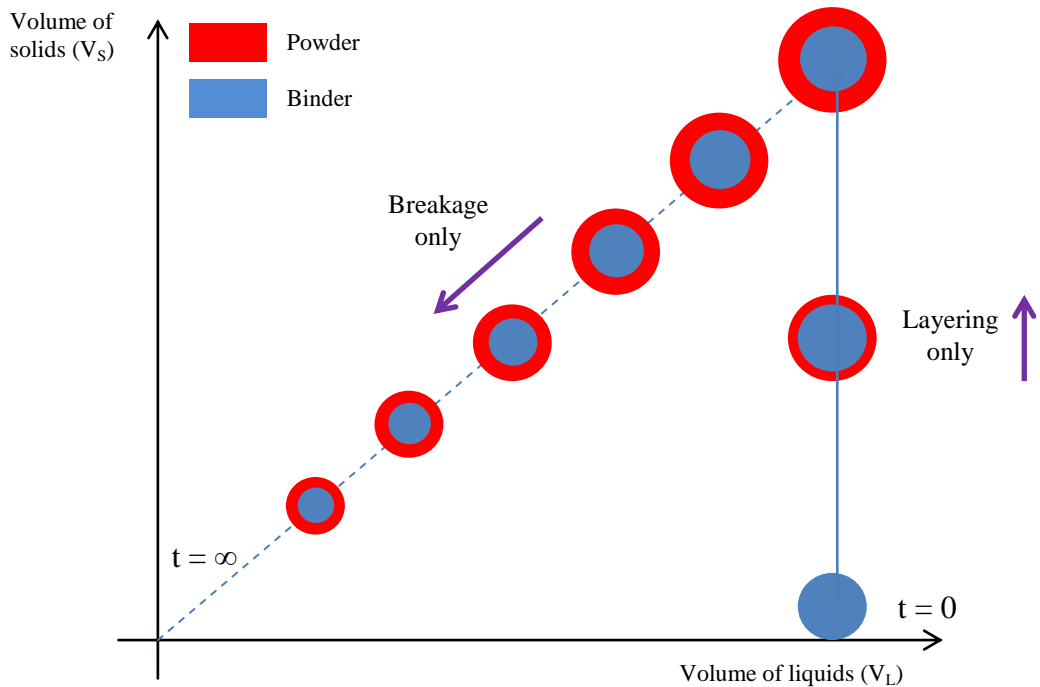


Figure 6.1. Phase changes during the binder dispersion process.

Prior to describing the breakage of a PCBP, it is necessary to have an appreciation of the concept of particle breakage as a whole, and identify what type of breakage occurs during the dispersion of a highly viscous paste binder. Particulate material is processed in many different ways in industry. Coal, for example, is ground for energy production to ensure complete combustion, iron ore is agglomerated prior to being introduced into a blast furnace, crystalline material produced in the chemical industry may be engineered to different sizes, and catalysts may be made in many different shapes to fit their end-use. Particle breakage can be a desired or an unwanted phenomenon. Consider milling, for example, where breakage is desired, but on the contrary when considering agglomeration process unwanted breakage of the material in a mixer could lead to reduced product quality, and result in more waste, which may have to undergo further downstream processing.

In the literature, several different terms have been used to describe the breakage phenomenon including abrasion, attrition, erosion, fragmentation and wear (Stanley-Wood, 2006). These variations of breakage have been classified based on the size and shape of

the daughter fragments, as well as the type of forces that act on the particle (Stanley-Wood, 2006):

- Wear – damage of the surface of a particle usually, gradually and mainly around its periphery - as a result, the shape of the particle remains more or less unchanged.
- Attrition – form of wear; any rough edges of a particle may be worn down by surface forces, and the particle retains its original shape.
- Abrasion – form of wear caused by tangential forces. Rolling of particles could lead to their peripheries becoming smoother.
- Fracture – internal breakage by relatively high forces (normal or shear). Particle shape and size may change significantly after fracture.
- Fragmentation – fracture caused by high normal forces – in some cases through head-on impact/stress.
- Chipping – another type of fracture caused by tangential forces acting on the surface. The particle does not become smooth, as fractures propagate in a random manner at a close proximity to the surface of the particle.

The most relevant term which describes the breakage seen when a semi-solid binder is distributed into a moving powder bed is, therefore, **fracture** or **fragmentation**. Both terms describe how a larger particle splits into a number of smaller particles.

6.8 The breakage kernel

The rate of breakage (D) of particles of size u is represented by Equation 6.12:

$$D(u) = S(u)n(u) \quad \text{Equation 6.12}$$

$S(u)$ is the selection rate constant i.e. the probability that particles of a certain size class will break (Ding et al., 2006). Now, consider particles u and v , where u is larger than v . Particles of size v are formed from the breakage of particles of size u . The mechanism of breakage will affect the rate of breakage and the probability of forming particles of

size v . Again, as with coalescence PBE, birth and death rates that are related to the breakage model have to be elucidated too.

The death rate is defined as follows:

$$D_{brea}(v) = S(v)n(v) \quad \text{Equation 6.13}$$

The birth rate of size v is the sum of the death rates of all particles larger than v that break to give size v . The fraction of deaths of u that result in particles of size v is given by $b(u, v)$.

$$B_{brea}(v) = \int_v^\infty b(u, v)S(u)n(u)du \quad \text{Equation 6.14}$$

Combining the above equations gives an expression for the rate of breakage:

$$B_{brea}(v, t) - D_{brea}(v, t) = \int_v^\infty b(v, u)S(u)n(u, t)du - S(v)n(v, t) \quad \text{Equation 6.15}$$

Some commonly used breakage distribution functions from the literature are summarised in Table 6.1.

Table 6.1. Breakage distribution functions (Hill and Ng, 2002). w is the parent particle volume and v is the child particle volume.

Description	$b_M(v, w)$	Source
Uniform	$2v/w^2$	Hill and Ng (1995)
Parabola	$24 \frac{v}{w^4} \left(1 - \frac{hv}{2}\right) \left(v^2 - vw + \frac{w^2}{4}\right) + \frac{hv}{w}$	Hill and Ng (1995)
	$\frac{\phi\gamma}{3w} \left(\frac{v}{w}\right)^{\frac{\gamma}{3}-1} + \frac{(1-\phi)\beta}{3w} \left(\frac{v}{w}\right)^{\frac{\beta}{3}-1}$	Austin et al. (1976)
Milling	$\frac{(v/w)^{-2/3} \exp(-v/w)}{3w(1-1/e)}$	Broadbent and Calcott (1956)
	$\frac{1}{w} \left[ac \left(\frac{v}{w}\right)^{c-1} + (1-a)d \left(\frac{v}{w}\right)^{d-1} \right]$	Shoji, Lohrasb, and Austin (1980)
	$\frac{1}{3w}(v/w)^{2/3}$	Reid (1965)
	$n(v/w)^{n-1}/w$	Randolph and Ranjan (1977)
Theoretical	$\frac{(2/\sqrt{2\pi}\sigma)(v/w) \exp[-(v-w/2)^2/2\sigma^2]}{\operatorname{erf}(\frac{w}{\sqrt{2}\sigma})}$	Pandya and Speilman (1982)
	$(2v/w^2)(2n+1)(2v/w-1)^{2n}$	Peterson, Scotto, and Sarofim (1985)
Fly ash formation	$\frac{K}{w} \exp[-\ln^2 \left(\frac{v}{cw}\right)/2\ln^2 \sigma]$	Peterson, Scotto, and Sarofim (1985)

6.9 Moments

It is not necessary to know the entire PSD, instead, some average quantities about the distribution may be sufficient to represent it. These average quantities are often expressed as moments of the distribution function.

The j^{th} moment of $n(x, t)$ is defined as follows:

$$m_j = \int_0^\infty x^j n(x, t) dx, \quad j \geq 0 \quad \text{Equation 6.16}$$

The number-based mean particle length ($\bar{l}_{1,0}$) is given by m_1/m_0 (when x is a length).

6.10 Assumptions of the present model

Up to now an introduction to population balance models has been given along with a synopsis of the types of specialised models that could be used to describe various aspects of the granulation process that take place within a mixer. From here onwards this

chapter focuses on developing a model that describes the breakage of PCPBs during the binder dispersion process.

Section 5.8 provides micrographic evidence that demonstrates breakage occurs randomly. For simplicity, it can be assumed that the random breakage is uniform and binary (Figure 6.2). This means that a particle of length l , and constant diameter d (cross-sectional area remains unchanged after breakage) breaks into 2 particles (of size x and $l-x$) and the size of the fragments is evenly distributed between $x=0$ and $x=l$ (Figure 6.3). The total length of the particles is therefore conserved. This model predicts the change in the length of the PCPBs (l) as a function of time (t) i.e. the average number of particles of length l per unit volume in the discrete case, $n(l,t)$, will be predicted.

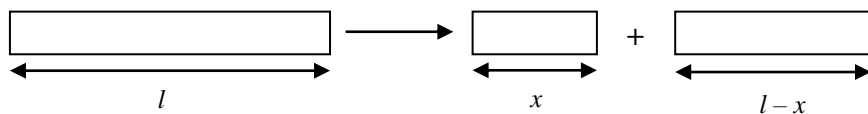


Figure 6.2. Diagrammatic representation of binary binder breakage.

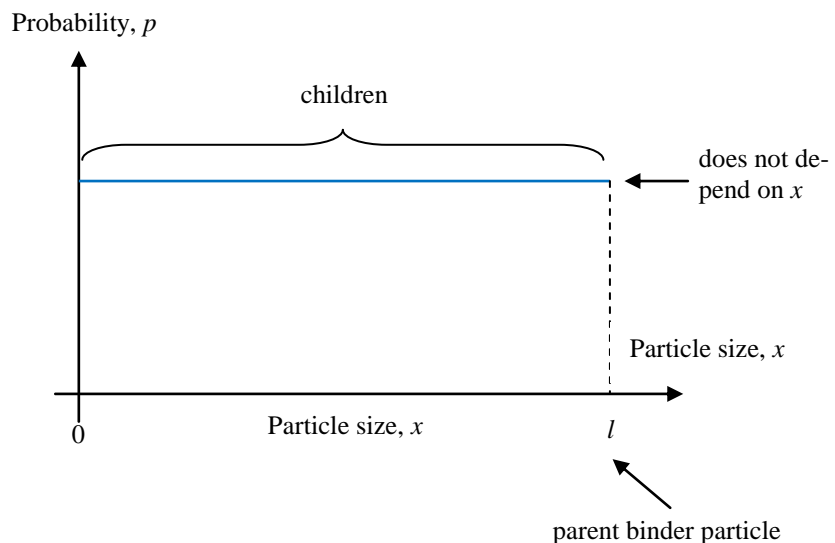


Figure 6.3. Probability distribution of the size of the fragments post-breakage.

The model suggested here assumes that the semi-solid binder undergoes breakage as any brittle solid would i.e. through the propagation of fractures. It is therefore assumed that the binder does not begin to flow as a result of the stresses acting on it. This model would therefore only be applicable to systems where the yield stress required to make

the binder flowable is sufficiently large. This model would therefore not be able to describe the dispersion of aqueous or low viscous binders in a moving bed of powder, largely because the mechanism of dispersion involves binder penetration via capillary action (not breakage).

Taking the j^{th} moment (Equation 6.16), 0 (m_0) would give number of PCBPs and 1 (m_1) would give length of granules. N_T refers to the total number of granules, and L_T refers to the total length. And therefore $N_T = m_0$ and $L_T = m_1$.

The total volume of the PCBP is given by:

$$V_T = \frac{\pi}{4} d^2 L_T = \frac{\pi}{4} d^2 m_1 \quad \text{Equation 6.17}$$

The number of fragments per breakage event is given by:

$$N_b(l) = \int_0^l b(x, l) dx = \left[\frac{2x}{l} \right]_{x=0}^{x=l} = 2 \quad \text{Equation 6.18}$$

i.e. it is consistent with binary breakage.

Length of the fragments post breakage should also add up to l . The total length of the fragments can be determined as follows:

$$L_b(l) = \int_0^l x b(x, l) dx = \left[\frac{x^2}{l} \right]_{x=0}^{x=l} = l \quad \text{Equation 6.19}$$

As discussed earlier in Section 6.8, a selectivity function, $S(l)$, has to be assumed. Larger or longer PCBPs are more likely to undergo breakage. $S(l)$ is therefore taken to be:

$$S(l) = k' l = \frac{k}{l_0} \cdot l \quad \text{Equation 6.20}$$

where l_0 is the length of the parent binder particle.

The kernel must include terms to account for both births and deaths. Substituting the key assumptions of the model into the general PBE (Equation 6.15) gives Equation 6.21.

$$\begin{aligned}
 \frac{\partial n}{\partial t} &= B_{brea}(x, t) - D_{brea}(l, t) \\
 &= \int_l^\infty S(x)b(l, x)n(x, t)dx - S(l)n(l, t) \\
 &= \frac{2k}{l_0} \int_l^\infty n(x, t)dx - k \frac{l}{l_0} n(l, t)
 \end{aligned} \tag{Equation 6.21}$$

It is assumed that initially, the binder particles are mono dispersed (N_0 number of particles with a uniform distribution of length l_0) i.e. $n(l, 0) = N_0\delta(l-l_0)$. The term δ is Dirac's delta function (refer to Appendix III for more details about this function and its uses).

6.11 Dimensionless form of PBE

Terms are made dimensionless as follows:

$$\hat{l} = \frac{l}{l_0} \tag{Equation 6.22}$$

where l_0 is the length of the parent fragment

$$\hat{t} = kt \tag{Equation 6.23}$$

where k is the selectivity constant with units (s^{-1})

$$\hat{n} = \frac{l_0}{N_0} n \tag{Equation 6.24}$$

where N_0 is the number of particles at $t = 0$

Multiplying both sides of the PBE (Equation 6.21) by the term $\frac{l_0}{kN_0}$ makes the population balance equation dimensionless, (as the term $\frac{l_0}{kN_0} \times \frac{\partial n}{\partial t}$ is dimensionless):

$$\frac{\partial \hat{n}}{\partial \hat{t}} = 2 \int_l^\infty \hat{n}(\hat{x}, \hat{t})d\hat{x} - \hat{l} \hat{n}(\hat{l}, \hat{t}) \tag{Equation 6.25}$$

6.12 Moment equation

An expression for the moment equation (Equation 6.26) was derived from Equation 6.25. Refer to Appendix IV for the complete derivation.

$$\frac{d\hat{m}_j}{d\hat{t}} = \frac{1-j}{j+1} \hat{m}_{j+1} \quad \text{Equation 6.26}$$

$j = 0$, gives the number of fragments with respect to time. It also follows that:

$$\frac{d\hat{m}_0}{d\hat{t}} = \hat{m}_1 \quad \text{Equation 6.27}$$

It also follows that:

$$\hat{m}_0 = \frac{m_0}{N_0} \quad \text{Equation 6.28}$$

$$\hat{m}_1 = \frac{m_1}{N_0 l_0} \quad \text{Equation 6.29}$$

In order to obtain m_0 , t and m_1 in their dimensional form, it is necessary to substitute the Equation 6.13, Equation 6.28 & Equation 6.29 into Equation 6.27 to obtain Equation 6.30.

$$\frac{1}{N_0} \frac{dm_0}{kdt} = \frac{m_1}{N_0 l_0} \rightarrow \frac{dm_0}{dt} = k \frac{m_1}{l_0} = k N_0 \quad \text{Equation 6.30}$$

It also follows that:

$$m_0 = m_0(0) + ktN_0 \quad \text{Equation 6.31}$$

The rate of change of the first moment is 0, i.e. the total length will be conserved:

$$\frac{dm_1}{dt} = 0 \quad \text{Equation 6.32}$$

The initial length is given by:

$$m_1(0) = N_0 l_0 \quad \text{Equation 6.33}$$

The number of particles at a given time can be calculated as follows:

$$m_0(t) = m_0(0) + m_1 t \quad \text{Equation 6.34}$$

It therefore follows that:

$$m_0 = N_0 + N_0 kt \quad \text{Equation 6.35}$$

The number based mean length (m_1/m_0) is defined as follows:

$$\bar{l}_{1,0} = \frac{l_0}{1 + kt} \quad \text{Equation 6.36}$$

6.13 Asymptotic self-similar solution of the PBE

Two objects are said to be geometrically similar if they have the same shape on any scale. The second object may be obtained from the first by uniform scaling (either enlargement or shrinkage) (Zohuri, 2015). Consider a square for example (Figure 6.4), it can be divided into 4 self-similar sub squares with a scaling factor of 2, or into 9 self-similar squares with a scaling factor of 3. A square can therefore be broken down into N^2 self similar sub squares, each of which can be multiplied by a scaling factor N in order to give the original square.

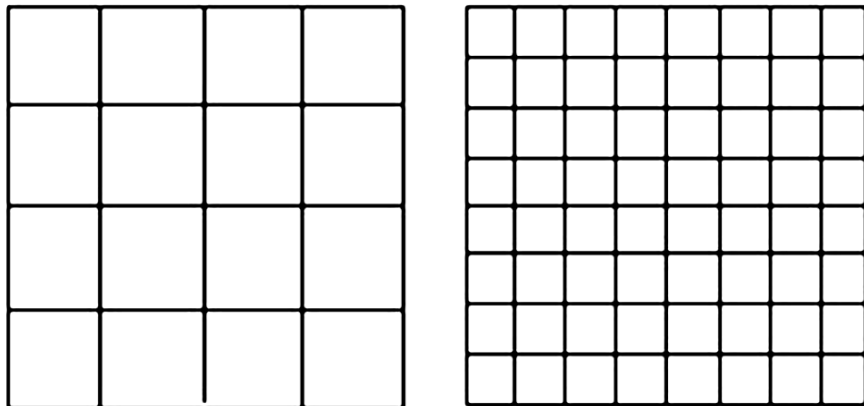


Figure 6.4. A square may be broken down into N^2 self-similar pieces, each with magnification factor, N (Zohuri, 2015).

When relating self-similarity to changes in a particles size distributions, it is often characterised by a maximum distribution function, that changes the position of its peak value with time, whilst retaining the shape of the original PSD. Self similarity can normally be condensed into a single time-invariant representation or distribution function through normalisation. For example, particle size can be represented by the mean particle length (l) or volume (v).

As time progresses, the mean size of the PCBPs decreases. The dimensionless mean length of the PCBPs varies as a function of the dimensionless time as follows:

$$\hat{l} = \frac{1}{1 + \hat{t}} \cong \frac{1}{\hat{t}} \quad \text{Equation 6.37}$$

Also, with time the number of particles increases. Thus, the moment, \hat{m}_0 , varies as follows:

$$\hat{m}_0 = 1 + \hat{t} \cong \hat{t} \quad \text{Equation 6.38}$$

It is hypothesised that there is a self-similar solution to the PBE. To re-iterate, self-similarity means the distributions are always the same shape when plotted after a similarity transformation and do not depend otherwise on time. A similarity transformation was applied to \hat{n} so that it could be represented as a function $f(\hat{l}/\hat{l})$ as follows:

$$f(\hat{l}/\hat{l}) = \frac{\hat{n}}{\hat{m}_0} \cdot \hat{l} \quad \text{Equation 6.39}$$

\hat{n} now becomes:

$$\hat{n} = \frac{f(\hat{l}/\hat{l}) \cdot \hat{m}_0^2}{\hat{m}_1} \quad \text{Equation 6.40}$$

where $\hat{m}_0 = \hat{t}$, $\hat{m}_1 = 1$ and $\hat{l} = \frac{1}{\hat{t}}$.

Equation 6.40 can be simplified to:

$$\hat{n} = \hat{t}^2 f(\hat{l} \cdot \hat{t}) \quad \text{Equation 6.41}$$

Transforming (\hat{l}, \hat{t}) into (u, v) , where $u = \hat{l} \times \hat{t}$ and $v = \hat{t}$ gives a representative equation for the PSD (Equation 6.43):

$$\hat{n}(u, v) = v^2 f(u) \quad \text{Equation 6.42}$$

When the PSD is written as a function of $f(u, v)$, self-similarity dictates that the PBE only depends on u and not on v (time). Solving the PBE, gives f and what follows is the

methodology for determining f . Once f has been determined, it is possible to elucidate \hat{n} using Equation 6.41.

Firstly, it is necessary to derive expressions for $\left(\frac{\partial \hat{n}}{\partial u}\right)_v$ and $\left(\frac{\partial \hat{n}}{\partial v}\right)_u$:

$$\left(\frac{\partial \hat{n}}{\partial u}\right)_v = \left(\frac{\partial \hat{n}}{\partial \hat{l}}\right)_t \left(\frac{\partial \hat{l}}{\partial u}\right)_v + \left(\frac{\partial \hat{n}}{\partial \hat{t}}\right)_l \left(\frac{\partial \hat{t}}{\partial u}\right)_v \quad \text{Equation 6.43}$$

where $\left(\frac{\partial \hat{l}}{\partial u}\right)_v = \frac{1}{v}$ as $\hat{l} = \frac{1}{\hat{t}}$ and $v(\hat{l}, \hat{t}) = \hat{t}$ and also $\left(\frac{\partial \hat{t}}{\partial u}\right)_v = 0$, as t is a function of v not u .

Therefore Equation 6.43 can be re-written as Equation 6.44.

$$\left(\frac{\partial \hat{n}}{\partial u}\right)_v = \left(\frac{\partial \hat{n}}{\partial \hat{l}}\right)_t \overbrace{\left(\frac{\partial \hat{l}}{\partial u}\right)_v}^{\frac{1}{v}} + \left(\frac{\partial \hat{n}}{\partial \hat{t}}\right)_l \overbrace{\left(\frac{\partial \hat{t}}{\partial u}\right)_v}^0 = \frac{1}{v} \left(\frac{\partial \hat{n}}{\partial \hat{l}}\right)_t \quad \text{Equation 6.44}$$

Similarly:

$$\left(\frac{\partial \hat{n}}{\partial v}\right)_u = \left(\frac{\partial \hat{n}}{\partial \hat{l}}\right)_t \left(\frac{\partial \hat{l}}{\partial v}\right)_u + \left(\frac{\partial \hat{n}}{\partial \hat{t}}\right)_l \left(\frac{\partial \hat{t}}{\partial v}\right)_u \quad \text{Equation 6.45}$$

where $\left(\frac{\partial \hat{l}}{\partial v}\right)_u = -\frac{u}{\hat{t}^2}$, as $\hat{l} = \frac{u}{\hat{t}}$ and $u(\hat{l}, \hat{t}) = \hat{l} \times \hat{t}$ and also $\left(\frac{\partial \hat{t}}{\partial v}\right)_u = 1$, as $v(\hat{l}, \hat{t}) = \hat{t}$.

Therefore Equation 6.45 can be re-written as Equation 6.46.

$$\left(\frac{\partial \hat{n}}{\partial v}\right)_u = \left(\frac{\partial \hat{n}}{\partial \hat{l}}\right)_t \overbrace{\left(\frac{\partial \hat{l}}{\partial v}\right)_u}^{\frac{-u}{\hat{t}^2}} + \left(\frac{\partial \hat{n}}{\partial \hat{t}}\right)_l \overbrace{\left(\frac{\partial \hat{t}}{\partial v}\right)_u}^1 = \frac{-u}{\hat{t}^2} \left(\frac{\partial \hat{n}}{\partial \hat{l}}\right)_t + \left(\frac{\partial \hat{n}}{\partial \hat{t}}\right)_l \quad \text{Equation 6.46}$$

Differentiating Equation 6.42 with respect to u gives:

$$\frac{\partial \hat{n}}{\partial u} = v^2 f'(u) \quad \text{Equation 6.47}$$

Combining Equation 6.44 and Equation 6.47 gives:

$$\frac{\partial \hat{n}}{\partial \hat{l}} = v^3 f'(u) \quad \text{Equation 6.48}$$

Differentiating Equation 6.42 with respect to v gives:

$$\frac{\partial \hat{n}}{\partial v} = 2v f(u) \quad \text{Equation 6.49}$$

Combining Equation 6.46 and Equation 6.49 gives:

$$2v f(u) = -\frac{\partial \hat{n}}{\partial \hat{l}} \frac{u}{v^2} + \frac{\partial \hat{n}}{\partial \hat{t}} \quad \text{Equation 6.50}$$

Substituting Equation 6.48 into Equation 6.50 gives the LHS of the PBE:

$$2v f(u) = v^3 f'(u) \cdot -\frac{u}{v^2} + \frac{\partial \hat{n}}{\partial \hat{t}} \rightarrow \frac{\partial \hat{n}}{\partial \hat{t}} = 2v f(u) + uv f'(u) \quad \text{Equation 6.51}$$

The right hand side of the PBE (Equation 6.25) is:

$$2 \int_l^\infty \hat{n}(\hat{x}, \hat{t}) d\hat{x} - \hat{l} \hat{n}(\hat{l}, \hat{t})$$

Substituting $n(l, t)$ with $n(u, v)$ and introducing an integration variable along the u -axis, whilst noting that $du = \hat{t} d\hat{x} \therefore d\hat{x} = \frac{du}{\hat{t}} = \frac{du}{v}$, gives:

$$= 2 \int \hat{n}(u', v) \frac{du'}{v} - uv f(u) = 2v \int_u^\infty f(u') du' - uv f(u) \quad \text{Equation 6.52}$$

Equating the LHS to the RHS, it follows that:

$$\begin{aligned} 2v f(u) + uv f'(u) &= 2v \int_u^\infty f(u') du' - uv f(u) \\ &= 2v f(u) + uv f'(u) + uv f(u) = 2v \int_u^\infty f(u') du' \end{aligned} \quad \text{Equation 6.53}$$

Dividing Equation 6.53 by v and differentiating gives:

$$\begin{aligned} 2f' + f' + uf'' + f + uf' &= -2f \\ uf'' + f'(3 + u) + 3f &= 0 \end{aligned} \quad \text{Equation 6.54}$$

Mathematica was used to solve Equation 6.54, and it was found that $f = e^{-u}$ satisfies the differential equation and the moment equations, therefore:

$$\hat{n}(\hat{l}, \hat{t}) = \hat{t}^2 e^{-\hat{l}\hat{t}} \quad \text{Equation 6.55}$$

as $\hat{n}(u, v) = v^2 f(u)$, $u(\hat{l}, \hat{t}) = \hat{l} \cdot \hat{t}$ and $v(\hat{l}, \hat{t}) = \hat{t}$.

6.14 Determining the number based frequency density, q_0 , with time

The dimensionless analytical solution for the population balance equation is $\hat{n}(\hat{l}, \hat{t}) = \hat{t}^2 e^{-\hat{l}\hat{t}}$.

From Equation 6.22 - Equation 6.24, it follows that:

$$n = \frac{N_0}{l_0} \hat{n} \quad \text{Equation 6.56}$$

Substituting the above terms into the analytical solution for the population balance equation gives Equation 6.57.

$$n = \frac{N_0(kt)^2}{l_0} e^{-\frac{lkt}{l_0}} \quad \text{Equation 6.57}$$

At long times $m_0 = N_0 kt$ and $m_1 = N_0 l_0$, therefore:

$$\bar{l}_{1,0} = \frac{m_1}{m_0} = \frac{l_0}{kt} \quad \text{Equation 6.58}$$

Hence:

$$n = \frac{N_0 l_0}{\bar{l}_{1,0}^2} e^{-\frac{l}{\bar{l}_{1,0}}} \quad \text{Equation 6.59}$$

However the results for $\bar{l}_{1,0} = \frac{l_0}{1+kt}$ is true at all times. Therefore n at all times is:

$$n = \frac{N_0(kt + 1)^2}{l_0} e^{-\frac{(kt+1)l}{l_0}} \quad \text{Equation 6.60}$$

Equation 6.60 has the correct moments at all times, and the correct shape for longer times. It can be used as an approximation of n for short times.

To get an expression for q_0 it is necessary to determine n/m_0 where $m_0 = \int_0^\infty n(l)dl = N_0 + N_0 kt = N_0(1 + kt)$:

$$q_0 = \frac{n}{m_0} = \frac{kt + 1}{l_0} e^{-\frac{(kt+1)l}{l_0}} \quad \text{Equation 6.61}$$

If the rate constant for binder breakage is known and the original length of the parent binder particle is specified, it is therefore possible to obtain the number based frequency density using the above expression.

6.15 Conclusions

A one dimensional population balance model has been developed to describe the breakage of powder coated binder particles. Breakage of particles has been discussed in a wide variety of other contexts, including milling and to describe the breakage that occurs during agglomeration (which may be undesirable). This study for the first time uses a model to describe how a semi-solid binder undergoes dispersion through fragmentation in the context of a high shear granulation process.

The key assumptions of this model is that breakage is uniform and binary i.e. when a particle of size l is selected for breakage it always breaks into 2 and the size of the fragments is evenly distributed between $x=0$ and $x=l$. It is, therefore, assumed that all sizes from 0 to l are equally likely. This means that a particle of length l , and constant diameter d (cross-sectional area remains unchanged after breakage) breaks into 2 particles of size x and $l-x$. The total length of the particles is conserved. It is also assumed

that initially mono-dispersed binder particles are present in the granulator i.e. a uniform distribution of granules of length l_0 and of number N_0 .

A self-similar solution for the population balance equation was found, which also satisfies the moment equations (m_0 and m_1). The non-dimensional numerical solution for the population balance equation is $\hat{n}(\hat{l}, \hat{t}) = \hat{t}^2 e^{-\hat{l}\hat{t}}$. An expression that predicts the change in the number based size distribution, q_0 , was subsequently determined. Some of the key properties of the model are summarised in Table 6.2. There are two parameters that could be changed in the model; the initial length of the parent binder particle (l_0) and the selection constant (k). The predicted size distribution is self-similar with time, in other words, the magnitude changes but the shape of the distribution does not.

Besides self-similarity in the calculated size distributions, other emergent properties include the change in the number of particles and the mean size. The number of particles increases linearly with time, as $m_0 = N_0 + N_0 kt$, whilst the number based mean size decreases with time, as $l_{1,0} = \frac{l_0}{1+kt}$.

Table 6.2. Key properties of the model.

	Dimensionless	Dimensional
Moments ($\forall t$)	$\hat{m}_0 = \hat{t}$ $\hat{m}_1 = 1$ $\hat{l}_{1,0} = \frac{1}{\hat{t}}$	$m_0 = N_0 + N_0 kt$ $m_1 = N_0 l_0$ $l_{1,0} = \frac{l_0}{1+kt}$
Size distribution	$\hat{n}(\hat{l}, \hat{t}) = \hat{t}^2 e^{-\hat{l}\hat{t}}$	$n = \frac{N_0(kt+1)^2}{l_0} e^{-\frac{(kt+1)l}{l_0}}$ $q_0 = \frac{kt+1}{l_0} e^{-\frac{(kt+1)l}{l_0}}$

Chapter 7 Validation of the population balance model for breakage

Chapter 6 describes a model for the breakage of PCBPs. There are two parameters that could be adjusted in the model these include: the initial length of the parent fragment (l_0) and the selection constant (k). The data from the experimental work that was presented in Chapter 5 is used to validate the model. The number based frequency densities (q_0) of the PCBPs were measured using a Camsizer. In all experimental work l_0 was kept constant. A value of k was determined from the experimental data, in order to validate the model.

7.1 Methodology for determining k

A selection function was defined and incorporated into the breakage model (Equation 6.20). It is assumed that larger and/or longer PCBPs are more likely to undergo breakage i.e. particles break at a rate proportional to their size.

The dimensional equation for the size distribution function (Equation 6.61) is:

$$q_0 = \frac{kt + 1}{l_0} e^{-\frac{(kt+1)l}{l_0}}$$

Taking the natural log of both sides gives:

$$\ln q_0 = \ln \left(\frac{kt + 1}{l_0} \right) + \left(-\frac{(kt + 1)}{l_0} \right) \cdot l \quad \text{Equation 7.1}$$

The gradient (z) of a of $\ln q_0$ vs. l (or x_{mean} from the Camsizer) plot should give $-\left(\frac{kt+1}{l_0}\right)$. l_0 is a constant (25000 μm) for all cases. k is therefore:

$$k = \frac{zl_0 - 1}{t} \quad \text{Equation 7.2}$$

7.2 Fitting trend lines to the experimental data

k was determined for all materials that were used in this study - zeolite, ground ash and light ash. The three powders have a volume based mean size of 9, 11 and 130 μm re-

spectively. For each material, experiments were conducted at two different impeller speeds – 300 and 600 rpm. Therefore, the effect of both particle size and impeller speed on the breakage selection constant was elucidated.

This study concerns the breakage of PCBPs, which only occurs during the initial stages of the binder dispersion process. Hence, values of the selection constant were only determined at time points where binder dispersion dominates within the granulator. At 600 rpm, for ground ash, the mixture transitions to the growth phase after 90 s of wet massing and for light ash the same phenomenon is observed after 15 s of wet massing. Therefore, data was only considered up to 90 s for ground ash. For light carbonate, it is not possible to get enough information after 15 s of wet massing, so the dataset was disregarded.

The number based particle frequency density (q_0) of the PCBPs was measured using the Camsizer P4. The Camsizer also detects primary powder particles that are smaller than 200 μm , which are shed from the PCBPs. These particles are not PCBPs and were therefore, excluded from the size distributions. The size distributions were subsequently re-normalized and number based mean length ($\bar{l}_{1,0}$) was determined from these distributions.

The natural log of q_0 was subsequently determined – refer to Figure 7.1- Figure 7.5 for the semi-log plots of $\ln q_0$ against particle diameter. Note that only selected time points have been displayed graphically. A linear trend line was fitted to all available time points in order to find z . The value of k was subsequently determined using Equation 7.2. Figure 7.1 - Figure 7.5 serve to show how well the model is able to predict the mean size of the PCBPs. As the data points lie on straight lines, they indicate the mean size may be predicted using the following expression: $l_{1,0} = \frac{l_0}{1+kt}$.

The values of the rate constants presented in Figure 7.6 and Figure 7.7 are only valid for parent binder particles that are 25,000 μm in size. It is expected that a smaller particle will have a breakage rate constant that is proportionally smaller. It appears that k varies as a function of time (Figure 7.6). This could be due to a change in the shape with time. Cylindrical particles of a given length are more likely to break than spherical particles

of that diameter. A phase change (i.e. as more solid gets loaded within its structure) may alter its breakage dynamics too. The results also suggest that breakage events on average, occur once every 2 s, as $k = 0.5$, which is much faster than the rate of change of k .

The value of k is highest for the light carbonate system and lowest for the zeolite system (Figure 7.6). This is in agreement with the findings reported in Chapter 5 in that larger and rougher particles are able to break and disperse the PCBPs more rapidly, in comparison to smaller more circular ones. Also notable is the larger value of k at higher impeller speeds (Figure 7.7). The greater stresses acting within the system at higher impeller speeds facilitate breakage events more often, thus increasing the value of k .

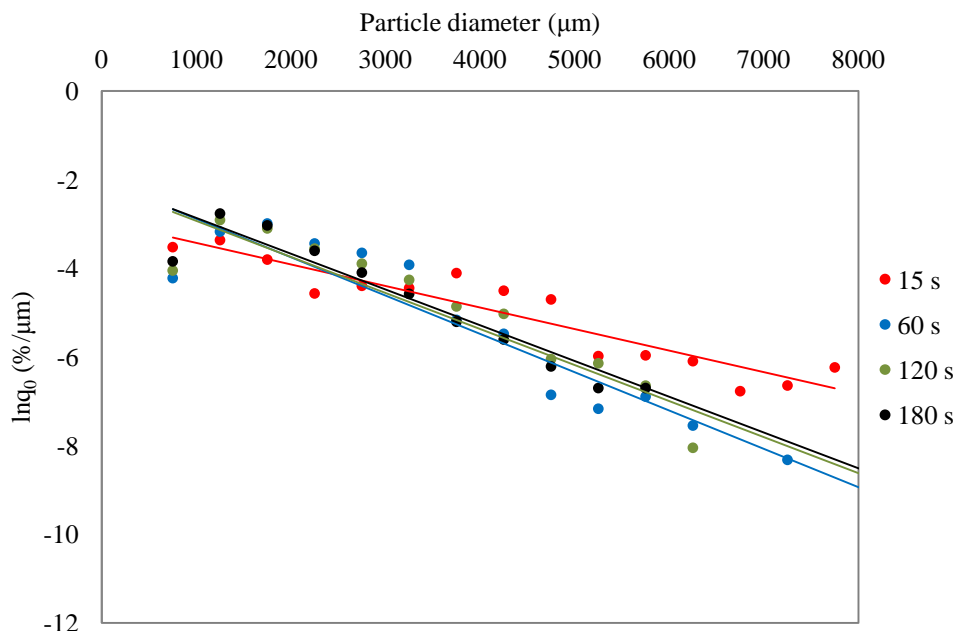


Figure 7.1. Experimental plot of $\ln q_0$ vs. particle diameter for zeolite at 300 rpm.

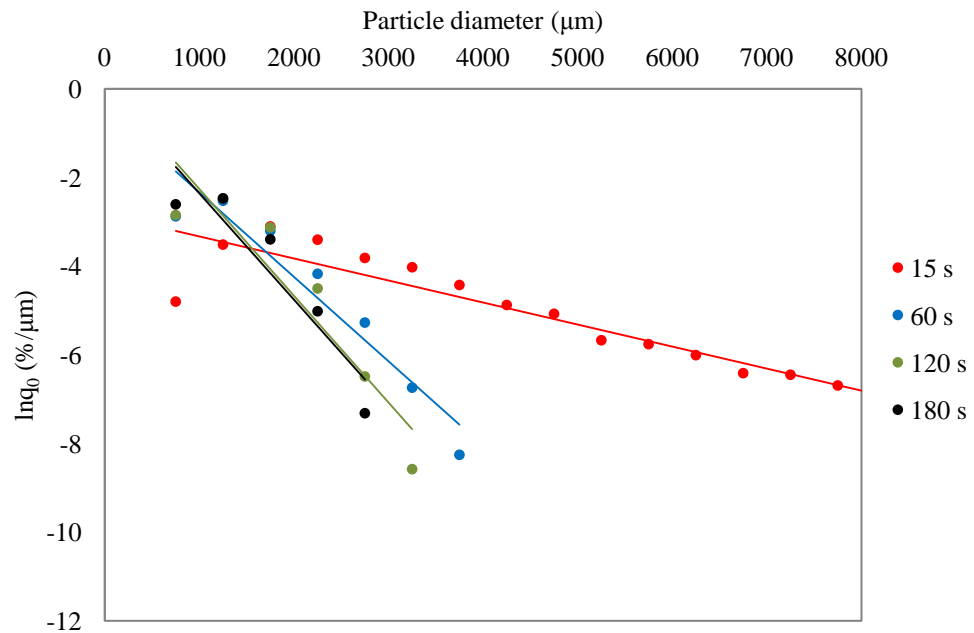


Figure 7.2. Experimental plot of $\ln q_0$ vs. particle diameter for zeolite at 600 rpm.

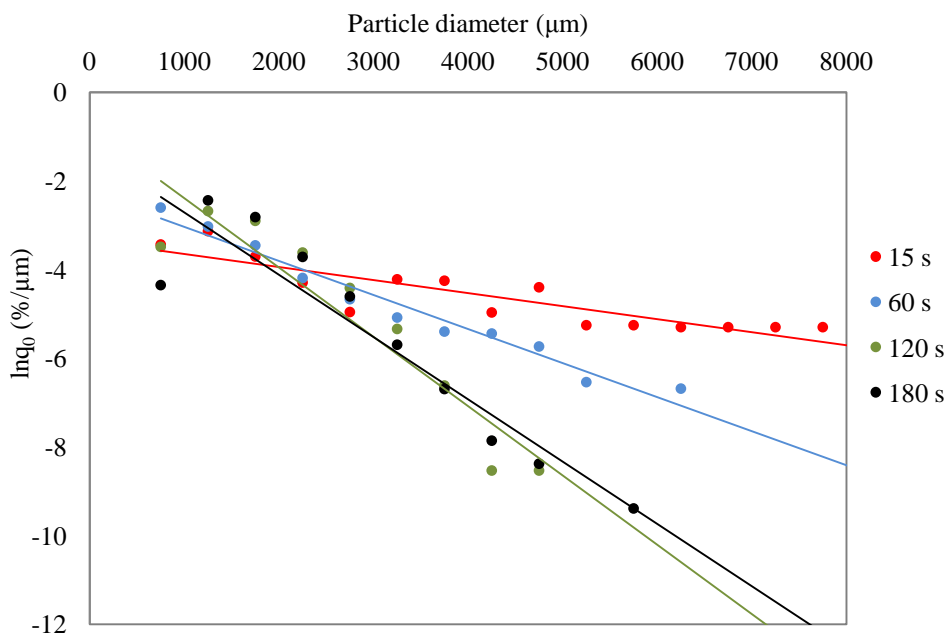


Figure 7.3. Experimental plot of $\ln q_0$ vs. particle diameter for ground ash at 300 rpm.

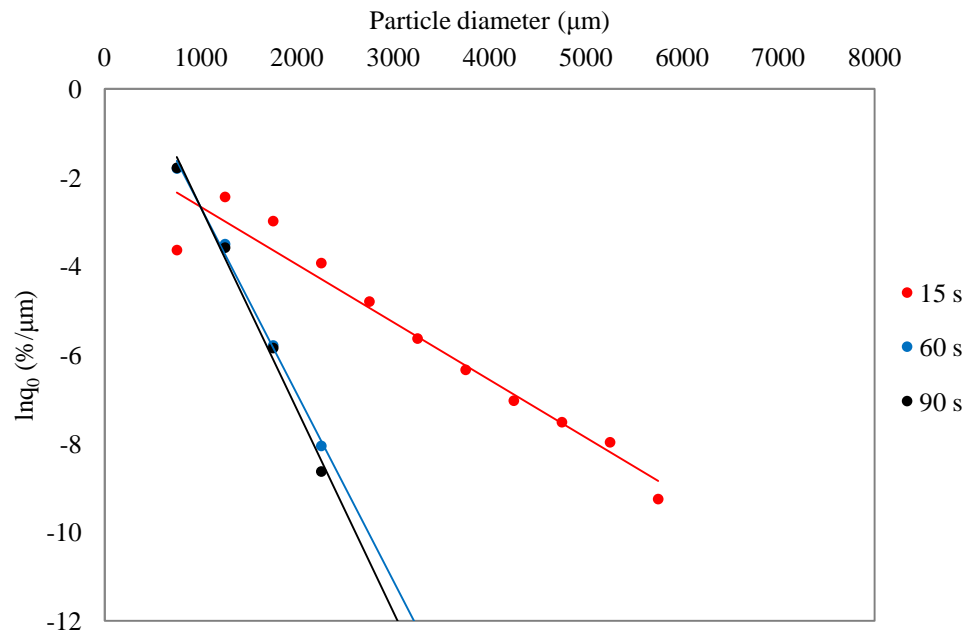


Figure 7.4. Experimental plot of $\ln q_0$ vs. particle diameter for ground ash at 600 rpm.

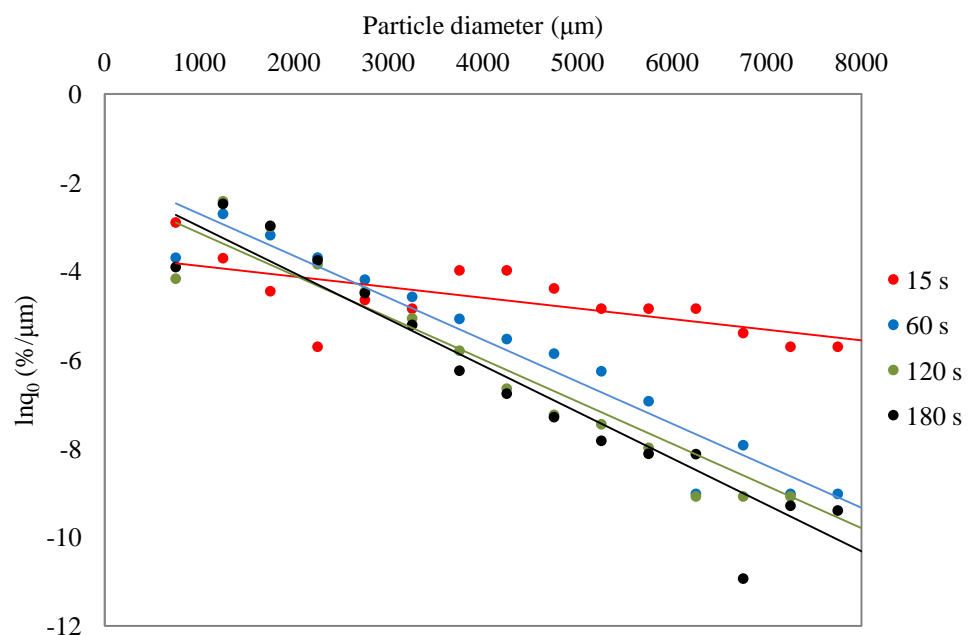


Figure 7.5. Experimental plot of $\ln q_0$ vs. particle diameter for light ash at 300 rpm.

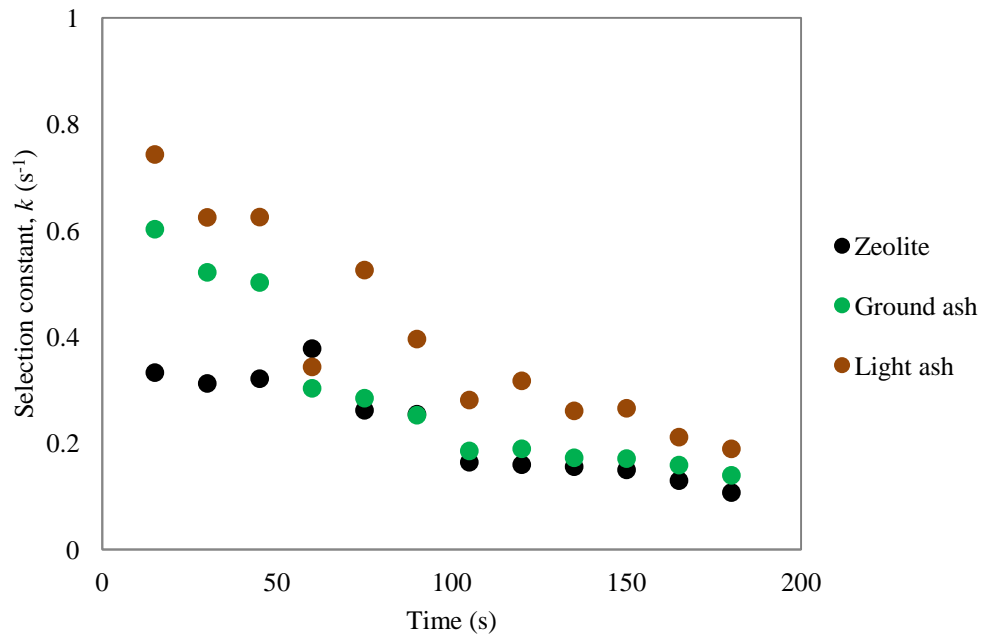


Figure 7.6. Selection constant against time for zeolite, ground ash and light ash at 300 rpm.

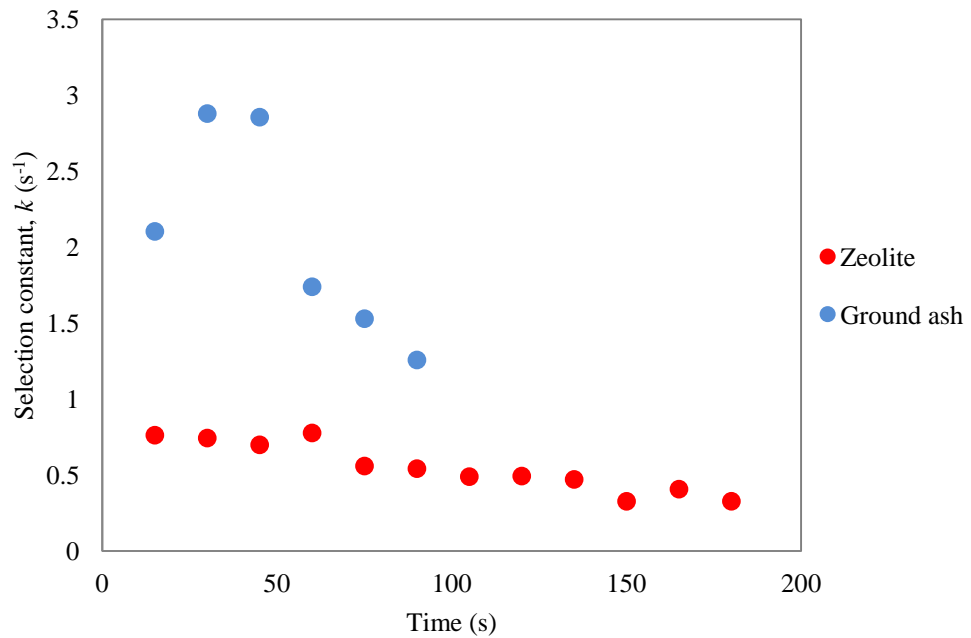


Figure 7.7. Plot of selection constant against time for zeolite and ground ash at 600 rpm.

7.3 Comparing the experimental mean length with the predicted mean length

For all experiments, the value of the mean length obtained from the Camsizer was compared with the calculated value of the mean length. Particles of a certain size class were excluded when conducting the size measurements, in order to eliminate the effect of any fine powder that was shed from the PCBPs from influencing the magnitude of the number based mean length. The experimental data is, therefore, truncated. However, when calculating the mean length of the PCBPs using Equation 6.36 in its current form, the number of particles in all the size classes ranging from 0 to ∞ were considered. An adjustment needs to be applied to the expression m_1/m_0 to account for this.

Mathematica was used to find and simplify an expression assuming a semi-infinite domain that ranges from l_{min} to ∞ . Both the moments (m_0 and m_1) were adjusted, taking into consideration this semi-infinite range (Equation 7.3 and Equation 7.4) and another expression for $\bar{l}_{1,0}$ was determined (Equation 7.5).

$$m_0(t) = \int_{l_{min}}^{\infty} q_0(l, t) dl = e^{-\frac{l_{min} + kl_{min}t}{l_0}} \quad \text{Equation 7.3}$$

$$m_1(t) = \int_{l_{min}}^{\infty} lq_0(l, t) dl = \frac{e^{-\frac{l_{min} + kl_{min}t}{l_0}} (l_0 + l_{min} + kl_{min}t)}{1 + kt} \quad \text{Equation 7.4}$$

It follows that:

$$\bar{l}_{1,0}(t) = \frac{m_1(t)}{m_0(t)} = \frac{l_0 + l_{min} + kl_{min}t}{1 + kt} = l_{min} + \frac{l_0}{1 + kt} \quad \text{Equation 7.5}$$

Consider Equation 7.5, when $t \rightarrow \infty$, $\bar{l}_{1,0} = l_{min}$. It becomes apparent that excluding the smaller size classes from the experimental data makes the experimental mean consistently larger than the predicted mean. Adjusting the calculated value to account for a minimum size l_{min} (where $l_{min} > 0$) corrects this.

l_{min} was determined from y-intercept of a plot of $\bar{l}_{1,0}$ against $\frac{l_0}{1+kt}$, and was found to be 1000 μm . Primary powder particles that are smaller than 200 μm were excluded by sieving. The discrepancy between the two values can be accounted for by the differences in size measurements techniques. Sieving separates particles based on their minimum chord length ($x_{c\ min}$), whilst the Camsizer measures size based on the projected area (x_{area}).

A plot of the experimental mean length against the predicted value of the mean, which now accounts for l_{min} , is shown in Figure 7.8. The mean size predicted using the asymptotic self-similar model for binder breakage is in good agreement with the experimental mean size. The model can therefore, be used to make a priori predictions of the change in the number based mean particle length with time.

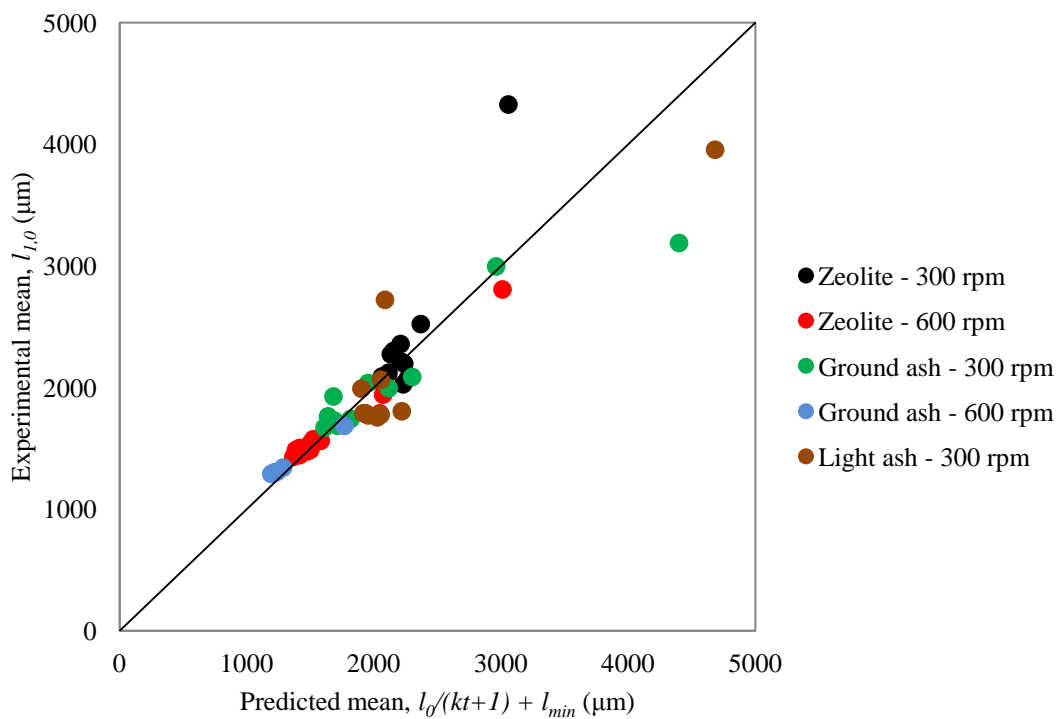


Figure 7.8. Comparing the experimentally determined value for the mean size ($\bar{l}_{1,0}$) with predicted mean ($l_0/(kt+1) + l_{min}$).

7.4 Conclusions

The model developed in Chapter 6 was successfully validated using the experimental data from Chapter 5. There are two parameters that could be adjusted these include: the

initial length of the parent fragment (l_0) and the selection constant (k). In all experimental work l_0 was fixed. The expression for q_0 was rearranged in order to determine a value of k from the experimental data plots of q_0 vs. mean length.

It was found that the k is time dependant. This was attributed to a change in the shape of the PCBPs with time. With increasing granulation time, the PCBPs become more spherical. In addition, a phase change (i.e. as more solid gets loaded within its structure) may alter its breakage dynamics too, and this has not been accounted for in the model.

It was also found that the changes in the particle size distribution, as a result of the breakage of PCBPs are self-similar with time. Self-similarity means the shape of the size distribution does not change, whilst $\bar{l}_{1,0}$ does. As the size distribution gets scaled and $\bar{l}_{1,0}$ changes, k also changes, but at a much slower rate. The system thus behaves as though k is a constant over a period of time. The experimental data suggests that breakage events on average, occur once every 2 s.

For experiments conducted at higher impeller speeds the value of k is larger due to greater mixing energy. Results also suggest that using larger primary particles enhances the rate of binder breakage.

This deterministic model is able to predict the change in the number based mean length of the PCBPs with time. An advantage of using this model is its simplicity i.e. it can be solved analytically to give a closed form solution that can be used to understand and quantify the early stages of the binder dispersion process. The breakage process has therefore, been successfully modelled using a kinetics approach in this study.

Chapter 8 Reactive granulation using linear alkylbenzene sulphonic acid

8.1 Introduction

As discussed in Section 2.4, both non-reactive and reactive surfactants are employed for the manufacture of dry laundry powders. This chapter looks into the dispersion of a reactive binder in a pilot scale high shear wet granulator.

Section 4.8 outlines the use of thermal imaging as a technique for monitoring the dispersion of a binder in a vertical shaft high shear mixer. The movement of individual lumps of binder could be tracked using a thermal camera, providing there is a temperature difference between the powder and binder.

This chapter discusses the use of thermal imaging for monitoring the dispersion of a reactive binder in a moving bed of powder. The interactions between the binder and powder under static conditions have also been investigated here, to gain some insight on the processes that take place on a meso-scale. A reactive binder was chosen for this study, as reaction between the binder and the powder is exothermic. This heat signature could be used to track the binder within a moving bed of powder.

8.2 Paddle mixers

A pilot scale, 32 L batch paddle mixer (Bella B-32-XN) with a horizontal twin-shaft was used in this study. The shafts are counter rotating and intermeshing. Material is charged from the top of the mixer, and discharged through two large doors located at the bottom of the mixer. The paddles have a radius of 9.5 cm. The equipment has a maximum speed of 225 rpm ($v = 2.24 \text{ m/s}$). More details about mixer can be found in Section 3.2.

Paddle mixers are used in applications where even and gentle mixing is required. The air space directly above the paddles aids in fluidising the material, during operation. The paddles lift material along the centre of the mixer where most of the mixing is believed

to take place. This section is referred to as the fluidised zone (Figure 8.1), as material is suspended momentarily, in a weightless state. Binder is injected from the bottom of the mixer in to the fluidised zone. Transport of the materials is axial and bidirectional. They are mainly used for bulk solids blending, which is carried out in a wide variety of industrial processes including ceramics, chemicals and fertilisers (Tekchandaney, 2012). The properties of the powders that are being mixed, such as particle size, shape, density, surface characteristics (roughness), and cohesiveness, have an influence on how well a mixture can be blended.

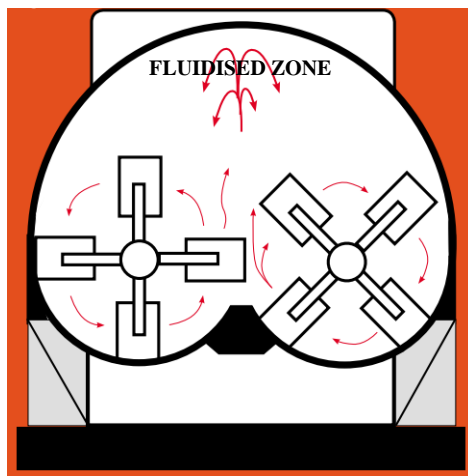


Figure 8.1. Cross-section through a paddle mixer indicating the location of the fluidised zone (Rodenburg, 2007).

Three main mechanisms of blending exist, including diffusion blending, convection blending and shear blending. These mechanisms occur to various extents depending on the type of mixers. Diffusion blending is characterised by small scale random motion of the particles, whereas convection blending is characterised by larger scale random motion, which leads to groups of particle being rapidly moved from one position to another. Shear blending refers to the formation of slip planes or shearing strains in a moving powder bed. Shear blending is ideal for creating small scale, localised uniformity. Within a paddle mixer, macro-scale blending occurs due to the convection blending mechanism, meso-scale blending occurs due to the shear blending and micro-scale blending at new interfaces through diffusion blending (Tekchandaney, 2012).

Generally, the intensity of mixing would depend on the speed and shape of the mixer. There are three distinct regimes which can be identified during operation (Muzzio et al., 2004). At lower speeds, the powder is carried by the rotation and descends by rolling and or sliding along the surfaces of the solids mass (similar to rotating drums). This is referred to as cascading. At medium speeds, the powder is carried by the paddle and drops either by sliding, rolling or cascading. This is referred to as cataracting. At higher speeds (equilibrium regime), the powder is mostly lifted by the paddles and slides off at the end. Paddles can be positioned to increase lateral/back mixing, as well as axial mixing. Scale up of paddle mixers is normally based on mixer speed (tip speed), mixing time and fill level (Muzzio et al., 2004).

So far some key aspects of bulk solids blending in a paddle mixer have been outlined. However, more recently, these mixers have been used in solid-liquid mixing applications, like granulation (Pasha et al., 2015, Hassanpour et al., 2011, Li et al., 2013). The time taken for the granulation end point to be reached is also dependent on the material cohesivity and the impeller speed. When distributing a liquid binder into a powder bed, the mixing time is greater if the cohesivity of the powder is high, as the powder has a tendency to segregate. This is true for powders like zeolite, which are very fine and have a tendency to adhere to one another, resulting in poor flowability (Miyazaki and Arika, 1983). An analysis of the particle motion in a paddle mixer was done by Hassanpour et al. (2011). A DEM simulation was used to model the velocity distribution within a paddle mixer. This model enabled the flow inside a paddle mixer to be predicted for a dry powder bed. Positron Emission Particle Tracking (PEPT) was used to validate the DEM simulation and there was reasonable agreement between the two techniques in terms of velocity distribution. Their work does however, conclude that there is a room for improvement in terms of eradicating the minor systematic difference between the distributions produced from the two different techniques. Only one particle can be tracked using the PEPT approach, and it may take a long time for the particle to visit all the locations inside the equipment several times. Also, since the tracer particle is made of a radioactive material, the properties of the tracer particle are not necessarily the same as those of the surrounding powder particles. The difference in particle properties, such as particle size, may cause an undesirable phenomenon such as segregation.

Furthermore, the signal (γ -rays) from the tracer particle may be scattered and attenuated by equipment and other particles. The scattering of the signal may cause a detection of an incorrect particle position and the attenuation of the signal may cause a failure to detect the particle position. This is the best available technology for predicting and visualising flow field in the paddle mixer at the time. The present study has developed an experimental technique for looking at flow field of the binder within the paddle mixer, which is germane to process understanding based on first principles and for developing models for process scale-up. This study is also the first attempt at looking at the flow and movement of a binder in a moving bed of powder, without the use of a tracer particle, in a wet granulation application.

8.3 Simulating nuclei formation using droplet of binder on a static powder bed

Section 2.9 discusses the properties of the reactive binder and the chemical changes it undergoes during the granulation process. The reaction between the binder and surfactant causes a localised increase in the viscosity of the binder. This may hinder its subsequent dispersion within the powder bed. Some meso-scale experiments were conducted on a static bed of powder (a compact) to understand the interactions between the binder and powder, and also to gain some insights, as to how the materials could behave within the mixer. The key outcomes have been discussed in this section.

Schöngut et al. (2011) also conducted experiments on a static bed of powder and they discuss the kinetics of the neutralisation process and identify two major steps when the binder comes into contact with the powder: (i) penetration of the liquid binder into the surface of the powder bed and (ii) an increase in the size of the droplet as a result of the evolution of carbon dioxide gas (due to chemical reaction). This work compares the interactions of the same binder on a reactive and a non-reactive system, and also studies the impact of binder temperature on its subsequent penetration and spreading.

5g of each test material (light ash, ground ash and zeolite) were compressed using a load of 500 N in a 30 mm die, using the Instron 3367 tensile test machine. At forces lower than this, it was not possible to produce a good compact. Ten compacts were made for each test material and the compression rate was set to 1 mm/min. A slow compression

speed was chosen to give the particles in the loose bed of powder sufficient time to rearrange themselves, thus ensuring better reproducibility. The porosity of the light ash, ground ash and zeolite compacts were determined to be 8.4, 3.4 and 2.8 % respectively (Figure 8.2). It is expected that larger particles will produce a compact with a higher porosity when compressed using the same load. All compacts were equilibrated in an environmental chamber for 24 hours at 25°C and 40% relative humidity.

The first set of experiments was conducted at room temperature (25°C). A small 50 µl droplet was added onto the surface of the loose compact using an Eppendorf Multipette Stream pipette. The distance between the pipette tip and the surface of the tablet was kept constant at 20 mm, which is small enough to neglect the influence of any impact forces (due to gravity) on both the deposition of the droplet and its subsequent spread on the surface of the test substrate. The droplet has a mass of 0.055g. The compact was stored in an air tight Petri dish for 48 hours, before the nuclei was removed and weighed. Of the three different materials, light ash showed the greatest interaction with the binder, whilst zeolite showed a minimal interaction with the binder (Figure 8.3 and Figure 8.4). The results also reveal that nuclei produced using the light ash are 31% heavier than the nuclei made with ground ash.

The binder does not spread very well on the surface of the zeolite compact, when compared to the surface of the light and ground ash compacts (Figure 8.4). It is also hypothesised that carbon dioxide evolution will result in an expansion of the droplet not just in the vertical direction, but also in the horizontal direction. This in turn will improve contact between the HLAS and un-reacted powder, thus increasing the mass of the resultant nuclei. The ground ash nuclei weigh less than the light ash nuclei, as ground ash particles are smaller. The smaller particle size results in a more rapid rate of reaction, and this in turn increases the viscosity of the binder and reduces its spread. Therefore, ground ash nuclei are lighter than light ash nuclei. Also, a powder bed consisting of larger particles has a higher porosity; therefore more binder can penetrate the bed, resulting in the formation of larger and heavier nuclei for light ash.

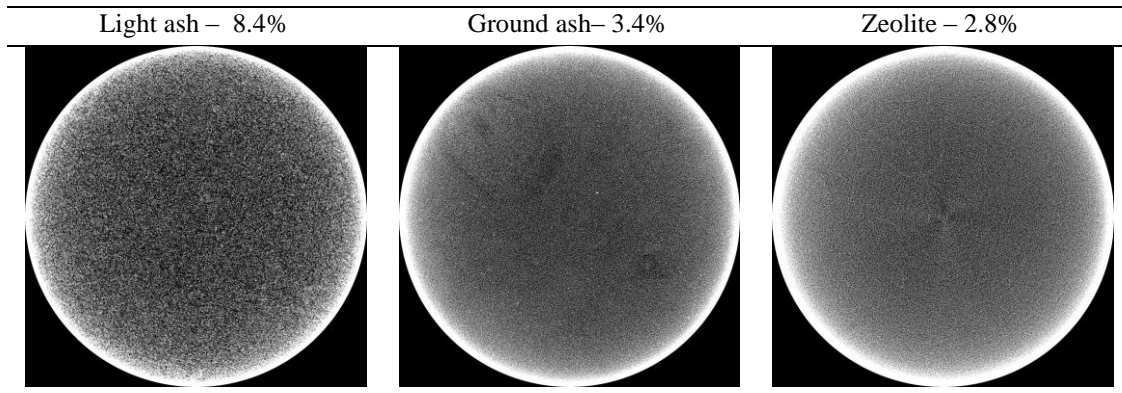


Figure 8.2. Porosity of the loose compacts was determined using X-ray tomography – compression load was 500 N.

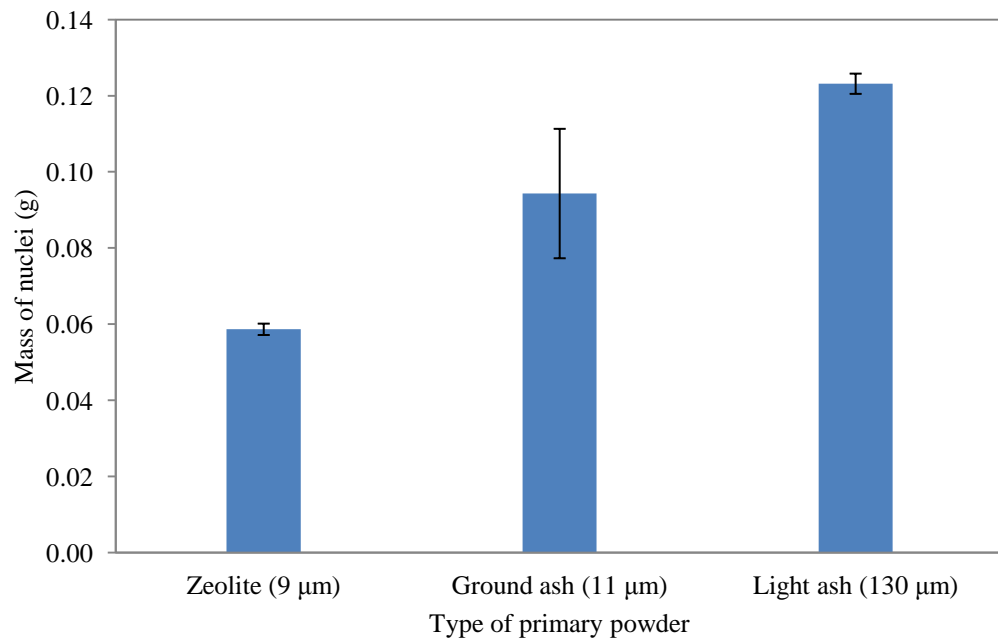


Figure 8.3. Mass of the nuclei - weighed after 48 hours.

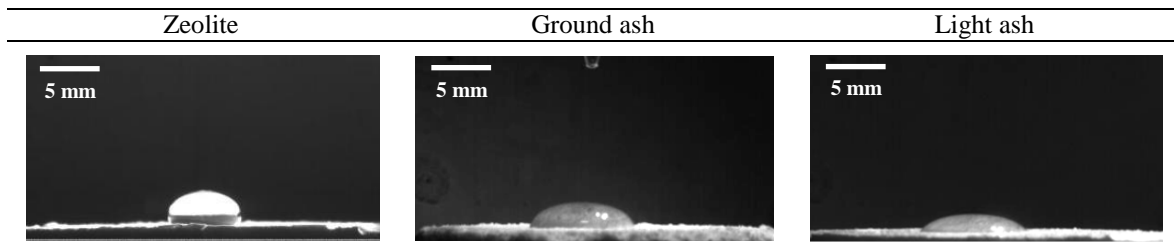


Figure 8.4. Spread of a droplet of LAS acid on the surface of a compact.

The effect of the change in the temperature of the binder was also investigated. Both the binder and the powder bed were equilibrated to the same temperature. It is known that an increase in the binder temperature results in a corresponding decrease in the binder viscosity (Figure 3.16). This in turn should make the binder more flowable on the surface of the substrate, thus increasing its spreadability. An increase in the spread of the binder should, therefore, increase the mass of the resultant nuclei that are produced. However, for HLAS, an increase in the temperature of the binder will also result in an increase in the rate of reaction between the powder and binder (when considering the compacts made of sodium carbonate). It is known that as the reaction progresses, the amount of LAS-Na at the boundary between the droplet and the surface of the substrate increases (refer to Section 2.9). LAS-Na has a much higher viscosity in comparison to HLAS. Therefore the viscosity at the interface starts to increase and this localised increase will limit its spread across the surface of the compact. This explains a reduction in the size (mass) of the nuclei, with an increase in the temperature of the binder (Figure 8.5). Also, as zeolite does not react with the LAS acid, there is a slight increase in the mass of the nuclei, with an increase in the temperature.

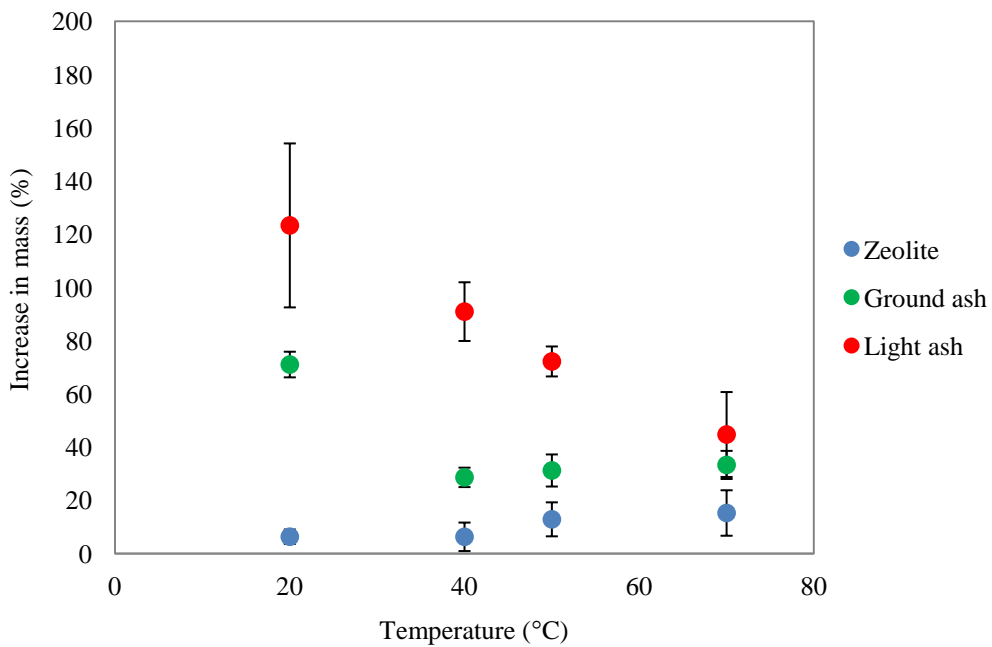


Figure 8.5. Percentage increase in the mass of the nuclei against temperature.

8.4 Monitoring the dispersion of HLAS in situ

So far the meso-scale effects of both the variation in the particle type and size, as well as the temperature of the binder have been studied, for static conditions. Studying the impact of binder temperature has helped elucidate the effects of the rate of reaction on the subsequent spread of the binder and nuclei formation. It is also of interest to understand the reactive binder dispersion process within an agglomerator, under dynamic conditions. A similar study was conducted on the vertical shaft 10 L Roto Junior high shear mixer using a non-reactive binder, and the results were discussed in section 4.8. In summary, the thermal camera was used to successfully track individual blobs of binder at tip speeds of around 3 m/s. The binder was heated to a higher temperature than the powder, so that its heat signature could be traced around the mixer. A similar approach for tracking the binder distribution is easier to apply to a granulation operation involving the use of a reactive binder in a paddle mixer, as the exothermic nature of the process enables the heat trail to be monitored and the mixing environment is not very aggressive (the maximum tip speed is less than 2.5 m/s for the 32 L paddle mixer used in this study).

The mixer was split into 5 sections based on the distance from the zone of binder injection (Figure 8.6). Binder was injected into the mixer in zones 3 and 4, through 4 individual inlets. Each inlet nozzle has a diameter of 3 mm. The dashed line in Figure 8.6 indicates the location of the fluidised zone along the axis of the mixing vessel. The mixer has also been split in two regions **Side A** and **Side B** in the horizontal direction (when viewed from above) in order to isolate and describe what happens along each mixing shaft.

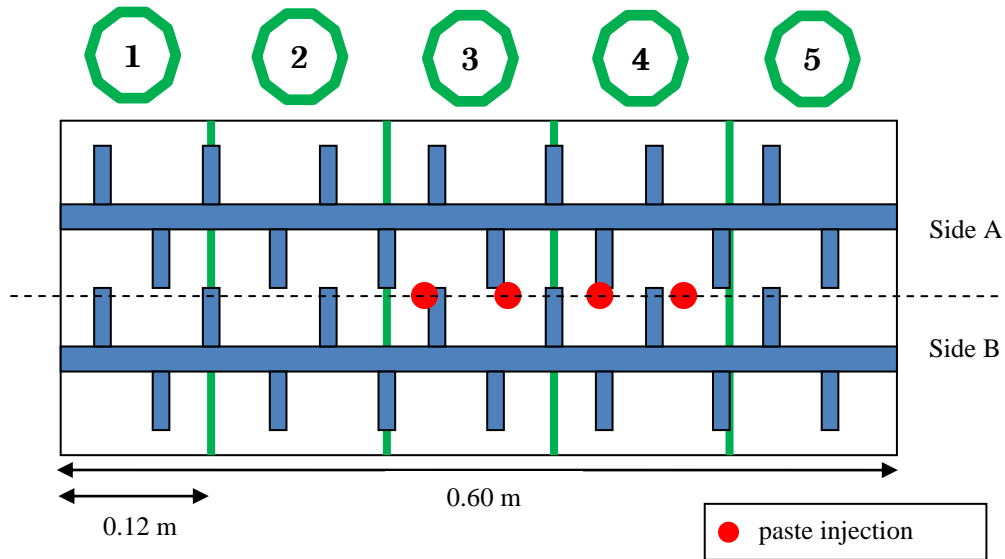


Figure 8.6. Schematic of the aerial view of the paddle mixer. The mixer was split into different zones and binder was injected in zones 3 and 4. The dashed line indicates the position of the fluidised zone.

The exothermic reaction between the carbonate and HLAS enables identification of the binder rich zones within the mixer. A coated blob of binder will appear hotter than the rest of the powder in the mixer (Figure 8.7). Good mixing between the powder and the binder will shorten the lifespan of any blobs of binder that are present in the moving bed. As these coated blobs get deformed within the mixer, a fresh liquid layer is exposed, providing a site for further particle contact and reaction. Refer to Section 3.13 for further details about the thermal imaging technique. The thermal camera was set to take images at 50 frames per second (resolution 640×480 pixels). The 32-bit colour thermal images were subsequently converted into the binary format using ImageJ software (Figure 8.7), and after appropriate threshold limits were applied, regions where binder is present were displayed as black spots. A particle image velocimetry (PIV) analysis was subsequently conducted on the binary images to determine the velocity vectors of the binder (Figure 8.8). More details about the PIV technique can be found in Section 3.14.

As the paddle mixer has twin shafts that are counter rotating, it was discovered that the direction of binder motion within the paddle mixer is strongly dependant on its position within the mixer (Figure 8.8). Side A conveys binder to the left whilst the Side B conveys binder to the right. Each shaft carries material in a different direction and the in-

termeshing paddles result in the exchange of material from the A to B and vice versa in the fluidised zone.

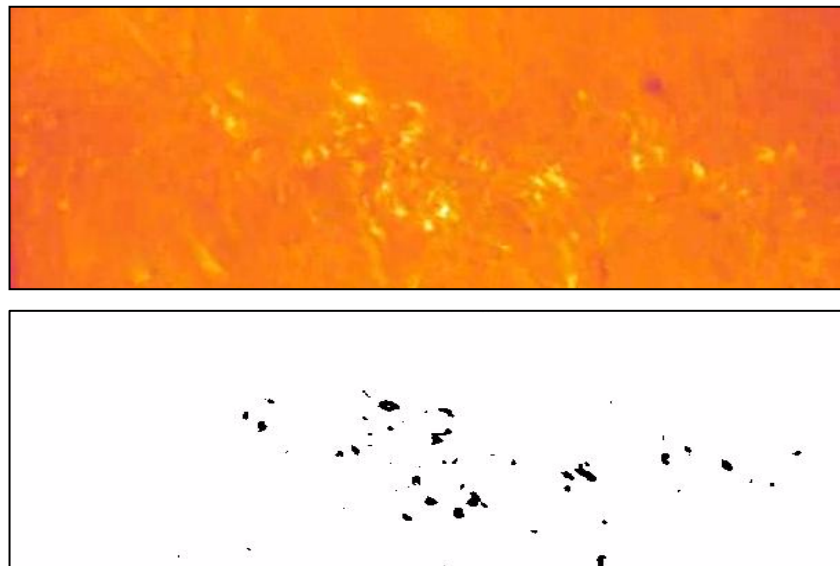


Figure 8.7. (a) thermal image and (b)binary image.

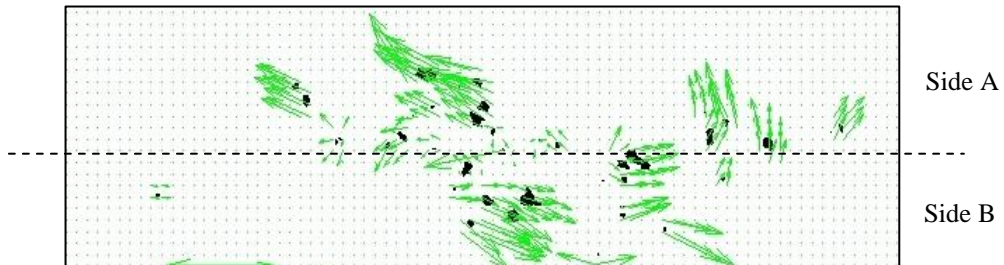


Figure 8.8. Output from PIV analysis showing binder movement within the paddle mixer as vectors.

The influence of particle size and impeller speed on the dispersion of the binder within the paddle mixer was investigated. Sodium carbonate powder was used for all experiments, as it reacts with the binder, and sufficient material (25 kg) was added to cover the paddles and shafts (fill level $\approx 40\%$) for each trial. Powder was charged into the mixer at an ambient temperature of 22°C. Binder was continuously injected at a rate of 2 L/min (Figure 8.9). The temperature of the binder was maintained at 40°C, and at this temperature the binder viscosity was measured to be 0.4 Pa.s (refer to Section 3.4 for more details on the viscosity measurement). The binder is the limiting reagent, and the powder is continuously conveyed immediately above the point of binder injection,

which helps to ensure the material is in continuous contact with the binder. Dispersion was monitored for 60 s. In order to assess the effectiveness of the binder dispersion process in a paddle mixer, thermal images were taken as a function of time to qualitatively observe the spread of the binder within the mixer. Also from Figure 8.6, it is evident that Zone 1 is furthest away from the point of binder injection; therefore the average temperature of Zone 1 was monitored and compared for different experimental conditions. If the dispersion process within the mixer is good, then the temperature of Zone 1 (and the contents of the mixer, as a whole) should increase rapidly. This was used as a measure of the efficiency of the binder dispersion process within the paddle mixer.

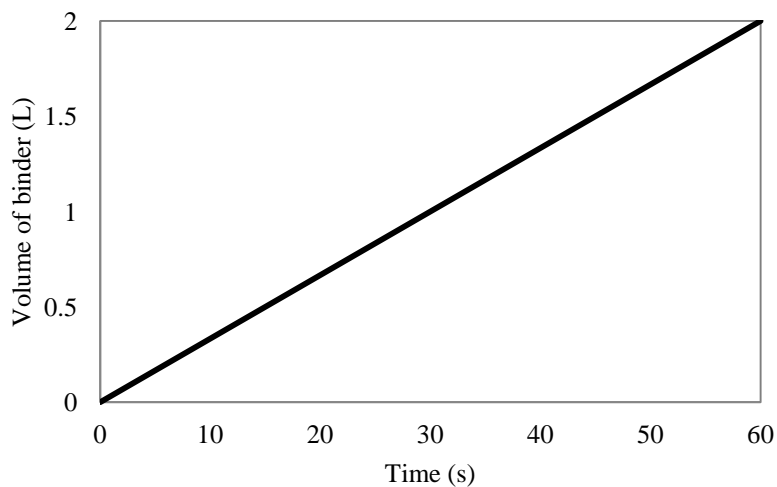


Figure 8.9. Volume of binder injected into the mixer.

8.5 Effect of particle size on binder dispersion

The dispersion of binder in a bed of light ash was compared with the dispersion in a bed of ground ash. The paddle mixer was operated at 50 rpm, and this corresponds to tip speeds of 0.5 m/s. The thermal images indicate the spread of binder in a moving bed of light ash is faster (Figure 8.10). Also comparing the average temperature of Zone 1 (Figure 8.6) indicates a more even distribution of binder for light ash, after 60 s of wet massing, as indicated by the higher average temperature (Figure 8.11). This confirms that better binder distribution is achieved in a powder bed consisting of larger particles.

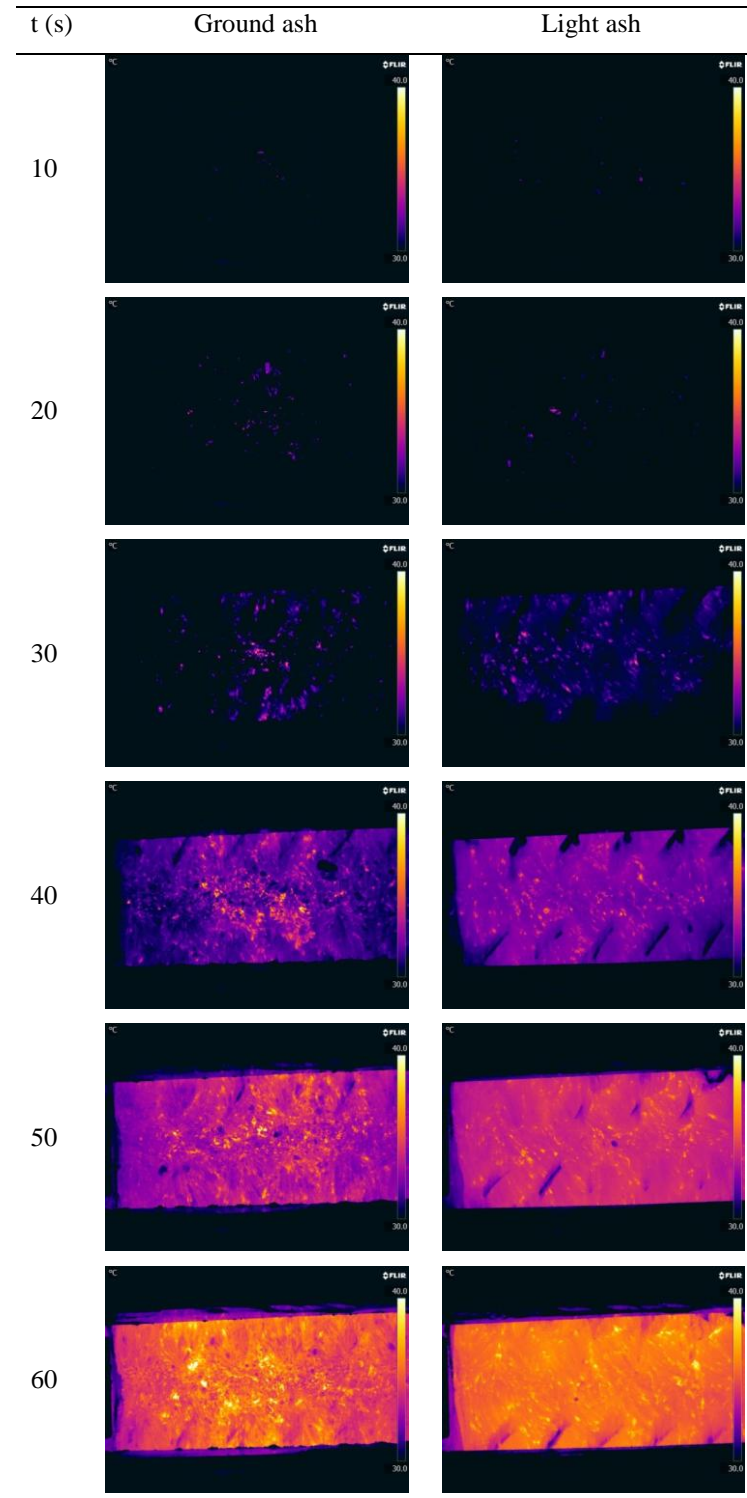


Figure 8.10. Thermal images comparing the dispersion of binder in a moving bed of ground and light ash at 50 rpm.

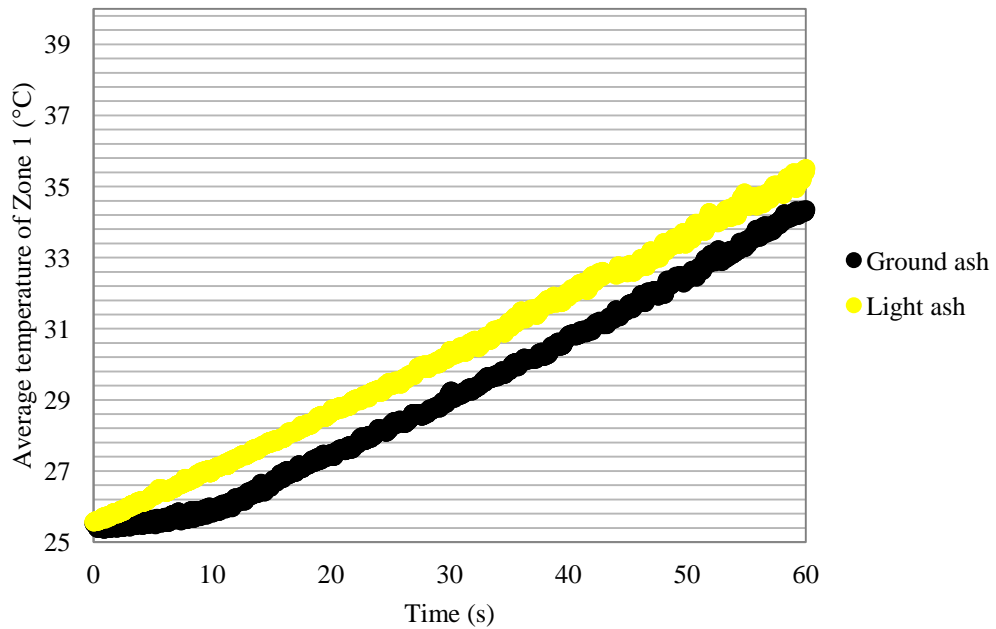


Figure 8.11. Average temperature of Zone 1 for a bed of light and ground ash at 50 rpm.

8.6 Effect of impeller speed on binder dispersion

This section compares the effect of impeller speed on the binder distribution process. The mixer was operated at a higher speed of 100 rpm, and this corresponds to a tip speed of 1 m/s. At this speed images were taken at 100 fps. A higher frame rate was chosen in order to be able to visualise the blobs of binder more clearly, therefore the resolution of the resulting images was lowered to 640×240 pixels. The results are shown in Figure 8.12. After 60 s, of wet massing the binder distribution is better at the higher impeller speed, as the average temperature of Zone 1 is higher at 100 rpm (Figure 8.13). Also the temperature distribution across the mixer seems more even (compare Figure 8.12 with Figure 8.10). Greater shear and impact, at higher impeller speeds, dissociates and disperses the blobs of binder more rapidly.

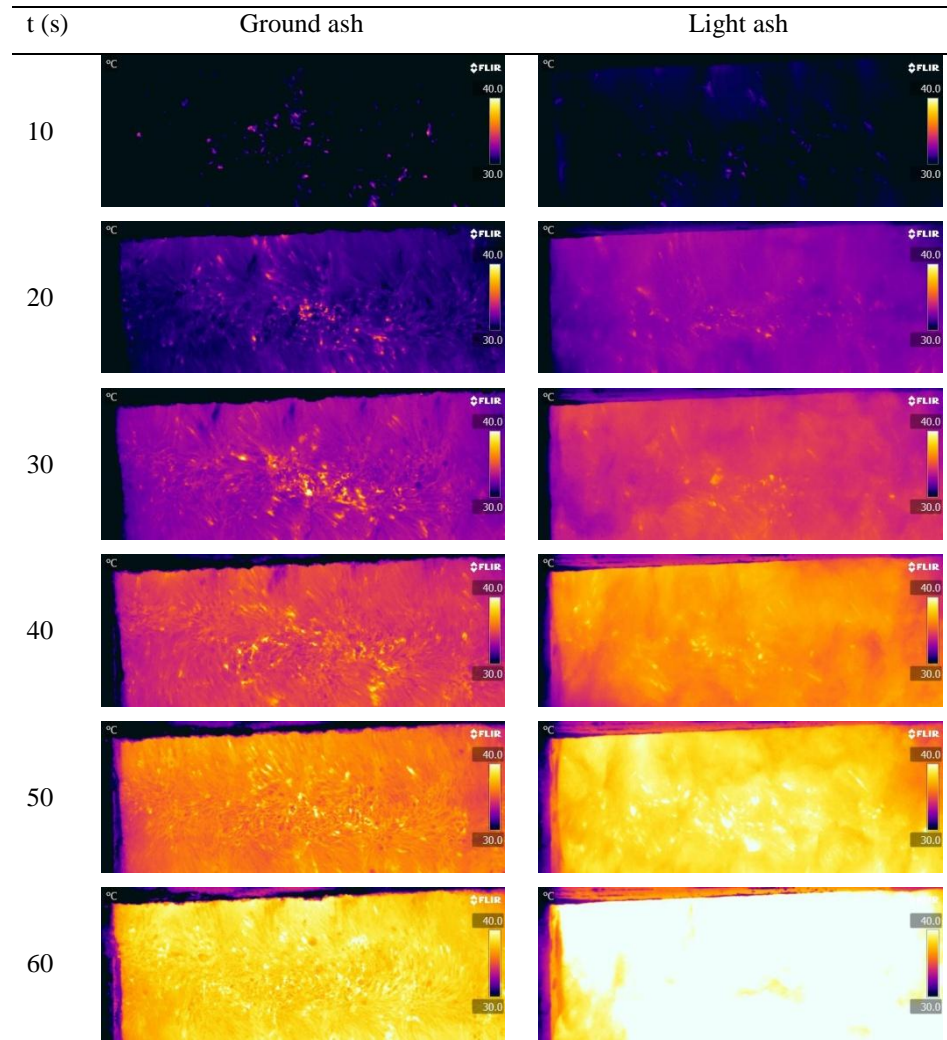


Figure 8.12. Thermal images comparing the dispersion of binder in a moving bed of light and ground ash at 100 rpm.

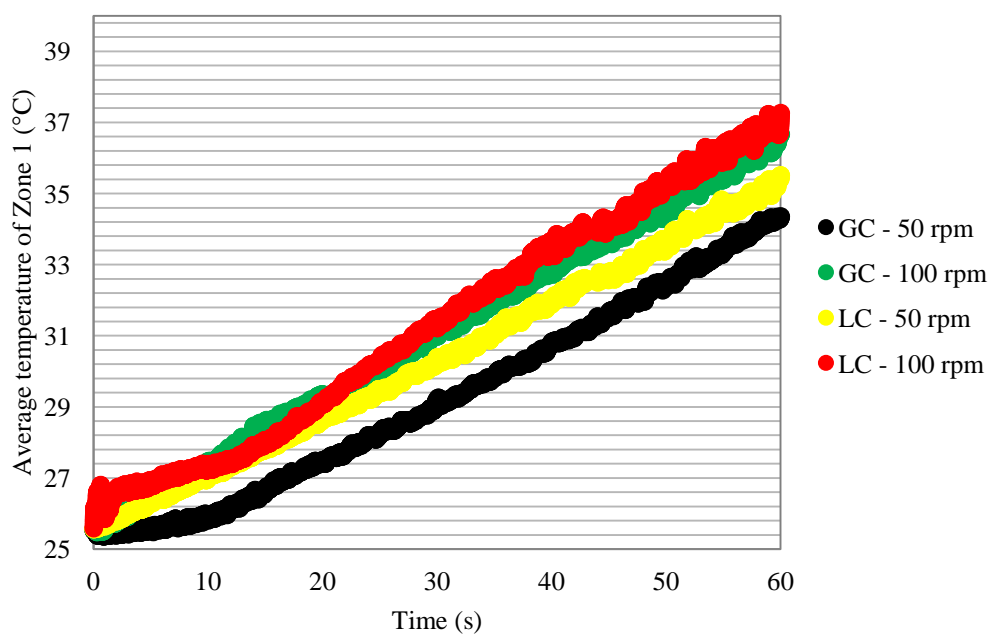


Figure 8.13. Average temperature of Zone 1 with time.

8.7 Conclusions

This chapter has looked into the meso-scale interactions between a reactive binder and some commonly used powders in detergent formulations. Droplet penetration on static compact indicates that the spread and penetration of the binder is better when there is a reaction between the binder and the powder. The size of the resulting nuclei is also greater when primary powder particles that make up the compact are larger. This suggests that binder dispersion is better when the particle size is larger.

The effect of an increase in the temperature of the binder on the size of the nuclei was also investigated. At all temperatures, the mass of the nuclei produced using carbonates is greater than the mass of the nuclei made using zeolite. However, if a reaction occurs between the powder and binder, an increase in the temperature results in a decrease in the mass of the resulting nuclei. This could be attributed to an increase in the viscosity of the binder during the reaction process, which starts to limit its spread at higher temperatures. As zeolite does not react with the binder, an increase in the binder temperature results in a slight increase in the mass of the zeolite nuclei.

Thermal imaging was used to visualise binder dispersion on a larger scale paddle mixer. This technique proved to be successful in being able to trace the movements of individ-

ual lumps of binder within the mixer. The impact of both the primary particle size and the impeller speed was investigated using the thermal imaging technique. Results reveal that binder dispersion is enhanced by increasing the size of the primary particles. This result is in agreement with the meso-scale study that was conducted on compacts of sodium carbonate i.e. binder is able to spread and disperse better, when the particle size is larger. Also as expected, an increase in the impeller speed improves the dispersion of the binder.

Chapter 9 Conclusions and further work

This thesis concerns a granulation process that is not conventional due to the ultra high viscosity of the binders that are employed for the manufacture of dry laundry powder. However, industrially, the process is of great importance. This research has primarily focused on understanding the initial dispersion of a highly viscous surfactant binder in a high shear environment. Studies were conducted with a view to outlining a mechanism for binder dispersion, which involves the break-up of large lumps of binder, as a result of the combined action of both the impeller and the moving bed of powder. Binder breakage has, therefore, been suggested as a new mechanism for the dispersion of a binder in this study. Experiments were performed to isolate binder breakage and quantify it, as a function of time. Studies were also conducted to elucidate the effects of various process, as well as formulation parameters that influence the initial dispersion of binder. The mechanistic understanding of the process, along with the experimental data was then used to create a population balance model that describes binder dispersion. Furthermore, a novel non-invasive technique for online monitoring of binder dispersion in a high shear environment was also developed as part of this study.

9.1 Effect of the method of binder delivery

Chapter 4 discusses the impact of the method of binder delivery on the granule size, binder content and granule strength. Experiments were conducted in a 10 L high shear mixer, at different impeller speeds. The binder was either injected into the mixer (as a continuous stream) or preloaded into the mixer (as one large blob). Altering the method of binder delivery changes both the rate of binder addition, as well as the initial size of the semi-solid binder. It was found that binder breakage is the dominant mechanism, at low impeller speeds, and at moderate to high speeds, granule growth commences more rapidly. Also, at low to moderate speeds, injecting the binder resulted in a product that contains less fines and a greater proportion of large granules. At the highest impeller speed of 800 rpm, there was no observable difference in the granule growth kinetics for the injected and preloaded case. As the shear and impact stresses within the mixer are

very high at this impeller speed, it is expected that the method of binder delivery is no longer a factor that influences the growth kinetics. However, there was no apparent impact on the granule strength and binder content, as a result of the method of binder addition – both methods showed similar trends.

In summary, an increase in the stresses within the system (impeller speed), increases the rate at which material progresses through the various stages of the granulation process (nucleation, growth, consolidation and coalescence). Also, adding the binder into the mixer as a smaller entity (i.e. as a continuous stream instead of one large blob) reduces the amount of time required to distribute the binder, thus providing more time for granule growth.

For a low viscous binder, Knight et al. (1998) report an increase in the average size of the granules when the rate of binder addition is greater. Their study suggests an increase in the rate of binder addition results in certain regions of the powder bed becoming over-wet, and this eventually results in the formation of larger granules. Wauters et al. (2002) also report similar findings when using a binder of a low viscosity. However, the present study reveals that increasing the rate of addition of a high viscous binder (by preloading all the material into the mixer at once) results in a decrease in the mean size of the granules. This could be attributed to the high viscosity of the binder, which does not spread and wet the primary particles until it has been completely dispersed into the moving bed of powder. Therefore, a more gradual addition (by injecting for example) is better for achieving faster granule growth kinetics.

9.2 Semi-solid binder breakage

Chapter 5 outlines a mechanism for binder dispersion. The nucleation step involves, coating the binder and subsequently breaking larger fragments into smaller ones, by mechanical action. This study has developed a technique for isolating and observing the process. This is the first study to introduce the concept of “breakage” for describing the dispersion of a semi-solid binder. Once coated the binder fragments are referred to as powder coated binder particles (PCBPs). A method has also been devised for quantifying the layering process by monitoring the variation in the mass, as well as the size of the PCBPs with time.

Three different materials were investigated including zeolite, and two different sizes of sodium carbonate. Results suggest that larger and rougher primary particles will disperse the binder more effectively in a moving bed of powder. A large particle is capable of exerting a larger force, leading to permanent deformation and breakage of the coated semi-solid binder fragments. A rougher particle is capable of penetrating a binder fragment to a greater extent than a smoother one.

There is also evidence that suggests the mechanical properties of the PCBs change with time, as a result of changes in their composition. The rate of powder loading into a binder particle has a direct influence on the mechanical response it exhibits, and this in turn influences the rate of binder breakage. When the rate of powder layering is faster, the PCB exhibits brittle behaviour within a shorter period of time.

9.3 Modelling binder breakage

A one dimensional population balance model has been developed to describe the breakage of PCBPs. This is the first study to develop a model that describes how a semi-solid binder undergoes dispersion, through breakage. The key assumptions of this model are that breakage is uniform and binary and the total length of the binder particles is conserved. Other assumptions include a selectivity function for the breakage of binder particles based on their size, i.e. a longer particle is more likely to break than a shorter one.

A self-similar solution for the population balance equation was found. The non-dimensional numerical solution for the population balance equation is $\hat{n}(\hat{l}, \hat{t}) = \hat{t}^2 e^{-\hat{l}\hat{t}}$. An expression that predicts the change in the number based size distribution, q_0 , was subsequently determined. There are two parameters that could be changed in the model: the initial length of the parent binder particle (l_0) and the selection constant (k). The predicted size distribution is self-similar with time, in other words, the magnitude ($\bar{l}_{1,0}$) changes but the shape of the distribution does not. In addition to the predicted size distributions exhibiting self-similarity, other emergent properties include the change in the number of particles and the mean size. The number of particles increases linearly with time, as $m_0 = N_0 + N_0 kt$, whilst the number based mean size decreases with time, as $l_{1,0} = \frac{l_0}{1+kt}$.

A value for k was determined from the experimental data in order to validate the proposed model. It was found that the k is time dependant. This was attributed to a change in the shape of the PCBs with time. With increasing time, the PCBs become more spherical. In addition, a phase change (i.e. as more solid gets loaded within its structure) may alter its breakage dynamics too. The experimental data suggests that breakage events, on average, occur once every 2 s. When experiments are conducted using larger primary particles or at high impeller speeds, an increase in the value of k is observed.

Furthermore, the mean length predicted using the model is in good agreement with the experimentally determined mean. As the size distribution gets scaled and $\bar{l}_{1,0}$ changes, k also changes, but at a much slower rate. The system thus behaves as though k is a constant over a period of time.

This deterministic model is able to predict the change in the number based mean length of the PCBs with time. An advantage of using this model is its simplicity i.e. it can be solved analytically to give a closed form solution that can be used to understand and quantify the early stages of the binder dispersion process. The breakage process has therefore, been successfully modelled using a kinetics approach in this study.

9.4 Online monitoring of binder dispersion in situ

This is the first study of its kind to introduce a non-invasive technique (thermal imaging) for online monitoring of binder dispersion in a moving bed of powder. Thermal imaging was used to visualise the movement of the binder in a 10 L mixer and study the influence of the method of binder delivery. There was a clear difference for the injected and preloaded cases, at the lower speed of 200 rpm. This study further confirms that better binder distribution can be achieved by injecting the binder. At a higher impeller speed of 400 rpm, it was not possible to see individual lumps of binder. However, the temperature of the mixer reached a steady state sooner for the injected case. Again, this suggests mixing is better when the binder is injected.

Thermal imaging was also used to visualise dispersion of a reactive binder in a pilot scale (32 L) paddle mixer. This technique proved to be very successful in being able to trace the movements of individual lumps of binder within the mixer. The impact of both

the primary particle size and the impeller speed were investigated and results reveal that binder dispersion is enhanced at high impeller speeds or when larger primary particles are used.

9.5 Further work

The scopes for avenues of further work stemming from this research are discussed in this section:

9.5.1 Understanding the formation of wall make-up

This study focused solely on the dispersion of a semi-solid binder in a moving bed of powder. Experiments were conducted to ensure all the binder comes directly into contact with the powder bed to minimise the amount of binder that adheres to the metal surfaces and other moving parts of the mixer. In reality, however, on large scale industrial systems, it is more difficult to avoid binder fouling the metal surfaces of the mixer.

If the fresh paste by-passes the moving bed of powder and comes into direct contact with the mixing tools, splashing is likely to occur. It is hypothesised that this could lead to the formation of a layer of material (binder and powder) on the surface of the mixer's wall – such a layer is commonly referred to as wall makeup (a form of fouling). This is an undesired effect. It is of interest to understand the factors that cause the formation of wall-makeup in more detail.

9.5.2 Online near infrared (NIR) imaging for monitoring binder distribution

The pharmaceutical industry has lead the way in continuous online monitoring of processes which enable process inputs to be adjusted in order to obtain the required product quality. This mechanism to design, analyse and control manufacturing processes is referred to as Process Analytical Technology (PAT) (Vudathala et al., 2010). Even though the concept was first introduced to improve the product quality in the pharmaceutical industry, it is now being adopted by a wide range of other industries in order to improve their product quality, maximise process efficiency and reduce wastage too. In detergent manufacture, the present study reveals that maximising paste dispersion is critical for ensuring proper and timely granule growth. This in turn, will help improve the granulation process by reducing recycle rates.

Most commonly employed surfactants contain –CH groups, which can be detected using an NIR chemical imager. This in turn could be used to monitor binder dispersion in much more detail on a granular scale. Furthermore, for a reactive agglomeration process, the NIR chemical imaging technique may also be used to monitor the progress of the reaction with time. Sanders et al. (2007) outline a method for determining the granule size distribution online. They refer to their technique as Visual Online Sizing (VOS). If an NIR imager can be integrated into VOS, it is then possible to obtain data, in real-time, regarding the binder distribution on a granular scale. This in turn, could be used to adjust formulation and process variables to vary product quality, in real time, or to determine the granulation end point during detergent manufacture.

9.5.3 Uses of the population balance model and further improvements

Recently, there is developing interest in being able to gain a better understanding of how to design and optimise solids processing operations. There are a few commercially available packages such as gSOLIDS by Process Systems Enterprise, UK, which could be used to make more informed decisions, with regards to process design and optimisation. The gSOLIDS package for example, predicts granulation operations, on any scale, by separating the process into a series of sub processes (for e.g. liquid addition, nucleation, growth, breakage, layering consolidation, etc.) and includes kernels for each process. These kernels could be combined to obtain insights on key process outputs. The model that has been developed in this study may be incorporated into such packages to enable highly viscous binder dispersion to be predicted. However, as discussed in Section 6.10, the application of this model is limited to describing granulation systems involving the use of a highly viscous binder i.e. binders that do not flow in a moving bed of powder unless the stresses acting upon them exceed a certain yield value.

It is common practice to scale up based on either the tip speed or the specific energy input (Mort, 2005). The k values can be related to the tip speed or stresses acting within system (which depends on the specific energy input), and this could in turn be used to predict binder breakage on different scales. It is, however, necessary to conduct experiments on larger scales of equipment in order to assess the validity of the model, and to make further recommendations on the scalability. Also in terms of improving this model, it is necessary to validate some of the assumptions that were made during its de-

velopment. It was assumed that the selection constant is proportional to the initial size of the binder particle. This needs to be further investigated by conducting experiments where l_0 is varied. It was also assumed that breakage is random and binary. The value of k suggests that breakage events occur once every 2 s; controlled experiments need to be conducted to study how often a binder particle breaks within the granulator, and to determine if the breakage is binary.

References

- ABBERGER, T. 2007. Population Balance Modelling of Granulation. In: SALMAN, A. D., HOUNSLOW, M. J. & SEVILLE, J. P. K. (eds.) *Handbook of Powder Technology: Granulation*. United Kingdom: Elsevier.
- ADAMS, M. J., MULLIER, M. A. & SEVILLE, J. P. K. 1994. Agglomerate strength measurement using a uniaxial confined compression test. *Powder Technology*, 78, 5-13.
- AGLAND, S. & IVESON, S. M. 1999. The impact of liquid drops on powder bed surfaces. *Chemeca 99: Chemical Engineering: Solutions in a Changing Environment*, 218.
- ALLEN, T. 2003. Data presentation and interpretation. *Powder Sampling and Particle Size Determination*. 1st ed. San Diego: Elsevier.
- ANSARI, M. A. & STEPANEK, F. 2008. The effect of granule microstructure on dissolution rate. *Powder Technology*, 181, 104-114.
- BASF 2012. GPS Safety Summary: Benzenesulfonic acid, 4-C10-13-sec-alkyl derivatives. In: BASF (ed.). BASF.
- BAYLY, A., SMITH, D. J., ROBERTS, N. S., YORK, D. W. & CAPECI, S. W. 2009. Detergent Processing. In: URI ZOLLER, P. S. (ed.) *Surfactant Science Series: Handbook of Detergents Part F: Production*. New York, USA: Taylor & Francis.
- BOHLIN. 1994. *A Basic Introduction to Rheology* [Online]. Cirencester, Glos., Great Britain: Bohlin Instruments. Available: <https://www.iesmat.com/iesmat/upload/file/Malvern/Productos-MAL/REO-A%20basic%20introduction%20to%20rheology.pdf>.
- BROWN, D. J., VICKERS, G. T., COLLIER, A. P. & REYNOLDS, G. K. 2005. Measurement of the size, shape and orientation of convex bodies. *Chemical Engineering Science*, 60, 289-292.
- BURNS, D. T. 1993. Principles of spectrophotometric measurements with particular reference to the UV-visible region. In: CLARK, B. J., FROST, T. & RUSSELL, M. A. (eds.) *UV Spectroscopy: Techniques, Instrumentation and Data Handling*. 1st ed. Great Britain: Chapman and Hall.
- CAPECI, S. W., LANGE, J. F., SMITH, D. J. & ROBERTS, N. S. 1996. *Process for making a high density detergent composition in a single mixer/densifier with selected recycle streams for improved agglomerate properties*. USA patent application US 08/309,215.
- CARR, R. L. 1965. Classifying flow properties of solids. *Chem. Eng.*, 1, 69-72.
- CARR, R. L. 1970. Particle Behaviour, storage and Flow. *British Chemical Engineering*, 15, 1541-1549.
- CEFIC 2000. Zeolites for Detergents: as nature intended. Brussels: Association of Detergent Zeolite Producers, European Chemical Industry Council.
- CHAN, E. L., REYNOLDS, G. K., GURURAJAN, B., HOUNSLOW, M. J. & SALMAN, A. D. 2013. Blade-granule bed stress in a cylindrical high shear granulator: I—Online measurement and characterisation. *Chemical Engineering Science*, 86, 38-49.
- CHITU, T. M., OULAHNA, D. & HEMATI, M. 2011. Wet granulation in laboratory scale high shear mixers: Effect of binder properties. *Powder Technology*, 206, 25-33.
- CHOUK, V., REYNOLDS, G., HOUNSLOW, M. & SALMAN, A. 2009. Single drop behaviour in a high shear granulator. *Powder Technology*, 189, 357-364.
- DING, A., HOUNSLOW, M. J. & BIGGS, C. A. 2006. Population balance modelling of activated sludge flocculation: Investigating the size dependence of aggregation, breakage and collision efficiency. *Chemical Engineering Science*, 61, 63-74.
- DYNKIN, E. B. 1961. Markov Processes. In: KOVARY, T. (ed.) *Theory of Markov Processes*. New York: Pergamon Press.

- ENNIS, B. J., TARDOS, G. & PFEFFER, R. 1991. A microlevel-based characterization of granulation phenomena. *Powder Technology*, 65, 257-272.
- ENNIS, B. J., WITT, W., WEINEKÖTTER, R., SPHAR, D., GOMMERAN, E., SNOW, R. H., ALLEN, T., RAYMUS, G. J. & LITSTER, J. D. 2008. Solid-Solid Operations and Processing. In: PERRY, R. H., GREEN, D. W. & MALONEY, J. O. (eds.) *Perry's Chemical Engineers' Handbook*. 8th ed. New York: McGraw-Hill.
- FAVELUKIS, M., LAVRENTEVA, O. M. & NIR, A. 2005. Deformation and breakup of a non-Newtonian slender drop in an extensional flow. *Journal of Non-Newtonian Fluid Mechanics*, 125, 49-59.
- FEIGL, K., F.M. KAUFMANN, S., FISCHER, P. & J. WINDHAB, E. 2003. A numerical procedure for calculating droplet deformation in dispersing flows and experimental verification. *Chemical Engineering Science*, 58, 2351-2363.
- FIGURA, L. O. & TEIXEIRA, A. A. 2007. Geometric Properties: Size and Shape. *Food Physics Physical Properties - Measurements and Applications*. 1st ed. Germany: Springer.
- FRIEDMAN, M. 2004. Detergents and the Environment: Historical Review. In: ZOLLER, U. & SOSIS, P. (eds.) *Handbook of Detergents Part B: Environmental Impact*. Boca Raton, Florida: Taylor & Francis.
- GELDART, D., ABDULLAH, E. C., HASSANPOUR, A., NWOKE, L. C. & WOUTERS, I. 2006. Characterization of powder flowability using measurement of angle of repose. *China Particuology*, 4, 104-107.
- GERMANÀ, S., SIMONS, S., BONSALL, J. & CARROLL, B. 2009. LAS acid reactive binder: Wettability and adhesion behaviour in detergent granulation. *Powder Technology*, 189, 385-393.
- GERMANÀ, S., SIMONS, S. J. R. & BONSALL, J. 2008. Reactive Binders in Detergent Granulation: Understanding the Relationship between Binder Phase Changes and Granule Growth under Different Conditions of Relative Humidity. *Industrial & Engineering Chemistry Research*, 47, 6450-6458.
- GODE, P. 1983. SODIUM ALUMINUM SILICATES IN DETERGENTS-INVESTIGATION OF THE INFLUENCE ON ALGAL GROWTH. *ZEITSCHRIFT FÜR WASSER UND ABWASSER FORSCHUNG-JOURNAL FOR WATER AND WASTEWATER RESEARCH*, 16, 210-219.
- GRIVET-TALOCIA, S. & GUSTAVSEN, B. 2015. Signals and Transforms. *Passive Macromodeling: Theory and Applications*. New Jersey: John Wiley & Sons.
- HAPGOOD, K. P., LITSTER, J. D., BIGGS, S. R. & HOWES, T. 2002. Drop Penetration into Porous Powder Beds. *Journal of Colloid and Interface Science*, 253, 353-366.
- HAPGOOD, K. P., LITSTER, J. D. & SMITH, R. 2003. Nucleation regime map for liquid bound granules. *AIChE Journal*, 49, 350-361.
- HASSANPOUR, A., KWAN, C. C., NG, B. H., RAHMANIAN, N., DING, Y. L., ANTONY, S. J., JIA, X. D. & GHADIRI, M. 2009. Effect of granulation scale-up on the strength of granules. *Powder Technology*, 189, 304-312.
- HASSANPOUR, A., TAN, H., BAYLY, A., GOPALKRISHNAN, P., NG, B. & GHADIRI, M. 2011. Analysis of particle motion in a paddle mixer using Discrete Element Method (DEM). *Powder Technology*, 206, 189-194.
- HENG, P. W. S., CHAN, L. W. & ZHU, L. 2000. Effects of process variables and their interactions on melt pelletization in a high shear mixer. *STP pharma sciences*, 10, 165-172.
- HIBARE, S. & ACHARYA, K. 2012. Effect of binder to solid ratio on mechanical properties of granules processed using reactive and non-reactive binder. *Powder Technology*, 229, 137-147.
- HILL, P. J. & NG, K. M. 2002. Particle size distribution by design. *Chemical Engineering Science*, 57, 2125-2138.

- HOLM, P., JUNGERSEN, O., SCHAEFER, T. & KRISTENSEN, H. G. 1984. Granulation in high speed mixers. II: Effects of process variables during kneading. *Pharmazeutische Industrie*, 46, 97-101.
- HOLM, P., SCHAEFER, T. & KRISTENSEN, H. G. 1985. Granulation in high-speed mixers Part VI. Effects of process conditions on power consumption and granule growth. *Powder Technology*, 43, 225-233.
- HOUNSLOW, M. J. 2005. Particle Rate Processes. 1st edition ed. Sheffield, UK: The University of Sheffield.
- HUANG, H., DABIRI, D. & GHARIB, M. 1997. On errors of digital particle image velocimetry. *Measurement Science and Technology*, 8.
- IVESON, S. M., LITSTER, J. D., HAPGOOD, K. & ENNIS, B. J. 2001a. Nucleation, growth and breakage phenomena in agitated wet granulation processes: a review. *Powder Technology*, 117, 3-39.
- IVESON, S. M., WAUTERS, P. A. L., FORREST, S., LITSTER, J. D., MEESTERS, G. M. H. & SCARLETT, B. 2001b. Growth regime map for liquid-bound granules: further development and experimental validation. *Powder Technology*, 117, 83-97.
- JACOBS, P., SEVENS, E. & KUNNEN, M. 1995. Principles of computerised X-ray tomography and applications to building materials. *Science of The Total Environment*, 167, 161-170.
- JENIKE, A. W. 1964. Storage and Flow of Solids. *Buletin of the University of Utah*, 53, 194.
- KENINGLEY, S. T., KNIGHT, P. C. & MARSON, A. D. 1997. An investigation into the effects of binder viscosity on agglomeration behaviour. *Powder Technology*, 91, 95-103.
- KNIGHT, P. C., INSTONE, T., PEARSON, J. M. K. & HOUNSLOW, M. J. 1998. An investigation into the kinetics of liquid distribution and growth in high shear mixer agglomeration. *Powder Technology*, 97, 246-257.
- KNIGHT, P. C., JOHANSEN, A., KRISTENSEN, H. G., SCHÄFER, T. & SEVILLE, J. P. K. 2000. An investigation of the effects on agglomeration of changing the speed of a mechanical mixer. *Powder Technology*, 110, 204-209.
- KRÜSS. 2014. CMC [Online]. Germany: KRÜSS GmbH Available: <https://www.kruss.de/services/education-theory/glossary/cmc/> [Accessed 06/06/2014 2014].
- LEVENSPIEL, O. 1999. *Chemical Reaction Engineering*, New York, USA, John Wiley & Sons.
- LEVINSON, M. I. 2009. Surfactant Production: Present Realities and Future Perspectives. In: ZOLLER, U. & SOSIS, P. (eds.) *Handbook of Detergents Part F: Production*. Boca Raton, Florida: Taylor & Francis.
- LI, J., FREIREICH, B. J., WASSGREN, C. R. & LITSTER, J. D. 2013. Experimental validation of a 2-D population balance model for spray coating processes. *Chemical Engineering Science*, 95, 360-365.
- LIDE, D. R. 2010. Physical Constants of Inorganic Compounds. *CRC Handbook of Chemistry and Physics*. 90th ed. Boca Raton: CRC Press Inc.
- LITSTER, J. D., HAPGOOD, K. P., MICHAELS, J. N., SIMS, A., ROBERTS, M., KAMENENI, S. K. & HSU, T. 2001. Liquid distribution in wet granulation: dimensionless spray flux. *Powder Technology*, 114, 32-39.
- MANGWANDI, C., ADAMS, M. J., HOUNSLOW, M. J. & SALMAN, A. D. 2010. Effect of impeller speed on mechanical and dissolution properties of high-shear granules. *Chemical Engineering Journal*, 164, 305-315.
- METCALFE, I. S. 1997. *Chemical Reaction Engineering A First Course*, Oxford, Oxford University Press.
- MICHAELS, J. N., FARBER, L., WONG, G. S., HAPGOOD, K., HEIDEL, S. J., FARABAUGH, J., CHOU, J.-H. & TARDOS, G. I. 2009. Steady states in granulation

- of pharmaceutical powders with application to scale-up. *Powder Technology*, 189, 295-303.
- MIYAZAKI, H. & ARIKA, J. 1983. *Zeolite powder having high flowability, process for preparing same and detergent composition containing same*. US 06/291,073.
- MORT, P. R. 2005. Scale-up of binder agglomeration processes. *Powder Technology*, 150, 86-103.
- MORT, P. R., CAPECI, S. W. & HOLDER, J. W. 2001. Control of agglomerate attributes in a continuous binder-agglomeration process. *Powder Technology*, 117, 173-176.
- MÜLLER, H. 1928. Zur allgemeinen Theorie der raschen Koagulation. *Kolloidchemische Beihefte*, 27, 223-250.
- MUZZIO, F. J., ALEXANDER, A., GOODRIDGE, C., SHEN, E. & SHINBROT, T. 2004. Solids Mixing. In: PAUL, E. L., ATIEMO-OBENG, V. A. & KRESTA, S. M. (eds.) *Handbook of Industrial Mixing Science and Practice*. New Jersey: Wiley - Interscience.
- MYERS, D. 2006. Fluid Surfaces and Interfaces. *Surfactant Science and Technology*. 3rd ed. Hoboken, New Jersey: Wiley-Interscience.
- OHNO, I., HASEGAWA, S., YADA, S., KUSAI, A., MORIBE, K. & YAMAMOTO, K. 2007. Importance of evaluating the consolidation of granules manufactured by high shear mixer. *International Journal of Pharmaceutics*, 338, 79-86.
- OKA, S., EMADY, H., KAŠPAR, O., TOKÁROVÁ, V., MUZZIO, F., ŠTĚPÁNEK, F. & RAMACHANDRAN, R. 2015. The effects of improper mixing and preferential wetting of active and excipient ingredients on content uniformity in high shear wet granulation. *Powder Technology*, 278, 266-277.
- OMAR, C. S., DHENGE, R. M., PALZER, S., HOUNSLOW, M. J. & SALMAN, A. D. 2016. Roller compaction: Effect of relative humidity of lactose powder. *European Journal of Pharmaceutics and Biopharmaceutics*, 106, 26-37.
- OSBORNE, J. D., SOCHON, R. P. J., CARTWRIGHT, J. J., DOUGHTY, D. G., HOUNSLOW, M. J. & SALMAN, A. D. 2011. Binder addition methods and binder distribution in high shear and fluidised bed granulation. *Chemical Engineering Research and Design*, 89, 553-559.
- PASHA, M., HASSANPOUR, A., AHMADIAN, H., TAN, H. S., BAYLY, A. & GHADIRI, M. 2015. A comparative analysis of particle tracking in a mixer by discrete element method and positron emission particle tracking. *Powder Technology*, 270, Part B, 569-574.
- POON, J. M. H., RAMACHANDRAN, R., SANDERS, C. F. W., GLASER, T., IMMANUEL, C. D., DOYLE III, F. J., LITSTER, J. D., STEPANEK, F., WANG, F.-Y. & CAMERON, I. T. 2009. Experimental validation studies on a multi-dimensional and multi-scale population balance model of batch granulation. *Chemical Engineering Science*, 64, 775-786.
- RAFFEL, M., WILLERT, C. E., WERELEY, S. & KOMPENHANS, J. 2013. *Particle Image Velocimetry: A Practical Guide*. New York, Springer.
- RAHMANIAN, N., GHADIRI, M., JIA, X. & STEPANEK, F. 2009. Characterisation of granule structure and strength made in a high shear granulator. *Powder Technology*, 192, 184-194.
- RAMAKER, J. S., JELGERSMA, M. A., VONK, P. & KOSSEN, N. W. F. 1998. Scale-down of a high-shear pelletisation process: Flow profile and growth kinetics. *International Journal of Pharmaceutics*, 166, 89-97.
- RAMKRISHNA, D. 2000. *Population Balances: Theory and Applications to Particulate Systems in Engineering*. San Diego, California, Academic Press.
- RAMKRISHNA, D. & BORWANKER, J. D. 1973. A puristic analysis of population balance - I. *Chemical Engineering Science*, 28, 1423-1435.
- RENARDY, Y., CRISTINI, V. & LI, J. 2002. Drop fragment distributions under shear with inertia. *International Journal of Multiphase Flow*, 28, 1125-1147.

- REYNOLDS, G. K., BIGGS, C. A., SALMAN, A. D. & HOUNSLOW, M. J. 2004. Non-uniformity of binder distribution in high-shear granulation. *Powder Technology*, 140, 203-208.
- RODENBURG, K. 2007. Horizontal twin-shaft paddle mixers – the ultimate in mixing technology. *International Aquafeed Journal*, 32-34.
- ROUGH, S. L., WILSON, D. I., BAYLY, A. & YORK, D. 2003. Tapping characterisation of high shear mixer agglomerates made with ultra-high viscosity binders. *Powder Technology*, 132, 249-266.
- ROUGH, S. L., WILSON, D. I., BAYLY, A. E. & YORK, D. W. 2005a. Influence of Process Parameters on the Tapping Characteristics of High Shear Mixer Agglomerates Made with Ultra-High Viscosity Binders. *Chemical Engineering Research and Design*, 83, 7-23.
- ROUGH, S. L., WILSON, D. I., BAYLY, A. E. & YORK, D. W. 2005b. Mechanisms in high-viscosity immersion–granulation. *Chemical Engineering Science*, 60, 3777-3793.
- ROUGH, S. L., WILSON, D. I. & YORK, D. W. 2005c. Effect of solids formulation on the manufacture of high shear mixer agglomerates. *Advanced Powder Technology*, 16, 145-169.
- ROUGH, S. L., WILSON, D. I. & YORK, D. W. 2005d. A regime map for stages in high shear mixer agglomeration using ultra-high viscosity binders. *Advanced Powder Technology*, 16, 373-386.
- SALMAN, A. D., REYNOLDS, G. K., TAN, H. S., GABBOTT, I. & HOUNSLOW, M. J. 2007. Breakage in Granulation. In: SALMAN, A. D., HOUNSLOW, M. J. & SEVILLE, J. P. K. (eds.) *Handbook of Powder Technology: Granulation*. United Kingdom: Elsevier.
- SANDERS, C., HOUNSLOW, M. J. & SALMAN, A. D. 2007. *Visual Sizing of Particles*. United Kingdom patent application PCT/GB2005/003479.
- SASTRY, K. V. S. & GASCHIGNARD, P. 1981. Discretization procedure for the coalescence equation of particulate processes. *Industrial & Engineering Chemistry Fundamentals*, 20, 355-361.
- SCHÄFER, T. & MATHIESEN, C. 1996a. Melt pelletization in a high shear mixer. IX. Effects of binder particle size. *International Journal of Pharmaceutics*, 139, 139-148.
- SCHÄFER, T. & MATHIESEN, C. 1996b. Melt pelletization in a high shear mixer. VIII. Effects of binder viscosity. *International Journal of Pharmaceutics*, 139, 125-138.
- SCHELLANDER, D. 2013. *CFD simulations of particle laden flows: Particle transport and separation*. Hamburg, Germany, Anchor Academic Publishing.
- SCHÖNGUT, M., GROF, Z. & ŠTĚPÁNEK, F. 2011. Kinetics of Dry Neutralization of Dodecyl-BenzeneSulfonic Acid with Respect to Detergent Granulation. *Industrial & Engineering Chemistry Research*, 50, 11576-11584.
- SCHÖNGUT, M., SMRČKA, D. & ŠTĚPÁNEK, F. 2013. Experimental and theoretical investigation of the reactive granulation of sodium carbonate with dodecyl-benzenesulfonic acid. *Chemical Engineering Science*, 86, 2-8.
- SCOTT, A. C., HOUNSLOW, M. J. & INSTONE, T. 2000. Direct evidence of heterogeneity during high-shear granulation. *Powder Technology*, 113, 205-213.
- SEO, A., HOLM, P. & SCHÄFER, T. 2002. Effects of droplet size and type of binder on the agglomerate growth mechanisms by melt agglomeration in a fluidised bed. *European Journal of Pharmaceutical Sciences*, 16, 95-105.
- SMIRANI-KHAYATI, N., FALK, V., BARDIN-MONNIER, N. & MARCHAL-HEUSSLER, L. 2009. Binder liquid distribution during granulation process and its relationship to granule size distribution. *Powder Technology*, 195, 105-112.
- STANLEY-WOOD, N. 2006. Particle characterisation in bulk powders. In: MCGLINCHEY, D. (ed.) *Characterisation of Bulk Solids*. Oxford, UK: Blackwell Publishing.

- STEPAN. 2010. *STEOL® CS-370* [Online]. Illinois, U.S.A. : Stepan GmbH. Available: http://www.stepan.com/uploadedFiles/Literature_and_Downloads/Product_Bulletins/Surfactants/STEOL%C2%AE/STEOLCS370.pdf.
- ŠTĚPÁNEK, F. & ANSARI, M. A. 2005. Computer simulation of granule microstructure formation. *Chemical Engineering Science*, 60, 4019-4029.
- SUMMERS, M. & AULTON, M. E. 2002. Granulation. In: AULTON, M. E. (ed.) *Pharmaceutics: The science of dosage form design*. 2nd ed. Leicester, UK: Churchill Livingstone.
- TABOR, D. 2000. *The Hardness of Metals*, Oxford, UK, Oxford University Press.
- TADROS, T. F. 2011. *Rheology of dispersions: principles and applications*, Weinheim, Germany, John Wiley & Sons.
- TAN, B. M. J., LOH, Z. H., SOH, J. L. P., LIEW, C. V. & HENG, P. W. S. 2014. Distribution of a viscous binder during high shear granulation—Sensitivity to the method of delivery and its impact on product properties. *International Journal of Pharmaceutics*, 460, 255-263.
- TARDOS, G. I., KHAN, M. I. & MORT, P. R. 1997. Critical parameters and limiting conditions in binder granulation of fine powders. *Powder Technology*, 94, 245-258.
- TEKCHANDANEY, J. R. 2012. Mixers. In: HOLLOWAY, M. D., NWAOHA, C. & ONYEWUENY, O. A. (eds.) *Process Plant Equipment: Operation, Control, and Reliability*. New Jersey: John Wiley & Sons.
- THIELICKE, W. & STAMHUIS, E. 2014. PIVlab—towards user-friendly, affordable and accurate digital particle image velocimetry in MATLAB. *Journal of Open Research Software*, 2, e30.
- TORO, M. D., HOERNIG, R. O. H. & NÉDÉLEC, J.-C. 2012. *Mathematical methods for wave propagation in science and engineering*, Santiago, Chile, Eds. Universidad Católica de Chile.
- VAN DEN DRIES, K. & VROMANS, H. 2002. Relationship between inhomogeneity phenomena and granule growth mechanisms in a high-shear mixer. *International Journal of Pharmaceutics*, 247, 167-177.
- VONK, P., GUILLAUME, C. P. F., RAMAKER, J. S., VROMANS, H. & KOSSEN, N. W. F. 1997. Growth mechanisms of high-shear pelletisation. *International Journal of Pharmaceutics*, 157, 93-102.
- VUDATHALA, G., RODGERS, S. & SIMMONS, J. E. 2010. Quality by Design and Process Analytical Technology in Granulation. In: PARikh, D. M. (ed.) *Handbook of pharmaceutical granulation technology*. Boca Raton: CRC Press.
- WAUTERS, P. A. L., VAN DE WATER, R., LITSTER, J. D., MEESTERS, G. M. H. & SCARLETT, B. 2002. Growth and compaction behaviour of copper concentrate granules in a rotating drum. *Powder Technology*, 124, 230-237.
- WRIGHT, H. & RAMKRISHNA, D. 1992. Solutions of inverse problems in population balances—I. Aggregation kinetics. *Computers & Chemical Engineering*, 16, 1019-1038.
- YORK, D. W. 2003. An industrial user's perspective on agglomeration development. *Powder Technology*, 130, 14-17.
- YU, Y., ZHAO, J. & BAYLY, A. E. 2008. Development of Surfactants and Builders in Detergent Formulations. *Chinese Journal of Chemical Engineering*, 16, 517-527.
- ZOHURI, B. 2015. Dimensional Analysis. *Dimensional analysis and self-similarity methods for engineers and scientists*. New York: Springer.

Appendix I Method for determining porosity from XRT

Figure I-1 is an example of a 16-bit image obtained from the X-ray scanner. The image was subsequently converted into an 8-bit format, using the ImageJ software. For an 8-bit image, the grey scale ranges from 0 to 255.

Firstly, it is necessary to determine the grey values that represent air within a granular sample. A histogram of the number of pixels against the grey scale value was then obtained for the air space surrounding the granule using the ImageJ software. The air space is presented by a yellow oval in Figure I-1.

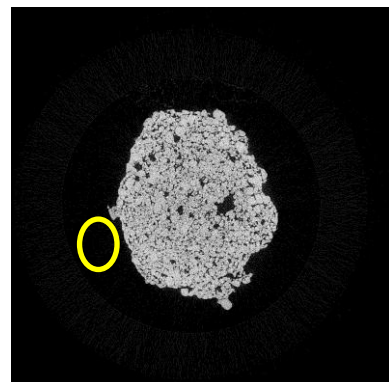


Figure I-1. Slice obtained from the X-ray scanner. Air space is represented by a yellow oval.

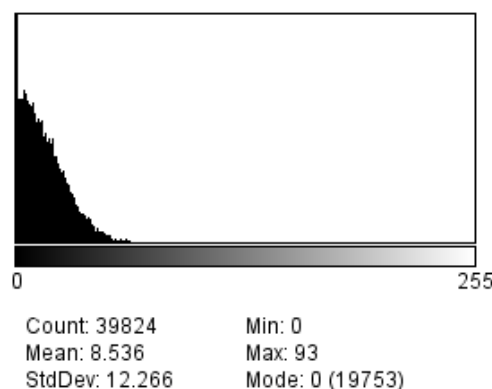


Figure I-2. Histogram of number of pixels for the 8-bit grey scale image.

Appendix I

Figure I-2 is the histogram for air and the grey values range from 0 to 95. Therefore, it was reasonable to assume that any components which have a grey value greater than 95 must be either binder or powder.

A threshold was applied to binarize the image, whereby components with a grey value greater than 95 appear to be white in colour and those below appear to be black (Figure I-3).

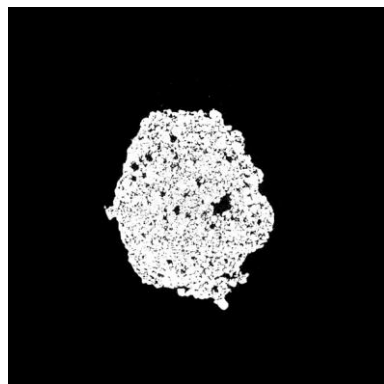


Figure I-3. Binarised XRT image of the granule.

A contour was carefully drawn around the granular structure shown in Figure I-3, and another histogram was generated for that area of interest. However now, after binarising all components have been assigned a grey value of either 0 (black pixels representing air) or 255 (white pixels representing both powder and binder), and from the relative proportion of pixels that are either 0 or 255, it is possible to determine a value for the porosity of the sample (Figure I-4).

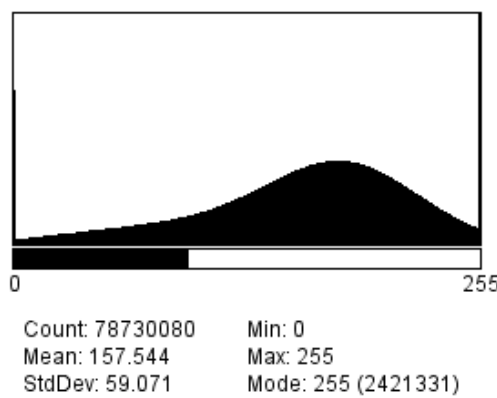


Figure I-4. Histogram of number of pixels for the binary image.

Appendix II Indentation of PCBPs

II.1 Zeolite

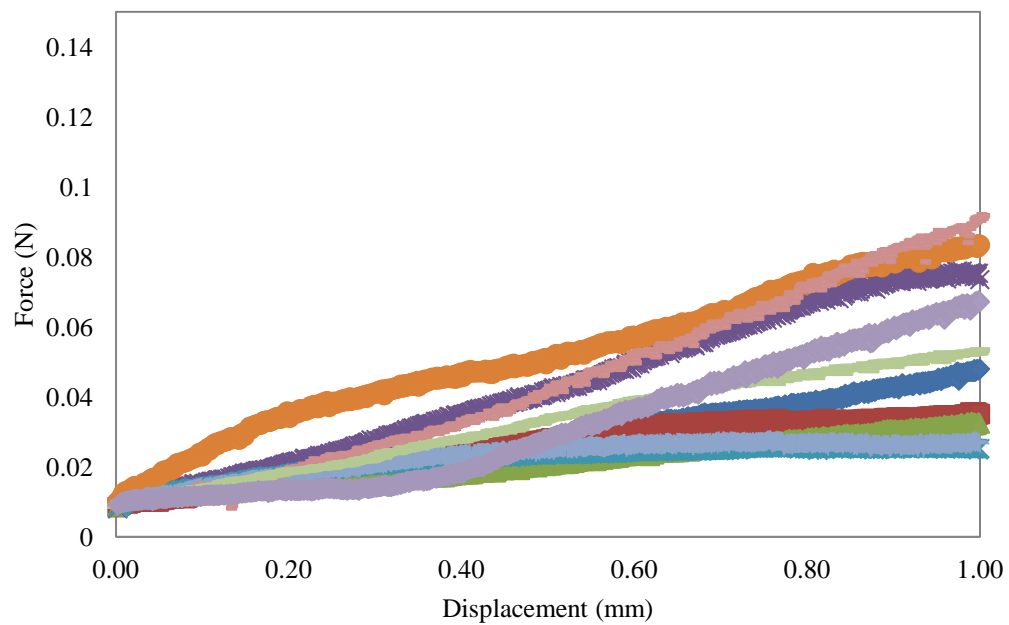


Figure II-1. Force vs. displacement for zeolite at 15 s.

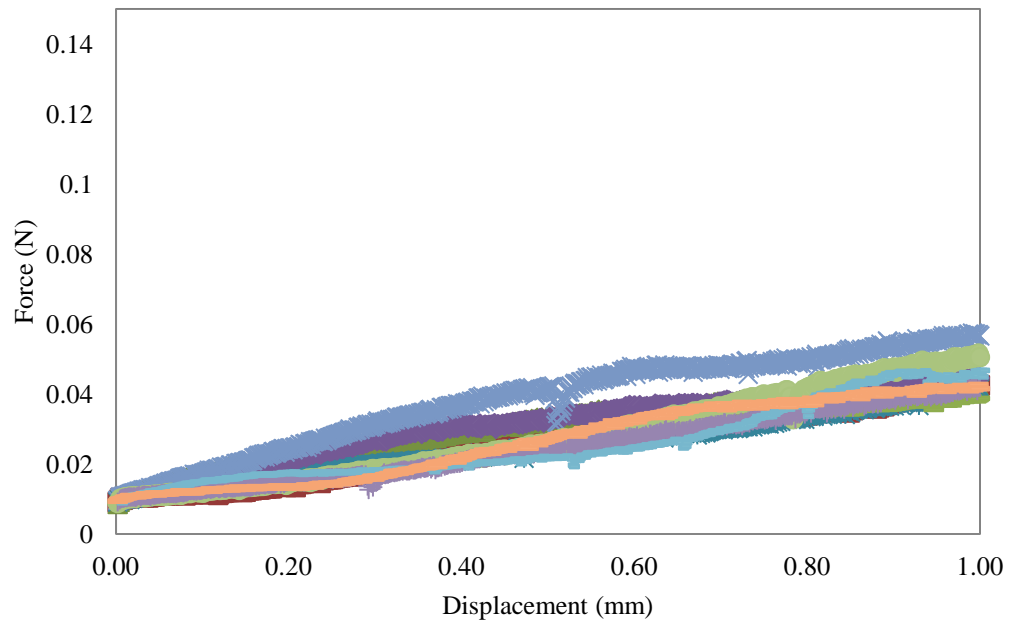


Figure II-2. Force vs. displacement for zeolite at 30 s.

Appendix II

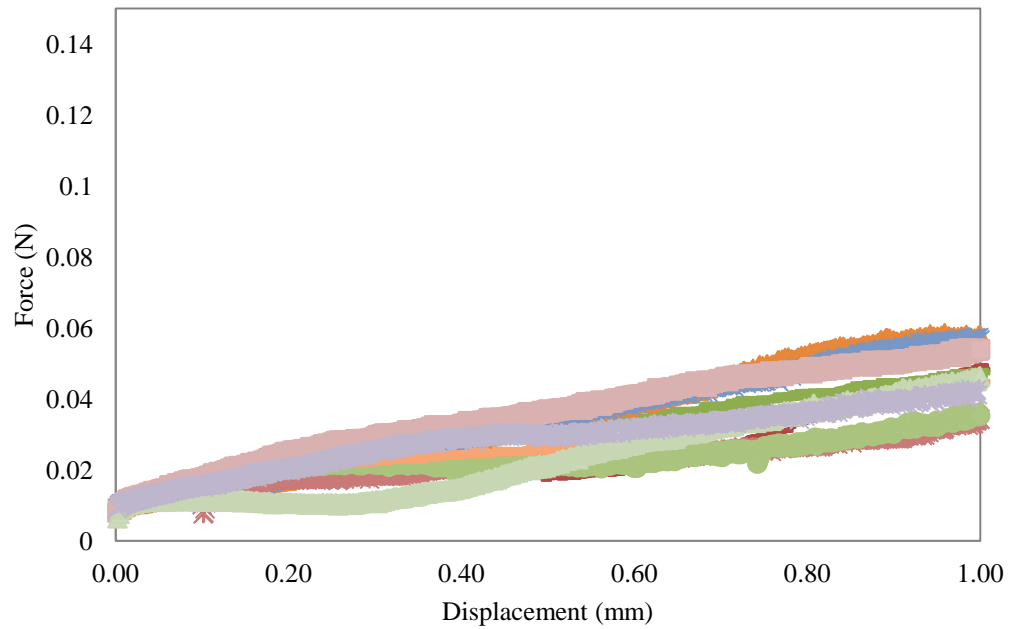


Figure II-3. Force vs. displacement for zeolite at 45 s.

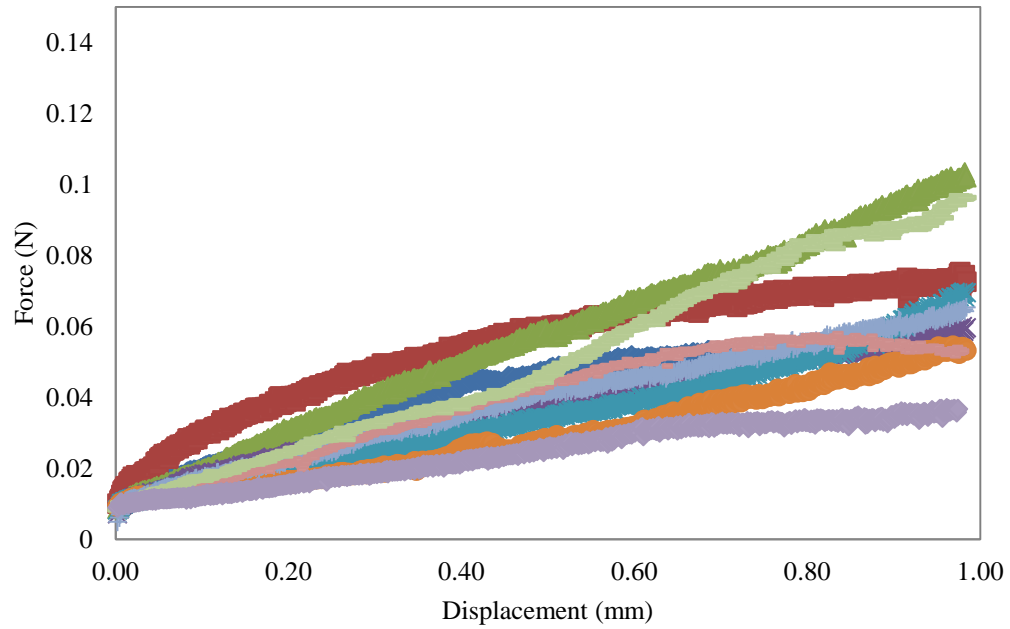


Figure II-4. Force vs. displacement for zeolite at 60 s.

Appendix II

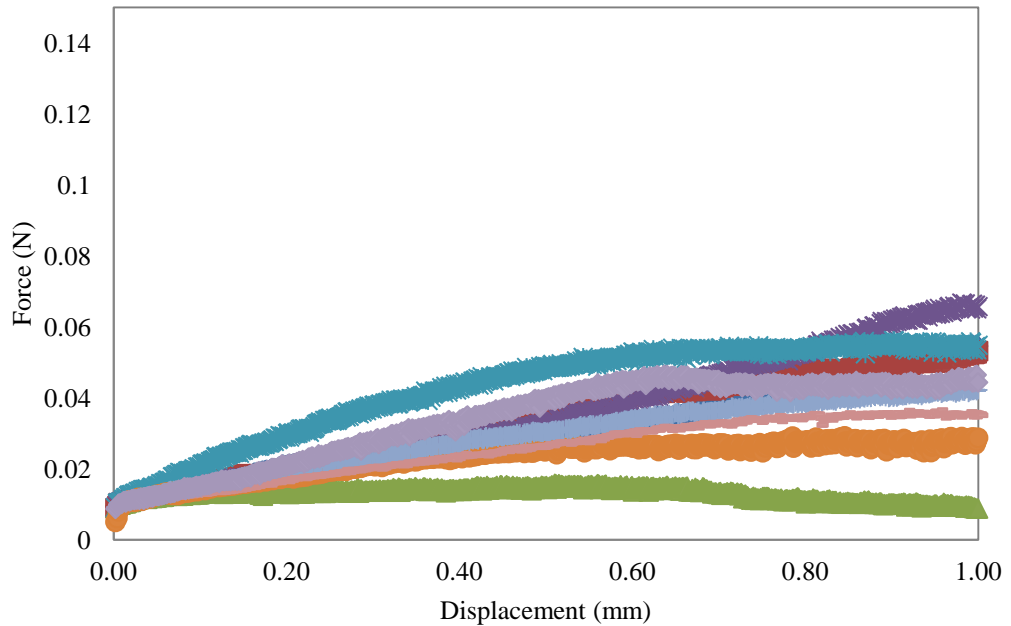


Figure II-5. Force vs. displacement for zeolite at 75 s.

II.2 Ground ash

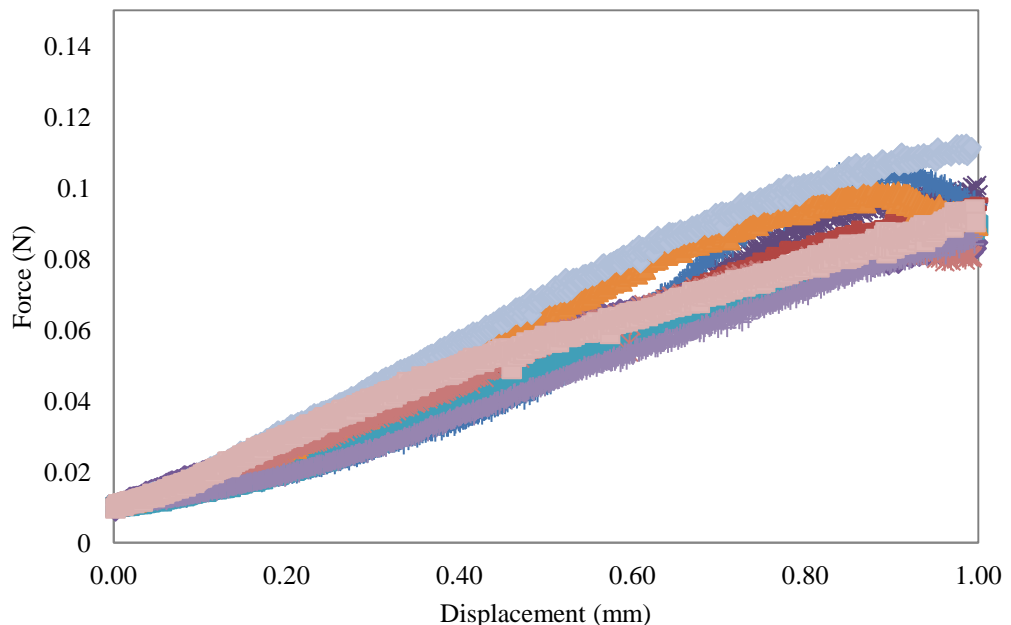


Figure II-6. Force vs. displacement for ground ash at 15 s.

Appendix II

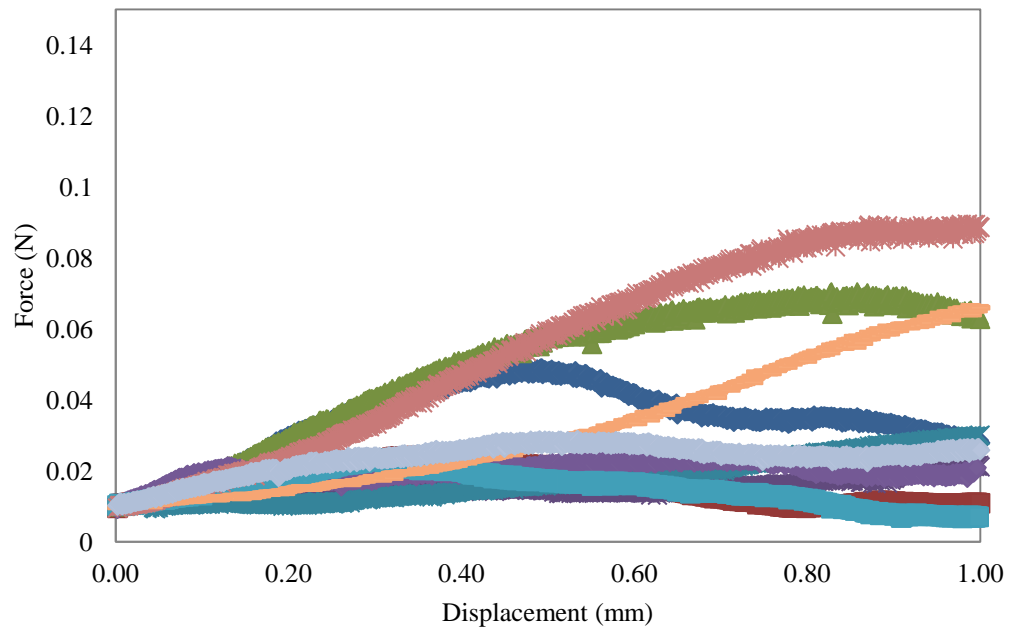


Figure II-7. Force vs. displacement for ground ash at 30 s.

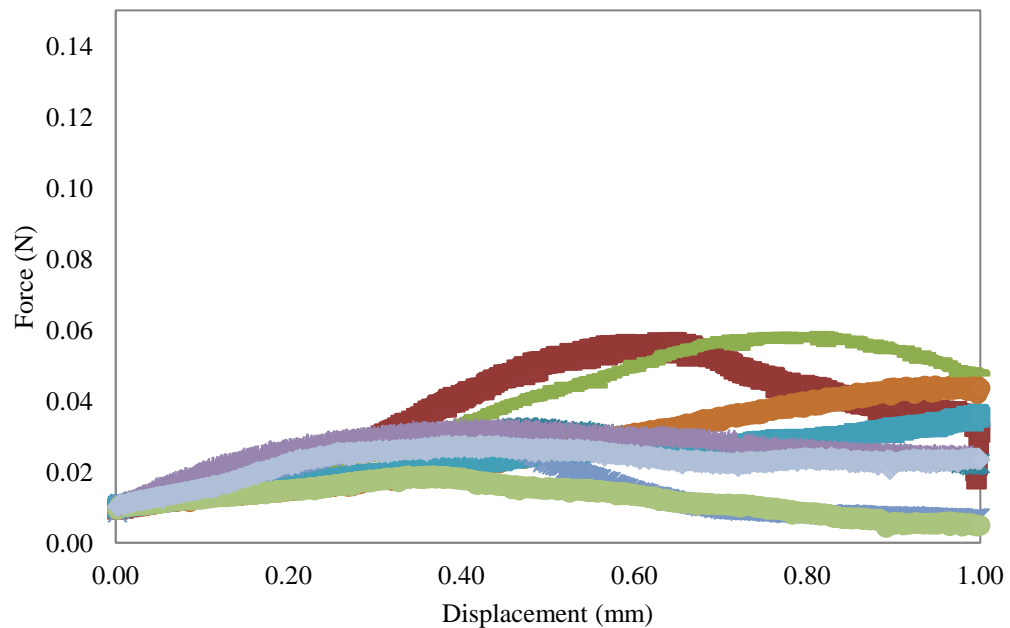


Figure II-8. Force vs. displacement for ground ash at 45 s.

Appendix II

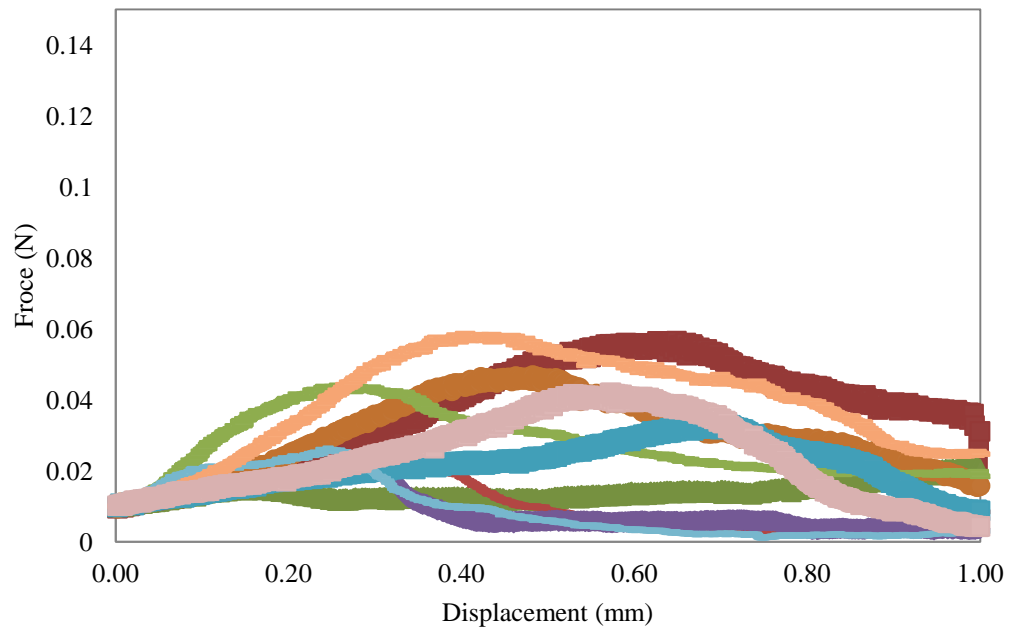


Figure II-9. Force vs. displacement for ground ash at 60 s.

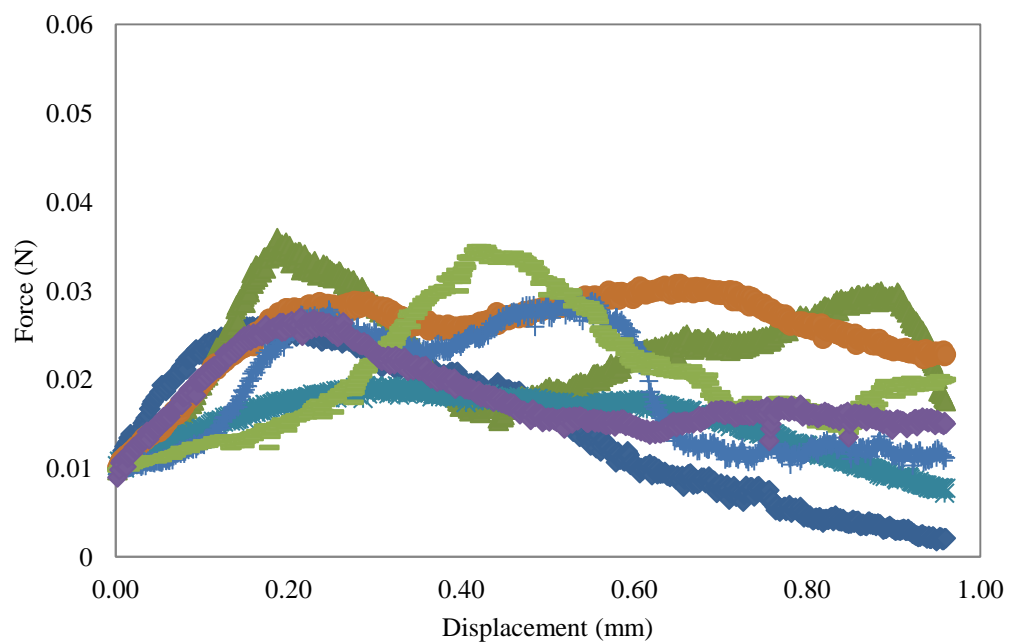


Figure II-10. Force vs. displacement for ground ash at 75 s.

Appendix II

II.3 Light ash

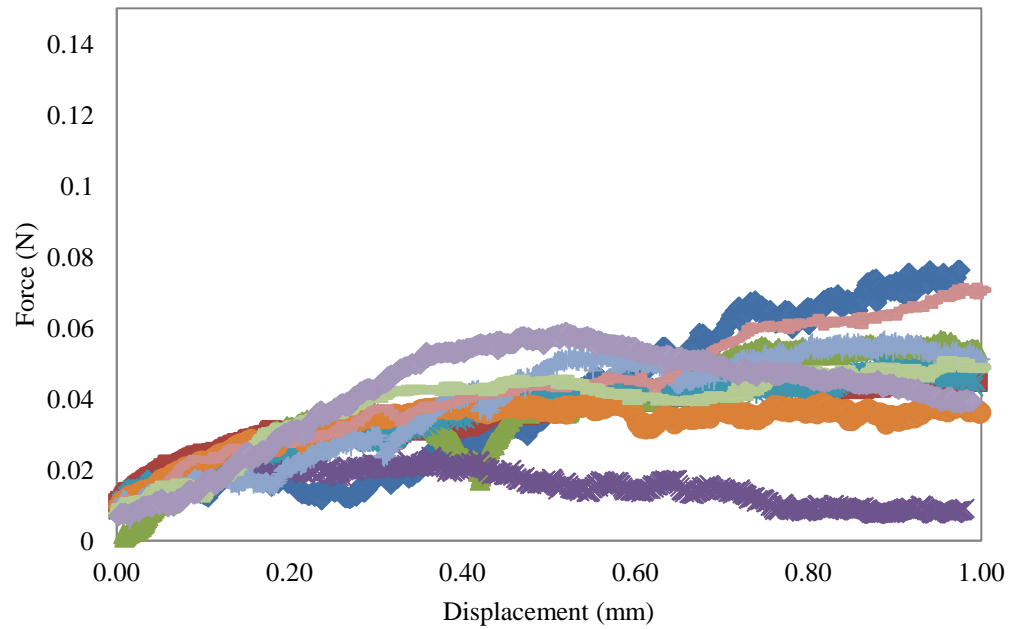


Figure II-11. Force vs. displacement for light ash at 15 s.

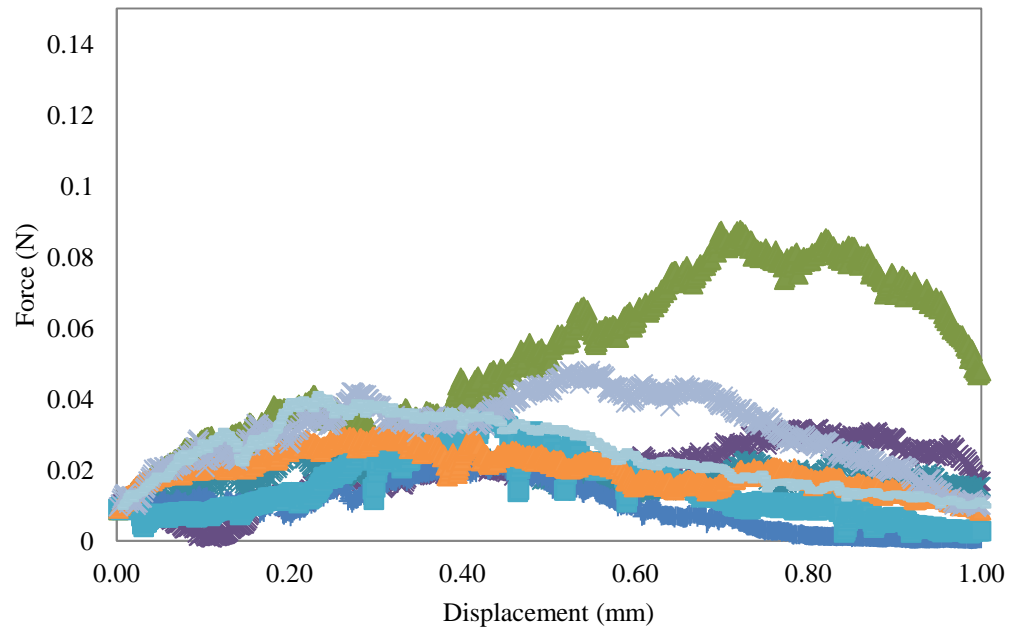


Figure II-12. Force vs. displacement for light ash at 30 s.

Appendix II

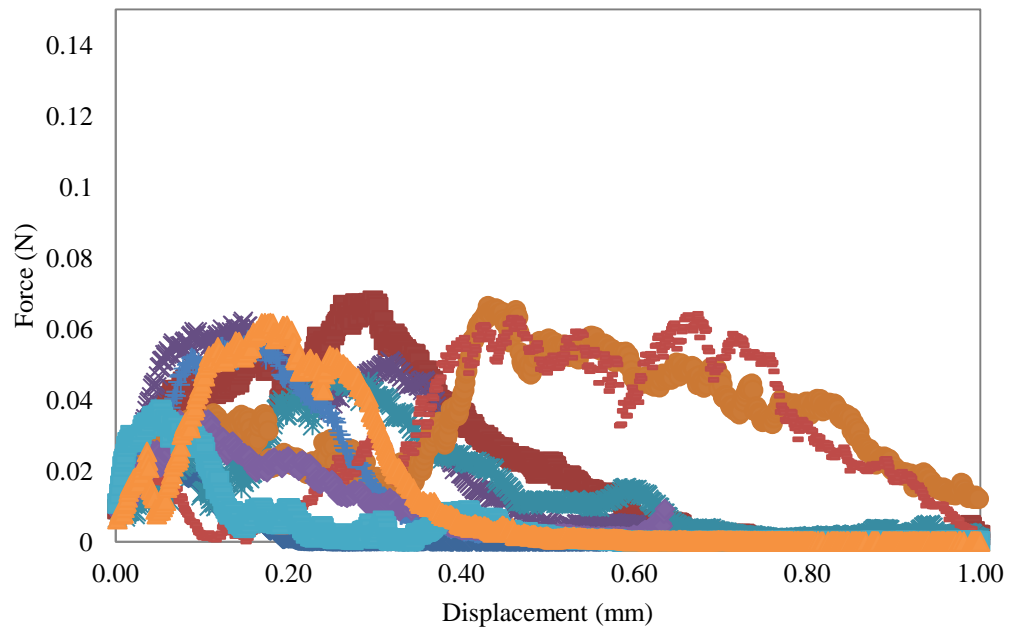


Figure II-13. Force vs. displacement for light ash at 45 s.

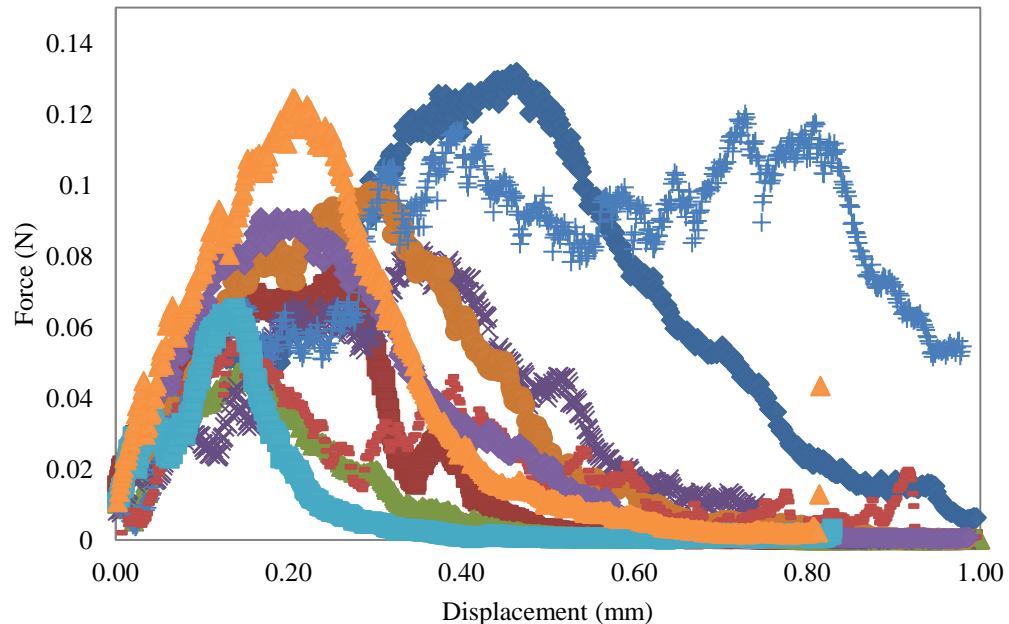


Figure II-14. Force vs. displacement for light ash at 60 s.

Appendix II

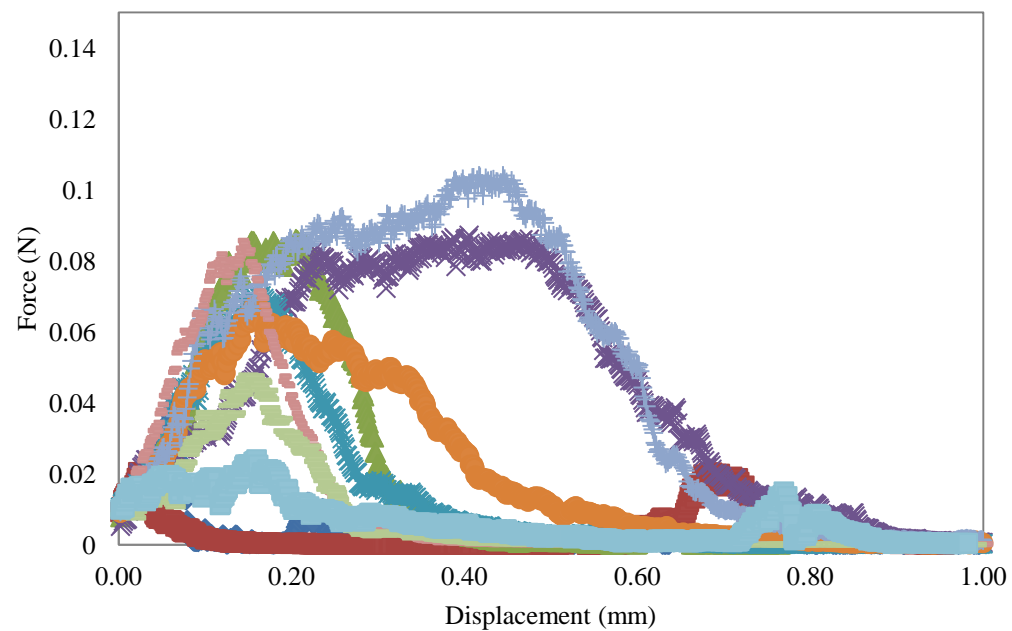


Figure II-15. Force vs. displacement for light ash at 75 s.

Appendix III The Dirac's Delta function

It is defined by the following property (Toro et al., 2012):

$$\delta(t) = \begin{cases} 0 & t \neq 0 \\ \infty & t = 0 \end{cases} \quad \text{Equation III-1}$$

With $\int_{t_1}^{t_2} dt \delta(t) = 1$

It is an operator that is often used in integrals. At $t = 0$, the function is infinitely peaked, with the total area under the curve being a unity (Figure III-1).

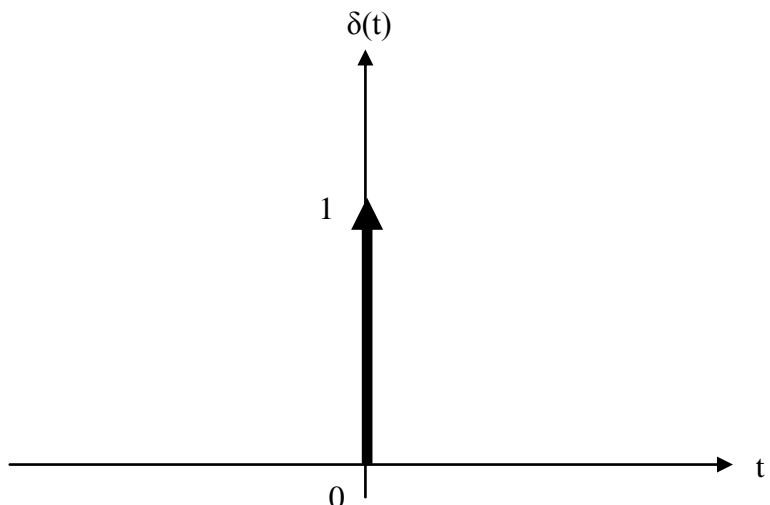


Figure III-1. Graphical representation of the Dirac's delta function (adapted from Grivet-Talocia and Gustavsen, 2015).

Appendix IV The moment equation

An expression for the moment equation was derived from Equation 6.25.

Terms on the left-hand side of Equation 6.25 must be equal to the terms on the right-hand side (Equation IV-1).

$$PBE_{LHS} = PBE_{RHS} \quad \text{Equation IV-1}$$

Therefore the following must also be true:

$$\int_0^\infty PBE_{LHS} \cdot l^j dl = \int_0^\infty PBE_{RHS} \cdot l^j dl \quad \text{Equation IV-2}$$

$$\begin{aligned} PBE_{LHS} &= \frac{\partial n}{\partial t} \therefore \int_0^\infty PBE_{LHS} \cdot l^j dl = \int_0^\infty l^j \frac{\partial n}{\partial t} dl = \frac{d}{dt} \int_0^\infty l^j n(l) dl \quad \text{Equation IV-3} \\ &= \frac{dm_j}{dt} \end{aligned}$$

Integrating the right hand side of the PBE gives an expression for the j^{th} moment (Equation IV-3):

$$= \int_0^\infty PBE_{RHS} \cdot l^j dl \quad \text{Equation IV-4}$$

$$= \int_0^\infty (2 \int_l^\infty \hat{n}(\hat{x}) d\hat{x} - \hat{l} \hat{n}(\hat{l})) \cdot \hat{l}^j d\hat{l} \quad \text{Equation IV-5}$$

Finding an analytical solution for Equation IV-7 in its current form is complicated; a transformation was used to simplify the expression. A function $f(l,x)$ (Equation IV-4) was converted into a function $g(u,v)$ (Equation IV-5) through the use of appropriate substitutions, where $f(l,x) = g(u,v)$. Now consider the planes x and l in

Appendix IV

Figure IV-1, where l represents the size of the parent fragment. For every value of l there will be a corresponding value of x . It is necessary to determine the area under the graph to determine the number density of the fragments. x and l were transformed into a function of u and v to simplify the integration.

$$I = \int_0^1 \int_0^{2x} f(l, x) dl dx \quad \text{Equation IV-6}$$

$$I = \iint g(u, v) du dv \quad \text{Equation IV-7}$$

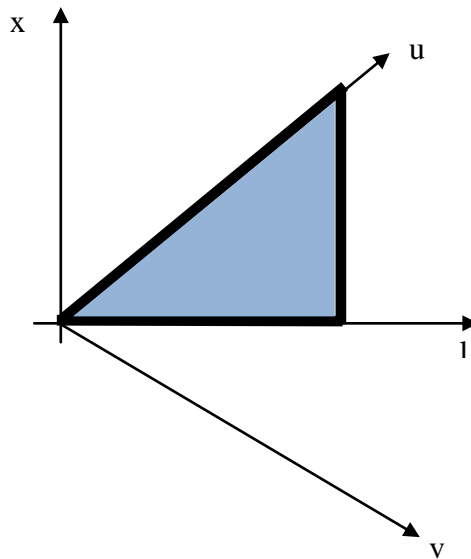


Figure IV-1. Transforming $f(l, x)$ into $g(u, v)$.

The limits change from $l \rightarrow \infty$ to $0 \rightarrow x$ after the transformation:

$$\begin{aligned} &= \int_0^\infty 2\hat{l}^j \int_0^x \hat{n}(\hat{x}) d\hat{x} d\hat{l} - \int_0^\infty \hat{l}^{j+1} \hat{n}(\hat{l}) \\ &= \int_0^\infty 2\hat{n}(\hat{x}) \int_0^x \hat{l}^j d\hat{x} d\hat{l} - \int_0^\infty \hat{l}^{j+1} \hat{n}(\hat{l}) = \int_0^\infty 2\hat{n}(\hat{x}) \frac{x^{j+1}}{j+1} d\hat{x} - \\ &\quad \int_0^\infty \hat{l}^{j+1} \hat{n}(\hat{l}) \\ &= \frac{2}{j+1} \int_0^\infty x^{j+1} \hat{n}(\hat{x}) d\hat{x} - \int_0^\infty \hat{l}^{j+1} \hat{n}(\hat{l}) \end{aligned} \quad \text{Equation IV-8}$$

Appendix IV

Substituting $\hat{m}_j = \int_0^\infty x^j \hat{n}(\hat{x}) d\hat{x}$ to simplify Equation IV-8 gives the moment equation:

$$\frac{d\hat{m}_j}{d\hat{t}} = \frac{2}{j+1} \hat{m}_{j+1} - \hat{m}_{j+1} = \frac{1-j}{j+1} \hat{m}_{j+1} \quad \text{Equation IV-9}$$